Ultra-Shallow Imaging Using 2D & 3D Seismic Reflection Methods

by

Steven Daniel Sloan
B.S., Millsaps College, 2003
M.S., The University of Kansas, 2005

Submitted to the Department of Geology
and the Faculty of the Graduate School of The University of Kansas
in partial fulfillment of the requirements for the degree of
Doctor of Philosophy
2008

Advisory Committee:

____
Don W. Steeples, Chair

____
Georgios P. Tsoflias

____
Carl D. McElwee

____
Jennifer A. Roberts

____
Robert L. Parsons

Date Defended:____________________________

The Dissertation Committee for Steven Sloan certifies that this is the approved
version of the following dissertation:

Ultra-Shallow Imaging Using 2D & 3D Seismic Reflection Methods

Advisory Committee:

____
Don W. Steeples, Chair

____
Georgios P. Tsoflias

____
Carl D. McElwee

____
Jennifer A. Roberts

____
Robert L. Parsons

Date Approved:____________________________

Abstract

The research presented in this dissertation focuses on the survey design, acquisition, processing, and interpretation of ultra-shallow seismic reflection (USR) data in two and three dimensions. The application of 3D USR methods to image multiple reflectors less than 20 m deep, including the top of the saturated zone (TSZ), a paleo-channel, and bedrock, are presented using conventional acquisition methods and a new automated method of acquiring 3D data using hydraulically planted geophones. Processing techniques that focus on near-surface problems, such as intersecting reflection hyperbolae caused by large vertical velocity changes and processing pitfalls, are also discussed. The application of AVO analysis of 2D USR data collected during a pumping test yielded amplitude variations related to the thickness of the partially saturated zone that correlated spatially and with changes in pumping. USR methods were also used to image the TSZ less than one meter deep, the shallowest TSZ reflection to date.

Acknowledgments

I would like to thank my wife Becky first and foremost for putting up with all of the late nights and weekends spent in the office and for supporting me along the way. I would also like to especially thank Don Steeples for his guidance and mentoring. I like to think that I have come a long way as a scientist since I first came to KU and it would not have been possible without him. Thanks to my committee members George Tsoflias, Jennifer Roberts, Carl McElwee, and Robert Parsons for serving on the committee and providing helpful suggestions and edits along the way. Dr. Parsons has been very generous in letting us use his property as a test site for the past several years and for that I am very grateful. Rick Miller provided financial support over my last year and made suggestions that have improved the quality of the final results of the Autojuggie research. I would also like to thank the numerous graduate students who have contributed their time in the field over the years, including: Paul Vincent, Rob Eslick, Gerard Czarnecki, Jon Jarvis, Ben Rickards, Brian Miller, Brooke Perini, and Kwan Yee Cheng.

Table of Contents

Chapter 1: 3D Seismic Reflection Methods

Chapter 2: Overview of 3D Seismic Survey Design

Chapter 3: Applying 3D seismic reflection methods to the ultra-shallow subsurface

Chapter 4: The 3D Autojuggie: Automating 3D near-surface seismic data acquisition

Chapter 5: 3D Autojuggie Survey Design & Acquisition

Chapter 6: 3D Autojuggie Processing & Results

Chapter 7: Seismic response to partial water saturation

Chapter 8: Acquisition and processing pitfall associated with clipped near-surface seismic reflection traces

Chapter 9: Ultra-shallow imaging of the top of the saturated zone

Chapter 10: Summary & Conclusions

List of Figures

Chapter 1

3D Seismic Reflection Methods

Introduction

Two-dimensional (2D) common-midpoint (CMP) surveys are by far the most common means of collecting shallow seismic-reflection (SSR) data. Although three-dimensional (3D) data can provide more detailed subsurface information and help to prevent misinterpretations that may be caused by out-of-plane reflections, at present 3D is too expensive and labor intensive to be a viable option for most shallow applications. The acquisition of 3D seismic-reflection data has become a common practice in the exploration industry (Vermeer, 2002), but is not commonly used for engineering and environmental applications due to budget limitations and the high costs of collecting 3D SSR data. SSR surveys may require receiver and/or source intervals as small as 10 cm to properly sample the wavefield in some ultra-shallow applications and acquisition costs rise rapidly as the depth of interest decreases. Despite this, 3D SSR surveys have been reported by Corsmit et al. (1988), Green et al. (1995), House et al. (1996), Barnes and Mereu (1996), Lanz et al. (1996), Büker et al. (1998), Spitzer et al. (2003), and Bachrach and Mukerji (2001a, 2004a, b).

Historical Perspective

Although 3D seismic reflection methods are widely used in the hydrocarbon-exploration industry and, many would argue, have become standard practice, they did not emerge until the early 1970s. The need for understanding subsurface reflector properties in three dimensions was observed early on. Perhaps the earliest 3D measurement was recorded by Westby (1935) in Oklahoma. Westby used a novel approach, referred to as “correlation shooting”, to correlate depths to a reflector

(Figure 1.1). The correlation method involves laying out a spread of geophones and shooting on either end to obtain CMP coverage at the center of the spread for depth correlation. Many of the source locations also included a star-shaped pattern of five source points at equal angles (Figure 1.2), yielding 3D measurements that could be used for depth correlation and dip calculations (Stone, 1994).

Although the need to understand the subsurface in three dimensions was acknowledged, recording 3D seismic data as we know it today was not practical due to equipment and technology limitations at the time. S. J. Allen (1980) published a history of seismic methods that discusses important advancements through the decades with respect to the exploration industry. The first successful reflections that led to a discovery were recorded from the Nash Dome in Brazoria County, Texas, in late 1926 (Weatherby, 1948). A successful discovery well that was drilled based on this information helped the reflection seismograph to gain acceptance. At the time, recording trucks had only one channel available. By the late 1930s, seismic systems had up to 12 channels, using 6 or more geophones per channel, and had automatic volume control. The 1940s saw the use of 24-channel systems with automatic gain control amplifiers, filtering capability, and the ability to mix traces using analog electronics.

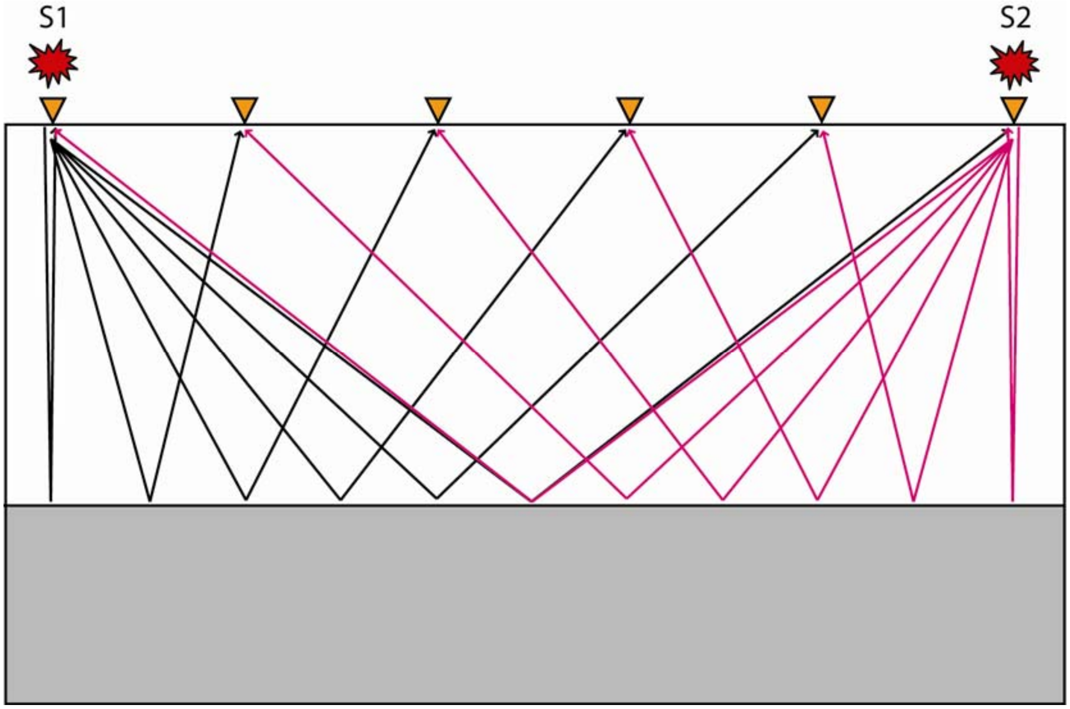

Figure 1.1. Illustration of the correlation shooting method. Shots are taken at each end of the receiver spread to record a common midpoint at the center of the spread. The common midpoint was used to correlate the depth to the reflector.

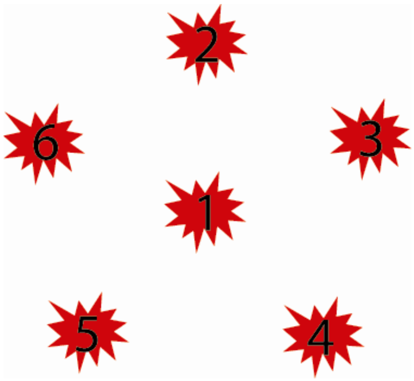

Figure 1.2. Example of the star-shaped shooting pattern employed by Westby (1935) to obtain multiple traces that could be used to correlate reflector depths. The five additional source locations are equally spaced from the center shot and maintain an angle of 72° between them.

Two important advancements were made in the 1950s. One was the development of computing technology to identify reflection energy immersed in noise by the Geophysical Analysis Group at the Massachusetts Institute of Technology. The other was a 12-channel seismograph developed by Mobil that could record data on a magnetic tape system based on an Ampex commercial audio tape recorder (Loper and Pittman, 1954). Prior to this, data were recorded using a "camera" that could produce a visible seismic record on photosensitive paper. The introduction of magnetic tape recording abilities was a major advancement that allowed for the reading, writing, and storage of seismic data that was not previously afforded by paper copies. Channel counts remained at 24 during this period.

The 1960s saw several new innovations. Although it was developed in the 1950s, it was not until the 1960s that the CMP method, described by Harry Mayne (1962), gained widespread use and changed seismic reflection methods forever. Vibroseis was developed by Conoco, digital field recording was developed by Texas Instruments, Mobil, and Texaco, and the recovery of true amplitudes was possible. By the end of the 1960s, the conversion to all-digital techniques was under way, 48-channel systems were available, and Shell had even developed a 100-channel seismograph.

The development of 3D seismic acquisition methods was hindered predominantly by the low number of channels available. With channel counts growing upwards of 100, 3D became more feasible. Walton (1972) of Esso Production Research Company designed the first method of acquiring 3D seismic reflection data. His technique utilized what he called an "X spread", or what is now known as a cross spread (Figure 1.3b). The cross-spread method uses a single receiver line and a single source line laid orthogonal to it with receiver and source intervals that are equal. The example shown here has source and receiver lines of 50 stations each (Figure 1.3b). This spread produces a single-fold subsurface coverage equal to half of the receiver and source line lengths, which is the same as setting off a single source in the center of a 50x50 receiver path (Figure 1.3a). This new technique allowed the geophysicist to view data as trace gathers or time slices using a custom-made "fiber optic viewer". Time slices allowed the interpreter to determine dip and normal moveout and to identify faults using a single gather.

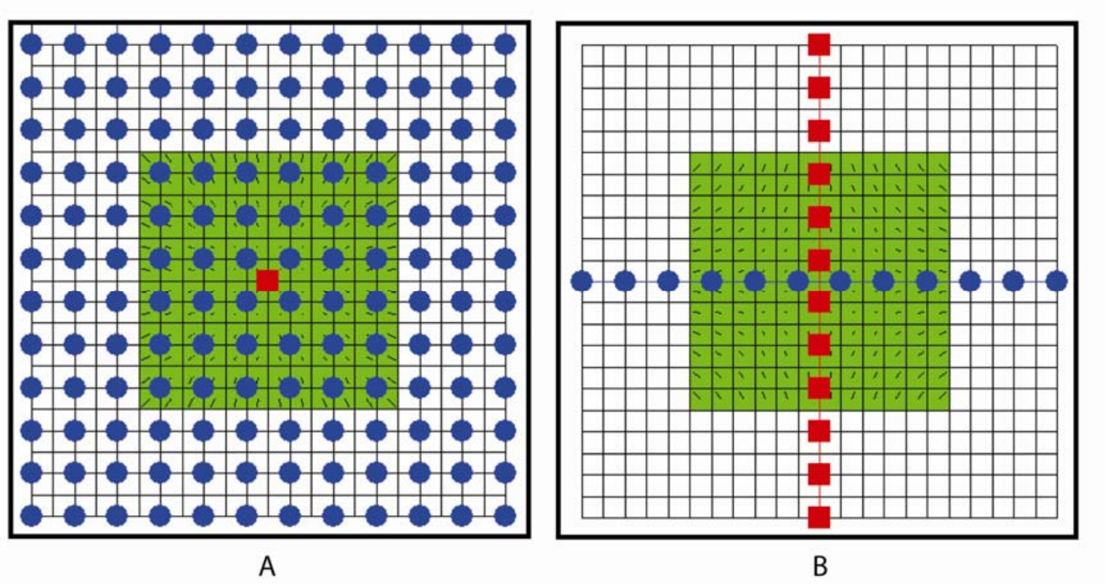

Figure 1.3. Comparison of a common-source spread (A) and a cross spread (B). Receiver and source locations are marked by blue circles and red squares, respectively. A bin grid is overlain and the single-fold subsurface coverage area is indicated by green shading.

The exploration industry's first complete land-based 3D seismic survey is presumed to have been acquired by Geophysical Service Incorporated (GSI) in Lea County, New Mexico, in August of 1973 (Allen, 1980). The GSI crew used two 48-channel systems and moved vibrators across receiver lines at right angles, just like modern orthogonal geometries, to collect true 3D data. Marine seismic acquisition was also moving towards three dimensions in the same year. Compagnie Generale de Geophysique (CGG) began collecting data using their "wide line profiling" technique, becoming the first contractor to tow three parallel marine streamers. The 1970s witnessed channel counts increase from ~100 to more than 1000, yielding seemingly unlimited possibilities for the future of 3D seismic data acquisition. As the size of data sets increased, processing technologies also had to evolve. Computers were seeing increased use due to rapid improvements, leading to the introduction of a finite-difference algorithm for migration using the scalar wave equation (Claerbout, 1971 and 1972).

3D techniques have continued to evolve and have seen major strides since the 1970s. In 1993 CGG introduced the 5-streamer vessel "Harmattan" for marine acquisition. The first 4D seismic surveys (time-lapse 3D) were acquired in 1994, again by CGG. Currently, land-based seismic systems commonly use channel counts of 5,000–10,000. Newer systems have 100,000 channel capacities, although their practical use has not seen the field yet. Marine acquisition methods commonly use 10–12 towed streamers and have seen the introduction of the wide-azimuth towed streamer (WATS) method to combat the problems with narrow-azimuth limitations inherent to marine methods. Marine acquisition is slowly moving towards land-based designs, albeit expensively, with the increased use of ocean bottom cables (OBC), where seismic cable and sensors are laid across the ocean floor, and ocean bottom seismic nodes (OBS) that use robotic submarines to plant cable-free seismic sensors in the seabed.

Previous 3D Shallow Seismic Reflection Surveys

The first 3D SSR survey that appears in the literature was reported by Corsmit et al. (1988). Their small-scale survey was conducted on a tidal flat in the Netherlands, covering an area of 22 m x 36 m. Four-fold data were acquired with a bin size of 1 m x 1m. Green et al. (1995) and Lanz et al. (1996) compared 2D and 3D SSR surveys over glacial sediments at a landfill site in Switzerland. 2D data were collected with a CMP interval of 1.25 m, while the 3D acquisition yielded 2.5 x 2.5 m bins. Although the 2D data densely sampled the subsurface, the complex geology at the site resulted in data contaminated by out-of-plane reflections and diffractions. The authors determined that 3D data were necessary to properly image shallow reflectors and delineate their geometries as 3D data allowed for the migration and proper positioning of out-of-plane and scattered energy.

House et al. (1996) describe the results of a 3D survey collected in Haddam, Connecticut. Although they were successful in identifying the bedrock surface using seismic methods, much of the data were unusable. Several factors contributed to this, including low fold and offset and azimuthal sampling variations across the survey area. This particular survey is a good example of the necessity of a well-planned 3D survey design and the importance of bin-to-bin offset and azimuth distributions. Barnes and Mereu (1996) reported a 3D SSR survey acquired near London, Ontario, over unconsolidated glaciolacustrine and till sediments overlying bedrock at ~70 m deep. Coarse sampling (3 m x 6 m bin size) led to shallow reflector images that were less favorable than their 2D counterparts due to decreased fold and poor offset distributions, compared to 2D lines acquired at the same location. Siahkoohi and West (1998) also reported results of a 3D survey, but I have not included a description as their data include interpreted “reflections” that are not likely to be real.

The 3D SSR surveys conducted to this point suffered from low fold, poor offset and/or azimuth distributions, relatively large bin sizes (coarse gridding), or a combination of several of the listed factors, resulting in poor imaging of shallow reflectors. Büker et al. (1998, 2000) report a comprehensive, high-resolution 3D SSR survey located in the Suhre Valley, Switzerland. The authors showed that dense sampling (bin sizes of 1.5 m x 1.5 m) and a relatively high population of near-offset traces (at least 6 traces <20 m in this case) in each bin were necessary to accurately image the shallowest reflector, ranging from 15–40 m in depth. Much of the survey area was covered by ~40-fold data. In short, the authors showed that high-fold data with well-sampled offset/azimuth distributions and multiple near-offset traces in each bin are necessary when considering the application of 3D seismic reflection methods to the shallow subsurface. However, collecting data in such a dense manner does come with a price. The authors report that it took a 5–7 person crew 85 days to permit, survey, and acquire the data, covering an area 357 m x 432 m in size.

Other applications of 3D SSR methods have been reported by Villella et al. (1997), Spitzer et al. (2003), Miller et al. (2004), and Schmelzbach et al. (2007). The common thread among all of the 3D SSR papers referenced here is that they have focused on the shallow subsurface (<200m). Considering the extensive use and development of 3D seismic reflection techniques since the early 1970s, there have been relatively few shallow applications, mainly due to the high costs of acquiring the densely sampled data necessary for near-surface use. Even fewer are the number of papers in the literature that address the application of 3D SSR methods to the ultra-shallow subsurface (<20 m). Papers authored by Bachrach and Mukerji (2001a, 2004a, b) are the only 3D ultra-shallow seismic references in the literature to date.

This dissertation will focus on the survey design, data acquisition, processing, and interpretation of ultra-shallow seismic reflection (USR) data and the automation of 3D USR data acquisition for increased cost-effectiveness. Subsequent chapters will discuss 3D seismic survey design, the 3D Autojuggie, and examples of 3D USR applications. Additional topics, such as processing pitfalls, AVO analysis, and ultra-shallow 2D imaging are also discussed.

Chapter 2

Overview of 3D Seismic Survey Design

Introduction

Three-dimensional (3D) seismic reflection surveys have become the standard in the exploration industry over the past two decades; however, few 3D surveys have been directed towards the shallow subsurface (<200 m depth) and even fewer have been conducted targeting the ultra-shallow subsurface (<20 m). 3D survey data are expensive to acquire because of the necessary short receiver and source intervals, which can be as small as 10 cm in some cases. Hence, the cost per square kilometer is exponentially higher in comparison to exploration-scale surveys, and 3D surveys are often too expensive to be commonly used for environmental and engineering purposes.

Seismic programs can be broken down into five main categories: planning and survey design, data acquisition, processing, interpretation, and drilling. Ultimately the quality of the processed data and subsequent interpretations are dependent on how well the survey was designed and acquired. Bad data are bad data no matter how experienced or proficient the processor is and a badly planned 3D survey can end up being a waste of money and time if it does not meet its objectives. This chapter aims to summarize some basic concepts of 3D seismic survey design; however, it is not intended to be comprehensive or to serve as the sole source of survey design information.

There are many different parameters to account for in the design process, so I will start with a few definitions, some of which are illustrated in Figure 2.1.

Inline Direction: The direction that is parallel to the receiver lines.

Crossline Direction: The direction that is perpendicular to the receiver lines.

Receiver Line Interval (RLI): The distance between adjacent receiver lines.

Receiver Interval (RI): The distance between adjacent receivers within a receiver line.

Source Line Interval (SLI): The distance between adjacent source lines.

Source Interval (SI): The distance between adjacent source positions within a source line.

Patch: All receivers that are live for any given source location.

Bin: A square or rectangular area whose dimensions are defined by half of the receiver interval in the inline and crossline directions or by half of the source interval multiplied by half of the receiver interval for surveys with a coarse receiver-line interval. All traces in a bin are assumed to have the same midpoint and will be stacked together in the common midpoint (CMP) stacking process.

Unit Cell: The area bounded by two adjacent receiver lines and two adjacent source lines.

Fold: The number of traces in a bin that are stacked together.

Nominal Fold: The highest fold achieved in the center of a patch.

Total Fold: The highest fold achieved over the entire survey area.

X_{min}: The largest minimum offset recorded.

X_{max}: The largest offset recorded.

Aspect Ratio: The ratio of the length to the width of a recording patch.

Migration Apron: Additional area added to a seismic survey to allow for the proper migration of the data set. The apron will be smaller for geologic settings with little or no dip and larger for steep dips and deeper reflectors.

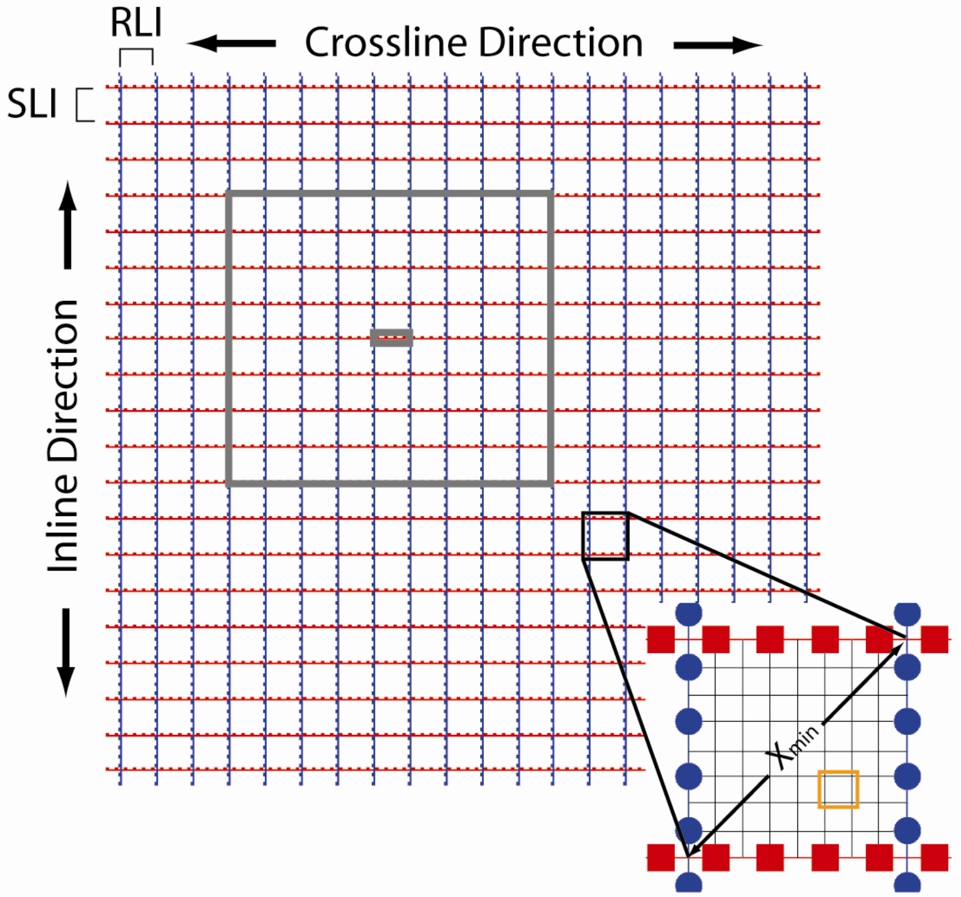

Figure 2.1. Illustration of several of the survey design terms defined in the text. The blue circles represent receiver locations and the red squares are source points. The gray square represents a patch where all receivers are live for the four source points highlighted in the middle. The enlargement depicts a unit cell (bounded by the source and receiver lines), a bin (the orange box), and the X_{min}.

When designing a survey several factors must be taken into consideration in determining the survey parameters. The depth of the deepest target is used to determine the maximum offset (X_{max}) that is necessary and the shallowest target of interest determines the X_{min} value. Rules of thumb suggest that the X_{max} be approximately equal to the target depth while the X_{min} should be less than the depth to the shallowest point of interest. Although these rules generally hold true in exploration-scale surveys, they do not apply to all situations and often do not apply to ultra-shallow surveys as we will see in subsequent chapters.

Fold ultimately determines the signal-to-noise ratio (S/N) of the acquired data and S/N theoretically increases at a rate of the square root of the fold. Figure 2.2 shows a fold map for a 4x48 patch (4 RLs of 48 receivers each). The fold ramps up on the edges from zero to some nominal value in the center of the patch and is referred to as the fold taper. The fold taper is not necessarily the same in the inline and crossline directions and its width is often times equal to roughly one fourth of the patch size in the inline and crossline directions, respectively. The fold is highest at the center of the patch and is referred to as the nominal fold. The nominal fold for a patch is typically lower than that of the entire survey area since the total fold is the sum of the nominal fold of multiple patches and increases as the patch is rolled across the survey areas in the inline and crossline directions. Because the fold tapers at the edges of the survey, the S/N ratio also decreases. To achieve maximum fold over the target of interest, the survey edges must be extended on all sides to ensure that the target is imaged with the highest S/N possible and is not overlain by the tapered edges.

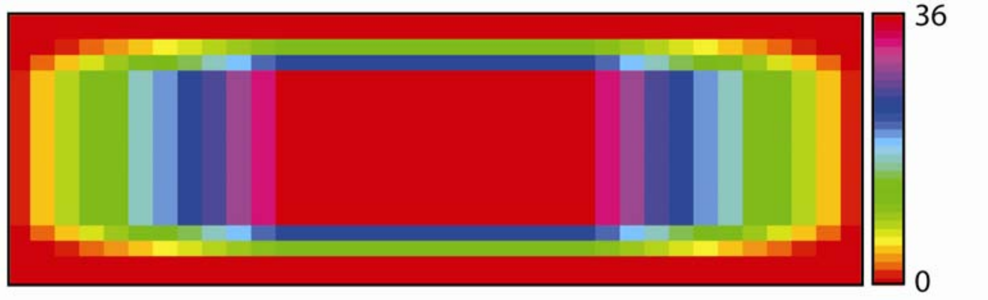

Figure 2.2. Fold map of a 4x48 patch. The fold taper builds from zero on the edges to a nominal fold of thirty-six in the center. The fold taper is much wider in the crossline direction than in the inline in this case.

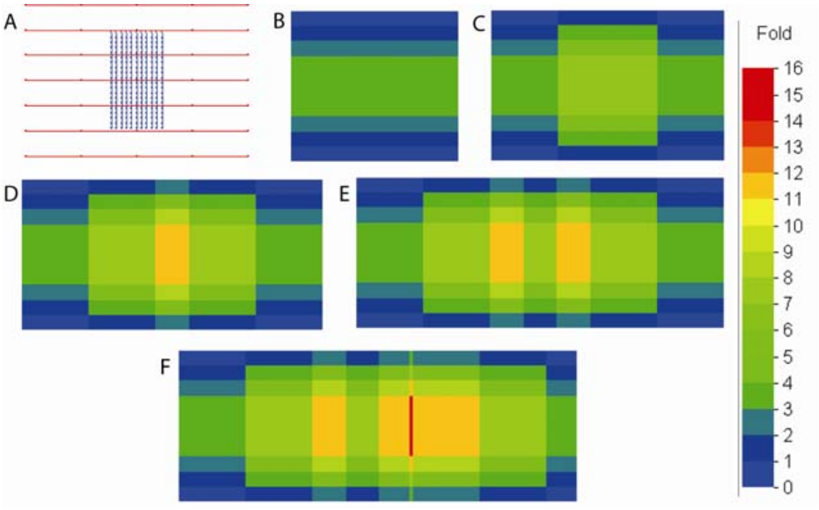

Figure 2.3. Fold maps for the 11x20 geometry in (A) for one patch (B), two patches (C), three patches (D), four patches (E), and five patches (F). Rolling six lines in each patch eventually produces the low-fold stripe in the center of (E). Rolling five lines (F) will fill in the low-fold area, but creates a one-bin wide high-fold stripe. This figure illustrates the fold-striping problems associated with patches of an odd number of lines.

Determining the appropriate patch size and the number of lines and stations to roll is critical to prevent fold striping from occurring. Figure 2.3 shows fold plots for an 11x20 patch as it is rolled along horizontally. B-E are fold plots for 1–4 patches, respectively, where the entire patch (11 lines) is rolled over. There is a low-fold stripe that occurs in the center of the plot from D to E because of rolling the entire patch. To fill this area in we must roll some number of lines less than 11. The width of the low-fold stripe is approximately the same as the high-fold stripes on either side, which indicates that rolling half of the lines should fill the low-fold area in. Since there are 11 lines, we must choose whether to roll 5 or 6 lines. Figure 2.3f shows the fold plot that results from rolling 5 lines. We see that this last roll did not produce another low-fold gap, but instead added a high-fold stripe that is one bin width in size. If we had rolled 6 lines instead of 5, a low-fold stripe would replace the high-fold stripe one bin width over. I am using this example to show that using an even number of lines in a patch makes the survey design process much easier and avoids the striping pattern. If an odd number of lines are used, there is no way to avoid striping and the stripes will continue to increase in fold as the patch is rolled vertically. Fold striping can lead to acquisition artifacts such as footprints, where an imprint of the acquisition geometry is visible on amplitude-time slices. Acquisition footprints will be discussed further in a later section.

Offset & Azimuth Distributions

When acquiring 2D seismic data each CMP has an offset distribution, or range of offsets that are sampled at each CMP location. This distribution is typically very uniform because source locations occur at regular intervals along a single line. Azimuthal distributions are of no concern because data are recorded along a single plane. The biggest difference between 2D and 3D acquisition is that data are recorded from many different azimuths. Since the subsurface may exhibit different properties in different directions, it is important to adequately sample those different azimuths, including multiple offsets along each azimuth.

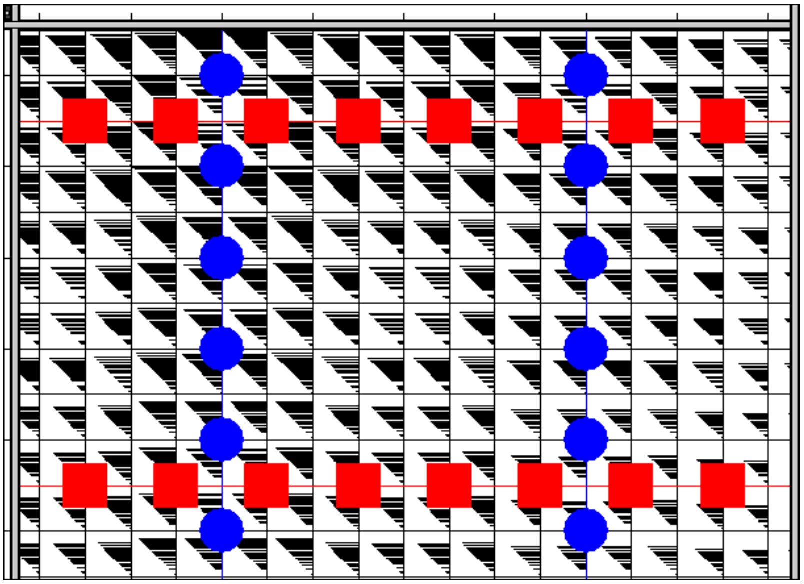

Figure 2.4. The offset distribution within a bin can be illustrated by stick diagrams, such as those shown here. A complete offset distribution would be represented by a solid black triangle, while gaps in the triangle correspond to missing offsets.

For every source-receiver pair in a patch, there is a corresponding offset and azimuth that is sampled. A single bin will have as many offsets and azimuths as traces and their distribution within a bin is predominantly controlled by the fold. Lower-fold data will have a poorer distribution of offsets and azimuths and higher-fold data will have a better distribution, assuming that the increase in fold is due to the sampling of varying raypaths. Stick diagrams (Figure 2.4) are often used to illustrate the different offsets sampled within a bin. Each offset is represented by a stick in a triangle where shorter sticks correspond to shorter offsets and likewise for longer offsets. If every offset were sampled, the triangle would be solid black. Gaps in the diagram represent offsets that have not been sampled. As traces are often moved from bin to bin by dip moveout (DMO) and migration processes, analyzing one bin is not as important as looking at a group of bins when considering how well a range of offsets has been sampled. A common rule of thumb is to look at a group that is the size of the first Fresnel zone. Even offset distributions are desired to aid in velocity analysis, NMO corrections, and migration. Limited or uneven offset distribution can lead to aliasing of dipping signal, source noise, and primary reflections (Cordsen et al., 2000) and may contribute to artifacts such as acquisition footprints.

Offset redundancy, or the number of times a particular offset is sampled, should also be considered when analyzing the offset distribution. Figure 2.5 displays an offset redundancy plot that is commonly utilized in survey design software packages. Each vertical line represents an individual bin and each colored rectangle represents a 0.25 m increment with the color indicating the number of times a particular offset has been sampled. Gray areas along the bin lines represent offsets that have not been sampled at all. This type of plot is a good quality-control tool for determining what offsets, if any, are over or under sampled or missing altogether.

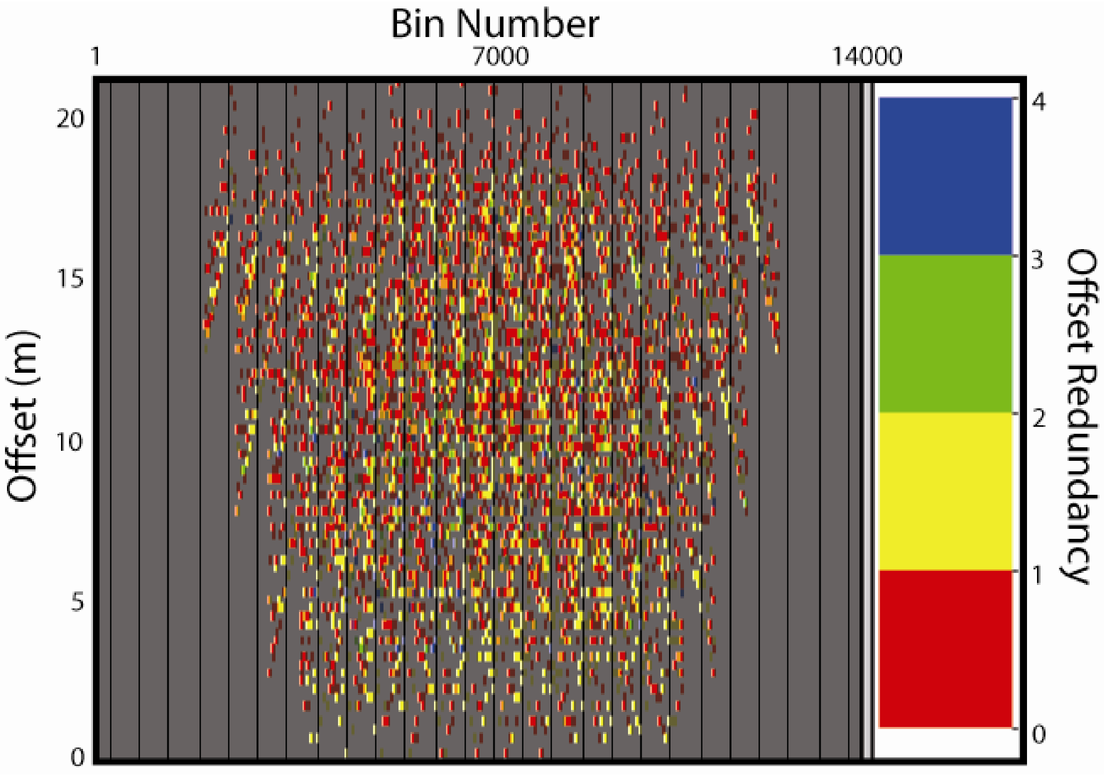

Figure 2.5. Offset redundancy plot indicating what offsets have been sampled in each bin and how many times. Gray shaded areas indicate offsets that have not been sampled.

Figure 2.6 shows a 48-fold CMP gather plotted by offset. Although this gather would be considered "high-fold", only a limited number of offsets have been sampled. Many of the trace groups have an offset redundancy of 3 or 4, which can be seen where multiple traces overlie one another at coincident offsets. This may aid in increasing the S/N ratio, but there are significant gaps between the trace groups that make reflection identification and velocity analysis nearly impossible without prior knowledge of the site and its subsurface properties.

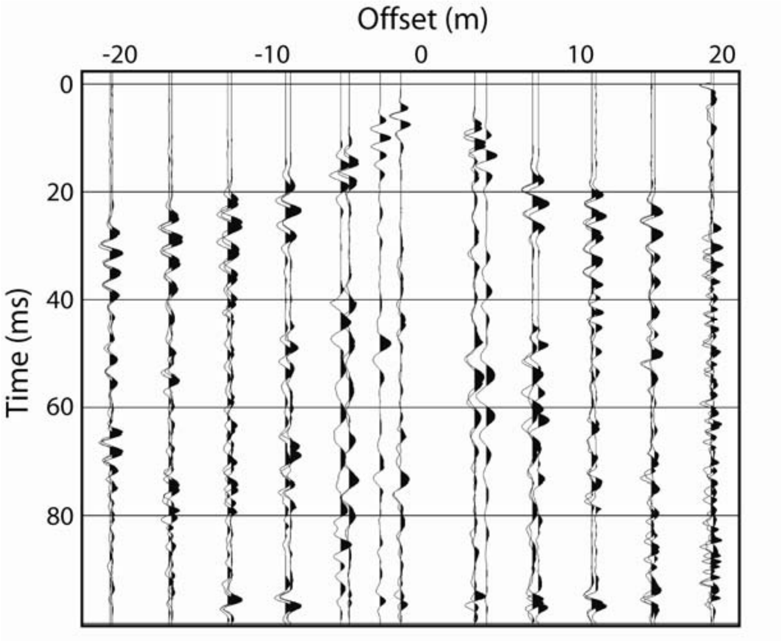

Figure 2.6. This CMP gather has a fold of 48, but a poor offset distribution. Many of the offsets have a redundancy of 3–4, where multiple traces overly each other, but the limited number of offsets sampled makes reflection identification and velocity analysis very challenging.

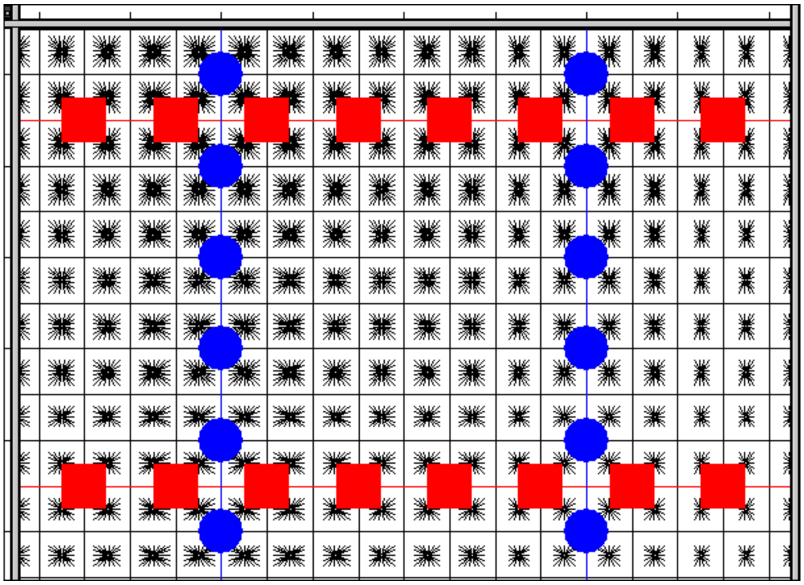

Figure 2.7. The azimuth distribution within a bin can be illustrated by a spider diagram, such as those shown here. Each leg represents an azimuth for a given source-receiver pair. The length of the leg indicates the offset.

Azimuth distributions are most affected by fold, but also by the aspect ratio (ratio of the length of the patch to its width) of a recording patch. Aspect ratios less than 0.5 will lead to poorer distribution; while an aspect ratio of 1.0 (square patch) will produce the best distribution. Azimuth distributions may be presented as spider diagrams (Figure 2.7) where each leg represents an azimuth from 0–360° and whose length corresponds to the sampled offset. Azimuth redundancy plots are also a common method of analyzing which azimuths have been sampled and how many times for a particular bin (Figure 2.8). Cordsen et al. (2000) warn that a poor mix of azimuths can lead to statics coupling problems and the inability to recognize azimuthally dependent variations caused by dip or anisotropy.

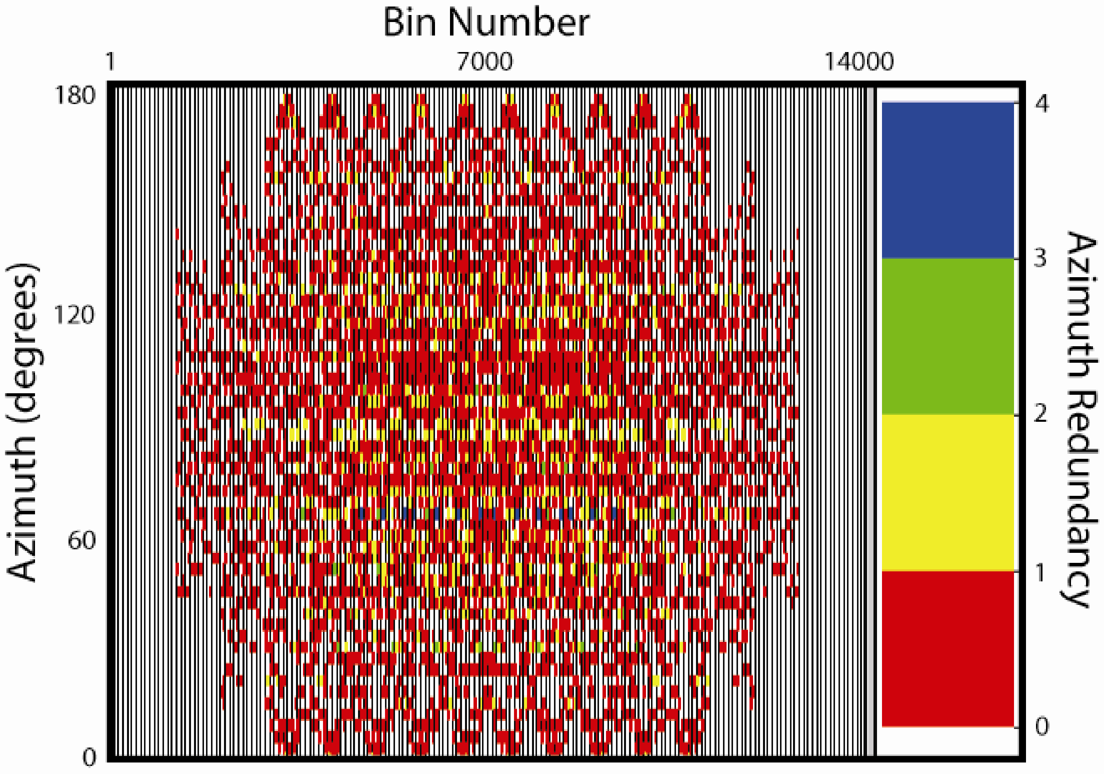

Figure 2.8. Azimuth redundancy plots indicate what azimuths have been sampled and how many times for a given bin.

Aspect Ratio

As previously mentioned, the aspect ratio of a patch is the ratio of the width of the patch to its length. For example, a square patch has an aspect ratio of 1.0 and a patch whose length is twice as long as the width has an aspect ratio of 0.5. Figure 2.9 shows five patches (4x16, 5x13, 6x11, 7x9, and 8x8) with aspect ratios of 0.25, 0.38, 0.55, 0.78, and 1.0, respectively.

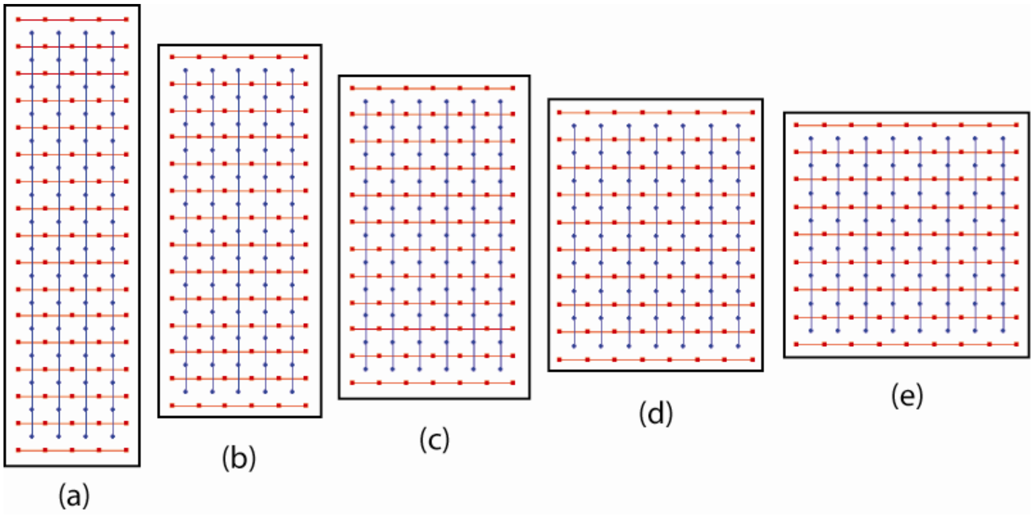

Figure 2.9. The five patches illustrated here have dimensions of 4x16 (a), 5x13 (b), 6x11 (c), 7x9 (d), and 8x8 (e) with aspect ratios of 0.25, 0.38, 0.55, 0.78, and 1.0, respectively.

Figure 2.10 illustrates that as the aspect ratio of a patch increases, the offset distribution shifts from a near-offset bias to a more uniform distribution. Azimuthal distribution shows a bias in the direction of the long axis with low aspect ratios, which becomes more uniform as the patch approaches a square. The plots shown in Figure 2.10a-e correspond to the patches illustrated in Figure 2.9a-e, respectively.

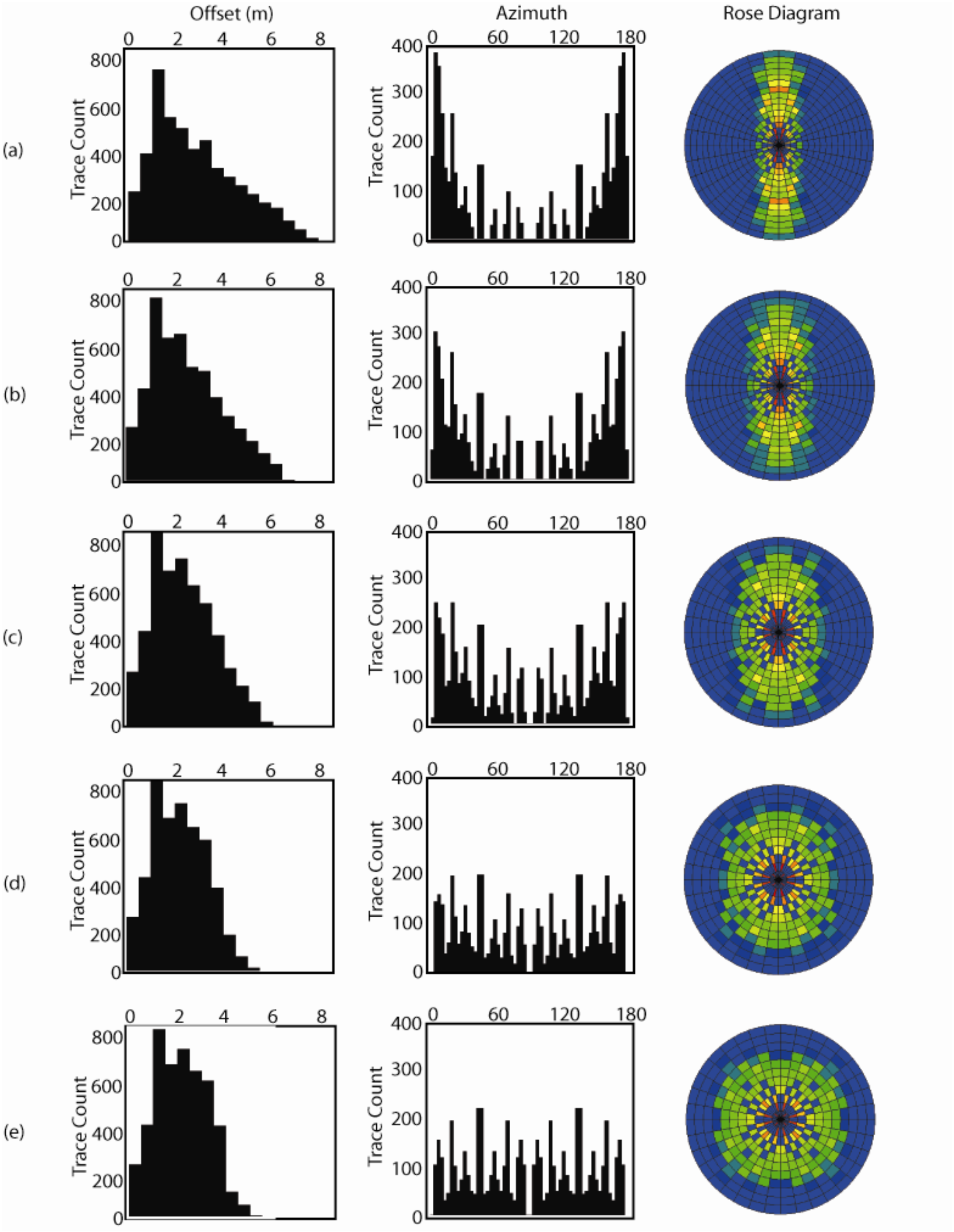

Figure 2.10. Plots of offset versus trace count (left), azimuth versus trace count (center), and the rose diagrams for the patches shown in Figure 2.9a-e, respectively, with aspect ratios ranging from 0.25–1.0.

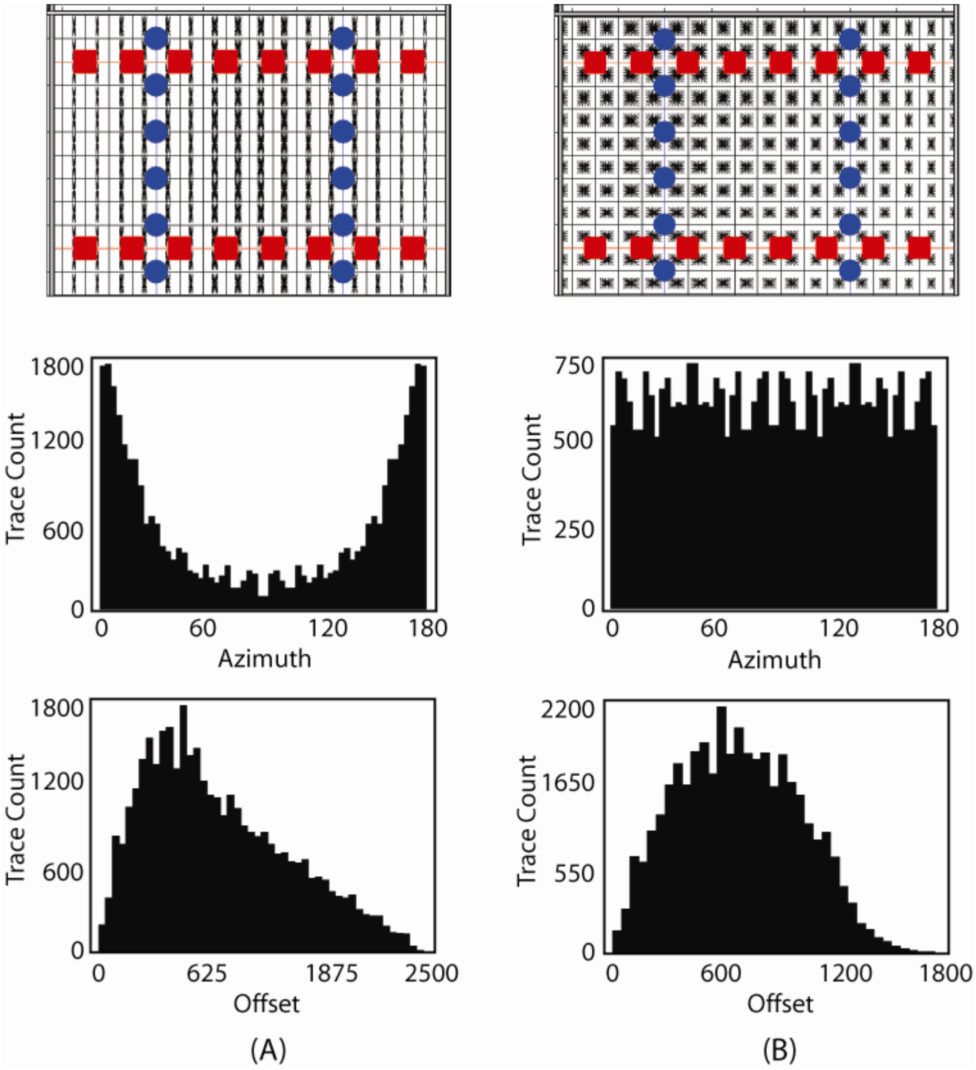

Figure 2.11. Blown-up sections of a NAZ patch (A) and a WAZ patch (B) showing spider diagrams and the corresponding azimuth-versus-trace count and offset-versus-trace count plots.

Seismic surveys are commonly referred to as narrow or wide azimuth. Patches with an aspect ratio of less than 0.5 are narrow azimuth (NAZ), while those with ratios of 0.6–1.0 are considered wide azimuth (WAZ). Figure 2.11 illustrates a blown-up portion of a NAZ (A) and WAZ (B) patch with spider plots and their corresponding plots of the azimuth-versus-trace count and offset-versus-trace count.

Their aspect ratios are 0.26 and 1.0, respectively. Clearly there is an azimuthal bias from top to bottom in the NAZ spider plot when compared to that of the WAZ, which is a square. NAZ patches will produce an offset distribution skewed towards the near offsets and an azimuthal bias. WAZ patches have a more uniform distribution of offsets and azimuths, as seen in the figure. Although NAZ patches yield poorer azimuth distributions, longer offsets are recorded. If laterally varying velocities are not a problem and long offsets are necessary, NAZ may be more economical to acquire than WAZ, considering the higher number of channels necessary to record the same long offsets in a WAZ patch.

Planning a Land 3D Seismic Survey

As discussed to this point, there are many different factors that will affect a survey design and the recorded data. This section will address a basic step-by-step approach to designing a 3D survey, although this should be viewed as a general flow and not set in stone. The most common type of land survey geometry is the orthogonal design where RLs and SLs are laid out orthogonal to one another. There are many other types of geometries, each having their own pros and cons, but this section will focus on an orthogonal geometry for simplicity. The initial stage of planning a survey should focus on identifying the problem or what the data will be used for. What is the target of interest? What types of interpretation will the data be used for? A list of some of the factors to identify includes:

- What is the shallowest layer to be mapped or that is necessary for static corrections?
- What is the deepest layer to be mapped?

- What are the resolution requirements?
- What is the maximum recorded frequency?
- What is the minimum velocity?
- What are the maximum dips expected?
- What are the S/N requirements?
- What is the necessary fold?
- What is the target size or area?

Previously acquired data from the survey area can be helpful in determining dip, velocity, and maximum frequency information. If only 2D data are available, the necessary fold for comparable 3D data is often less because 3D migration allows for the proper positioning of energy and eliminates out-of-plane reflections and diffractions. Some survey design specialists recommend using half of the 2D fold. If higher frequencies are expected, using a 3D fold equal to that of the 2D is a safe bet and, depending on its vintage, modern seismic data are likely to be of higher frequency than older data anyway. A rule-of-thumb presented by Krey (1987) suggests determining 3D fold by multiplying the 2D fold times the frequency of interest divided by 100. If previously acquired data sets are not available, preliminary tests such as walk-away (WA) tests or vertical seismic profiles (VSPs) can provide the necessary information.

Bin size is often determined based on the desired resolution or continuity of the data. The equation:

$$A_{x,y} = \frac{V_{\min}}{2.0 * F_m * \sin b},$$

is sometimes used in exploration-scale survey designs, where A is the spatial sampling interval in x and/or y, V_{min} is the minimum velocity, F_m is the maximum frequency expected, and b is the maximum dip expected to be encountered. This equation yields the minimum necessary spatial sampling interval, but smaller intervals may be desirable for shallow and ultra-shallow applications. As one might expect, higher frequencies, larger dips, and smaller velocities will require smaller bin sizes. Square bins are desirable to maintain symmetric sampling in both directions; however, if reflector dip changes with direction, rectangular bins may be used.

Two to three traces that pass through a target are usually enough to image that target with 3D data, generally speaking, although three to four are even better. Those two to three traces on a line translate to four to nine traces on a time slice. If the size of a specific target, such as a channel, is known then another way to determine the initial bin size is *bin size ≤ target size/3*. Although this bin size is generally too large, it does give the designer a starting point to work from (Cordsen et al., 2000).

Once the bin size has been determined, the RI and SI selection are straight forward since they are just twice the bin size in the x and y directions, i.e. a 1 m x 1 m bin would yield a RI and SI of 2 m for symmetric sampling. The RLI and SLI are largely dependent on the required X_{min}, which is based on the shallowest target of interest. The shallower the target is, the smaller X_{min} needs to be, which leads to smaller RLIs and SLIs. For a symmetrically sampled survey, the RLI and SLI are the same. For an orthogonal survey, the RLI and SLI are related to X_{min} by:

$$X_{\min} = (RLI^2 + SLI^2)^{1/2} .$$

X_{max} is determined based on the deepest target of interest and should be at least as long as the target is deep. Far-offset traces are often necessary for velocity analysis and imaging deeper reflectors. For exploration-scale surveys, the mute function should also be considered when determining the maximum offset. If unnecessarily long-offset (wide-angle) traces are acquired, they may be muted due to NMO-stretch related artifacts or wide-angle artifacts such as phase distortion. Acquiring these traces is a waste of channels that could be utilized elsewhere and of the time and money necessary to remove them during processing.

Migration of 3D seismic data is often necessary to reposition energy to its appropriate subsurface location and to properly image dipping beds and faults. Because of this a "migration apron" should be added to the survey area to properly image the target. The migration apron can be large or small and is dependent on the depth of the reflector and its dip. For a constant-velocity medium, the required migration apron is given by the equation:

$$MA = Z \tan\theta ,$$

where MA is the migration apron, Z is depth, and θ is the true reflector dip. Curved raypaths will help to reduce the necessary apron as velocity changes with depth. If a representative velocity function for the area is available, it can be used to determine by how much the apron can be reduced. Because dip may not be the same in all directions, the migration apron should be calculated for each edge of the survey to ensure that enough data are recorded, but not too many.

The rule of thumb given by Cordsen et al. (2000) suggests using the larger of: 1) the lateral migration movement of the expected dip; 2) the distance required to record diffractions coming upwards at a scattering angle of 30°; or 3) the radius of the first Fresnel zone. The apron may be very small in areas with little or no dip or lacking shallow reflectors and can be very large in structurally complex areas with steep dips and/or very deep reflectors.

To this point we have only considered the parameters necessary to properly image a target; however, these are only a part of the decision-making and survey-design process. Budget, time, and equipment limitations can also play a role. Densely sampled data volumes may be ideal for processors and interpreters, but high fold and small bin sizes may not be economical or may cost more than the budget will allow. In the field we are limited to the available equipment. Patch sizes must agree with the number of available channels, hence smaller bin sizes may not be an option if large maximum offsets are also necessary.

Acquisition Footprints

One of the most common artifacts in 3D seismic reflection data is the "acquisition footprint", which may also be referred to as a geometry imprint. An acquisition footprint is defined by amplitude variations related to the acquisition geometry that is used to collect the data. They may not be noticeable in data gathers or inline and crossline sections, but can be very prominent in amplitude slices displaying the seismic amplitudes for a particular time or horizon. Footprints can be especially problematic when basing interpretations on time-amplitude slices as they can mask stratigraphic changes or structural features such as faults and channels (LaBella et al., 1998).

To understand what causes an acquisition footprint, let us first consider the basic processes that traces undergo in a general 3D processing flow. In the most basic of flows traces will be binned, CMP sorted, NMO corrected, and CMP stacked. All of the traces within a bin will be sorted into a single CMP gather with each trace representing a source-to-receiver offset and azimuth. CMP gathers are then NMO corrected to flatten reflections. All of the NMO-corrected traces within a CMP gather are then stacked, or summed, together to produce a single trace where the reflections have been enhanced and random and source-generated noise (SGN) have been attenuated.

Neglecting AVO effects, random noise, and SGN, a homogeneous and isotropic medium will yield stacked traces with exactly the same amplitudes for bins with the same offset distribution, regardless of azimuth. Thus, there will not be a footprint. However, that is not the case in the real world. Seismic reflection data do exhibit AVO effects, so traces from different offsets will have slightly different amplitudes, which will affect the amplitude of the stacked trace. However, if the offset distribution is the same for every bin, the AVO effects will also be the same, again yielding stacked traces with the same amplitude and no footprint. If the offset distribution varies from bin to bin, the AVO effects will also vary to some degree, yielding some variation in the amplitude across stacked traces.

So far we have established that, in a homogenous and isotropic medium, AVO can cause a footprint itself, but it is not a problem if there are no bin-to-bin variations in offset distribution. The same can also be said for SGN. If offset distributions remain constant, various wavetrains (ground roll, airwave, multiples, refractions, etc.) are sampled and stacked in the same manner for each bin, thus there are no amplitude variations or footprint.

If offset distribution is not consistent among bins, which is likely for land-based 3D seismic data, SGN will not be continuously sampled spatially. Attenuation of SGN during stacking is achieved by destructive interference during summing. If ground roll is not continuously sampled spatially, it will not be canceled out during stacking and will "leak" through to the stacked volume. Anstey (1986) describes this and how it can be avoided using the stack-array approach, which results in an equally-spaced, continuous succession of traces in a gather. Offset-dependent energy such as primary reflections, mode-converted waves, multiples, SGN, and AVO are the most likely to be affected by bin-to-bin offset distributions. Random noise is not offset dependent, so it will not affect amplitudes in a periodic manner.

Now that we have established that offset distribution is a key factor in determining the presence of a footprint, we can consider how the survey design parameters and acquisition geometry affect the footprint. Most common acquisition geometries do not produce uniform offset distributions with the exception of *full fold* and *swath or parallel* geometries (Figure 2.12). Periodicity in the offset distribution leads to the sampling of the same offsets, which will yield periodicities in the seismic amplitudes. Similarly, if there is a systematic change in the way offsets are sampled from bin to bin, then the amplitude effect will also be systematic. Although most geometries do not produce regular distributions from bin to bin, the distribution can be periodic across unit cells, or the area between two adjacent source lines and two adjacent receiver lines (Figure 2.1).

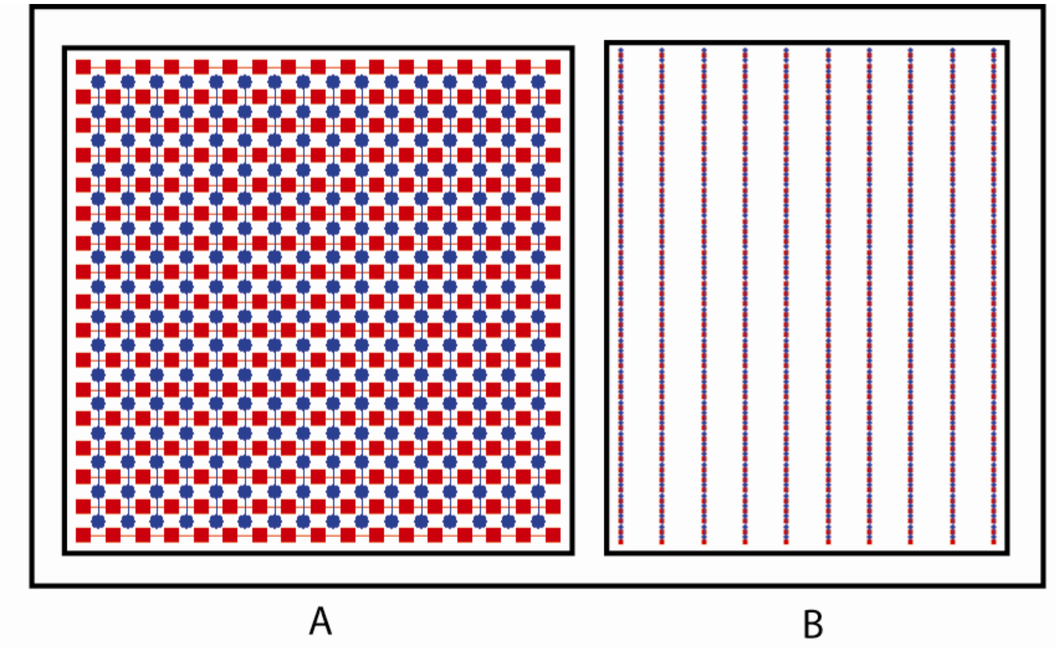

Figure 2.12. Examples of a full-fold (A) and swath (B) geometry layouts. Full-fold, swath and parallel geometries produce uniform offset distributions, unlike other commonly used layouts. A parallel geometry is just like a swath, but with the source lines shifted to lie between the receiver lines.

Azimuthal distributions can play a similar role, especially in areas with laterally changing velocities. Azimuthal bias or polarization can lead to amplitude striping like that shown in Figure 2.13. If subsurface properties are different in different directions, then the seismic data properties will also change with direction. Inadequately sampling SGN and reflections in multiple azimuths can lead to amplitude variations in stacked traces. Aspect ratio plays a key role in azimuth distribution. NAZ patches will exhibit more of an azimuthal bias, which increases as the aspect ratio decreases, while WAZ patches will be less affected as the aspect ratio approaches 1.0. Figure 2.13 illustrates an example of an orthogonal survey acquired at a test site near Lawrence, Kansas. The aspect ratio of the live patch was ~0.32, which led to an azimuthal bias along the long axis evident in the spider diagram (Figure 2.13c). Even though there are no fold variations in the center of the survey, a striped pattern is still present due to the long-axis bias of the azimuthal sampling.

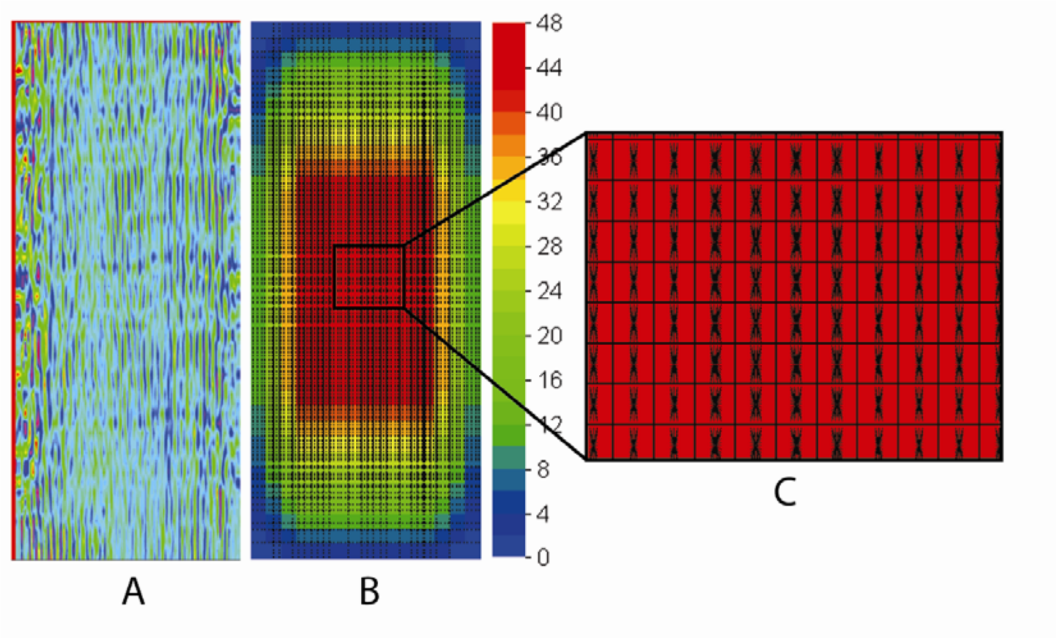

Figure 2.13. A time slice (A) from a 3D USR survey, fold and spider plots (B) of the survey design used to acquire the data, and an enlargement from the middle of the fold plot (C). Amplitude variations in the time slice correspond to changes in the azimuthal distribution in the survey design. An aspect ratio of ~0.32 caused an azimuthal bias along the long axis, which is evident in the data.

Figure 2.14 shows time-amplitude slices that correspond to data collected using the patches in Figure 2.9a-e. The square patch on the far right (e) exhibits some amplitude variability related to fold and offset-distribution variations, especially towards the edges. In comparison, (a) (aspect ratio of 0.25) is also affected by fold and offset variations, but the amplitude variations are even more pronounced because of the azimuthal bias, marked by the vertical striping.

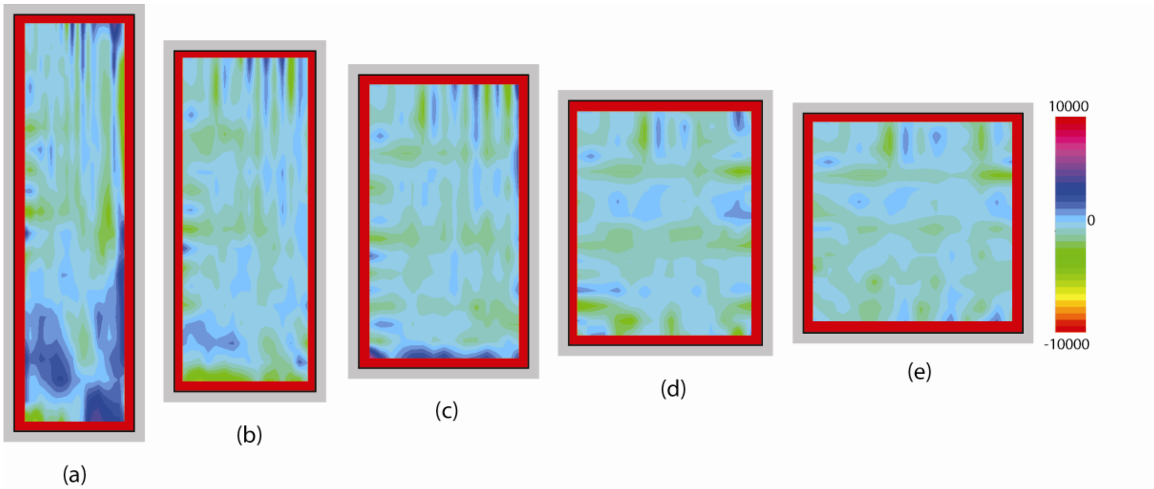

Figure 2.14. Time-amplitude slices taken from data corresponding to the patches illustrated in Figure 2.7a-e. Note the vertical striping in (a) caused by a small aspect ratio (0.25) that is less evident as the ratio increases to 1.0 (e).

Aside from offset and azimuth distributions, the selection of an appropriate NMO-correction velocity can also impact the amplitudes of stacked traces. Hill et al. (1999) showed that NMO corrections made with velocities that erred by as little as 5% would lead to amplitude variations. Incorrect NMO-correction velocities will lead to wavelet shifts that are either too big or too small at progressively farther offsets, which can destructively interfere in the stacking process.

Acquisition footprint artifacts are usually more prevalent in the shallower sections of exploration-scale data due to lower fold and lower signal-to-noise ratio.

Offset and azimuth distributions that do not adequately sample the 3D wavefield do not allow for the attenuation and elimination of SGN.

Shallow 3D Survey Design Considerations

The acquisition of SSR and USR data requires dense receiver and source spacings to properly sample the near-surface wavefield and prevent signal aliasing. Small intervals are also necessary to take advantage of high frequencies. Knapp and Steeples (1986a,b) discuss the selection of acquisition and equipment parameters. Although their papers focused on 2D design, many of the same concepts and rules-of-thumb still apply to 3D in terms of sampling the wavefield.

The most obvious difference between exploration-scale and near-surface seismic methods is scale. Surveys with deeper targets of interest often use source and receiver line spacings in the 100s of meters, while surveys focused on the shallow subsurface may use intervals in the 10s of centimeters to 10s of meters. While each survey type has its own challenges, much of the source of error in deeper surveys can be attributed to the effects of the weathering zone. Considering that a much higher percentage of shallow data is recorded from the weathering zone (and all of it in many ultra-shallow cases), SSR and USR data acquisition must deal with unique complexities not often faced by exploration or to the same degree. Although exploration surveys combat various types of noise such as surface waves and multiples, most of the noise contained in the shallow section (direct, refracted, airwave) is not a problem as it usually exhibits much lower phase velocities than the target reflections and is simply removed. Near-surface reflections can be totally or partially obscured by numerous types of source-generated noise (SGN), creating limited offset ranges where reflections can be identified.

Early examples of 3D SSR (House et al., 1996; Barnes and Mereu, 1996) show the importance of regular subsurface coverage, fold, well-sampled offset distribution, and near-offset traces. Coarse sampling grids (relatively large RLI, SLI, RI and SI) precluded the imaging of shallow targets and, in some cases, rendered 3D migration useless because of poor offset distributions among bins. Büker et al. (1998, 2000) demonstrated the importance of near-offset traces by comparing their acquisition design and resulting images to those of earlier surveys using the same data. They determined that, for their particular site, at least 6 traces with source-to-receiver offsets ≤ the depth of the shallowest reflector were necessary to image it. Near-offset traces can also improve t_0 and depth control. 3D methods can produce images superior to their 2D counterparts, but only if the necessary sampling criteria are met.

Typical shallow and ultra-shallow surveys may have larger ranges of angles of incidence than their petroleum-exploratory counterparts and those angles can change faster with depth. Pullan and Hunter (1985) showed the effects of source-to-receiver offset and angles-of-incidence on shallow seismic reflections. Synthetic and field data examples exhibited amplitude and phase variations at source-to-receiver offsets ≥ the critical distance (X_{crit}) (the nearest offset at which refracted energy can be received). Although this phenomenon is not limited to the shallow subsurface, the nature of SSR data requires us to be aware of it, especially during the data processing stages. SSR data contain numerous types of SGN, including the direct wave, refracted waves, ground roll, and the airwave. Ultimately the seismic velocity properties of the subsurface determine the *x-t* relationships of these wavetrains, where reflections may be observable only at a particular range of offsets, or the "optimum window" (Hunter et al., 1984), without being masked by other types of energy.

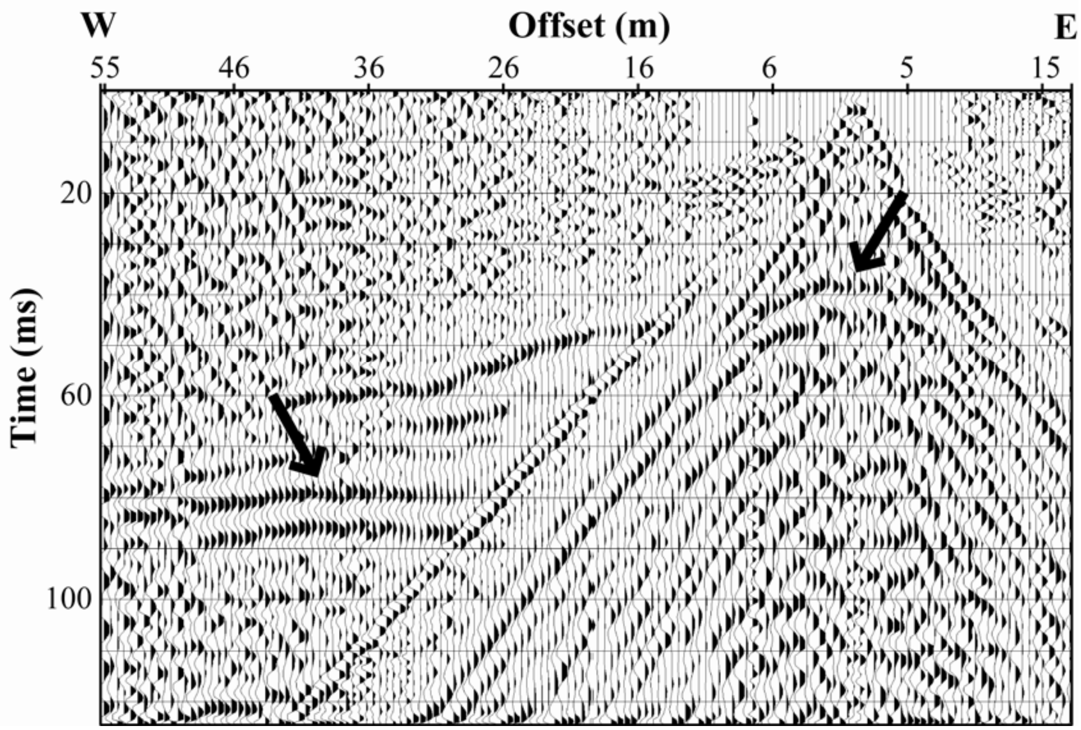

Figure 2.15. Example 2D common-shot gather with reflections from the top of the saturated zone (~37 ms) and bedrock (~80 ms), indicated by the arrows. The TSZ reflection is coherent between offsets of ± 6 m; however, the bedrock reflection is not observable at offsets less than 26 m.

Figure 2.15 shows an example seismogram with reflections from the top of the saturated zone (TSZ) (~37 ms) and from the bedrock surface (~80 ms). Note that the TSZ reflection is coherent between offsets of ~± 6 m, while the bedrock reflection is not observed until ~26 m. In certain geologic settings, the optimum window may be limited to or incorporate offsets beyond X_{crit}, where reflected energy is referred to as post-critical reflection. Why does this matter? The answer is two-fold. If post-critical reflected energy is of a different polarity, then the pre- and post-critical reflections can destructively interfere during the CMP stacking process, harming the resulting image instead of enhancing it. If sufficient pre-critical reflected energy is not present and the post-critical portion is used for NMO corrections and stacking, then the resulting CMP-stacked reflection can be out of phase by as much as 180°, which will lead to erroneous depth calculations. The simple solution suggests tossing out the post-critical portion of a reflection, but this may not always be feasible.

Figures 2.16 and 2.17 illustrate the range of angles-of-incidence recorded at various depths with patches having aspect ratios of ~0.32 (NAZ) and ~0.74 (WAZ), respectively. In both figures, (B-F) represent depths of 1, 5, 10, 20, and 40 m, respectively. Both the NAZ and WAZ patches record wide-angle traces at the shallowest depth (1m), nearly all of which would lie in the post-critical range in most situations. As the target depth increases, the WAZ patch records more traces at smaller angles-of-incidence. This difference is solely based on the patch geometry, but this example illustrates how the choice of aspect ratio impacts the recorded data. A WAZ patch will produce more traces that are closer to vertical or near-vertical incidence (which is assumed in many processing techniques); however, a NAZ patch will record a wider range of incidence angles, which may be desirable for amplitude-versus-offset (AVO) or amplitude-versus-angle (AVA) analysis.

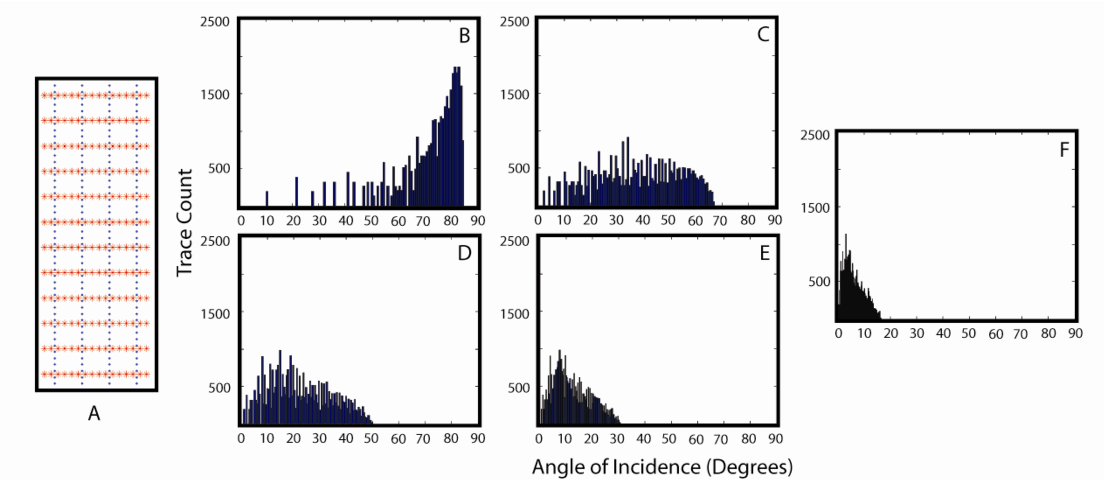

Figure 2.16. A NAZ patch (A) and the trace counts of angles-of-incidence recorded for depths of 1, 5, 10, 20, and 40 m (B-F), respectively.

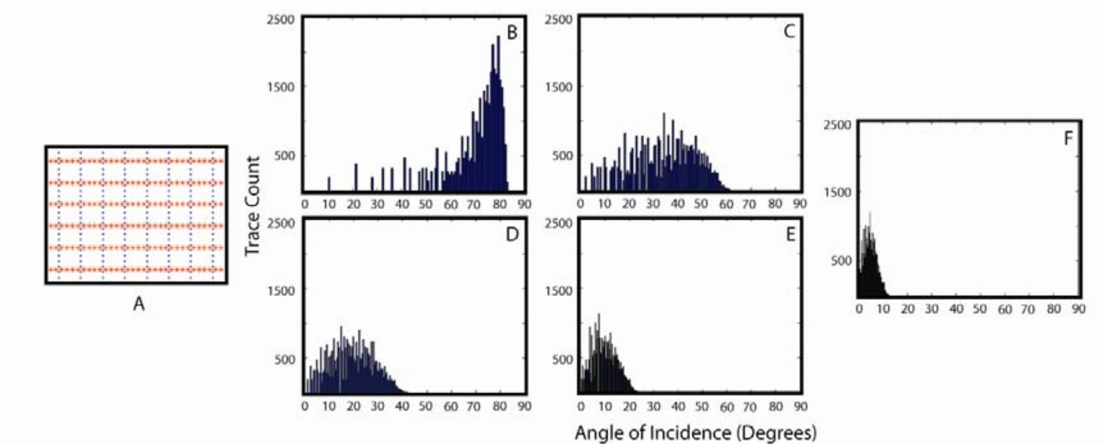

Figure 2.17. A WAZ patch (A) and the trace counts of angles-of-incidence recorded for depths of 1, 5, 10, 20, and 40 m (B-F), respectively.

Low-velocity reflections with steep curvatures, such as those produced at the overburden-bedrock or unsaturated-fully saturated interfaces, are often subjected to significant stretch due to the NMO-correction process. Wavelet stretch increases with the source-to-receiver offset and should be removed by way of a stretch mute and adequate taper to prevent a decrease in S/N, decreased reflection frequency, and subsequent loss of resolution. Severe stretch muting is often necessary for shallow, low-velocity reflections, sometimes as low as 5% (Miller, 1992). Figure 2.18 shows two 24-fold, 2D CMP gathers that have had an early mute applied to remove the direct and refracted arrivals. The hyperbolic event at ~23 ms on the left gather is a reflection from the top of the saturated zone. An NMO velocity of 456 m/s has been applied to flatten the event, combined with a 23% stretch mute to remove the significantly stretched wavelets. The fold for this particular reflection has been reduced from 24 to 9. In comparison, Figure 2.19 displays CMP gathers from the same survey, but with a deeper reflection from a paleo-channel surface, marked by the arrows. The gather on the left and right show the reflection before and after NMO corrections, respectively, using a velocity of 1200 m/s. Because of the lesser curvature of the reflection, there is less moveout and minimal stretch. Thus, the effective fold for this reflection remains the same.

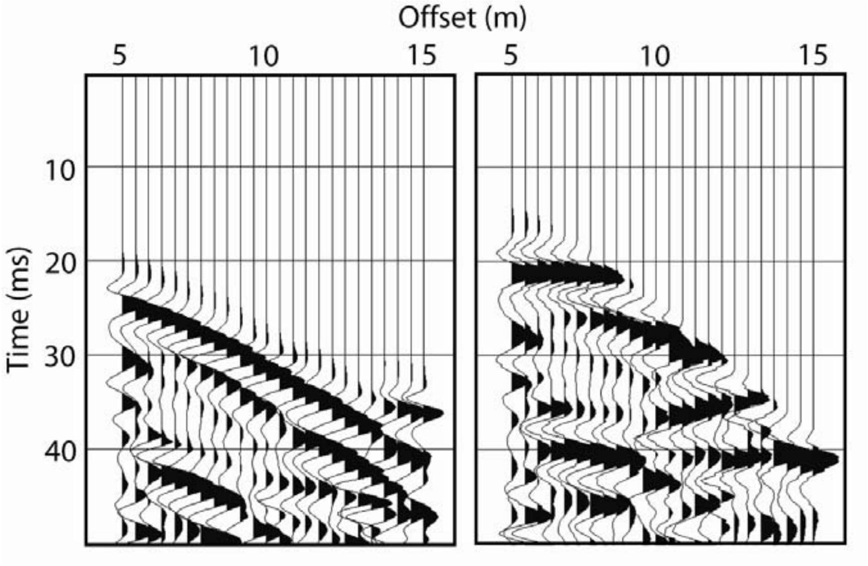

Figure 2.18. Coincident 2D CMP gathers after an early mute was applied to remove the first arrivals. The hyperbolic event at ~23 ms on the left-hand gather is the reflection from the TSZ. The gather on the right shows the same reflection after NMO corrections and stretch muting. The fold has been reduced from 24 to 9.

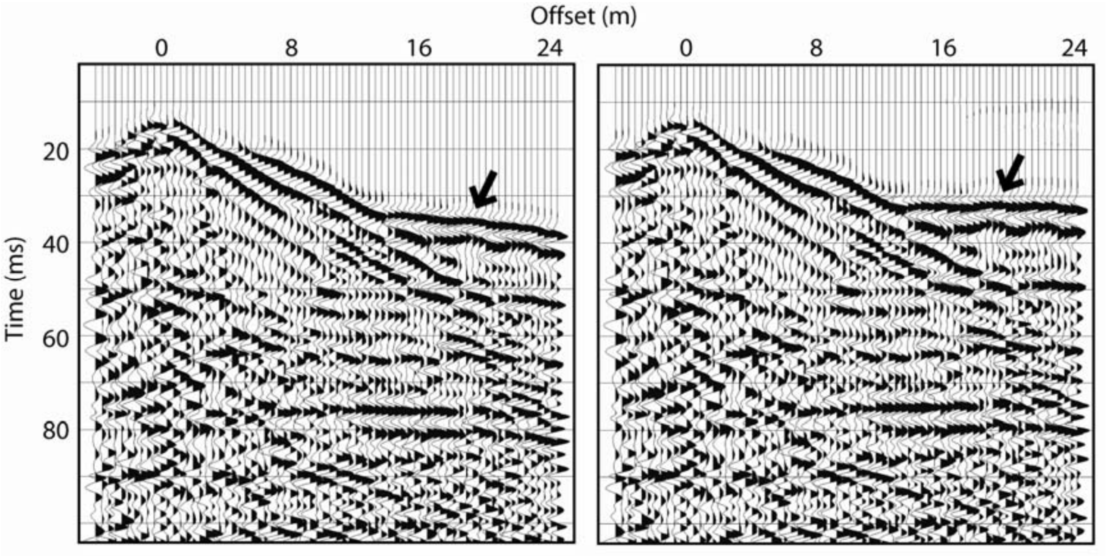

Figure 2.19. Coincident 2D CMP gathers after an early mute was applied to remove the first arrivals. The hyperbolic event at ~32 ms on the left-hand gather is the reflection from a paleo-channel. The gather on the right shows the same reflection after NMO corrections. This reflection exhibits less moveout than the TSZ reflection in Figure 2.18, due to a higher velocity, and subsequently less wavelet stretch.

The purpose of this example is to demonstrate that fold is not a constant, but instead varies with time. A survey geometry design may lead to a total fold of 48, for example, but each reflection will have its own fold value, which may vary in time and from bin to bin. Reductions in fold may be caused by early muting to remove the first arrivals, surgical muting to remove the airwave, tail muting to remove ground roll, or stretch muting to remove the stretched portion of NMO-corrected traces, among other processing techniques. If the objectives of a survey call for a minimum fold for a particular reflection of interest, these factors should be taken into consideration. Pre-survey testing, such as a walk away test, can be used to approximately determine some of these factors such as the necessary stretch mute for various reflections. However, it should also be realized that the subsurface properties impose their own limitations. The shallower a reflection is, the more likely it is that there will be interference from other energy, such as the direct or refracted arrivals. If a reflection merges with a refraction and can not be separated, then useable fold can only be increased by adding more traces at offsets smaller than that at which the two events are no longer distinguishable (assuming that higher frequencies can not be enhanced).

Clipped seismic traces can also present problems, especially in the ultra-shallow subsurface (Sloan et al., 2008). Dense receiver and source spacing, sometimes as small as 5–10 cm, can create a situation where the source energy overdrives the geophone or saturates the digital word, causing clipped wavelets that, when filtered, can create hyperbolic "pseudo-reflections" (Figure 2.20). Removal of clipped traces is required to avoid possible artifacts, which subsequently reduces fold.

This phenomenon is discussed in more detail in chapter 6. Source testing should be conducted prior to each survey to ensure that the optimal source is chosen to meet the survey objectives.

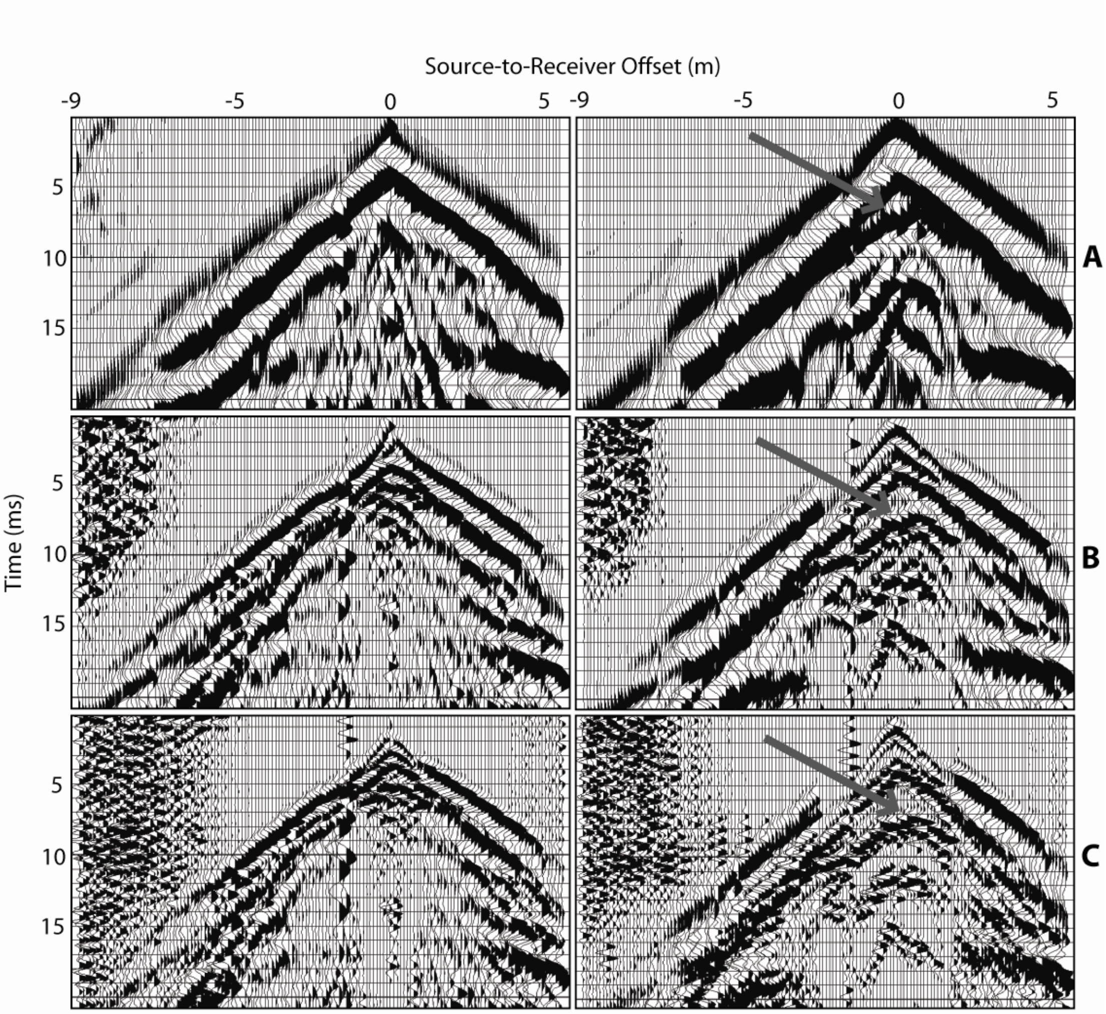

Figure 2.20. Field records collected with the .22-caliber rifle (left) and .223-caliber rifle (right) at the same location. Data are displayed with bandpass filters of 200–500 Hz (A), 600–900 Hz (B), and 1000–1300 Hz (C). Arrows indicate hyperbolic events created by filtering clipped wavelets.

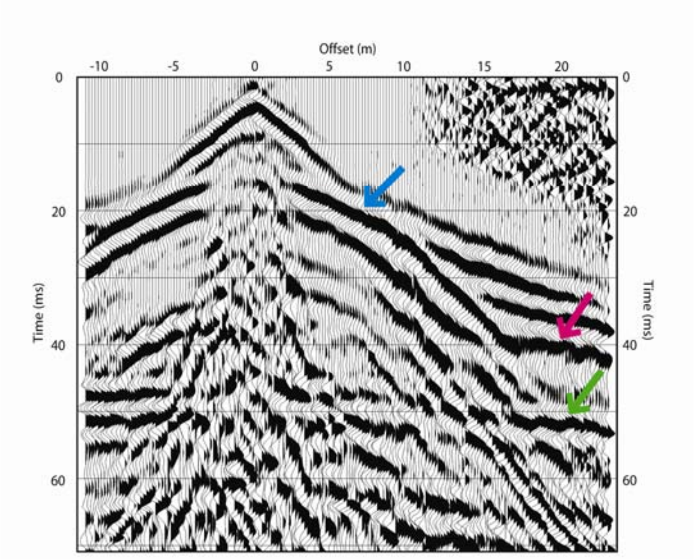

Figure 2.21. 2D CMP gather from a survey acquired near Lawrence, Kansas.

Figure 2.21 shows a CMP gather from a 2D survey acquired at a test site located near Lawrence, Kansas. The reflection marked by the pink arrow is located at a depth of ~7–8 m. Due to a very large vertical velocity contrast (~300–1600 m/s), which is common in the ultra-shallow subsurface, this reflection is not observed at offsets less than ~15 m. Using the rule-of-thumb of selecting an X_{max} equal to the depth of the reflection of interest, there would not even be a hint of this reflection in the data. This example serves to show that pre-survey testing, such as walkaway tests, should always be conducted prior to acquiring USR data to ensure that appropriate acquisition parameters are selected.

This chapter is not intended to be all inclusive or serve as the sole reference for designing a 3D survey. It is intended to present the reader with some of the basic terminology and concepts to better understand subsequent chapters on my own survey designs and why some of the parameters were chosen.

Chapter 3

Applying 3D seismic reflection methods to the ultra-shallow subsurface

Results of this study have been published or are currently under review under the following citations:

Sloan, S. D., Steeples, D. W., Tsoflias, G. P., 2008, Imaging a Shallow Paleo-Channel Using 3D Ultra-Shallow Seismic-Reflection Methods: SAGEEP, Expanded Abstracts, **21**, 586-578.

Sloan, S. D., Steeples, D. W., and Tsoflias, G. P., 2008, Ultra-shallow imaging using 3D seismic-reflection methods: Near Surface Geophysics, in review.

Introduction

There are multiple examples of three-dimensional (3D) shallow seismic reflection (SSR) surveys in the literature (Corsmit et al., 1988, Green et al., 1995; House et al., 1996; Barnes and Mereu, 1996; Lanz et al., 1996; Büker et al., 2000; Spitzer et al., 2003), but they are still relatively uncommon and 3D ultra-shallow seismic reflection (USR) surveys are even more rare (Bachrach and Mukerji, 2001a, 2004a,b). The dense source and receiver intervals necessary to properly sample the wavefield in the shallow subsurface quickly drive acquisition-related costs up as target depth decreases and this increase is exponentially faster when working in three dimensions. For example, conducting a 3D survey the size of a football field on a 3 x 3 m grid would require 527 geophone locations, whereas a 1 x 1 m grid would require 9 times that number of locations. Although two-dimensional (2D) data are less cost- and labor-intensive to acquire, 3D SSR data can yield more accurate subsurface images and avoid artifacts and misinterpretations caused by out-of-plane reflections and scattered energy (Green et al., 1995; Lanz et al., 1996).

With the emerging field of hydrogeophysics continuing to grow, the use of 3D USR and SSR surveys may become even more important. 3D seismic methods allow the continuous tracking of reflectors in the subsurface, which may allow the identification of potential flowpaths and/or sinks where contaminants can migrate and pool. With respect to the remediation of contaminated sites, this gives the advantage of prioritizing the placement of wells for specific targets and reduces the time and costs associated with drilling unnecessary wells. The high costs inherent to the acquisition and processing of 3D USR data often preclude the method as an economical option; however, as the protection of our fresh water supplies continues to become a larger issue, these methods may become a more viable option.

The objectives of the study presented here were to image multiple reflectors less than 20 m deep, including the top of the saturated zone (TSZ), paleo-channel features, and bedrock, using 3D USR techniques. A small 3D USR survey was designed and acquired, covering an area of ~15.5 m by 35.5 m. Data were processed using commonly applied SSR processing techniques. The test site is an open field located four miles south of Lawrence, KS in the floodplain of the Wakarusa River (Figure 3.1). Dickey et al. (1977) characterize the near-surface material as a Wabash Series silty clay loam. Bedrock consists of alternating layers of shale and limestone characteristic of the Pennsylvanian System in Kansas. Two-dimensional (2D) surveys previously acquired at the test site have imaged a channel feature at ~7–8 m depth. The channel feature coincides with a linear surface expression, marked by changes in the soil makeup, which is lower in elevation than the surrounding area (Figure 3.1).

One of the challenges encountered during processing is the presence of a large vertical velocity gradient. It is not uncommon for USR and SSR data to be collected in geologic settings where large velocity contrasts are present. Two common scenarios where this is likely to be observed include a shallow water table located within unconsolidated sediments and unconsolidated materials overlying bedrock. The interface between unsaturated and fully saturated materials can exhibit contrasting velocities ranging from as low as 200–300 m/s to 1600 m/s or more in the span of one or two seismic wavelengths (Birkelo et al., 1987; Sloan et al., 2007). The velocity contrast between unconsolidated overburden and bedrock has been shown to vary by as much as 800% (Miller et al., 1989; Goforth and Hayward, 1992).

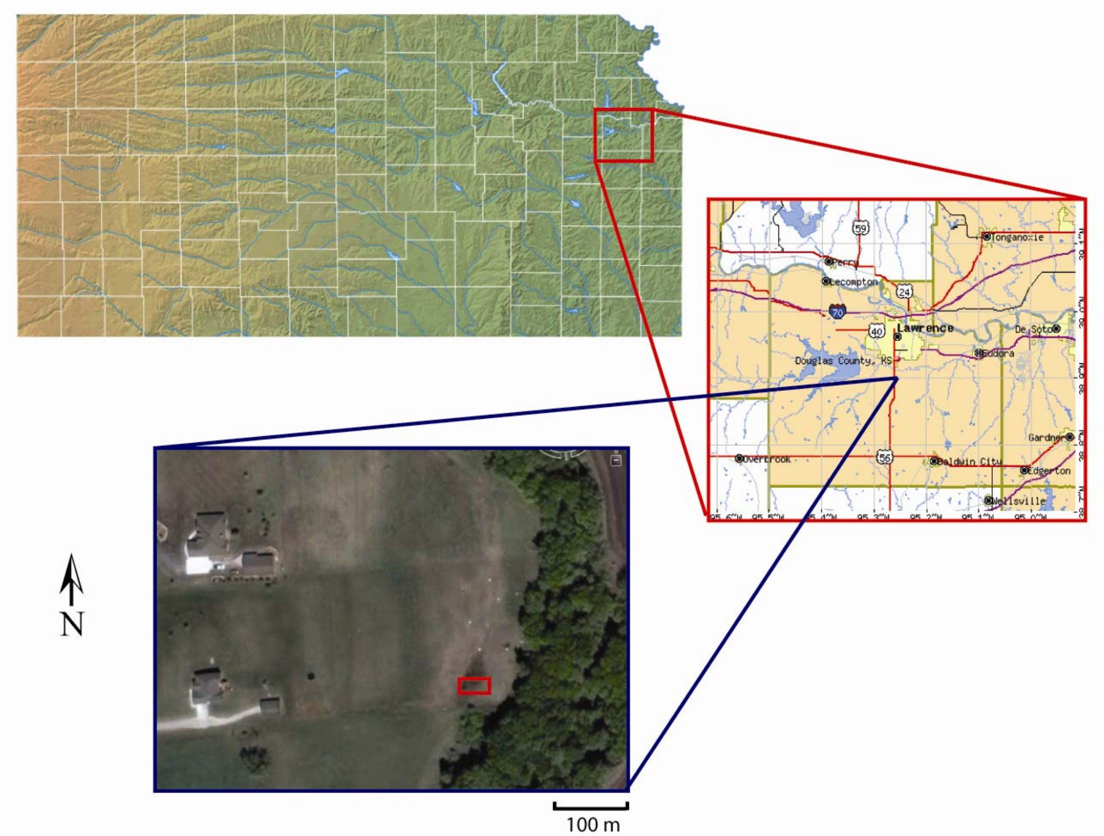

Figure 3.1. Site map indicating the location of the field site and the position of the 3D survey, which is bounded by the red box. Note the N-S trending surface feature perpendicular to the survey.

Processing USR and SSR data collected in such an environment can be challenging, to say the least. The combination of large velocity contrasts and multiple shallow reflectors often leads to intersecting reflection hyperbolae.

Applying normal moveout (NMO) corrections to low-velocity (steep curvature) reflections may require severe stretch muting to combat stretch-related artifacts (Miller, 1992); however, NMO correcting intersecting reflections can cause even more problems (Miller and Xia, 1998). Previous work by Buchholtz (1972) and Dunkin and Levin (1973) has demonstrated the effects of wavelet stretching inherent to the NMO-correction process, including amplitude variations, decreasing frequency and resolution, and decreasing the signal-to-noise (S/N) ratio. Nonstretch-related artifacts can also be created due to abrupt changes in velocity, including wavelet duplication and sample compression and reversion (Miller and Xia, 1998).

The negative effects of large vertical velocity gradients on SSR data have been demonstrated in previous studies (Miller and Xia, 1998; Shatilo and Aminzadeh, 2000; Bradford, 2002; Bradford and Sawyer, 2002; Brouwer, 2002). Bradford (2002) and Bradford and Sawyer (2002) showed that depth estimates calculated using interval velocities determined by the Dix equation may exhibit an error of 10–100% due to NMO-associated errors. The authors suggest applying prestack depth migration (PSDM), which was found to produce more accurate images at their test sites.

Miller and Xia (1998) demonstrated the effects of NMO corrections on intersecting reflection hyperbolae due to large vertical velocity gradients using synthetic and field data examples. Effects such as stretch, sample reversion, sample compression, wavelet smear, and duplicate wavelet mapping were shown to require severe stretch mutes to prevent processing artifacts and a decrease in the signal-to-noise ratio (S/N) (Figure 3.2). Such severe muting may ultimately lead to the loss of reflection signal and degraded stacked sections. The authors successfully employed an optimum-window based processing scheme where reflections were segregated by offset and NMO corrected independently, resulting in a more accurate stack than that produced using a multiple-velocity NMO correction.

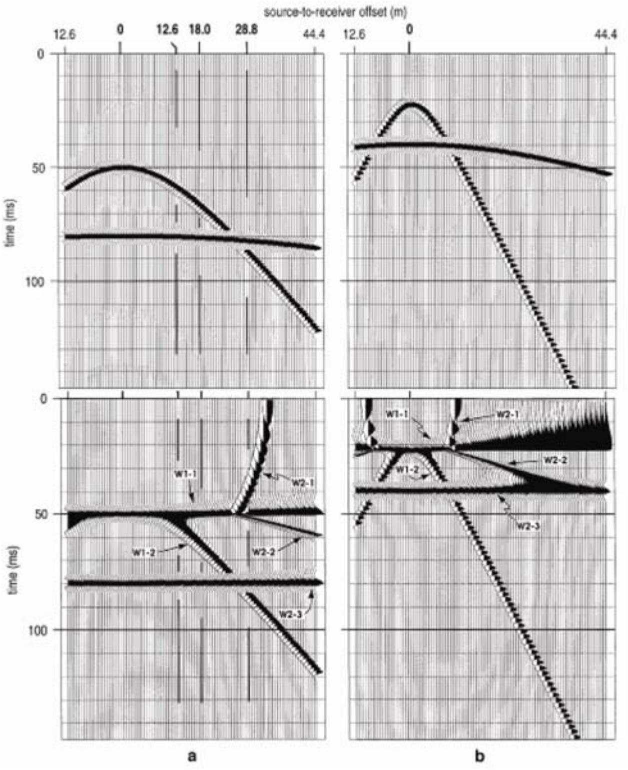

Figure 3.2. NMO corrections applied to intersecting reflection hyperbolae result in undesirable noise and artifacts that require severe stretch mutes (modified from Miller and Xia, 1998).

The NMO correction process is not perfect and some of the underlying assumptions that it is based on may be violated in the shallow subsurface. PSDM may help to avoid this problem, but the necessary software or computer code and resources to run it may not be readily available. The data presented here were processed using a scheme similar to that described by Miller and Xia (1998). Unconsolidated sediment velocities ranging from ~300–600 m/s overlie a fully saturated sediment with a velocity of ~1500 m/s, leading to the intersection of reflection hyperbolae. The NMO correction of optimum-window based subsets for each reflection produced better images of the ultra-shallow subsurface than using a velocity function that includes the NMO velocities for all of the reflections.

Survey Design & Acquisition Parameters

Previously acquired walkaway and 2D seismic data (Figure 3.3) have shown that the TSZ reflection is best recorded at offsets >3–4 m; however, the channel reflection is not observable at a source-to-receiver offset of less than ~15 m. Bedrock reflections are observed at a wide range of offsets ≥~5 m. In order to record the necessary offsets to image each of the reflectors an orthogonal survey design was employed with a patch consisting of four receiver lines (RLs), with 48 receivers each, and twelve source lines (SLs), with 16 source locations each (Figure 3.4). The receiver and source line intervals (RLI, SLI) were both 2 m, with receiver and source intervals (RI, SI) of 0.5 m.

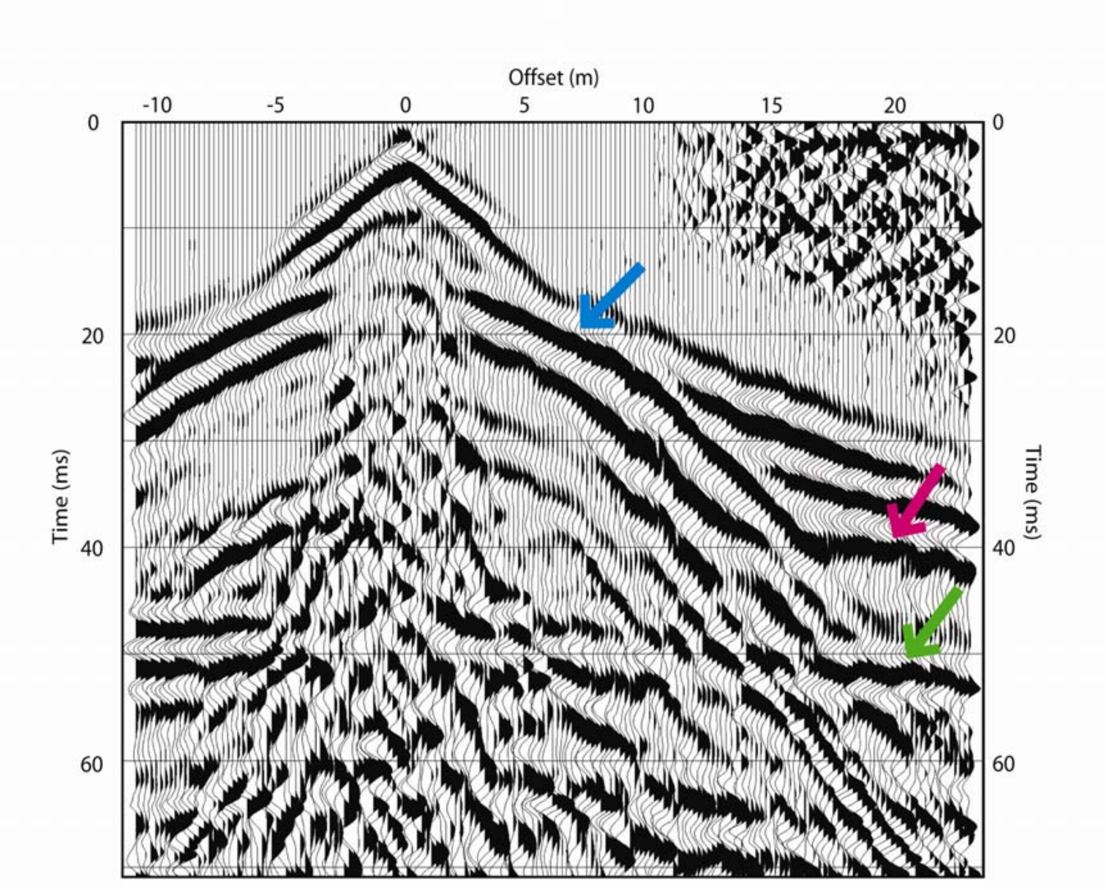

Figure 3.3. 2D CMP gather from a survey previously acquired at the test site. The TSZ reflection (blue) is coherent at a wide range of offsets; however, the channel reflection (pink) is not observable until a source-to-receiver offset ≥ 15 m. The bedrock reflection (green) is observed at a wide range of offsets, although it is partially obscured by ground roll from ~9–15 m.

Each patch consisted of 192 shots, after which the patch was rolled. There were a total of six patch locations, including two lateral passes. Three patches were used in the first lateral pass, rolling two RLs each time in the crossline direction (S-N). The patch was then rolled in the inline direction (E) by half of the RL length and the second lateral pass was made in the opposite direction (N-S). This design led to a total fold of 48. Minimum and maximum recorded offsets were 0.35 and 23.11 m, respectively. Due to a limited number of channels and geophones and the long offsets necessary to image the channel, the resulting aspect ratio of the recording patch is ~1:3, which leads to an offset distribution shifted towards the near offsets and an azimuthal bias along the long axis (Figure 3.4). The survey was acquired in ~10 hours with an eight-person crew and a total of 1152 recorded shots. The limiting factor ended up being the amount of time required to punch the holes for the source.

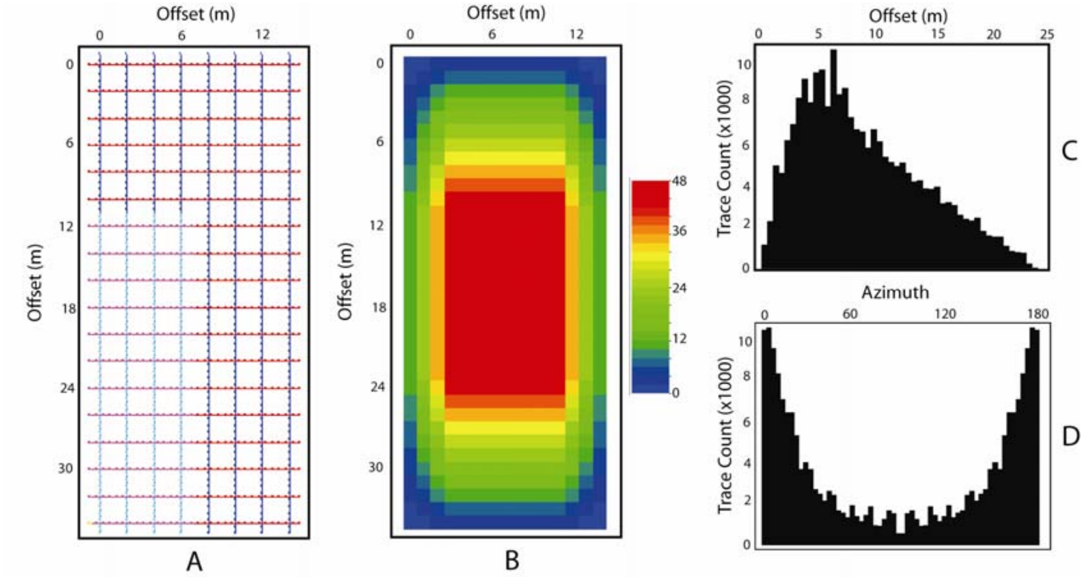

Figure 3.4. Survey design and attributes. (A) shows the receiver (blue) and source line (red) layout and the live patch (light blue and pink). (B) illustrates the resulting fold diagram, reaching a total fold of 48. (C) and (D) depict the trace counts for offset and azimuth, respectively, for the survey.

Common midpoint (CMP) data were collected using 192 (4x48) Mark Products L-40A 100-Hz vertical-component geophones. The source was a .22-caliber rifle firing short ammunition into ~15-cm deep pre-punched holes. Data were recorded using a 96-channel Bison and two 72-channel Geometrics StrataView seismographs with 24-bit A/D conversion. The sampling interval was 0.25 ms for 256 ms. Elevation data were also collected. Figure 3.5 portrays a shot gather, sorted by receiver line, from the survey with interpreted reflections indicated by the arrows.

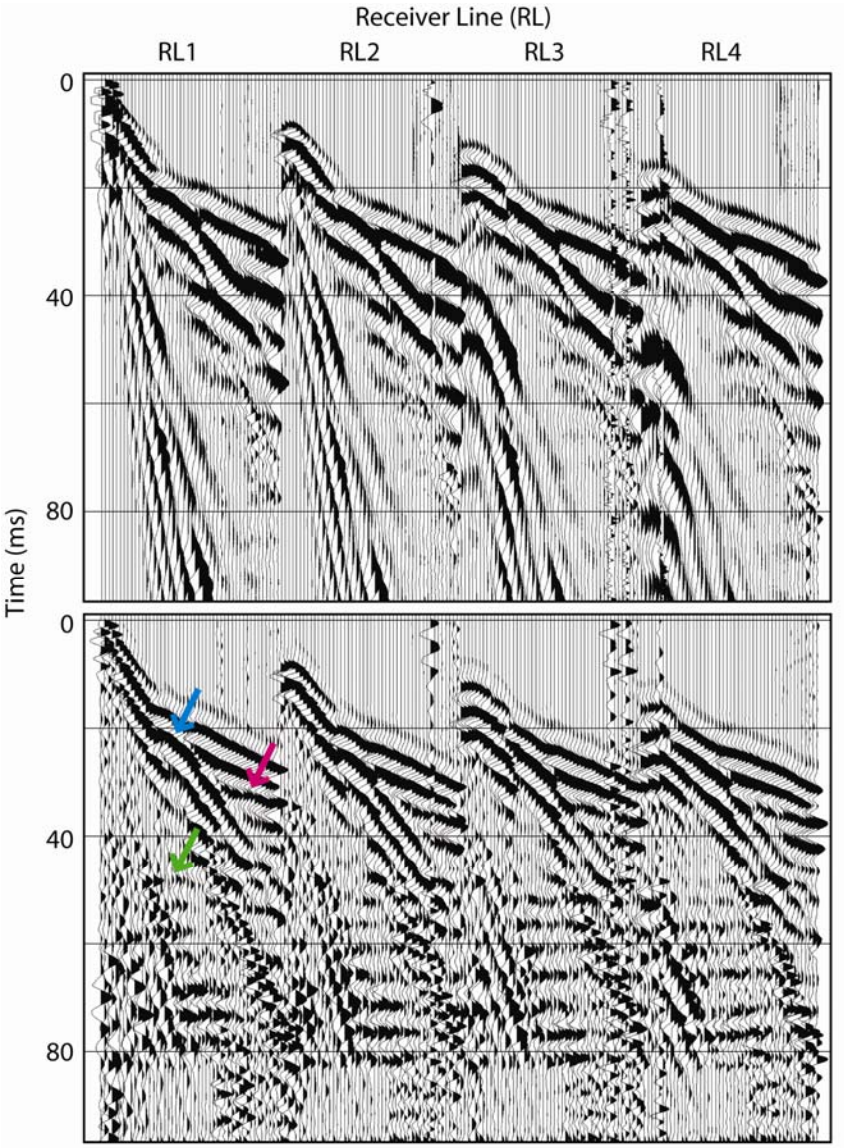

Figure 3.5. A common-shot gather that displays the data recorded by each of the four receiver lines in the live patch prior to processing. The top gather is raw and the bottom gather is displayed with a 175–500 Hz Butterworth filter and a 30-ms AGC window. The interpreted TSZ (blue), channel (pink), and bedrock (green) reflections are indicated by the arrows.

Data Processing

Data were processed using commonly applied techniques as described in Table 1. The data set was binned (0.25 x 0.25 m) and elevation statics were applied using elevation data collected at the site. Trace and record editing eliminated noisy traces caused by bad geophones and records contaminated by noise such as aircraft passing overhead. Figure 3.6 compares fold diagrams extracted from the survey design (A) and from the actual data after editing (B). Although the fold plots are comparable, fold is reduced in a number of bins due to the editing procedure.

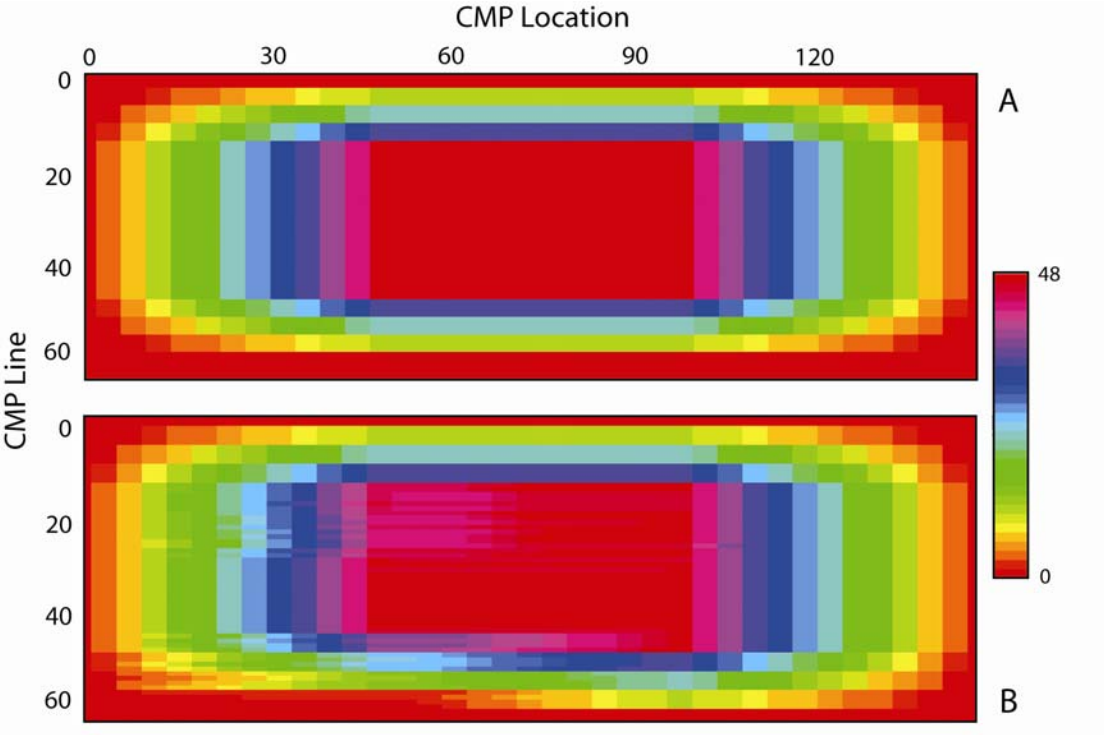

Figure 3.6. (A) shows a fold plot generated using the survey design template. (B) shows a fold plot constructed from the data after the editing of bad traces and records. The fold has been reduced in some bins due to the removal of noisy traces.

Table 1: Processing applied to the 3D USR volume.

Data Processing

Full Data Set		*	***Subset 1***	
Geometry Definition			NMO Corrections	~550 m/s
Binning	0.25x0.25 m		***Subset 2***	
Trace Editing			NMO Corrections	~1075 m/s
Elevation Statics			***Subset 3***	
Early Muting	5-sample taper		NMO Corrections	~1300 m/s
Surgical Muting	5-sample taper			
f-k Muting				
CMP Sort				
Surface-Consistent Statics/Velocity Analysis	3 iterations			
Subset Extraction	Offset segregation and muting, 3-sample tapers			
*Subset NMO Corrections				
Merge Subsets				
CMP Stack				
Butterworth Filtering	175-500 Hz, 18 dB/octave rolloff			
AGC	60-ms window			
3D Migration	Post-stack Kirchhoff time			

Early muting was applied to remove the direct and refracted waves and *f-k* muting helped to remove a portion of the ground roll. After the necessary mutes were applied the data were CMP sorted. Surface-consistent static corrections were iteratively calculated and applied based on velocity analysis of the TSZ reflection since it is coherent at a wide range of offsets. To account for the intersecting reflection hyperbolae, the data were divided into three subsets (Figure 3.7). Subset 1 (S1) includes the TSZ reflection ranging in offset from -14.99 to +14.99 m and 0–44 ms. Subset 2 (S2) includes the channel reflection with offsets ≥ ±15.0 m and 0–44 ms. The third subset (S3) includes the bedrock reflections, encompassing all offsets and limited in time from 44–100 ms.

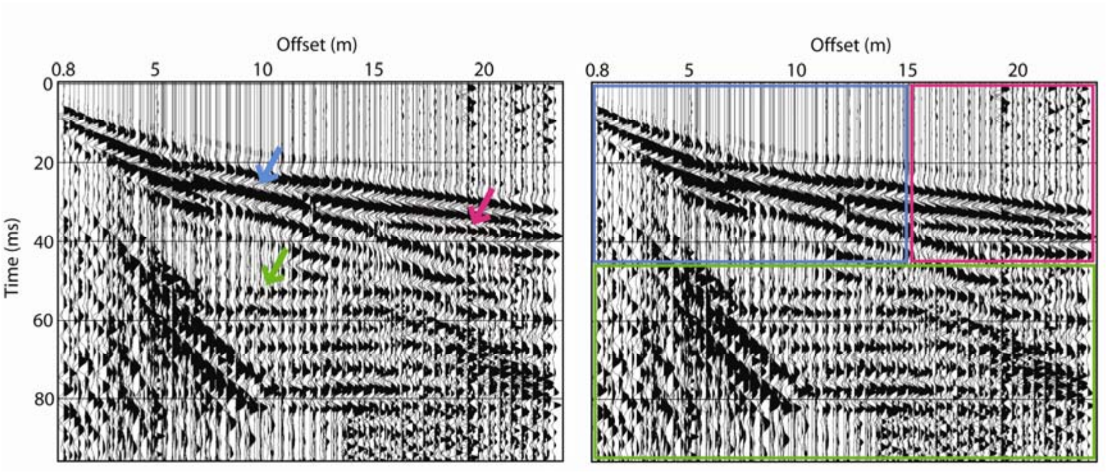

Figure 3.7. Raw shot gather, sorted by offset and including all azimuths, indicating the presence of reflection hyperbolae before processing. Arrows mark the TSZ (blue), paleo-channel (pink), and bedrock (green) reflections. The same shot gather is displayed on the right showing the different subsets including S1 (blue), S2 (pink), and S3 (green). Data are displayed with a 175–500 Hz Butterworth filter with 18 dB/octave rolloff slopes and a 60-ms AGC window.

The bedrock reflection at ~52 ms, marked by the green arrow in Figure 3.7, is coherent at a wide range of offsets from ~5–23 m. Including it with the TSZ reflection could still lead to stretch-related artifacts, hence the necessity of a third subset. S1 and S2 were segregated based on the optimum window of the channel reflection, which is not identifiable until a source-to-receiver offset of 15 m. S3 was removed using a combination of early and tail mutes with a 3-sample overlap. Each subset was NMO corrected independently with its respective velocity based on picks made using constant velocity stacks and velocity semblance plots. To account for lateral velocity variations, velocity picks were made in both the inline and crossline directions with smoothing applied to the resulting velocity functions. All data were then merged and CMP stacked. A 175–500 Hz Butterworth filter with 18 dB/octave rolloff slopes and a 60-ms AGC window were also applied to the stacked volume. Interval velocities for the TSZ, channel, and bedrock were ~550, 1485, and 1600 m/s, respectively. Figure 3.8 depicts the frequency-amplitude spectra for a raw shot gather (A) and the same gather after applying a 175–500 Hz Butterworth filter (B). Data containing frequencies upwards of ~400 Hz were successfully recorded at this site.

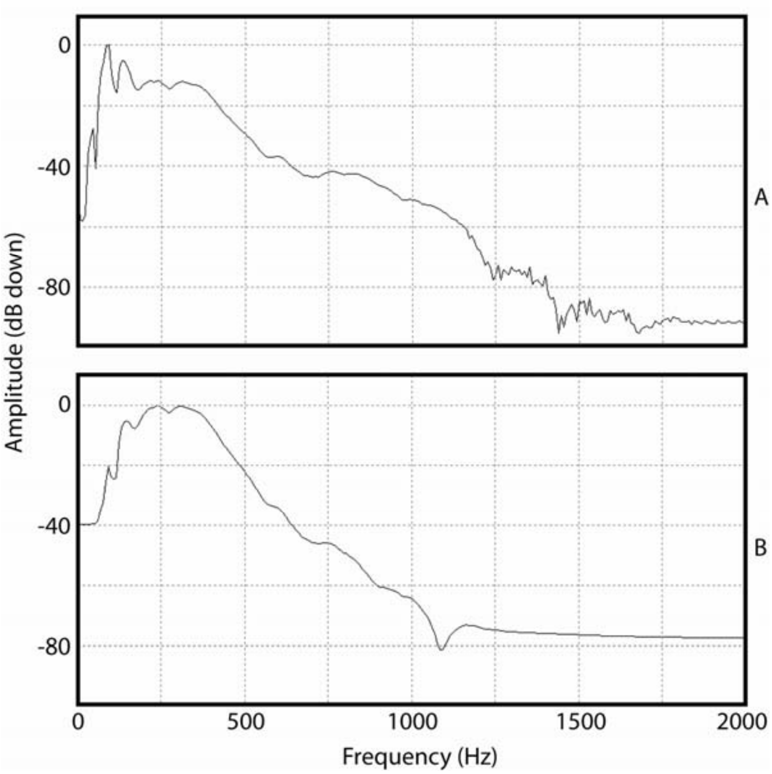

Figure 3.8. Frequency-amplitude spectra of a raw field file (A) and after a 175–500 Hz Butterworth filter with 18 dB/octave rolloff slopes.

Several possible pitfalls exist with this processing scheme that should be noted. Cutting data in time without a taper can result in squared wavelet corners at the edges, which will mirror the filter operator applied and can produce coherent high-frequency events that may stack constructively (Sloan et al., 2008). Even with a taper, dividing data in time and then recombining can lead to data seams. However, this was not a problem with this particular data set after selecting an appropriate taper overlap of 3 samples for the early and tail mutes. Static corrections should be calculated and applied prior to segregation as they would no longer be whole-trace shifts and may lead to erroneous results.

Results & Discussion

Figure 3.9 shows a coincident CMP line extracted from independently processed data volumes. (A) and (B) were NMO corrected using a single velocity function that included the appropriate NMO velocities for the TSZ, channel, and bedrock reflections using stretch mutes of 20% and 40%, respectively. The TSZ reflection is a little smoother and more coherent in (A) due to the more severe stretch mute; however, the channel feature is very weak. Although the channel feature is more evident in (B), since more of the necessary far-offset traces are included, it is still not clearly imaged due to interference induced by the NMO correction of the intersecting hyperbolae. The bedrock reflections are largely unchanged since they are coherent at a wide range of offsets. (C) has been processed by NMO correcting the offset-dependent subsets based on the respective optimum window of each reflection. The TSZ and bedrock reflections are much the same as in (A) and (B), but the channel feature is more clearly imaged without the interference of the artifacts associated with NMO correcting the intersecting hyperbolae.

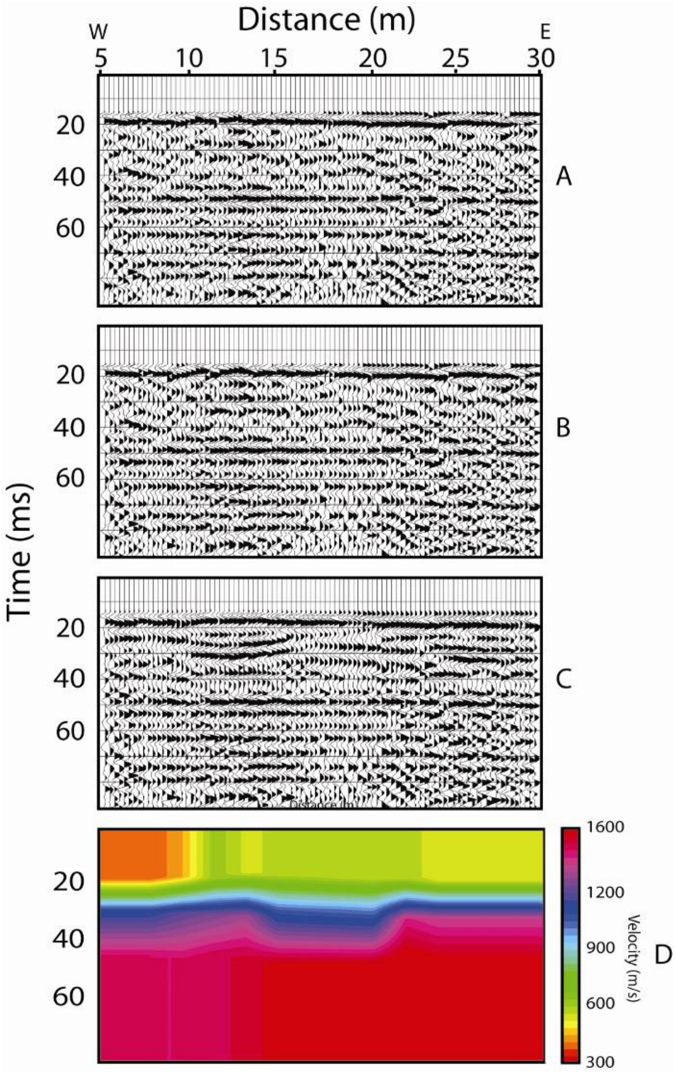

Figure 3.9. (A) Stacked section that has been NMO corrected with a single velocity function including the NMO velocities for each of the reflections and a stretch mute of 20%. (B) The same as (A), but with a 40% stretch mute. (C) Stacked section that has been NMO corrected using optimum-window based subsets for each reflection. (D) Velocity field used to NMO correct sections A-C.

Figure 3.10 illustrates the comparison of the three subsets after independent NMO corrections and CMP stacking (A) and the same data with the exception that the data were merged after NMO corrections and prior to CMP stacking (B). Small dissimilarities exist, but overall the reflections show the same structure and their characteristics are much the same.

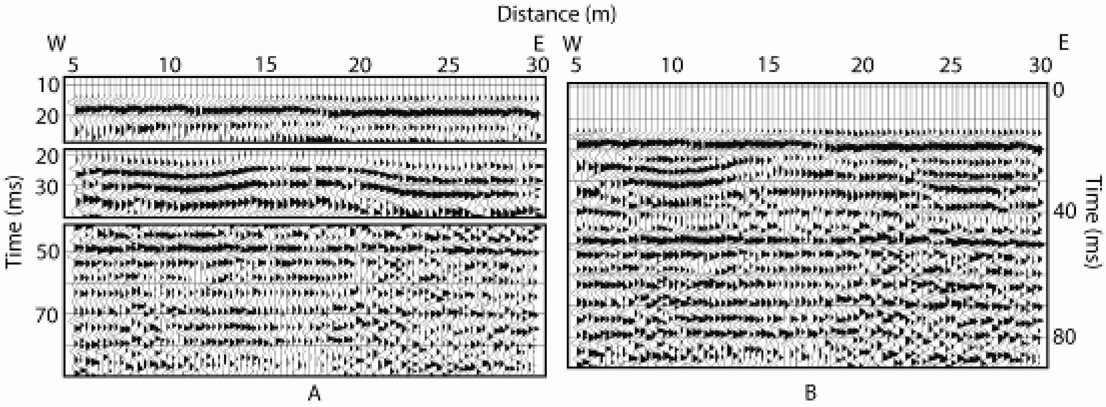

Figure 3.10. Comparison of Subsets 1–3 after independent NMO corrections and CMP stacking (A) and the same NMO-corrected data, but merged before stacking (B).

The final stacked volume was interpreted using a commercial seismic software package. Figure 3.11 shows a chair diagram with the interpreted TSZ (blue), paleo-channel (pink), and bedrock (green) reflections. A 3D rendering of the interpreted surfaces is displayed in Figure 3.12. The TSZ, paleo-channel features, and bedrock are located at depths of ~5, 8.2, and 14.4 m, respectively. The interpreted channel features run approximately N-S and appear to dip slightly to the north. These features could potentially serve as flow paths for contaminants to migrate, ultimately settling in topographic lows (Figure 3.13). The channel features are coincident with a topographic low and soil variation that can be identified in the aerial photograph in Figure 3.1 as the N-S trending linear surface expression, which is adjacent to a creek that borders the property and is within 30 m of the survey area.

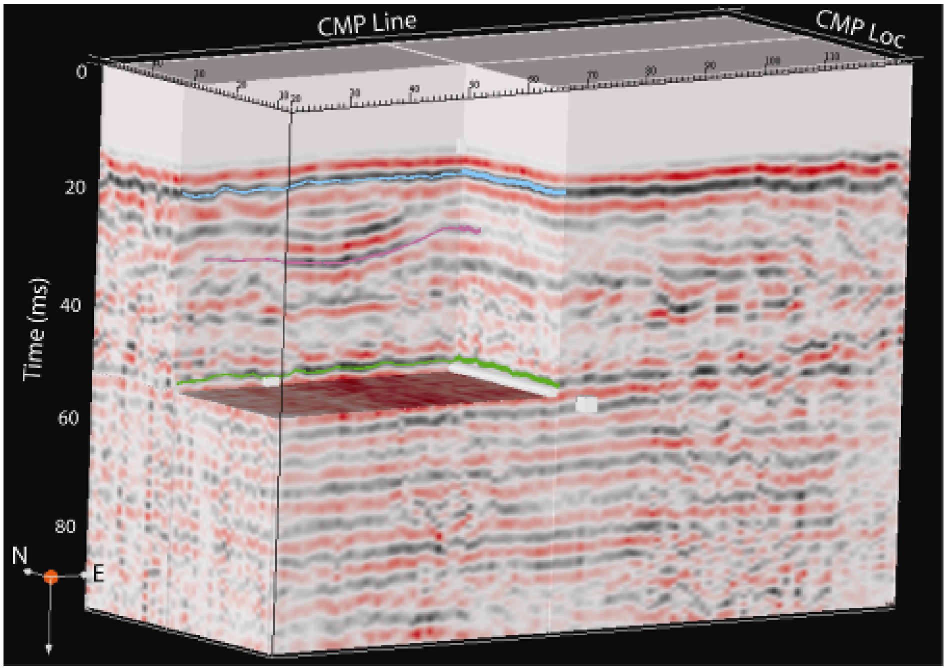

Figure 3.11. Chair diagram of the final stacked volume. The interpreted reflections are highlighted in blue (TSZ), pink (paleo-channel), and green (bedrock).

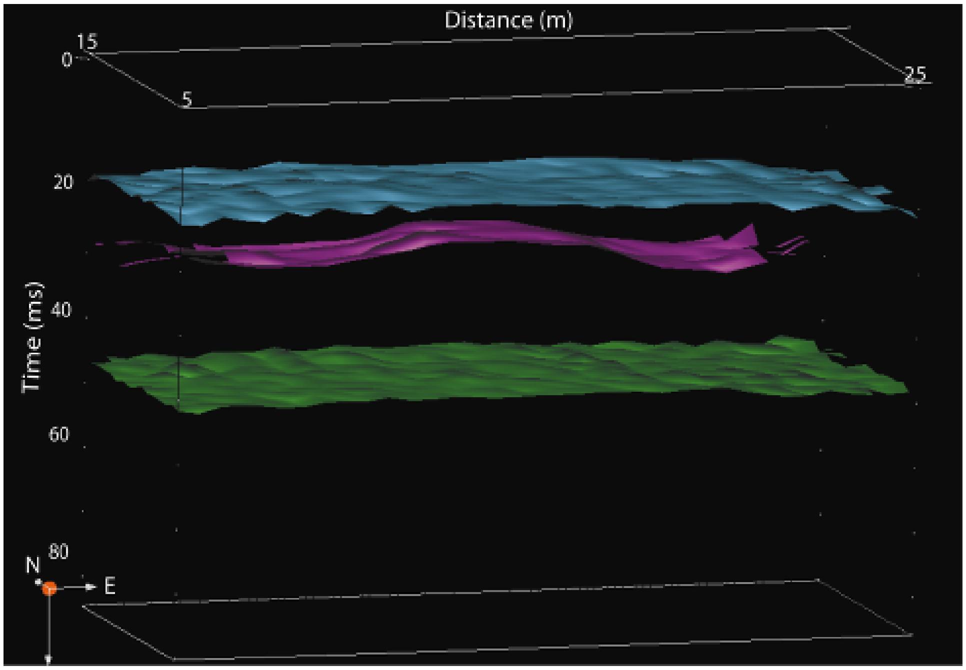

Figure 3.12. 3D graphic showing the TSZ (blue), channel (pink), and bedrock (green) surfaces.

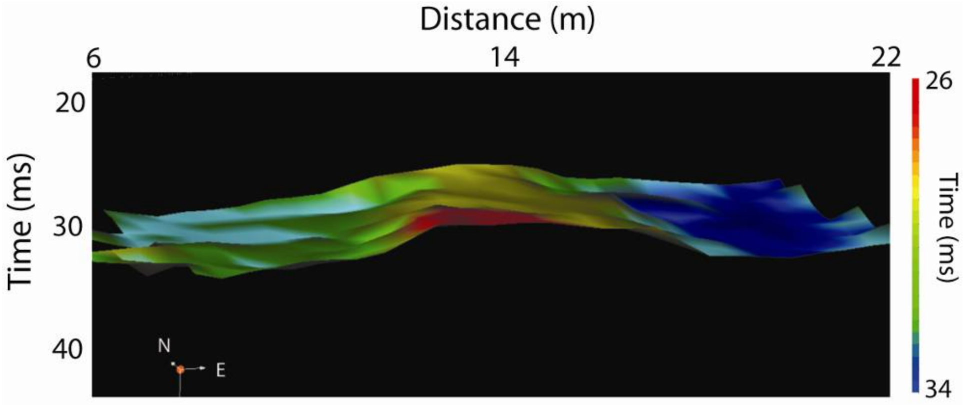

Figure 3.13. Interpreted channel surface. Cooler colors indicate topographically lower areas, which may serve as sinks for contaminants to pool.

Figure 3.14 shows two time-amplitude slices from 30 (top) and 31 (bottom) ms. The two structural lows illustrated in Figure 3.13 are depicted by the black (left) and red (right) linear features, bound by the green lines on the interpreted slices. The channel surface in Figure 3.13 indicates that the two structural lows begin to merge into one to the north. The 31-ms time slice in Figure 3.14 also indicates that the two features are merging on the north side of the slice. Multiple 2D lines would be necessary to determine the path of the channel features; however, the surfaces can be tracked continuously with 3D methods.

The ability to image ultra-shallow structures using seismic reflection techniques provides a viable alternative to other geophysical methods that may not be suitable for certain sites or geologic settings. Three-dimensional imaging yields more accurate representations of the subsurface and can aid in the remediation strategies of contaminated sites by identifying specific areas where contaminants may pool or migrate. 3D USR and SSR surveys can be expensive to acquire, but may ultimately be more cost effective than the costly drilling of unnecessary boreholes that may exacerbate the vertical migration of contaminants.

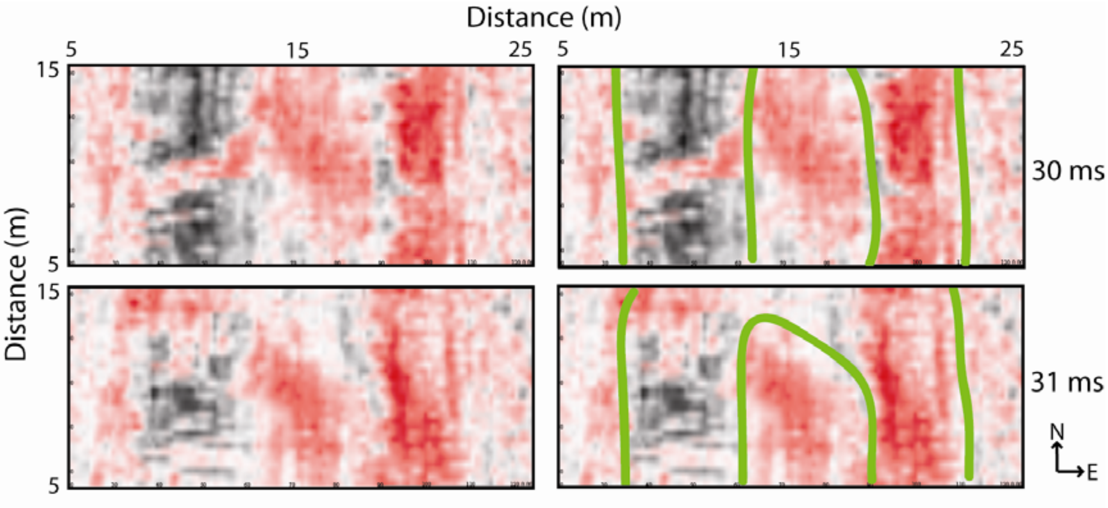

Figure 3.14. Uninterpreted (left) and interpreted (right) time slices from 30 (top) and 31 ms (bottom). The channel features are marked by the green lines.

Conclusions

The objectives of the study presented here included imaging multiple reflectors less than 20 m deep in three dimensions, including the top of the saturated zone, paleo-channel features, and bedrock. The 3D survey was successful and the results are in agreement with previous studies conducted at the site. Processing the data by dividing them into offset-dependent subsets based on the respective optimum window of each reflection was successful in eliminating artifacts of NMO-correcting intersecting reflection hyperbolae with a vertical velocity ranging from ~300–1600 m/s. Despite segregating the data set in time, data seams were not a problem in merging and stacking the subsets after an appropriate overlap taper was selected. It is possible, however, to generate processing artifacts using subsets, and caution should be exercised throughout the processing stage when using this technique to ensure that quality control is maintained.

The ability to image ultra-shallow structures using seismic reflection techniques provides a viable option that can be used in conjunction with other geophysical methods for subsurface characterization, or as an alternative when other methods that may not be suitable for certain sites or geologic settings. Three-dimensional imaging allows continuous reflector tracking and yields more accurate representations of the subsurface, which can aid in the remediation strategies of contaminated sites by identifying specific areas where contaminants may pool or migrate. 3D USR and SSR surveys can be expensive to acquire, but may ultimately be more cost effective than drilling unnecessary boreholes that may facilitate the vertical migration of contaminants.

Chapter 4

The 3D Autojuggie: Automating 3D near-surface seismic data acquisition

Introduction

Two-dimensional (2D) common-midpoint (CMP) surveys are the most common means of collecting shallow seismic reflection (SSR) data. Although three-dimensional (3D) data can provide more detailed subsurface information and help to prevent misinterpretations that may be caused by out-of-plane reflections (Green et al., 1995; Lanz et al., 1996), at present it is too expensive and labor intensive to be a viable option for most shallow applications. The acquisition of 3D seismic reflection data has become a common practice in the hydrocarbon-exploration industry (Vermeer, 2002), but is not commonly used for engineering and environmental applications due to budget limitations and the higher costs per unit area of collecting 3D SSR data. SSR surveys may require receiver and/or source intervals as small as 10 cm to properly sample the wavefield in some ultra-shallow applications. Despite this, 3D SSR surveys have been reported by Corsmit et al. (1988), House et al. (1996), Barnes and Mereu (1996), Lanz et al. (1996), Büker et al. (1998), Spitzer et al. (2003), and Bachrach and Mukerji (2001a, 2004a,b).

Shallow 3D seismic profiles previously collected have been either low fold with relatively coarse grids (Corsmit et al., 1988; Barnes and Mereu, 1996; House et al., 1996; Lanz et al., 1996; Siakoohi and West, 1998) or high fold with denser spacing (Buker et al., 1998; Spitzer et al., 2003). Although densely-sampled high-fold surveys provide better subsurface coverage and images, they are much more expensive to acquire. For example, Buker et al. (1998) reported using an average field crew of 5–7 people for 85 days to cover a 357 m x 432 m area.

The cost of acquiring 3D SSR data increases as target depth decreases due to the necessary increase in source and receiver density; several attempts have been made to make 3D surveying more cost effective. Spitzer et al. (2001) decimated a 3D volume into subsets using various acquisition parameters and found that comparable data could be acquired with 25% of the field effort and 75% less expensive than the original survey conducted by Büker et al. (1998). However, this is highly site dependent and requires prior knowledge of subsurface properties at the test site and target size and geometry. Van der Veen et al. (2001) discuss using a towed land-streamer system to collect pseudo-3D SSR data; however, this method limits the azimuthal range of subsurface coverage and may still include out-of-plane energy. Bachrach and Mukerji (2001a, 2004a,b) describe a portable geophone array used to collect dense (0.125 m bin size), 3D SSR data. Their method uses a 2D array of 72 geophones with 0.25 m receiver intervals to be able to move all of the geophones at once from one location to another using a canvas and PVC pipe frame. Each of the 72 geophones must still be planted by hand with every move of the array, although accurate location is guaranteed with their method.

The study presented here describes new instrumentation developed to acquire 3D ultra-shallow and shallow seismic reflection data in a more cost-effective manner than the techniques currently in use. The 3D Autojuggie is capable of hydraulically planting 220 geophones, with 0.5 m spacing in the inline and crossline directions, simultaneously in approximately one minute. Likewise, all 220 geophones can be picked up in the same amount of time so that the entire spread can be moved and redeployed. Data acquired using conventional hand-planted geophones and those collected using the 3D Autojuggie during a walk-away test are compared and have found to be nearly indistinguishable. Receiver spacing remains fixed and the geophones remain connected to the cables while the geophones are repositioned, thereby reducing the amount of time and number of personnel necessary to roll geophones and cables and the associated costs to do so. Conceptually, this approach could be expanded to plant several hundred geophones very quickly.

Prior Work

Two-Dimensional

Research at the University of Kansas over the past decade has focused on developing a more cost-effective method of acquiring SSR data. Steeples et al. (1999a) showed that comparable seismic data could be collected using geophones rigidly attached to a wooden board, but they observed a low-velocity mode introduced into the data by the board. Steeples et al. (1999b) took this initial study a step further by using a tractor and plow to hydraulically plant 72 geophones mounted to lengths of channel iron in approximately two seconds. They identified direct waves, refracted waves, the airwave, and surface waves, but did not record any reflections. Schmeissner et al. (2001) determined that seismic reflections could be recorded using rigidly interconnected geophones and determined that the low-velocity mode was caused by vibrations in the planting implement. Spikes et al. (2005) demonstrated that the 2D Autojuggie can be used to collect comparable CMP data and that processing techniques common to CMP data can still be applied to data collected using rigidly attached geophones.

Previously acquired data were collected using channel iron as the rigid medium, so Blair et al. (2003) analyzed the response of geophones rigidly attached to steel media of various shapes. Their findings show that data collected using steel media exhibit a damping effect on the airwave and that steel square tubing was the best medium of those tested. Clark et al. (2004) furthered the study of varying media by comparing cylindrical steel tubing to other media, such as PVC pipe. Negligible differences were found and the authors concluded that square tubing remained the optimal choice due to strength, the square shape, and the airwave damping properties. An analysis of the effect of the airwave on bar-mounted geophones was conducted by Vincent et al. (2004). Their study compared airwave coherency with respect to the orientation of the source to the bar. The authors determined that the airwave is less coherent and exhibits a smaller amplitude when the source is within 60° of the inline direction and is most coherent within 30° of the crossline direction.

Three-Component

The studies discussed thus far have dealt only with vertical-component data. Ralston et al. (2001) collected and analyzed data using rigidly interconnected Gal'perin three-component (3C) geophones. They concluded that the vertical component was largely unaffected; however, the transverse and radial components were severely distorted due to the preferential attenuation of high wavenumbers with respect to the channel iron. High angles of incidence or low apparent velocities are the largest contributors to distortion, which limits the range that useful 3C data can be collected.

A later study by Ralston et al. (2002) introduced a method of linear filtering to eliminate the effects of crosstalk in data collected using rigidly interconnected 3C geophones. Their tests indicated that the seismic wavefield is not destroyed or lost when using the Autojuggie acquisition device and can be recovered from the data with an appropriate filter. An important drawback of this method is that the appropriate filter is not only site specific, but is also specific to each array, meaning a different filter must be devised and applied for each time the array is planted. 3C seismic data can be very time consuming and costly to acquire compared to single-component data and a 3C survey can be 3–5 times more costly in man hours alone. However, Ralston et al. (2002) determined that 3C data can be acquired 6–10 times faster using the Autojuggie than by conventional methods.

Three-Dimensional

All studies conducted to this point have focused on 2D SSR, but research is now moving into three dimensions. A 2D pilot array (Figure 4.1) measuring 2 m x 1 m was built for 3D SSR testing using steel square tubing, which houses 72 geophones and can be planted using the front-end loader of a tractor (Czarnecki et al., 2006; Tsoflias et al., 2006). To avoid the bar-induced noise, the geophones are separated from the square tubing hydraulically so that they are not touching the array and are analogous to hand-planted geophones. Testing showed that 3D SSR data can be collected and are comparable to data from hand-planted geophones (Figure 4.2)

(Czarnecki et al., 2006). Although this array can be used to collect 3D SSR data, it is limited by its small size and is only useful for small ultra-shallow surveys that do not require long offsets. The need to be able to cover larger areas faster and record longer offsets within the receiver spread has led to the development of the larger 3D Autojuggie (3DAJ).

Figure 4.1. Photo of the pilot array, capable of planting 72 geophones simultaneously using the front-end loader of a tractor.

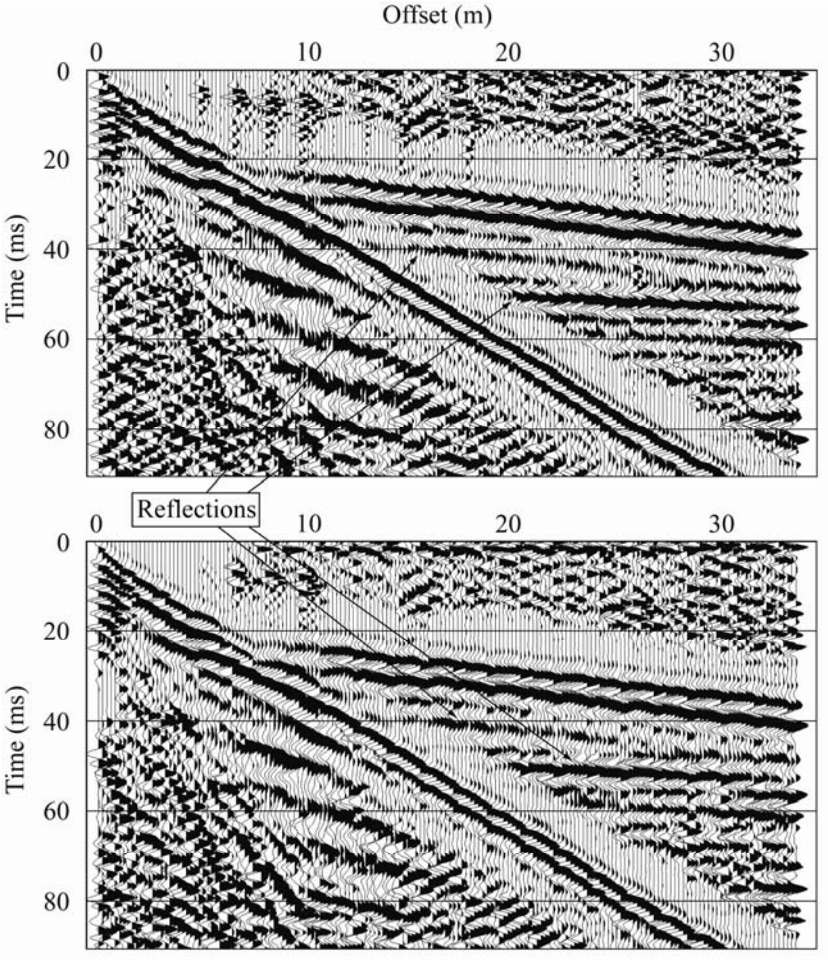

Figure 4.2. Walkaway data acquired using the pilot array (top) and hand-planted geophones (bottom) (from Czarnecki, 2006).

3D Autojuggie Description & Operation

The 3DAJ is a ~11.6 m (38’) long tandem-axle trailer, weighing ~6,350 kg (14,000 lbs.), that can be pulled by a truck or tractor (Figure 4.3). The trailer is comprised of three sections, including the main body and two hydraulically retractable wings. Eleven receiver lines house 220 geophones (20 geophones per line), with 5 lines within the body and 3 lines in each wing. Receiver line interval and receiver spacing are each 0.5 m, but can be increased by multiples of 0.5 m by changing the placement of geophones. The 3DAJ contains its own hydraulic system, including an electric-start gasoline engine. The receiver spread measures 9.5 m long by 5 m wide, when the wings are in the down position. To make the trailer street-legal, the two wings fold up over the main body, reaching an overall height of ~3.5 m (11.5').

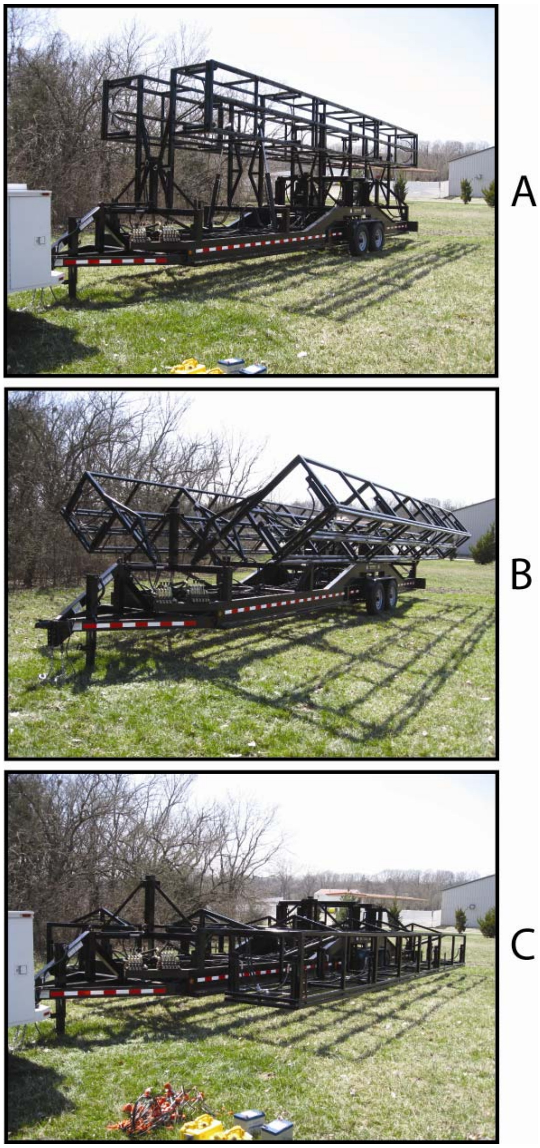

Figure 4.3. Photos illustrating the transition of the 3DAJ from the transportable "folded" position (A) to the "down" position (C).

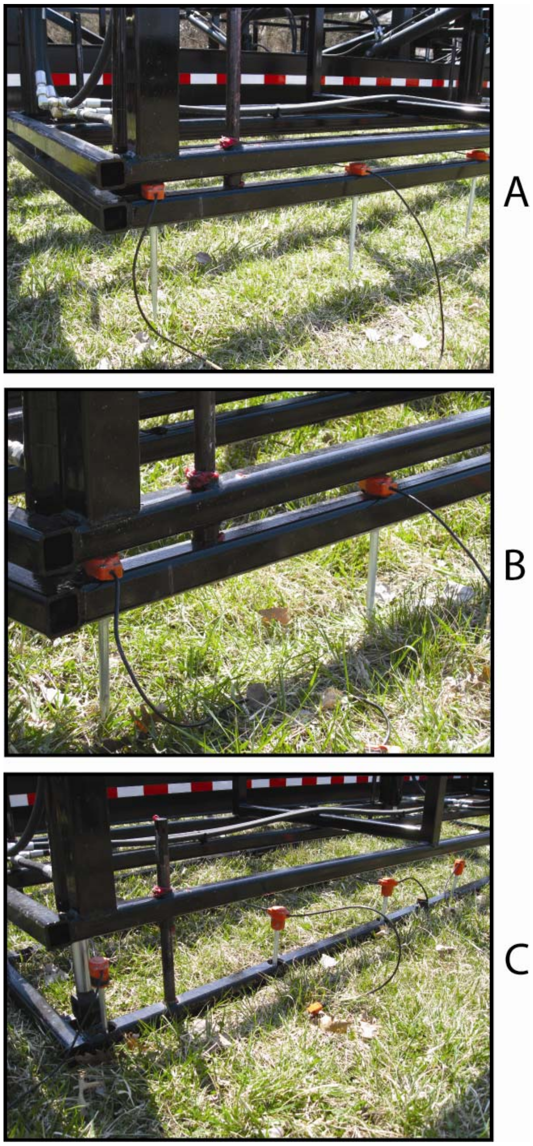

Figure 4.4. Photos illustrating the geophone-planting process including: (A) before planting, (B) the geophones being pushed into the soil, and (C) the separation of the bars so that the geophones are free-standing and unattached to the planting apparatus.

From the transportable folded position (Figure 4.3a), four hydraulic rams (2 on each side) lower the wings to the “down” position (Figure 4.3c). Four more rams lower the entire trailer body to the ground. The geophones are housed in a grid constructed of 5.1 cm (2”) steel square tubing with chamfered holes slightly larger in diameter than the geophone casing (Figure 4.4). An identical grid, with the exception of the holes, rests on top of the geophones to hold them in place as they are planted. Once the geophone spikes are adequately planted, a total of 26 rams (10 on the main body and 8 on each of the wings) spread the two steel grids apart so that each geophone is free standing and is not attached to the apparatus. The only difference between an automated plant and a hand-planted geophone is that the receiver is raised above the ground surface to allow for the 5.1-cm tall grid to be lowered clear of the bottom of the geophones. Longer geophone spikes (12.5 cm) are used to compensate for the height of the geophone above the ground surface (Figure 4.5). To pick the geophones back up the sequence is followed in reverse where the rams contract to reposition the geophones in the holes and the entire trailer body is raised back to its starting position. The hydraulic rams are manually operated by 8 hand levers located at the front of the trailer.

Figure 4.5. Photo illustrating the difference in spike length for 3DAJ-planted geophones (top) and hand-planted geophones (bottom).

Initial Testing & Results

A walk-away test was conducted at the University of Kansas West Campus in Lawrence, Kansas, on May 15, 2008 to compare data collected with hand-planted geophones to those acquired with geophones planted using the 3DAJ. Figure 4.6 illustrates the layout of the walk-away test. The control line (hand-planted) was located adjacent to the 3DAJ line on the outside of the wing (1). 3DAJ and hand-planted geophone spacing was 0.5 m in the inline and crossline directions. The source was a .223-caliber rifle firing a single round into pre-punched holes. The initial source-to-receiver offset was 0.5 m and subsequently moved away at a 10-m interval for a total of seven shots. Data were recorded using 24-bit A/D Geometrics Geode seismographs with a 0.25-ms sampling interval and 256-ms record lengths.

Figure 4.7 shows a comparison of the walk-away data collected from the control line (a) to 3DAJ receiver lines (RL) 1 (b) and 5 (c). Control-line data and those from RL1 are nearly indistinguishable, clearly imaging the direct and refracted arrivals, air wave, ground roll, and multiple reflections. The same events are also present in the data from RL 5; however, the S/N ratio is slightly lower, which is likely due to noise caused by the 3DAJ structure itself. Figure 4.8 shows the frequency-amplitude spectra for the control-line data (black) and RL 1 (gray). The spectra follow each other very closely and are practically identical.

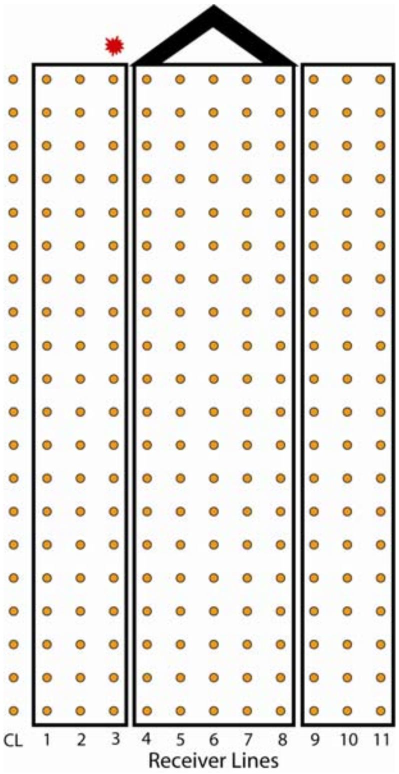

Figure 4.6. Diagram illustrating the layout of the walk-away test. The control line was placed adjacent to the outside 3DAJ receiver line on the left (1). The initial source location is indicated by the red burst. Subsequent shot points were positioned at 10-m intervals.

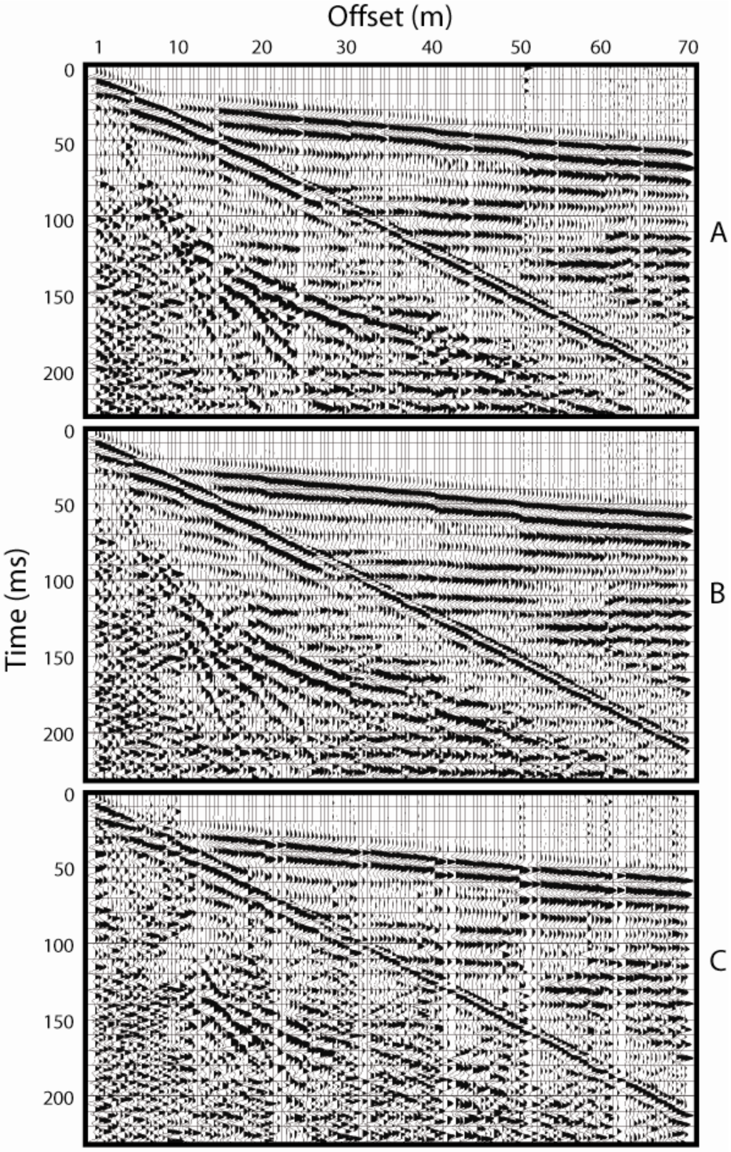

Figure 4.7. Walkaway data collected with hand-planted geophones (A) and the 3DAJ (B&C). Data in B and C are from RLs 1 and 5, respectively, as displayed in Figure 4.6. Data are displayed with a 100–500 Hz bandpass filter and a 60-ms AGC window. Trace gaps are due to the removal of noisy or dead traces.

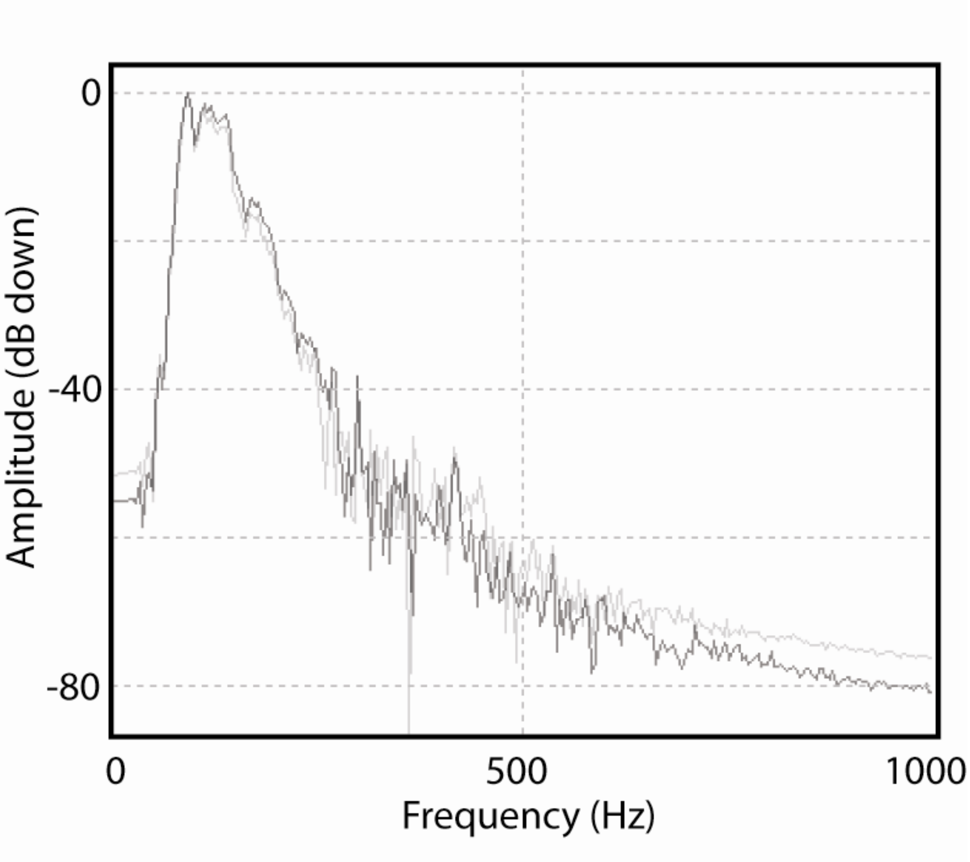

Figure 4.8. Frequency-amplitude spectra corresponding to the walkaway data in figure 4.7. Control-line data are represented by the spectrum in black and the spectrum of the RL1 data is displayed in gray.

Chapter 5

3D Autojuggie Survey Design & Acquisition

Introduction

The initial testing of the 3DAJ, described in the previous chapter, showed that the new, full-size version of the 3D Autojuggie is capable of collecting 3D seismic-reflection data comparable to those of hand-planted geophones. Based on the physical performance of the 3DAJ during testing, minor design modifications were made to prepare for production use. Steel spacers, used to keep the two geophone frames from crushing the geophones while maintaining a snug fit, were too large. Consequently, a 1.27 cm (0.5 in) gap remained between the geophones and the upper steel frame, which allowed some of the geophones to stray from vertical during planting. Several geophone holes were also too tight, preventing the frame from sliding off of the geophone casing and locking them in the frame. The next phase of the project was to acquire a comprehensive 3D USR survey large enough to be scientifically meaningful. This chapter will discuss pre-survey testing, survey design, and data acquisition. The field site is the same as described in Chapter 3, located several miles south of Lawrence, Kansas (Figure 5.1).

Walkaway Test

The site chosen for the 3DAJ survey is the same as that used for the conventional 3D USR survey discussed previously; however, this survey covered an area upslope of the previous one. A walkaway survey was conducted in November of 2007 to determine appropriate acquisition parameters and to see if subsurface properties varied from one location to another. Data were collected using 144 100-Hz Mark Products L-40A2 vertical-component geophones and a .22-caliber rifle firing single long-rifle rounds into ~15-cm deep holes. Since the 3DAJ receiver line interval (RLI) and the receiver interval (RI) are 0.5 m, a walkaway receiver spacing of 0.25 m was chosen to make sure spatial aliasing would not be a problem. The total spread length of 35.75 m was sufficient to record all shallow reflections of interest, so multiple source locations were not necessary. The receiver line was laid out in a north-south orientation with the source location offset by 1 m to the south of the nearest receiver. The walkaway layout is illustrated in Figure 5.2. Data were recorded by two 72-channel Geometrics StrataView seismographs with 24-bit A/D conversion using a 0.25-ms sample interval for record lengths of 256 ms.

The data are displayed in Figure 5.3 with the various wave types indicated by colored lines as follows:

Red: Direct wave
Orange: Refraction from the fully saturated zone
Yellow: Refraction from bedrock
Blue: Reflection from the top of the saturated zone (TSZ)
Pink: Reflection from stratigraphic boundary
Green: Reflection from bedrock
Purple: Air wave
Brown: Ground roll

Using the walkaway data as a guide, the 3DAJ RLI and RI of 0.5 m should be sufficient to image the reflections of interest in the 3D survey.

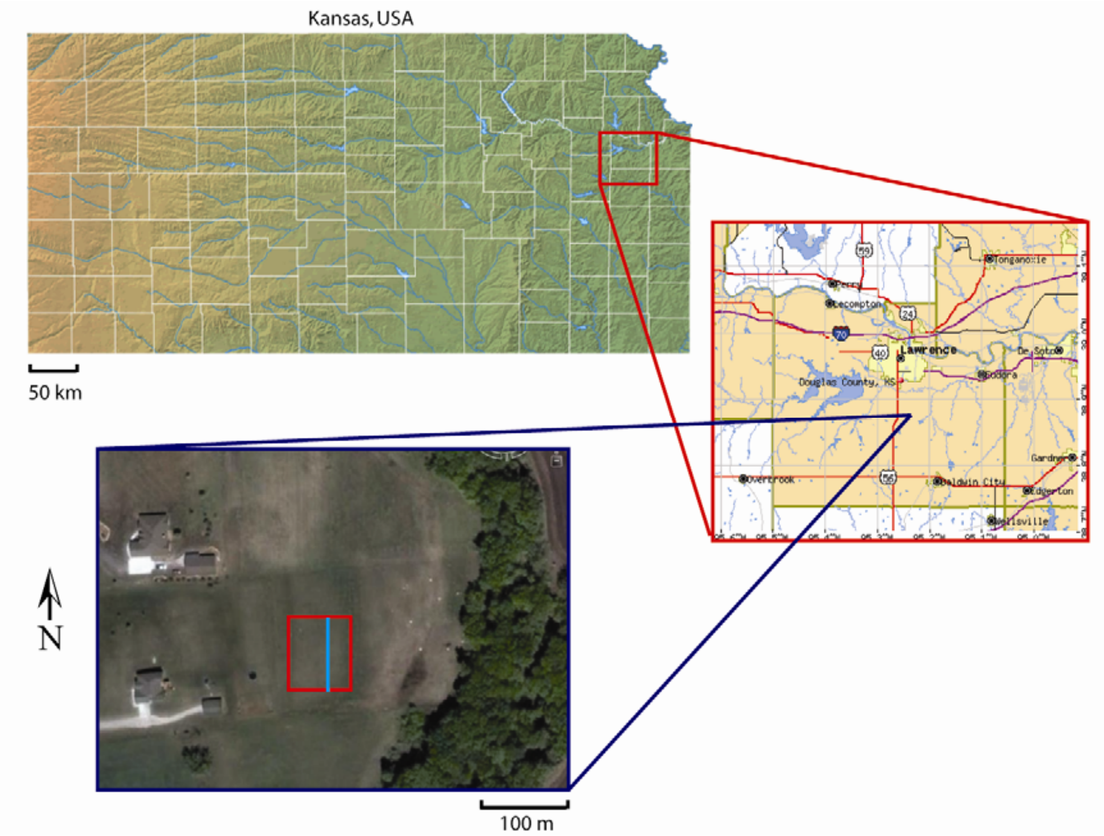

Figure 5.1. Map illustrating the location of the field site, located near Lawrence, Kansas. The approximate location of the 3D survey area and walkaway test are indicated by the red square and blue line, respectively.

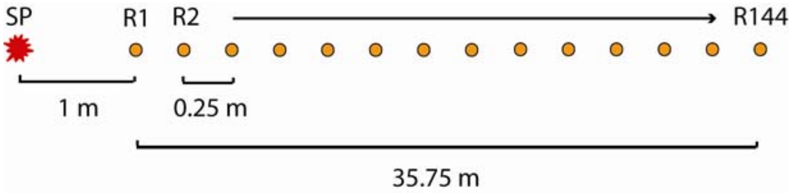

Figure 5.2. Diagram of the walkaway test layout. The source point (SP) is indicated by the red burst and the receivers are marked by the orange circles.

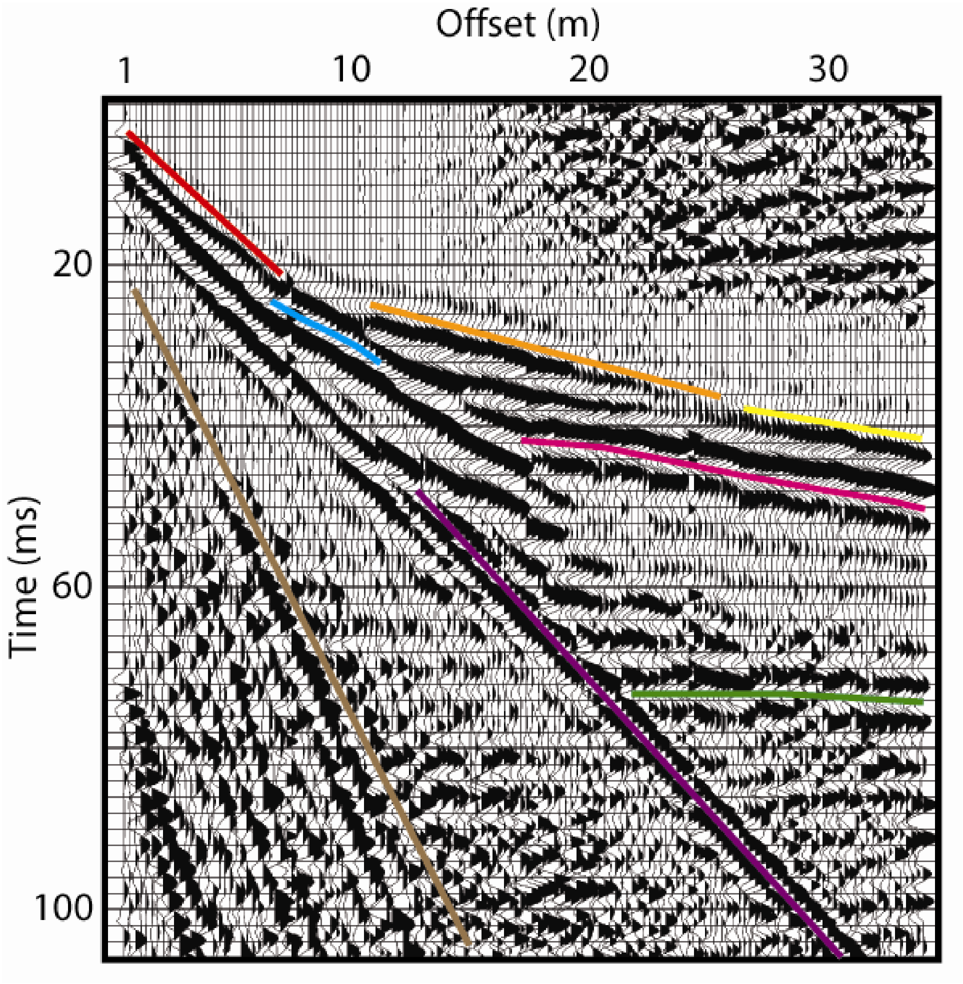

Figure 5.3. Walkaway data collected to determine survey design parameters. The direct wave, refractions, reflections, air wave, and ground roll are indicated by colored lines, which are described in the text.

My initial 3D survey design called for a rolling patch, which required multiple coincident source locations for different patch locations. The limiting factor for acquisition time in our first survey was the time necessary to punch holes for each source location. To determine if we could fire multiple shots in the same hole, i.e. reuse the same holes for different patches, multiple shots were recorded using the same hole during the walkaway test. Figure 5.4 compares traces from the first three meters using one (a), two (b), and four (c) shots. The first two records are comparable with the first arrivals recorded at the same time, 4 ms on the first trace in each. However, by the fourth shot there is a 1-ms delay in the first arrivals and a noticeable decrease in amplitude below 14 ms.

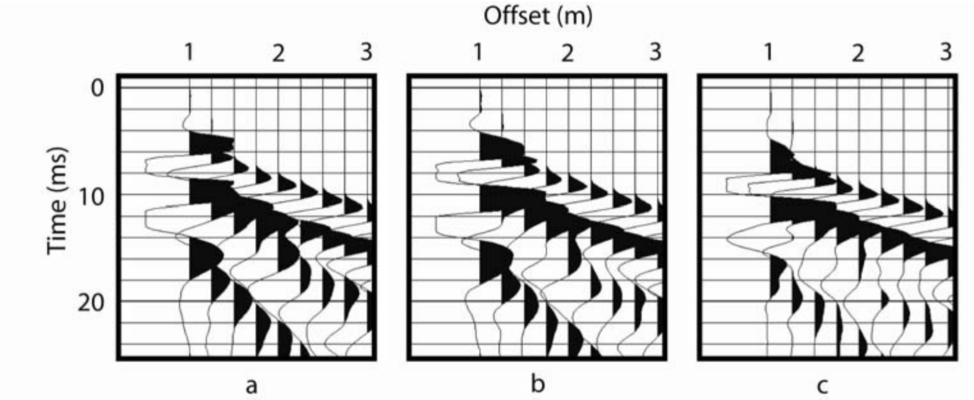

Figure 5.4. Comparison of one shot (a), two shots (b), and four shots (c) fired into the same hole.

Figure 5.5 illustrates the difference in frequency-amplitude plots of the first (a) and fourth (b) shots. Higher frequencies (above ~250 Hz) are attenuated more rapidly and there is a notch at ~125 Hz. Discrepancies between the spectra are likely to be caused by increased void volume beneath the muzzle and soil-particle compaction that would increase with each subsequent shot and affect the character of the source wavelet. It was determined that a source hole could be used twice, but subsequent shots could cause a change in the source wavelet, which may lead to adverse effects in the processing stage.

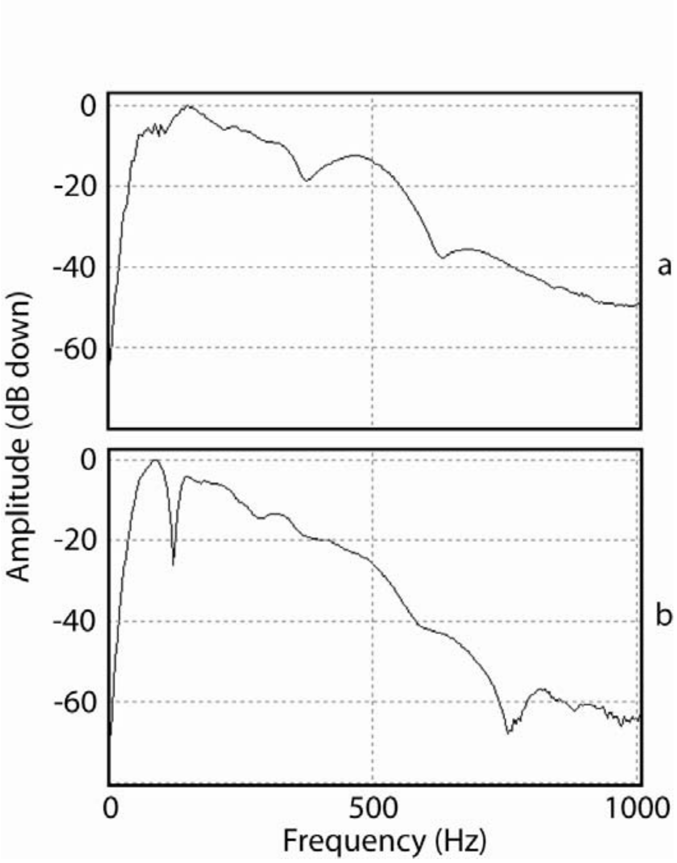

Figure 5.5. Frequency-amplitude plots from data collected from one shot (a) and four shots (b) fired into the same hole.

3DAJ Survey Design

Survey design and attribute analyses were done using a commercial 3D design package. Since the RLI and RI are fixed on the 3DAJ, the biggest parameters to determine were the source line interval (SLI), source point interval (SI), minimum and maximum offsets (X_{min}, X_{max}), and RL/R rolling parameters. The stratigraphic reflection is not observable until offsets greater than ~15 m, so X_{max} was chosen to be a minimum of 20 m to ensure the event is identifiable and coherent enough to measure a stacking velocity. SLI and SI were selected as 2.5 m each to obtain even fold coverage and a well-populated offset distribution in each CMP bin, while keeping the total number of source points to a minimum. Since the receiver spread is twice as long as it is wide, the SLs were widened to increase the aspect ratio of the subsurface sampling area and improve the azimuth distribution. The patch is rolled 5 RLs for each lateral move and 10 receiver stations for each vertical move, or half a spread in either direction, to minimize acquisition time while maintaining high fold.

Figure 5.6 shows the survey layout (a) and corresponding fold plot (b). The green, dashed rectangle indicates the area of a live spread, with live receiver and source lines indicated by light blue and purples lines, respectively. Ultimately the survey design parameters included 7 SLs with 13 source locations each, spaced 2.5 m in each direction, 10 RLs with 20 receivers each, spaced 0.5 m in each direction, and an X_{min} and X_{max} of 0.35 and 21.16 m, respectively, per patch. The patch was repositioned using receiver-spread rolls of half a receiver-spread length and width (2.5 m laterally, 5 m vertically). This design led to a total fold of 210 with an approximately symmetrical offset-distribution curve. The patch aspect ratio is 0.69, technically termed wide-azimuth.

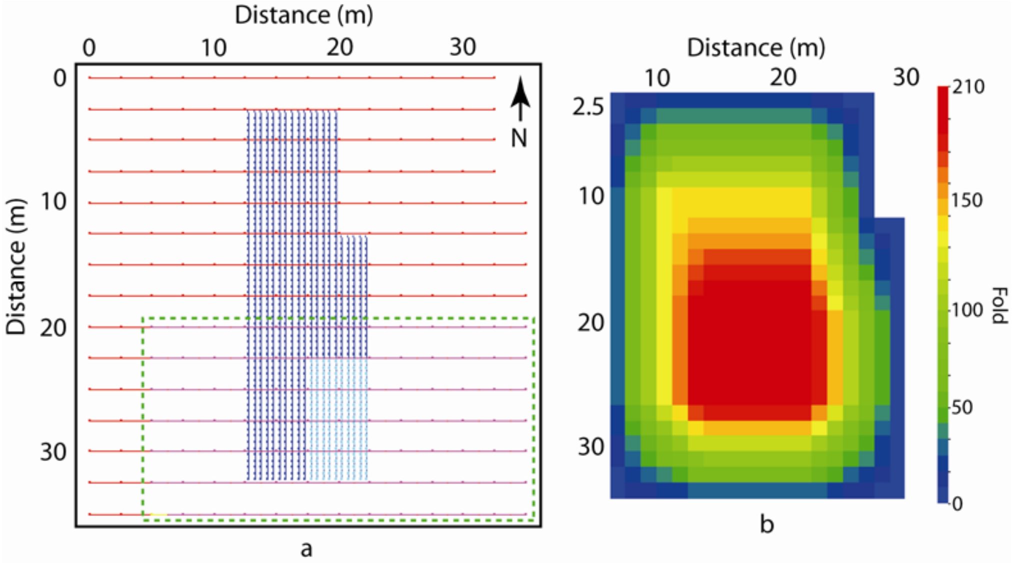

Figure 5.6. Survey layout (a) and corresponding fold map (b). The live-patch area is indicated by the green, dashed rectangle.

Figure 5.7 displays the offset- (a) and azimuth- (b) distribution curves for the 3D survey design. The majority of the traces fall between offsets of 3–17 m, while still recording ~2000 traces out to 19 m. This distribution allows us to image the top of the saturated zone (TSZ), the stratigraphic boundary, and bedrock reflections. North and south are represented by 0° and 180°, respectively, in the azimuth-distribution plot. The distribution shows a higher concentration of traces in the 60–120° range, which is caused by the higher percentage of shots on the east and west sides of the receiver patch (Figure 5.6). Judging by the trace counts for the two plots,

(b) does not appear to equal (a), but the azimuth trace count only represents half of the total traces since it is mirrored in the 180–360° range.

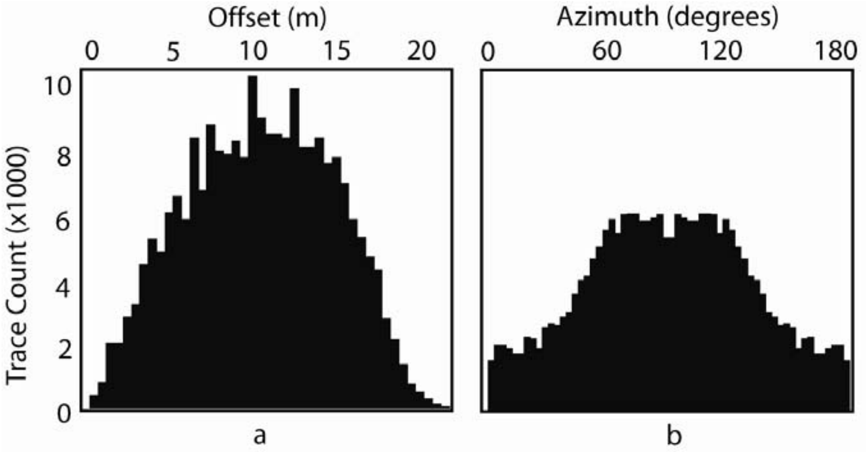

Figure 5.7. Offset- (a) and azimuth- (b) distribution plots of the 3DAJ survey design.

An offset-redundancy plot is shown in Figure 5.8. This type of plots shows the range of offsets sampled within each bin. Bins are represented by a vertical line divided into colored blocks, with each block representing 0.25 m of offset. The color of the block indicates the number of times a particular offset was sampled, regardless of azimuth. Bins in the very center of the design have a higher number of near-offset traces and lower number of far-offset traces. The opposite can be said for bins towards the outside of the survey. This is due to the design itself, as the low-fold areas also correspond to the farthest shots in the patch layout.

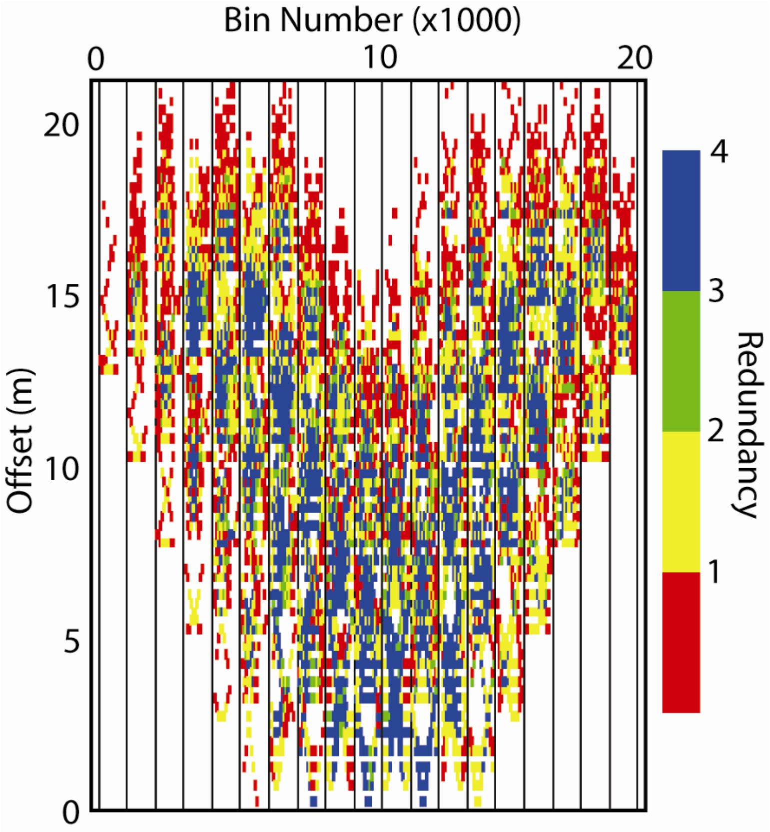

Figure 5.8. Offset-redundancy plot for the 3D survey design.

Field Acquisition

Data acquisition spanned two and a half days from June 30-July 2, 2008. The 3DAJ was pulled to the field site using a Ford F-350 truck. The long spikes on the geophones preclude pre-survey rigging of the geophones and cables as there is not enough ground clearance beneath the trailer body to prevent damage to the geophones as it is pulled across high and low spots. It took approximately 2.5 hours to emplace 200 geophones, attach the cables to the frame, and connect the geophones to the cables. The 3DAJ was left at the field site overnight during acquisition, so this was not a daily task. Cables were attached to the frame above the geophones, where they were least likely to be damaged, using zip ties and electrical tape. Each receiver line houses 20 geophones; however, the custom seismic cables have 24 takeouts for ease of use with 24-channel seismographs. To simplify cable placement and geometry input during processing, the last four takeouts on each cable were left open so that there was one cable per line to avoid snaking leftover takeouts to the next line. Figure 5.9 shows several field photographs.

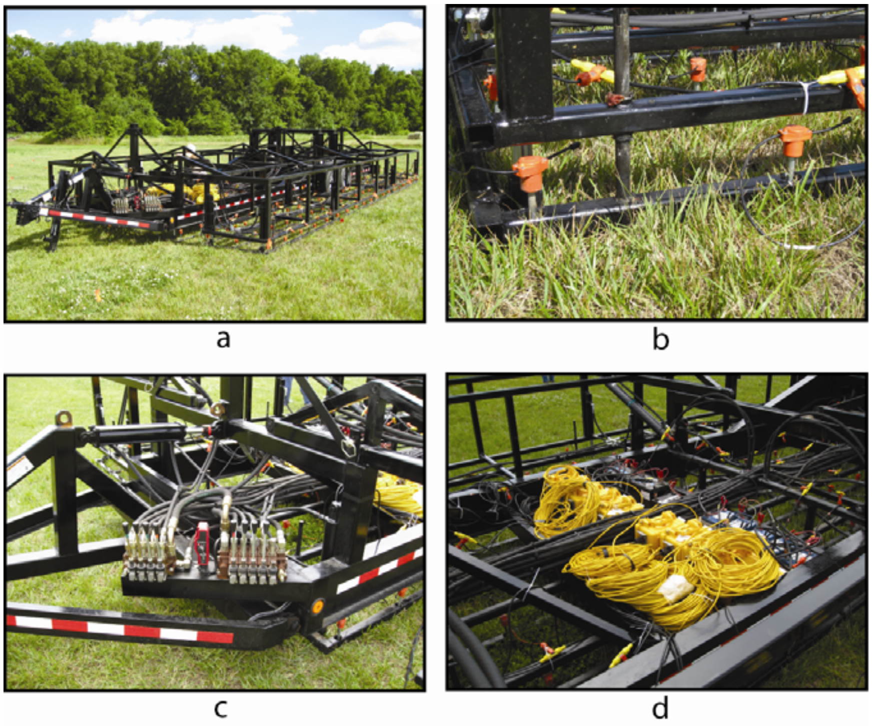

Figure 5.9. Photographs depicting the 3DAJ after planting (a), a close-up of the geophones after deployment (b), the hand levers used to control the hydraulics (c), and a platform installed to house the recording equipment (d).

As the 3DAJ moves from location to another, so must the seismographs, batteries, connector cables, etc. A platform was built that sits within the trailer frame

(Figure 5.9d) to house the recording equipment. With so many moving parts, this was especially helpful to ensure nothing was tangled, pinched, or run over during spread moves.

Once everything was connected and ready to go, the 3DAJ was planted for production for the first time (Figure 5.9a-b). Planting the geophones took an average of ~1 minute. The positioning of the axles prevents the geophone frames from closing completely in the middle of the frame. This led to several geophones either not planted deep enough or away from vertical. Bad plants were accepted up to 2% (4 geophones) of the total, as the gain from replanting would be negligible compared to time lost trying to get every geophone positioned perfectly.

Data were acquired using ten 24-channel Geometrics Geode seismographs with 24-bit A/D and a field laptop computer. Sampling interval was 0.25 ms for trace lengths of 256 ms. The receivers were Mark Products L-40A2 100-Hz vertical-component geophones. The source was a .22-caliber rifle firing single long-rifle rounds into ~15-cm deep pre-punched holes. It took an average of ~31 minutes to acquire a complete patch and ~7 minutes to pick up the geophones, reposition the 3DAJ, and redeploy the spread. The first several spread moves were slower, but took less time as the operator became more comfortable with the hand levers used to control the hydraulics (Figure 5.9c). As with the conventional survey, the limiting factor was the time required to punch holes for the source. The weather during the survey was mild with temperatures in the low 90s and occasional wind gusts. Nearby mowers and a tractor cutting and baling hay were the most notable sources of noise.

Data were acquired by rolling the patch along N-S transects. Five patches were shot along each line, then the 3DAJ was shifted 2.5 m laterally to the east, and so on. We began the survey by decoupling the 3DAJ from the truck during shooting to avoid blocking the northernmost source locations. However, this took ~10 minutes per spread move by the time the truck was backed into position, the trailer hooked up and repositioned, decoupling the trailer, and moving the truck. After the second spread move, the 3DAJ was left hooked to the truck to save time and affected source locations were shifted 0.25 m to the south. This adjustment affected the fold of the northernmost bins, but only by a small percentage. A four-person crew was used each day, which allowed two people to record data (one source operator and one observer) while the other two measured and punched holes for the next spread. This method worked very efficiently.

Three spreads were acquired the first day, seven on the second, and three on the third day, for a total of 13 spreads, 1183 source locations, 2600 receiver locations, and 236,600 traces. Structural failures in the trailer frame on the third day prevented any further data from being acquired. With so much hydraulic force, weak points in the frame failed with some bending of the frame and broken welds. To avoid potentially stranding the 3DAJ at the field site, the survey was halted and the trailer hauled back to the geophysics shop to be repaired. Although the survey ended prematurely, ~1225 m^2 area was covered, compared to ~550 m^2 in the first 3D survey. After initial data analysis and processing, it was determined that enough data were acquired to meet the survey objective—to show that the 3DAJ is capable of acquiring

3D USR data in production mode—and further data collection was not necessary for this study. The following chapter will discuss analysis, processing, and interpretation of the data collected during this survey.

Chapter 6

3D Autojuggie Processing & Results

Introduction

The 3D data set acquired using the 3D Autojuggie (3DAJ), discussed in the preceding chapter, was processed with a flow similar to that described in Chapter 3 using subsets based on the optimum window (Hunter et al., 1984) of each reflection. Unprocessed common-source gathers are displayed in Figures 6.1–6.3 to show the presence of reflection hyperbolae prior to processing. Several reflections were recorded by the survey, including the top of the saturated zone (TSZ) (Figure 6.1), two stratigraphic boundaries (S1 and S2) (Figures 6.2 and 6.3), and bedrock (BR) (Figure 6.3). Shot gathers are displayed with a 200–500 Hz bandpass filter with 16 and 12 dB/octave rolloff slopes on the low and high sides, respectively, and a 60-ms automatic gain control (AGC) window. The TSZ, S1, and BR reflections were coherently imaged across the entire survey area; however, the S2 reflection appears only on the east side of the area, which will be discussed further in the results section. This chapter focuses on the data-processing parameters and results of the 3DAJ data set.

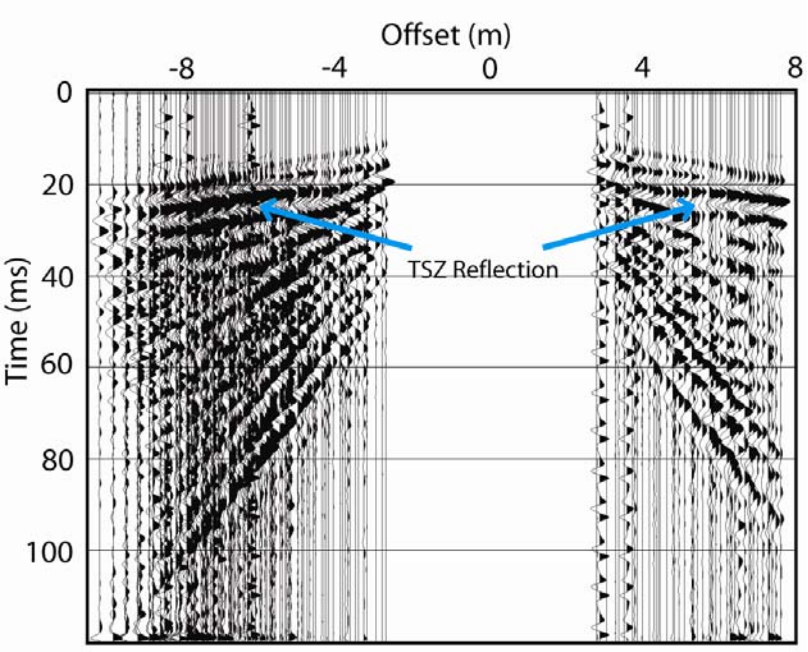

Figure 6.1. Raw shot gather showing the TSZ reflection, indicated by the blue arrows.

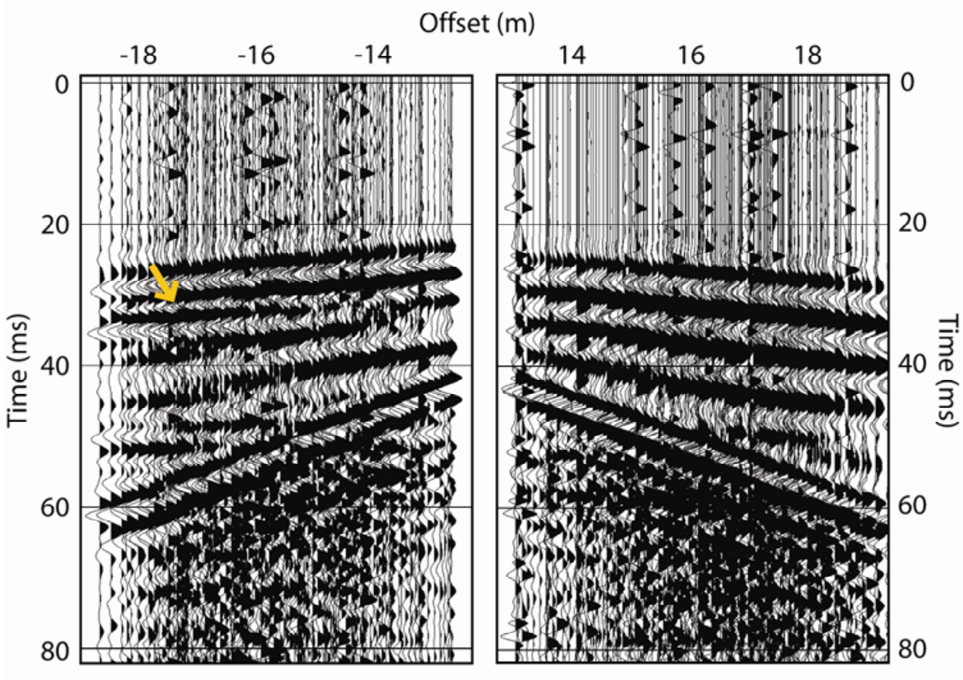

Figure 6.2. Corresponding raw shot gathers from the east (left) and west (right) sides of the survey area. Notice that the S2 reflection, indicated by the orange arrow, is present in the left-side gather, but not the right.

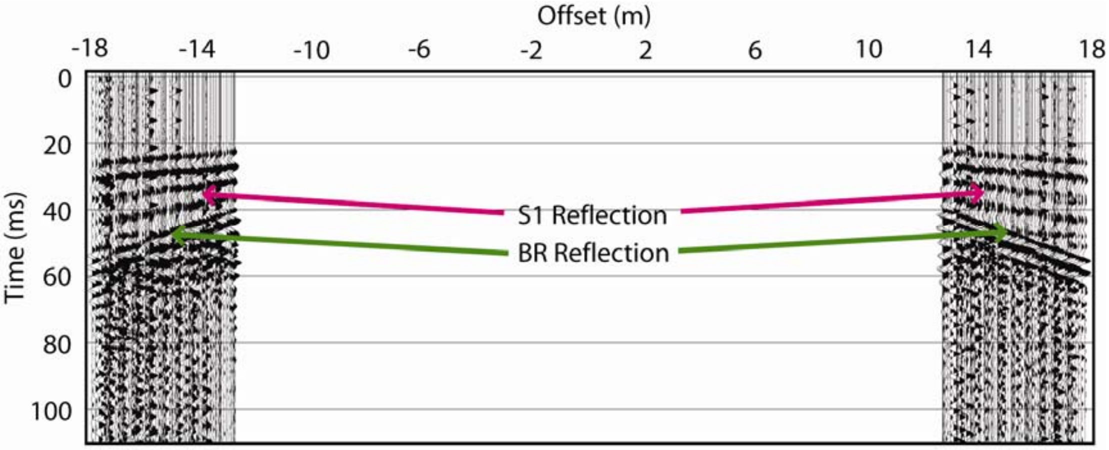

Figure 6.3. Raw shot gather displaying the S1 (pink) and BR (green) reflections.

Processing

Preprocessing

Data were processed using Seismic Processing Workshop (SPW) by Parallel Geoscience. Data were first converted from SEG-2 (recorded format) to SPW-formatted files to be recognized by the processing software. Survey geometry was then defined by assigning an *(x,y)* coordinate to each receiver and source location to assign each trace to its respective common-midpoint (CMP) location and for accurate offset and velocity determination. Traces were grouped into 0.5 by 0.5 m bins to improve offset distribution and provide for more accurate velocity calculations. Noisy traces and field files were removed from the data set.

Because the two geophone frames on the 3DAJ do not close completely beneath the trailer axles, there was a gap above the receivers large enough for them to stray from vertical during automatic planting. In some instances where the geophones were planted at an angle, the geophone spikes would be in contact with the steel frame. This caused the affected traces to appear ringy, which can be seen prior to the first arrivals in Figure 6.2, and decreased the signal-to-noise ratio (S/N).

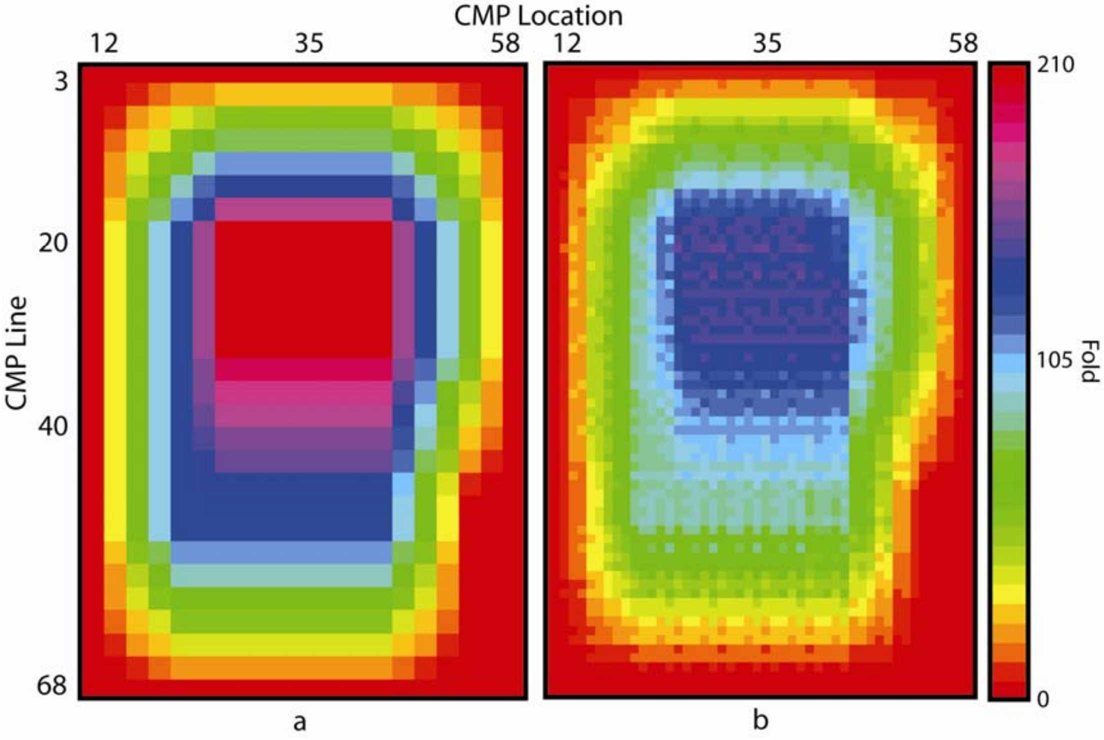

Figure 6.4. Fold plot comparison from data before (a) and after (b) trace editing.

Three shots per spread were fired along the center line of the 3DAJ, within the trailer frame. A significant number of traces were removed from these records due to high noise levels; however, there were only three affected shots per spread (39 out of a total of 1183 in the data set). It is suspected that the increased noise is caused by air wave reverberations from the 3DAJ frame. Nearby mowers and a tractor baling hay in an adjacent field to the south also led to the removal of records with high noise content. Figure 6.4 compares fold plots before and after trace editing. Maximum fold was 210 prior to trace editing, after which it averaged ~100 across the area with a high of ~175. The area covered by the survey is relatively flat topographically and did not warrant elevation corrections. The data were sorted into CMP gathers following trace editing (Figure 6.5). Walkaway data are shown in Figure 5.3 for reference.

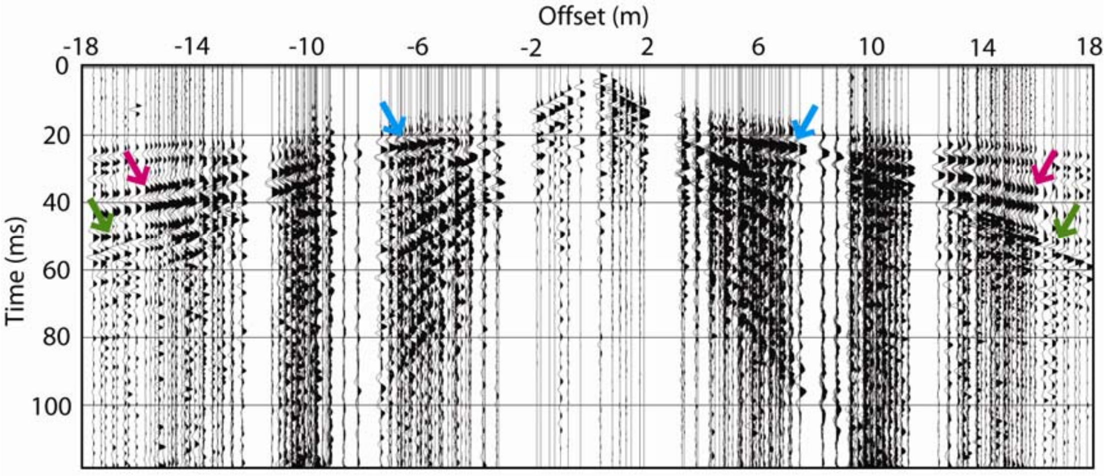

Figure 6.5. CMP-sorted gather with reflections indicated by the blue (TSZ), pink (S1), and green (BR) arrows.

Muting

Early mutes were picked on CMP gathers to remove first arrivals and were applied with a Hanning-style 10-sample taper (Figure 6.6a). Surgical mutes were picked and applied in the same manner to remove the air wave (Figure 6.6b). *F-k* mutes were also used to remove low-velocity ground roll and improve S/N. Figures 6.7 and 6.8 illustrate a representative *f-k* spectrum and corresponding shot gather. The ground roll (yellow), air wave (gray), and TSZ refraction (orange) are clearly visible and appear as linear events with apparent velocities of 180, 335, and 1550 m/s, respectively. Because reflections are hyperbolic in the *x-t* domain, they are represented by an area in the *f-k* domain instead of a line, indicated by the dark green oval in Figure 6.8.

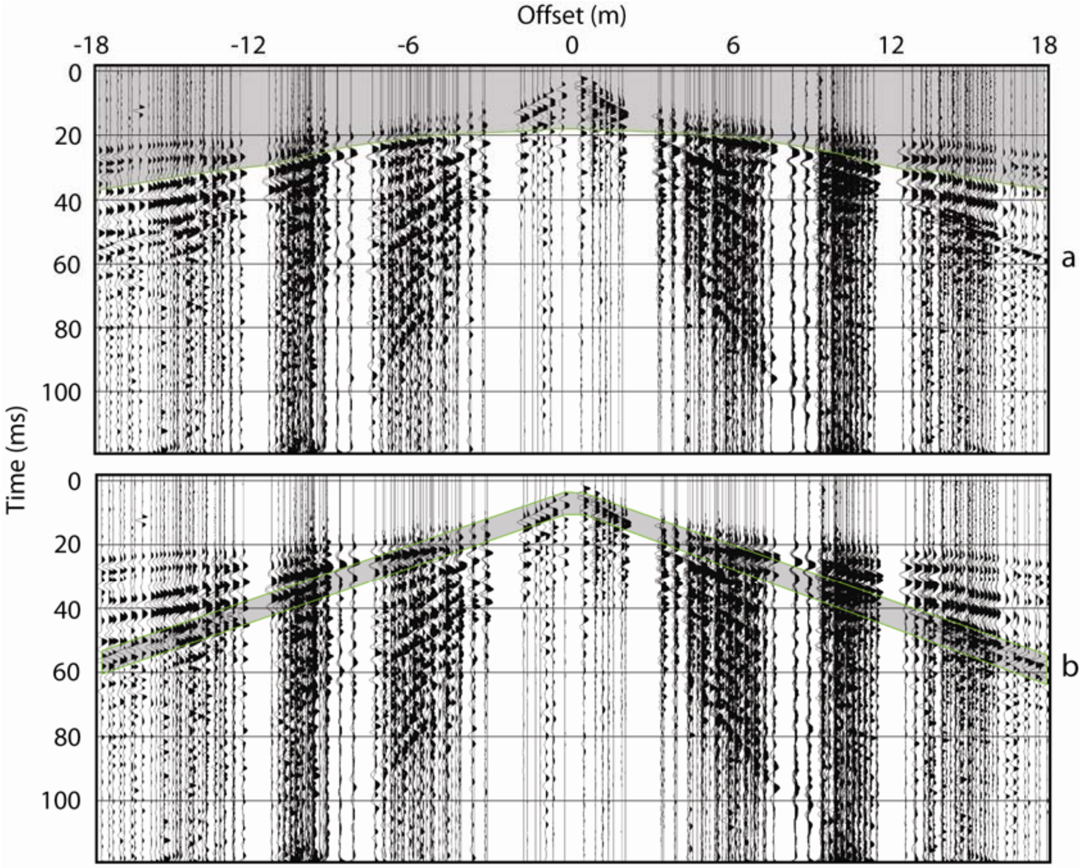

Figure 6.6. CMP gathers with representative early (a) and surgical (b) mutes displayed. The shaded areas mark the muted portions of the records.

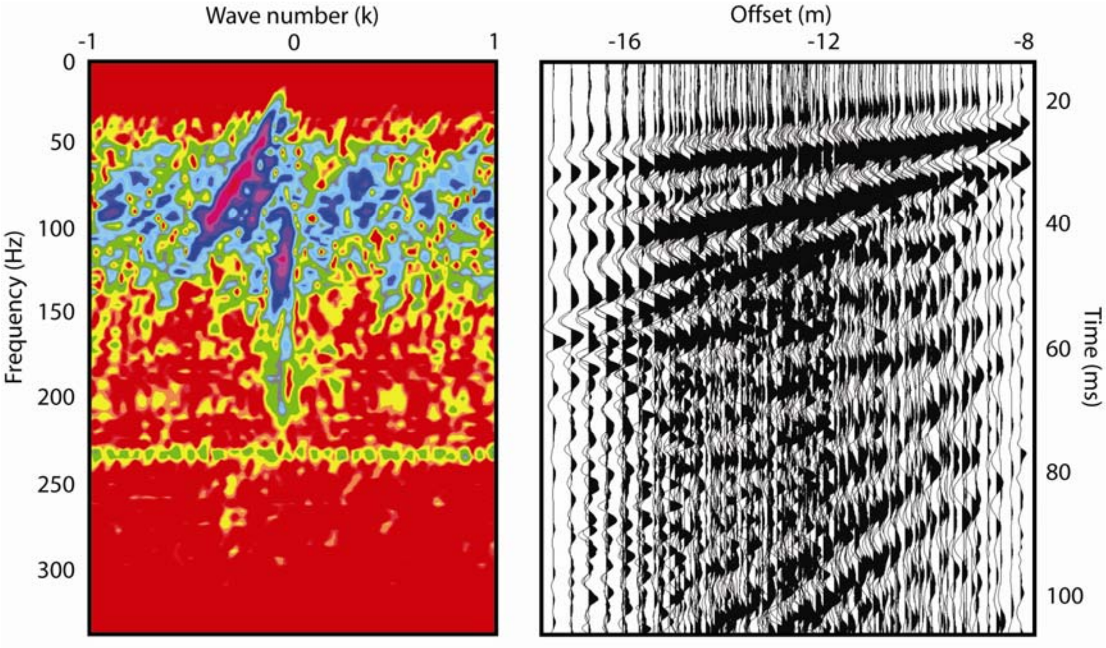

Figure 6.7. *F-k* spectrum and corresponding shot gather.

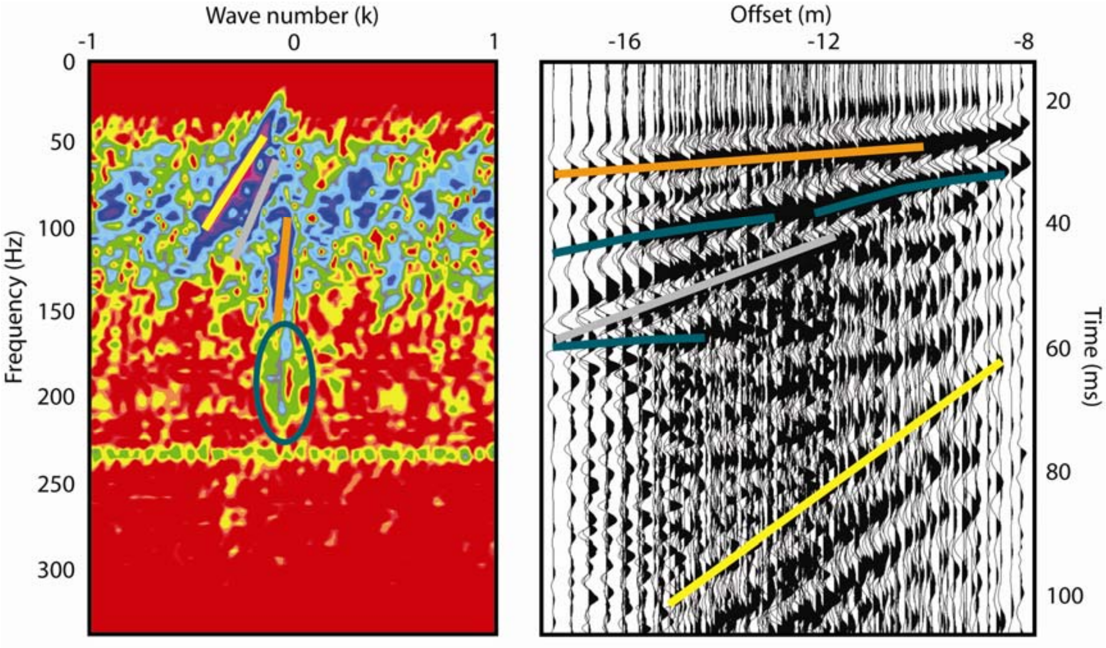

Figure 6.8. Same as Figure 6.7, but with interpreted features. Colored lines indicate ground roll (yellow), air wave (gray), TSZ refraction (orange), and reflections (dark green) on both records.

Subset Division

Data were processed in the same manner as those discussed in Chapter 3 using optimum-window based subsets to avoid artifacts associated with the normal-moveout (NMO) correction of intersecting reflection hyperbolae (Miller and Xia, 1998). Figure 6.9 shows a CMP gather with colored rectangles indicating the subsets. Subset I (blue) includes the TSZ reflection, II (pink) includes S1 and S2 reflections (where present), and III (green) contains the BR reflection. Subset I includes offsets up to ~12 m and 0–48 ms in time. Subset II encompasses offsets greater than 12 m and in the same time range. Subset III contains all offsets and 48–100 ms in time.

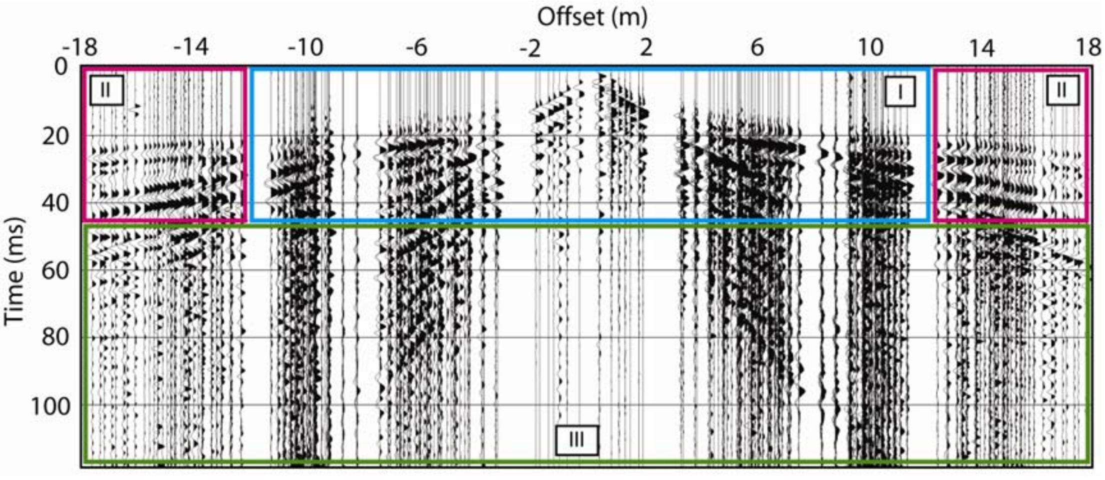

Figure 6.9. CMP gather with data subsets outlined by the colored rectangles. Subset I (blue) includes the TSZ reflection, II (pink) includes the S1 and S2 reflections, and III (green) contains the BR reflection.

Velocity Analysis/Statics

The location of the conventional 3D survey (~60 m to the east) exhibited lateral velocity variations in the upper five meters ranging from ~300–600 m/s;

however, this was not an issue for this survey. Direct wave and TSZ reflection velocities did fluctuate across the area, but only by ~10–20%. Velocity analysis was performed using constant-velocity stacks for each reflection with iterative surface-consistent statics corrections. Velocities were picked at every 5th CMP location. Statics corrections were calculated using NMO-corrected CMP gathers by cross-correlating each CMP gather with the average of a three-gather window. Three iterations of velocity picking and statics corrections were applied with an allowable shift of 1 ms for the first iteration and 0.5 ms for each successive iteration. Constant-velocity-stack ranges used for picking varied from ±20 m/s on the first pass, to ±10 m/s on the second, and ±5 m/s on the final pass.

Figure 6.10 illustrates the change in the TSZ reflection from the first-pass brute velocity analysis to the final analysis after iterative velocity picking and statics corrections. Note that the improved reflection coherency is not entirely dependent on statistically calculated static shifts, but is largely due to the refined stacking-velocity analysis, evidenced by the alignment of the highs and lows with velocity pick locations.

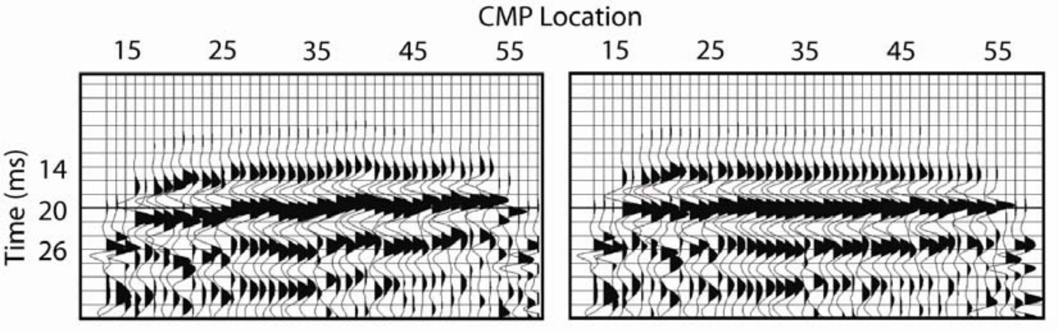

Figure 6.10. Comparison of the stacked TSZ reflection (~20 ms) from the initial velocity analysis (left) to the final analysis after three iterations of refined velocity picks and surface-consistent statics calculations (right).

NMO velocities for the TSZ, S1, S2, and BR reflections averaged ~525, 775, 825, and 1300 m/s, respectively. NMO stretch mutes, used to remove overly stretched portions of the record resulting from the NMO-correction process, were 17% for the TSZ and 30% for all others. Following NMO corrections, the three subsets were merged into one data volume, and CMP stacked. Data were merged using a 5-sample temporal overlap to prevent data-seam artifacts. A 195–500 Hz bandpass filter with 16 and 12 dB/octave rolloff slopes on the high and low sides, respectively, and a 60-ms AGC window were applied.

Results

Data were interpreted using the Kingdom Suite commercial seismic interpretation software package by picking reflection horizons on each line in the inline and crossline directions. Rendered surfaces are directly from the interpreted horizons and no interpolation has been applied. Four different reflections were identified during data processing, which are highlighted in Figure 6.11. Selected colors are consistent with those used in previous figures: the TSZ reflection is represented by the blue line, S1 is pink, S2 is orange, and BR is green. Figure 6.11 is a CMP-stacked line taken from the volume with interpreted reflections. Peaks are displayed in dark blue with troughs displayed in brown. Velocity increases with depth and each successive reflection, which would lead to peak-trough-peak wavelet sequences. Hence, the second blue peak beneath the TSZ interpretation is also part of the TSZ reflection "packet", and the same can be said for the S1 and BR reflections. Dominant frequencies, interval velocities, wavelengths, vertical resolution, and thicknesses for each reflection are listed in Table 6.1.

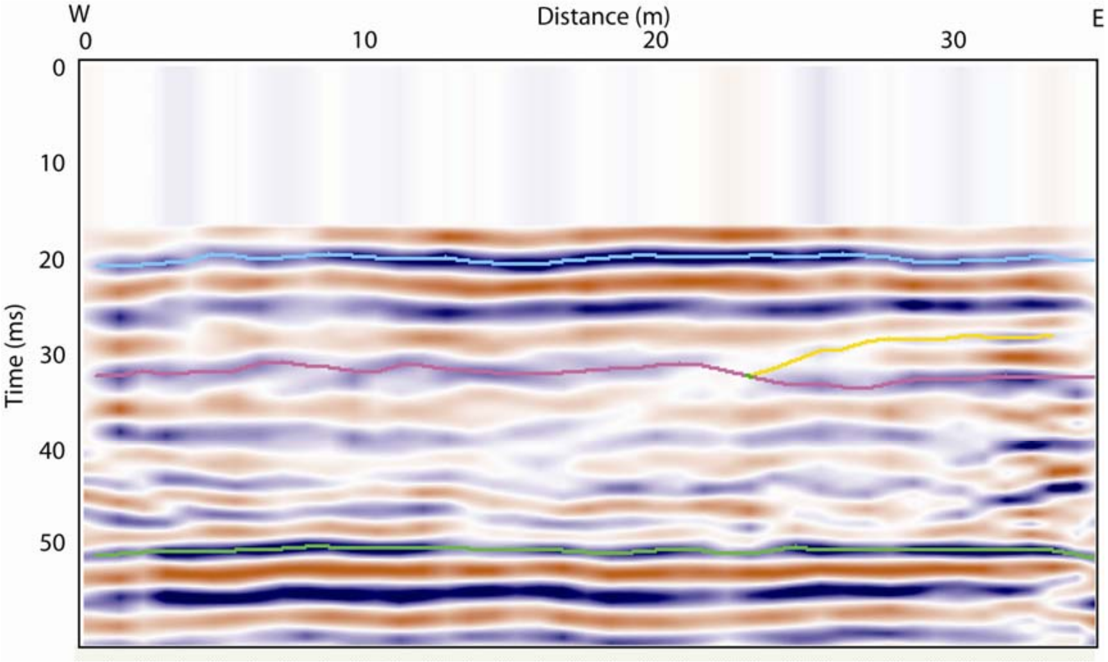

Figure 6.11. CMP-stacked line with interpreted reflections indicated by colored lines. TSZ is in blue, S1 in pink, S2 in orange, and BR is in green.

Table 6.1.

Reflection	**TSZ**	**S1**	**S2**	**BR**
Dominant Frequency (Hz)	225	150	150	125
Average Interval Velocity (m/s)	525	1030	1100	1500
Wavelength (m)	2.4	6.9	7.3	12
Vertical Resolution (m) (1/4 λ)	0.6	1.7	1.8	3
Thickness (m)	4.7	4.5-6.2	1.9	7

Figure 6.12 illustrates a 3D chair plot of the data volume. Each of the interpreted reflections is clearly visible in the seismic data. The BR reflection (green) was interpreted as the blue peak at ~50 ms because of its coherency throughout the volume. However, there is also a semi-coherent peak immediately above it at ~47 ms, most notably seen on the west side of the volume. The bedrock in this area consists of alternating layers of shale and marine limestone characteristic of the Pennsylvanian System in Kansas. It is possible that this discontinuous reflection marks the top of a weathered shale layer where more coherent rock would provide a more distinct reflecting interface; however, core samples would be necessary to confirm this. Because of the coherency and high amplitude of the 50-ms peak, and its prominent identification in common-source and CMP gathers, it was interpreted to be the top of the bedrock surface.

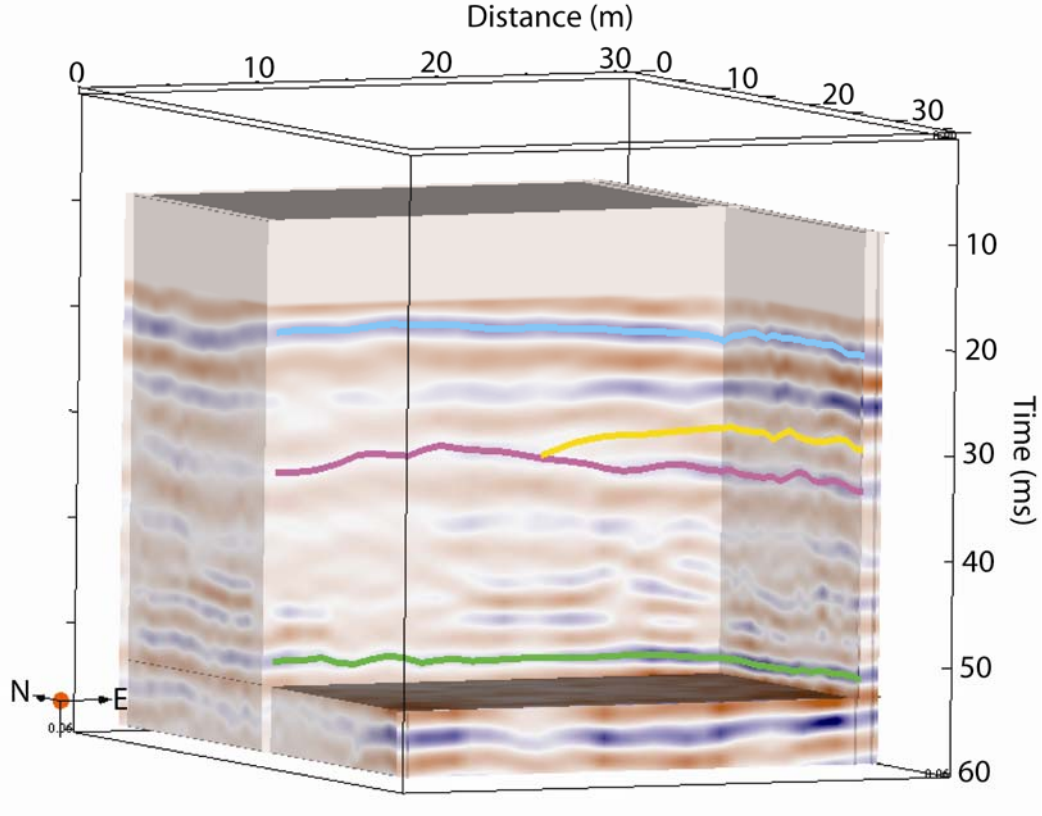

Figure 6.12. 3D chair diagram with interpreted reflections.

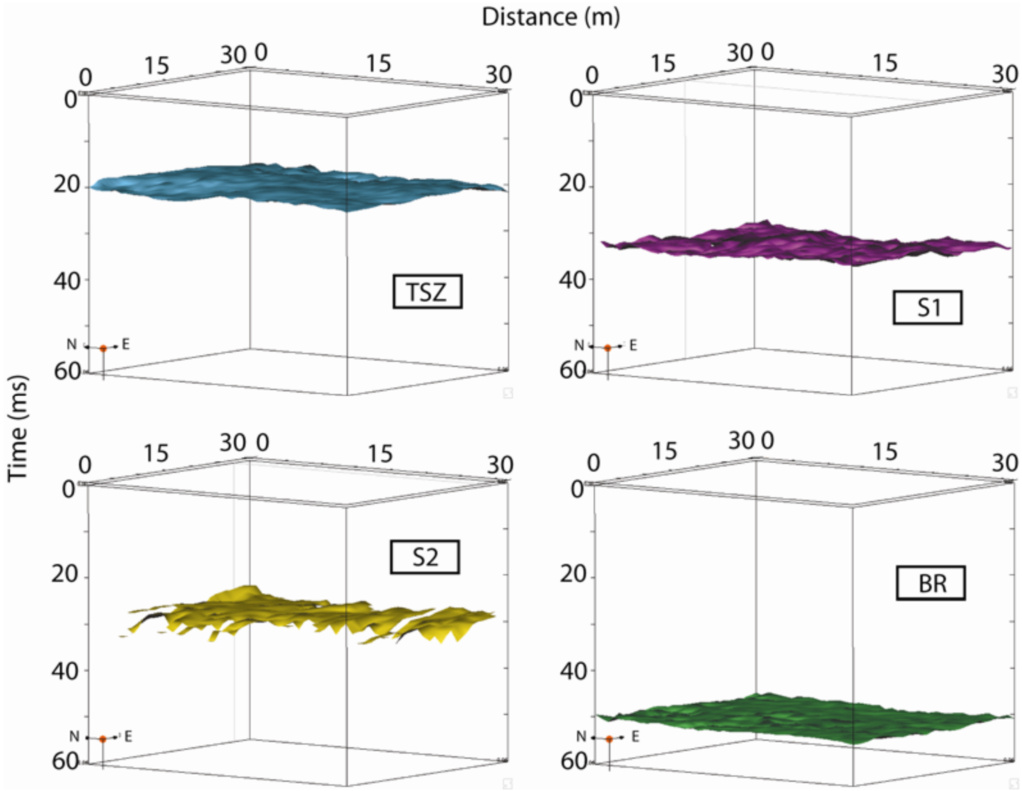

Figure 6.13. 3D surfaces interpreted from the seismic volume.

Each of the 3D surfaces rendered from the interpreted horizons is illustrated in Figure 6.13. The TSZ and BR surfaces are relatively flat. S1 dips slightly to the east (down slope and towards the creek), and S2 is relatively flat, but dips downward to the west where it meets the S1 surface. Horizontal resolution is loosely related to the radius of the first Fresnel zone (r_F):

$$r_F = \frac{V}{4}\sqrt{\frac{t}{f_d}},$$

where V is the velocity, t is the two-way travel time, and f_d is the dominant frequency. The larger the radius, the more horizontal "smear" there is at a point in the subsurface. Lower velocities and higher frequencies produce a smaller Fresnel zone radius and higher horizontal resolution. For the S1 and S2 reflections r_F is ~3.7 m, meaning the exact point where S2 meets S1 and its dip are interpretive at best and can not be conclusively pinpointed. Higher frequencies would be necessary to further distinguish the intersection of the two reflections.

Figure 6.14 depicts the top (left) and bottom (right) views of the interpreted S2 surface with a time-amplitude slice from 30 ms. The selected time slice cuts through the trough between the S1 and S2 reflections on the east side of the survey (Figure 6.11) to show the intersection of the two surfaces marked by the transition from negative amplitude (brown) to positive (blue). This boundary also coincides with the interpreted western edges of the S1 surface.

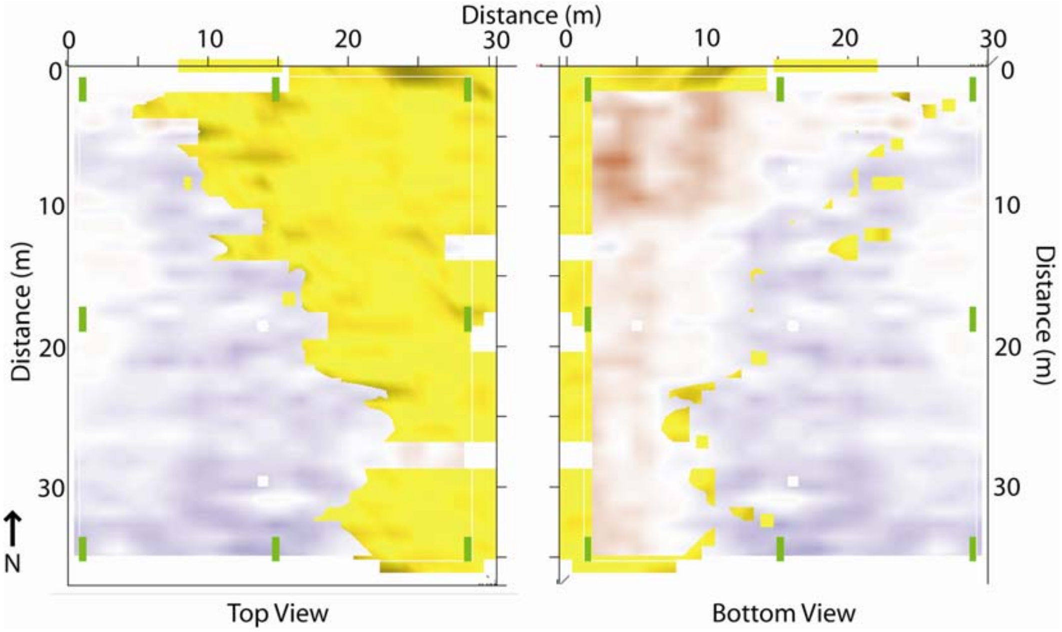

Figure 6.14. Top (left) and bottom (right) views of the 30-ms time slice indicating the intersection of the S1 and S2 reflections.

Figures 6.15 and 6.16 illustrate the spatial relationship between the S1 and S2 reflections. S1 (pink) is relatively flat on the west side of the survey area, buts breaks downward to the east at ~20 m. S2 adjoins S1 approximately at this downward break and continues eastward with a thickness of ~1.9 m between the two surfaces. The change in slope of S1 may be indicative of a depositional feature, such as a paleo-channel, but is unknown without boreholes on either side or a larger-scale survey to confirm.

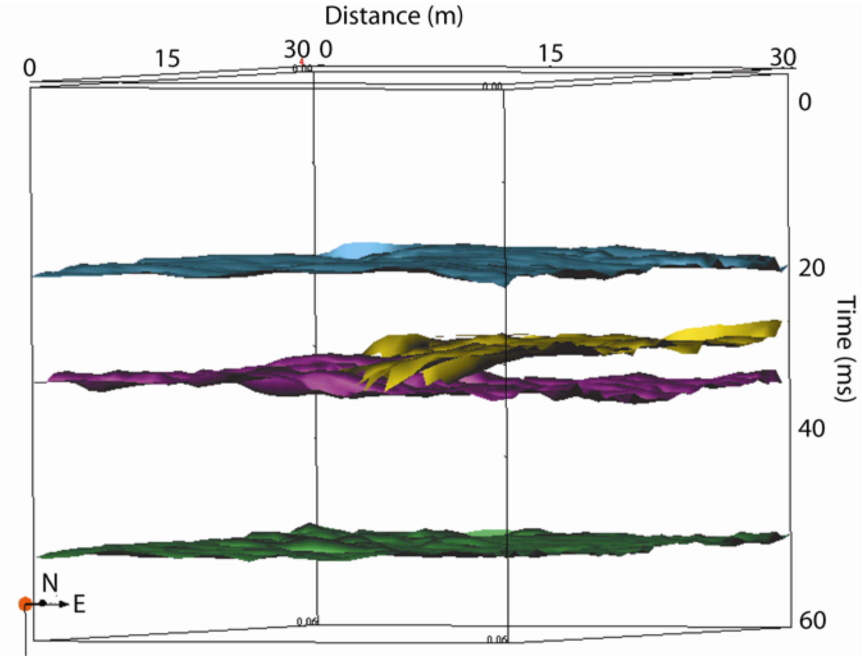

Figure 6.15. 3D view of the interpreted surfaces from the south-southwest.

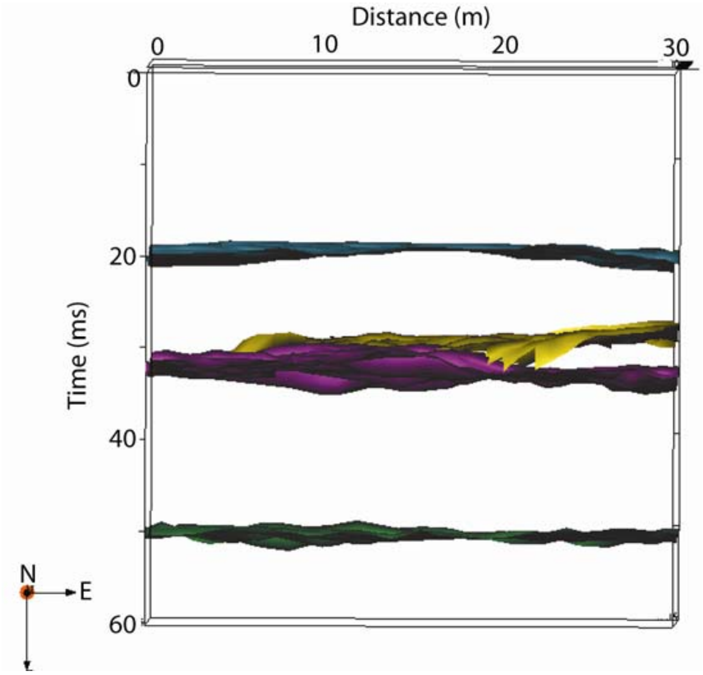

Figure 6.16. 3D view of the interpreted surfaces from the south.

The site lies within the Wakarusa River valley and is adjacent to a creek that drains into the river from the south. Previous seismic studies conducted at the site (Sloan et al., 2008; Czarnecki, 2006; Vincent, 2005) have imaged depositional features associated with a fluvial depositional environment, including a paleo-channel feature. The results of this survey are consistent with previous studies; however, an additional depositional reflector overlying bedrock was imaged by this study. This survey is located ~60 m west of all previous seismic lines. Considering the lateral geologic variations possible in a fluvial environment, it is likely that heterogeneities in the near-surface unconsolidated materials exist.

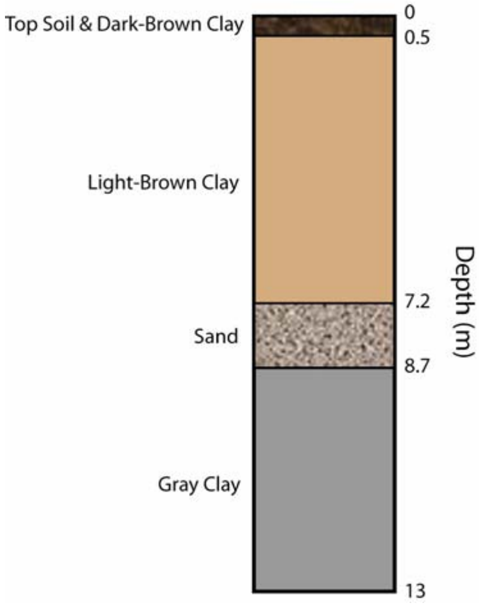

Figure 6.17. Illustration of sediments encountered during drilling. The top layer represents top soil and a dark brown clay, followed by a stiff light-brown clay, sand, and a plastic light-gray clay.

A borehole was drilled on October 28, 2008, on the east side of the 3DAJ survey area to verify the presence and depth of reflectors. A 15.24 cm (6") auger was used to drill to bedrock and a split-spoon sampler was used to sample unconsolidated materials in 0.61-m (2') sections (Figure 6.17). The upper 0.5 m was comprised of topsoil and dark-brown clay with organics, followed by 6.6 m of stiff light-brown clay. No samples were recovered deeper than ~7.2 m, where it was determined that a sand interval was encountered. The water table was reached at ~4.2 m. In a fully saturated environment, unconsolidated sand samples are unlikely to be recovered using a split-spoon sampler. Although further sampling could not be completed, a spear tip was used to drill deeper to determine the depth of bedrock. Cuttings recovered from the augur flights showed a plastic, light-gray clay, which was continuous to ~13.5 m. At a depth of ~13.5 m, drill advancement was halted which led the driller to believe bedrock may have been reached.

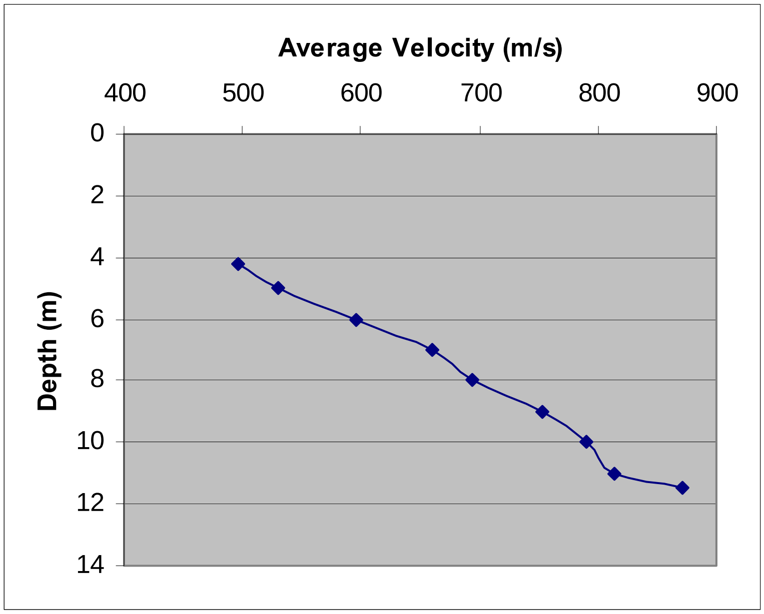

Figure 6.18. Plot showing the change in average velocity with depth measured by a down-hole seismic survey.

A down-hole seismic survey was conducted at the same time to measure the change in average velocity with depth (Figure 6.18). The source and receiver consisted of a Mark Products hydrophone and a 1-lb. hammer striking a steel plate located 2 m from the borehole. Three successive hammer strikes were recorded at 1-m depth intervals and stacked to improve the S/N ratio. Data were recorded using a Geometrics Geode with 24-bit A/D conversion and a field laptop. The sampling interval was 0.125 ms. Foam padding was placed in the top of the hole to dampen noise from the hydrophone cable and prevent air wave contamination. Wall failure in the uncased hole prevented sampling of the entire interval, but measurements were made from the water table at ~4.2 m to a depth of 11.5 m. Hydrophones are sensitive to changes in pressure and must be submerged for accurate measurements. Because of this requirement, the first measurement was made just beneath the water table instead of beginning at the surface.

Results of the down-hole survey and drilling correlate relatively well with the interpretation of the 3DAJ data set. The average down-hole velocity to the water table was ~496 m/s, while the surface seismic exhibited an average velocity of ~525 m/s. The average down-hole velocities to the top of the sand (S2) and top of the gray clay (S1) were ~695 and 815 m/s, compared to surface-seismic velocities of ~775 and 825 m/s, respectively. Velocity errors of 10% are not uncommon considering that the velocity for a common midpoint is determined using traces whose raypaths traverse different parts of the subsurface (and varying properties) spanning an area and not a point.

Drilling showed the presence of a sand layer at 7.2 m overlying a clay layer at a depth of 8.7 m, which correspond to the S2 and S1 reflections, respectively. Depths to the sand and clay layers were determined to be 9.2 m and 10.9 m using the 3D seismic data. This discrepancy is likely explained by an overestimation of NMO-correction velocities, where surface-seismic velocities were consistently higher than down-hole velocities by 6–10%. The best match between the down-hole and surface velocities was from the sand interval, which were 815 and 825 m/s, respectively.

Drilling determined that the sand layer is ~1.5 m thick, compared to the seismic estimation of ~1.9 m.

Discussion

Despite its advantages, the 3DAJ also has some limitations. It is not well suited for rough topography. The wings and main body can be operated independently of each other, which provides some ability to deal with small changes in topography, but because of the rigid frames abrupt changes such as ditches will present acquisition obstacles. Recording source locations within the frame is also problematic. The foremost concern is safety and one must be very cautious when moving over, under, or around the frame. Because there is so much material in a confined space, i.e. multiple horizontal and vertical steel bars, axles, tires, hydraulic cylinders and lines, etc., much of the data recorded within the frame are contaminated with airwave reverberations. Depending on the survey design parameters, skipping source locations in the middle will lead to gaps in subsurface coverage and a loss of near-offset traces. Possible solutions include wrapping the square tubing with foam padding, or something comparable, to reduce the echo effect or compensating for the missing offsets with additional shots around the edges of the 3DAJ.

Practical acquisition considerations include the accurate measurement of spread locations. The 3DAJ can be difficult to maneuver to a precise location and bearing in confined areas. For ultra-shallow applications spread positioning errors as small as 0.25 m can make a difference in fold and CMP coverage. Conventional surveying techniques or GPS coordinates of the four corners of the 3DAJ would aid in correctly positioning traces and bins in the subsurface during geometry assignment.

In general, the limiting time factor in planting geophones is the rate at which the hydraulic system can raise and lower the different components; however the operator is the biggest variable. As all of the components are manually controlled using hand levers, the level of experience and familiarity of the operator with the controls can definitely make a difference. The overall factor that affected acquisition time, both in this survey and the previous, was the time required to punch holes for the source. The development of a better method to punch holes or a high-frequency source that does not need holes would increase the efficiency of acquisition.

Future testing with the 3DAJ may include adapting it for use with three-component (3C) geophones to acquire 3D-3C data, which would require minor modifications to the geophone frames to allow increased separation or modified geophone-spike couplers. Surface-wave recording is also a possibility as the 3DAJ would allow multiple lines to be recorded simultaneously to develop a pseudo-3D shear-wave velocity profile of the subsurface.

Conclusions

This study has shown that the 3DAJ is capable of acquiring 3D near-surface seismic-reflection data and is more efficient than conventional acquisition methods in some instances. A survey area of ~1225 m^2 was covered in ~19 hours with a crew of four people and a total fold of 210. In comparison, the previously acquired 3D survey at the same test site covered an area of ~550 m^2 in ~10 hours with a crew of 10–12 people and a total fold of 48. This represents an 18% increase in square meters covered per hour, a 60–67% decrease in labor, and a 500% increase in fold. Several reflectors less than 20 m deep were imaged and stratigraphic boundaries were confirmed by drilling.

Other factors to be considered that cannot be directly measured are the efficiency and morale of the crew. Every geophone planted by the 3DAJ is one that does not have to be planted by hand resulting in less physical labor. Happy crewmembers with less fatigue are likely to translate into increased efficiency and more source locations recorded per day. Developments, such as the 3DAJ, that increase acquisition efficiency and lower the cost of collecting 3D seismic data may lead to more widespread use of 3D USR and SSR techniques in the future.

Chapter 7

Seismic response to partial water saturation

Results of this study have been published under the following citations:

Sloan, S. D., Tsoflias, G. P., and Steeples, D. W., 2006, Frequency effects of the partial water saturation zone thickness on shallow seismic reflection data: 76th Annual Meeting, SEG, Expanded Abstracts, 1362–1366.

Sloan, S. D., Tsoflias, G. P., and Steeples, D. W., 2007, Seismic AVO variations related to partial water saturation during a pumping test: 77th Annual Meeting, SEG, Expanded Abstracts, 1212–1216.

Sloan, S. D., Tsoflias, G. P., and Steeples, D. W., 2007, Shallow seismic AVO variations related to partial water saturation during a pumping test: Geophysical Research Letters, **34**, L22405, doi: 10.1029/2007GL031556.

Introduction

High-resolution shallow seismic reflection experiments were conducted to image the cone of depression during and after a pumping test of an agricultural irrigation well. Although variations in the reflection time from the top of the saturated zone were not observed, frequency and amplitude-versus-offset (AVO) analysis revealed changes in reflection character that correlate temporally and spatially to expected changes to the partially saturated zone induced by the pumping and recovery of the aquifer. The AVO responses exhibit dependence on aquifer drawdown and recovery cycles and the distance from the pumping well. We propose that near-surface soil heterogeneity and relatively rapid changes in the water table elevation during irrigation cycles caused a thickening of the partially saturated zone above the water table, which resulted in detectable changes in seismic reflection amplitudes and dominant frequencies. This study offers insights about the response of shallow seismic reflections to changes in subsurface water saturation and the potential application of seismic techniques to hydrogeophysical problems.

Multiple attempts have been made to image the cone of depression around an agricultural pumping well using shallow seismic reflection (SSR) techniques (Birkelo et al., 1987; Johnson, 2003; Sloan, 2005), however none have been successful. The experiment by Birkelo et al. (1987) was unsuccessful in part due to a previously unknown clay layer that produced a perched water table. However, the authors observed a decrease in the dominant frequency of the reflection from a survey acquired before pumping in comparison to one collected while the water table was at maximum drawdown. The study described here was intended to image the cone of depression by conducting multiple SSR surveys during and after a pumping test at a site near Clay Center, Kansas (Figure 7.1). The field site was an agricultural field located in north-central Kansas. The water table was located at ~5 m depth in an unconfined aquifer comprised of unconsolidated sands and gravels, coarsening downward below the water table. A hand-augured hole at the site revealed ~5 m of fine-to-coarse sand with a 0.3-m thick silty-sand layer at ~3.1 m depth. An observation well installed ~6 m from the pumping well showed a water table elevation change of ~0.5 m at maximum drawdown.

Despite water table fluctuations of ~0.5 m, which were within the resolution limits of the seismic data, we were unable to observe temporal changes in the reflection from the top of the saturated zone (TSZ) that were attributable to pumping. However, AVO analysis of the data revealed seismic amplitude variations that correspond to differences in the applied pumping stresses and distances from the pumping well. We suggest that the thickness of the partially saturated zone (PSZ) above the water table is affected by a continuous cycle of pumping and recovery of an unconfined aquifer. Relatively rapid changes in the height of the water table in concert with small-scale soil heterogeneities have caused a thickening of the PSZ, which results in detectable changes in the AVO response of the TSZ reflection. Figure 7.1 illustrates the zone affected by pumping where (A) represents the water table surface prior to pumping and (B) is the water table during pumping once it has reached steady-state conditions, forming the cone of depression.

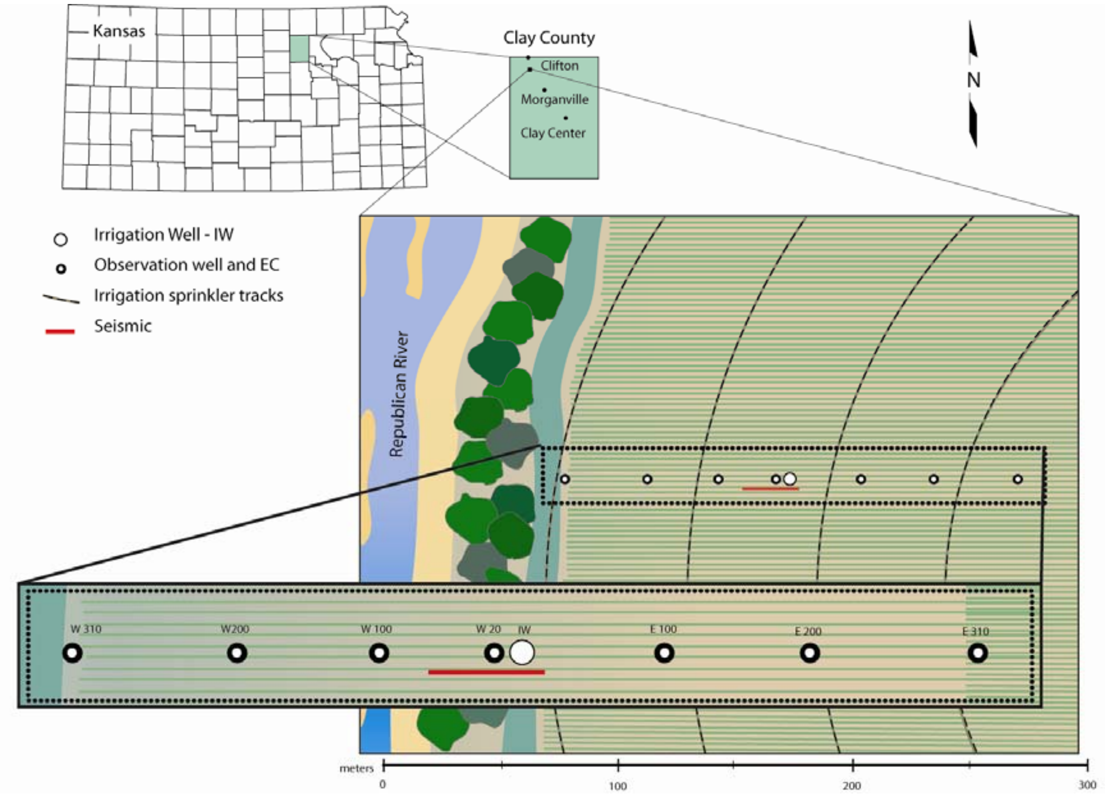

Figure 7.1. Illustration of the field site located near Clay Center, Kansas. The location of the seismic lines is indicated by the red line.

In order to relate the observed changes in reflection amplitude to the subsurface, we consider how the seismic properties of the subsurface might change as a result of the pumping cycles. The water table represents the fully saturated interface where water pressure is equal to atmospheric pressure. Immediately above the water table is the fully saturated capillary fringe, which underlies the PSZ. At steady-state conditions the thicknesses of the capillary fringe and PSZ are controlled by the grain size of the surrounding sediments. The enlarged section in Figure 7.2 depicts the increase in water saturation (S_w) from some residual value in the unsaturated zone to 100% in the fully saturated zone. During pumping, pore-bound water may remain above the drawn-down water table and as water levels return to pre-pumping conditions air can be trapped in the pore space beneath the water table. Such conditions would be expected to influence the seismic-velocity profile of the PSZ.

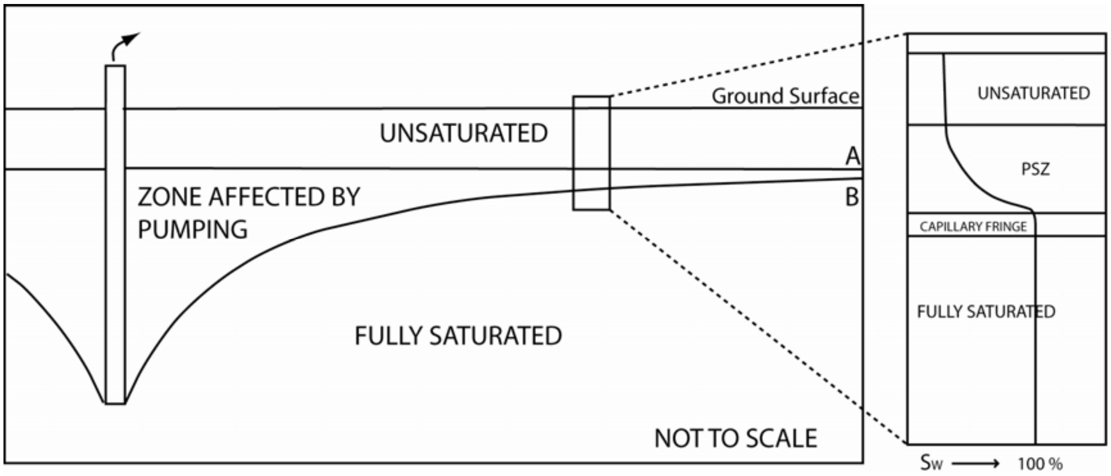

Figure 7.2. Illustration showing the water table before pumping (A), during pumping (B), and the zone affected by the raising and lowering of the water table. The enlarged section illustrates the soil-moisture profile.

Knight and Nolen-Hoeksema (1990) showed the effects of partial saturation on *P*-wave velocity (V_p) in a sandstone using two different methods of varying water saturations (Figure 7.3). One method increased S_w through imbibition, yielding velocities similar to those predicted by the Biot-Gassman-Domenico equations (Domenico, 1976) where velocities remain relatively constant with increasing saturation and increase very rapidly at saturations greater than ~90%. The second method achieved partial saturation through drainage, where velocities follow more of a curved path on the graph and increase exponentially with increased water saturation. These observations were made at the pore scale using ultra-sonic frequencies and consolidated sandstone samples under laboratory conditions. We suggest that analogous seismic velocity behavior, although not at the pore scale, will result in the PSZ from drainage and imbibition during irrigation cycles.

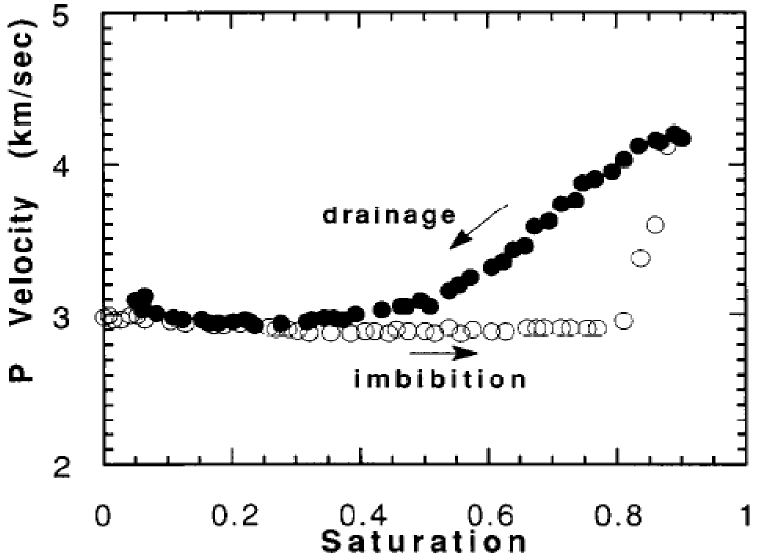

Figure 7.3. Plot displaying the changes in *P*-wave velocity with water saturation (from Knight and Nolen-Hoeksema, 1990).

Mavko and Mukerji (1998) relate this difference in velocity response to patchy and uniform saturation (Figure 7.4). They define uniform saturation as fine-scale, uniform mixing and patchy saturation as heterogeneous saturation on a coarser scale. They determined that patchy saturations always lead to higher velocities than uniform saturations. Saturation scales separating uniform from patchy behavior may be from 0.1–1 cm in the laboratory to tens of centimeters in the field.

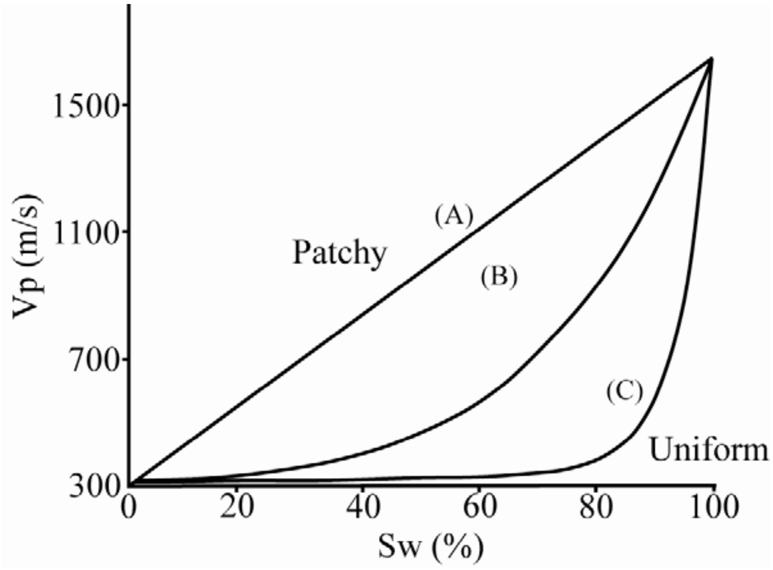

Figure 7.4. Illustration depicting the (A) patchy and (C) uniform saturation curves as upper and lower velocity bounds. (B) represents the velocity profile used in the numerical model discussed later (modified from Mavko, 2003).

In a homogenous medium, such as a clean, well-sorted sand, water will drain evenly as the water table is lowered, resulting in a vertical translation of the PSZ (Bevan, 2005). However, at our field site, thin, discontinuous clay layers interbedded with fine- and medium-grain sands form small scale heterogeneities. These varying near-surface soils have different field capacities, i.e. different abilities to retain moisture under gravity drainage. As the water table is drawn down, clays and silts will retain greater amounts of water than well-sorted sands causing patchy saturation. Localized areas of higher water saturation, which can be on the scale of 10s of centimeters, will influence the seismic response. During imbibition, sediments will saturate more evenly, which is akin to uniform saturation. Although it is possible that the TSZ reflection coincides with a change in stratigraphy, we do not believe that a stratigraphic boundary is the controlling factor of the AVO response that we are observing in the data. Similar to our study, prior shallow seismic reflection experiments of fluctuating water table surfaces did not show changes in reflection times (Birkelo et al., 1987; Johnson, 2003).

We propose that we are observing a hysteretic effect analogous to that of Knight and Nolen-Hoeksema (1990), but on a larger scale due to patchy saturation caused by small scale subsurface heterogeneities. At the pore scale, hysteresis is possible because no interpore communication occurs with ultrasonic frequencies and seismic velocities are affected by fluid distribution (Endres and Knight, 1989). At lower frequencies interpore communication does occur and the pore contents act as a single effective pore fluid (Endres and Knight, 1997). Therefore a homogeneous medium will not exhibit a hysteretic velocity behavior. At our field site we suggest that lower frequencies respond to a velocity hysteretic effect caused by patchy saturations. Endres et al. (2000) also reported localized areas where, as the soil-moisture profile translated downward, sediments had higher water saturation and were detectable by GPR.

Sengbush et al. (1961) describe the effects of various velocity functions on a reflected wavelet as a process of linear filtering. A sharp interface represented by a step-velocity function produces a reflection having the same waveform as the source pulse. A gradational interface represented by a ramp-velocity function produces a reflection that is the integrated source pulse. The effect of moving from a step-velocity function to a ramp-velocity function on a reflected wavelet is an overall lowering of the wavelet frequency and decrease in amplitude (Figure 7.5). Velocity changes related to imbibition would correlate with uniform saturation, approximated by a step-velocity function, and those related to drainage would correlate to patchy saturation, approximated by a ramp-velocity function.

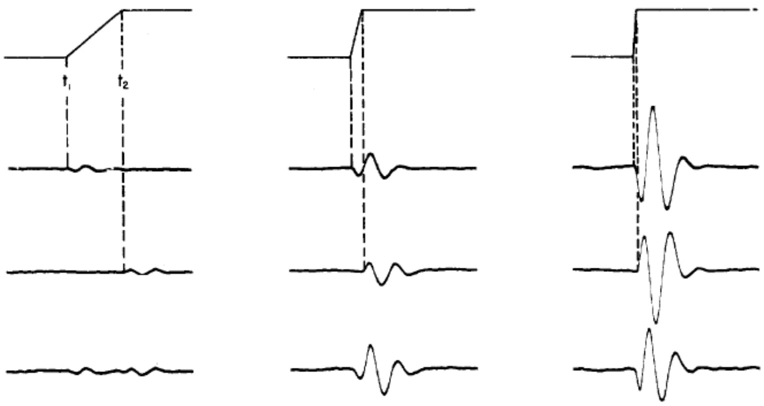

Figure 7.5. Illustration of the effects of a ramp-velocity function on a reflection with changes in slope (from Sengbush et al., 1961).

Data Acquisition & Processing

Common mid-point (CMP) seismic reflection surveys were conducted in the summers of 2003 and 2004 to image changes in the TSZ reflection during pumping of an agricultural irrigation well. The first survey (A) was conducted on August 13, 2003 after the pump had been allowed to run continuously for three days. Following aquifer recovery, ~18 hours after the pump was turned off, a second survey (B) was acquired. A third survey (C) was shot the following summer when, due to cooler temperatures, the pump had not been run for at least two weeks and water table fluctuations had been limited to natural processes. The pump was located ~5 m away from the east end of each of the surveys.

Each survey was conducted using 144 Mark Products L-40A2 100-Hz geophones planted at a 10-cm interval. The source was a .22-caliber rifle firing single short-rifle ammunition into 15-cm deep pre-punched 2-cm diameter holes. The source interval was 10 cm beginning and ending 5 m off of each end of the spread. Data were recorded using two Geometrics 72-channel StrataView seismographs with 24-bit A/D conversion, 256 ms record lengths, and a 0.25 ms sampling interval. Acquisition parameters were identical for each survey, with the exception of the shot holes of (B) being punched on the opposite side of the spread from (A) to avoid using the same holes.

Data were processed using techniques common to CMP seismic processing, including geometry definition, elevation corrections, trace editing, bandpass frequency filtering, early muting, *f-k* filtering to remove pump noise, CMP sorting, NMO corrections, iterative residual statics, CMP stacking, and AGC (60 ms window). Figure 7.6 shows the processed sections with selected horizons overlain. Horizon times and frequencies were picked using a commercial seismic interpretation software package. Data used for the AVO analysis were processed using commonly applied techniques for AVO data, as described by Castagna (1995) and Resnick (1995), to avoid unwanted changes in the amplitudes. Processes included geometry definition, elevation corrections, spherical spreading corrections, *f-k* filtering, CMP sorting, NMO corrections, and partial stacking.

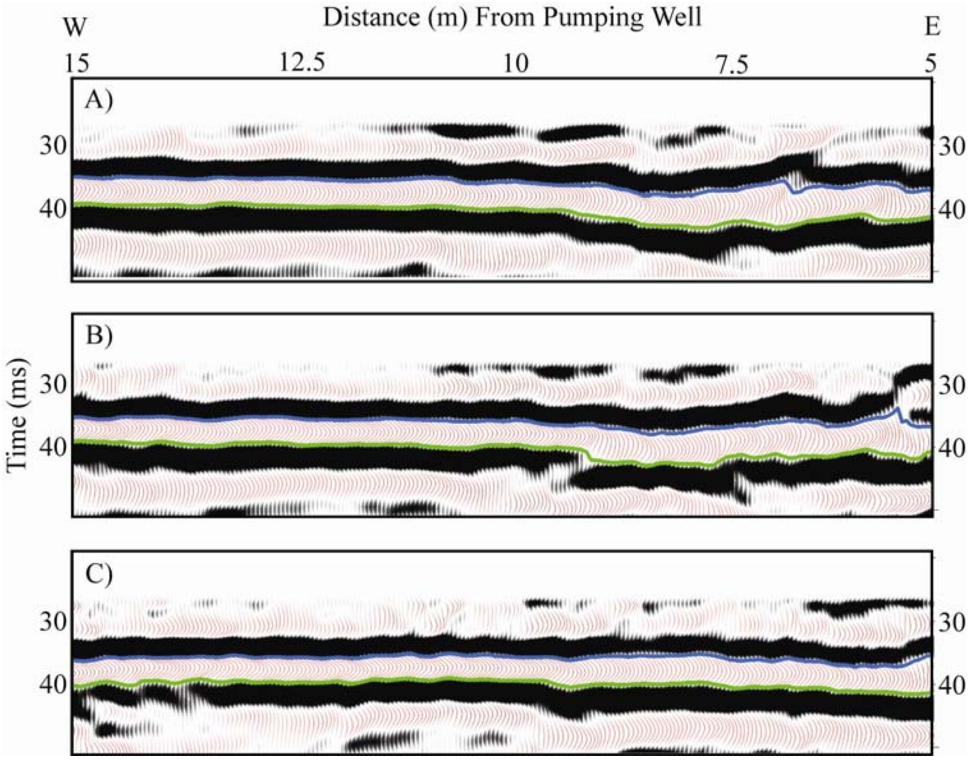

Figure 7.6. SSR stacks showing data collected at steady-state conditions during (A) drawdown, (B) recovery, and (C) undisturbed hydrologic conditions.

AVO Analysis

Although AVO methods and techniques are widely used in hydrocarbon exploration, little work has been done in shallow subsurface investigations. The near surface presents complexities that must be overcome to provide a data set of high enough quality to perform AVO analysis. The air wave, refractions, direct wave, and surface waves often prevent a wide range of offsets from being used due to interference with the reflections. Despite the associated problems, there are a few examples of SSR AVO studies (Bradford et al., 1997; Bachrach and Mukerji, 2001;

Waddell et al., 2001). Bachrach and Mukerji (2001) showed that the unsaturated/saturated sand interface exhibits an increase in reflection amplitude with increasing offset.

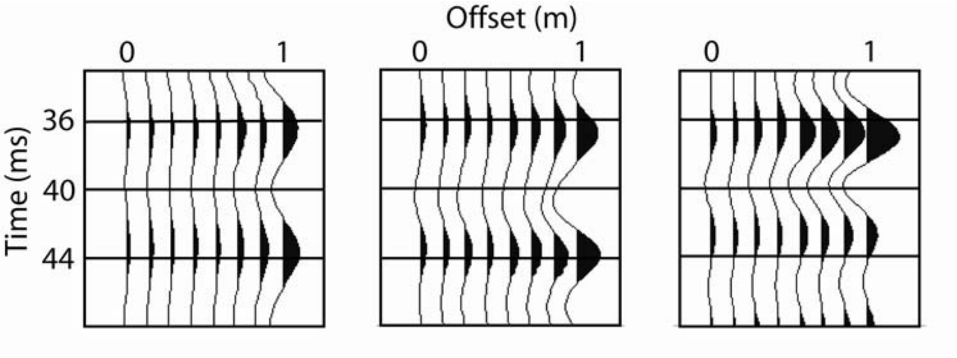

Figure 7.7. CMP supergathers from data collected during pumping (left), after pumping (center), and with no pumping (right). Data have been displayed with a -3 dB gain to illustrate trace-to-trace amplitude changes.

Supergathers were created by partially stacking the common offsets of five adjacent CMP gathers (Figure 7.7). Each CMP gather was separated by 5 cm, spanning a distance of 20 cm. Each of the three data sets was normalized to its respective RMS amplitude. The RMS amplitudes were calculated for each trace from a window around the TSZ reflection from 32–48 ms for offsets ranging from -1 to +1 m in 10-cm increments. The supergathers displayed in figure 7.7 show data collected during pumping (drainage), after aquifer recovery (imbibition), and from the following summer when the pump was not used. The TSZ reflection consistently occurs at ~35 ms; however, the data collected during drainage (left) exhibit noticeably lower amplitudes and lower frequencies.

Figures 7.8a-c show plots of the relative amplitude versus CMP offset within a supergather for a range of distances from the pumping well during drainage and imbibition. The AVO response is represented by exponential curves fit to the data points using least-squares regression. For all distances from the pumping well, imbibition reflection amplitudes are greater than drainage reflection amplitudes, and reflection amplitudes increase overall with increasing offset. As the distance of the CMP supergather from the pumping well increases, the relative amplitude of each curve increases. Furthermore, the separation between the two amplitude curves in each plot is greatest near the pumping well. This effect is illustrated in Figure 7.8d using the difference of the two curves for each distance.

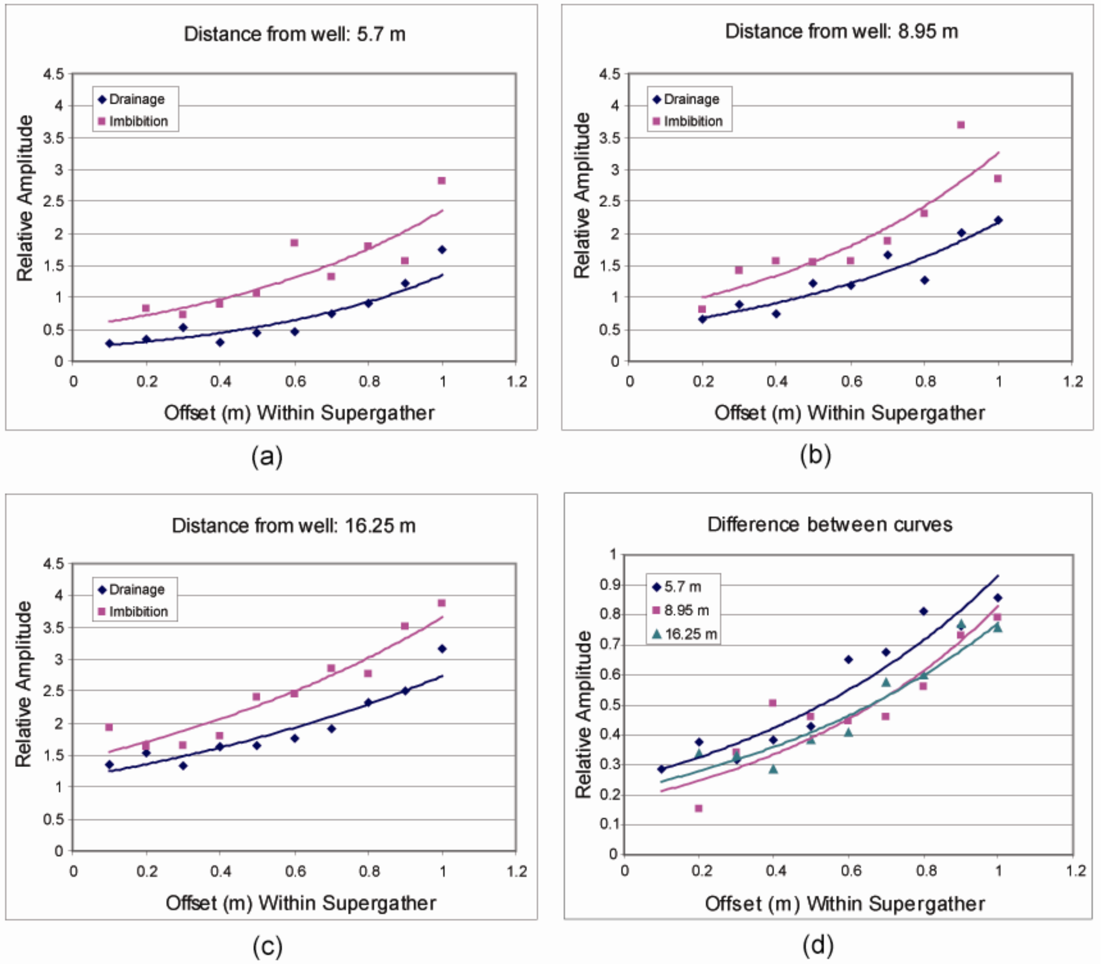

Figure 7.8. AVO curves from data collected during (drainage) and after (imbibition) pumping for CMP supergathers at three different distances from the pumping well (a-c). (d) shows the difference between the two curves for each distance.

Figures 7.9a and b show plots of relative amplitude versus CMP offset within a supergather for a range of distances from the pumping well for data collected during drainage and data from the following summer when the pump had not been used, respectively. During drainage, the relative amplitudes increase as the distance from the pumping well increases. In comparison, the amplitudes of the data acquired without pumping remain relatively consistent despite changes in the distance from the pumping well and display higher amplitudes than the drainage data.

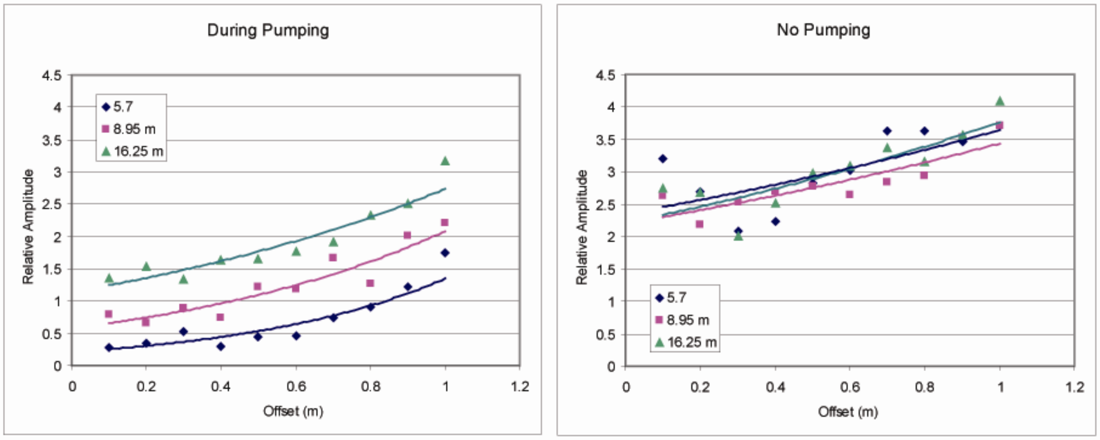

(a) (b)

Figure 7.9. AVO curves for all data collected during pumping and without any pumping are illustrated by (a) and (b), respectively.

AVO Results

The graphs in Figures 7.8 and 7.9 show that seismic data collected during drainage exhibit lower amplitudes than those acquired both during imbibition and at no pumping conditions. This seismic amplitude relationship to pumping condition is observed at all distances from the pumping well and at all offsets within the supergathers. This observation is consistent with the seismic response expected from a patchy saturation velocity profile formed by drainage. Furthermore, the lowest amplitudes are observed at the supergather closest to the pumping well. As the distance of the supergather from the pumping well increases, so do the amplitudes, suggesting an increasingly sharper velocity transition away from the pumping well.

As illustrated in Figure 7.2, drawdown will decrease as the distance from the pumping well increases. This response is illustrated by Figure 7.8d where as the distance from the pumping well increases, the separation between the curves decreases. Thus, as the distance from the pumping well increases, both hydrologic and geophysical responses decrease, suggesting a causal relationship. Figure 7.9a shows that as the distance from the pumping well increases, the amplitude increases while the pump is running. However, when the pump was not used and the water table was not drawn down, as in Figure 7.9b, the curves are clustered together and display higher amplitudes. These results further suggest that changes in the thickness of the PSZ due to elevation changes of the water table result in corresponding detectable seismic reflection amplitude changes.

At undisturbed water table conditions (no pumping) it is expected that the PSZ will exhibit the most abrupt seismic velocity transition from unsaturated to fully-saturated conditions (step velocity function). As the water table is drawn down (drainage) and the thickness of the PSZ increases, the seismic velocity profile shifts from a step-velocity function to a ramp velocity function, where velocity increases incrementally instead of abruptly (Figure 7.5). The change in slope of the ramp-velocity function leads to lower seismic reflection amplitudes (Sengbush et al., 1961) and frequencies (Wolf, 1937). As the water table returns to equilibrium (imbibition) and the thickness of the PSZ decreases, the slope of the velocity ramp more closely approaches a step-velocity function. This leads to an increase in reflection amplitudes and frequencies relative to those during drainage. The same PSZ disturbance behavior explains the seismic response as the distance from the pumping well increases and the drawdown of the water table decreases. At distances farther from the pumping well there are smaller changes in the elevation of the water table and a lesser effect on the thickness of the PSZ, which would lead to increasingly higher reflection amplitudes at farther distances. The observations of shallow seismic reflection amplitude response during pumping cycles are in agreement with the suggested PSZ thickness changes and analogous to the seismic velocity response to varying water saturation presented by Knight and Nolen-Hoeksema,(1990), and Mavko and Mukerji (1998).

Changes in the TSZ reflection amplitude may serve as an indicator of permeability near the water table. A more homogeneous and permeable material, such as a clean or well-sorted sand, would allow more uniform drainage during drawdown. Uniform drainage would have a lesser or no effect on the thickness of the PSZ, resulting in a smaller change in seismic amplitude. Conversely, lowering the water table in poorly-sorted heterogeneous soils would increase the thickness of the PSZ and exhibit a larger variation in amplitude. The results of this study could yield a more accurate representation of subsurface hydraulic properties when used in tandem with techniques that are sensitive to pore fluids, such as ground-penetrating radar and electrical methods. These techniques may also prove useful in understanding changes in water table and saturation fluctuations, which may be desirable in time-lapse studies at contaminated sites where non-invasive techniques might be necessary.

Frequency Effects

Model Description

To test our hypothesis of a decrease in reflection frequency with increasing thickness of the PSZ, we created a density-normalized model of the subsurface (Figure 7.10) that represents the PSZ as a wedge of increasing thickness. The wedge is subdivided into multiple layers with increasing velocities. The velocities used for the unsaturated (295 m/s) and saturated (1650 m/s) zones were derived from the field data. The velocity profile used for the wedge was determined using the previously mentioned work of Knight and Nolen-Hoeksema (1990) and Mavko and Mukerji (1998) by choosing an exponential curve that lies between the approximations of the upper and lower bounds. Heterogeneity within the subsurface sediments can cause changes in the height of the capillary fringe and roughness of the unsaturated/saturated interface, which led us to base our V_p/S_w function on patchy saturation where fluid and gas phases are mixed at a coarse scale. The velocity function exhibits a higher rate of change as water saturation approaches 100%.

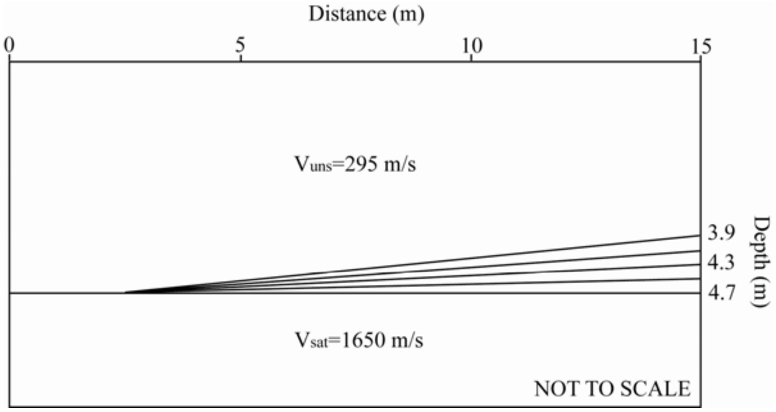

Figure 7.10. Illustration of the subsurface model used in modeling the effects of changes in thickness of the PSZ (the wedge).

Synthetic seismic traces were generated using a finite-difference elastic wave-equation model that is fourth order in space and second order in time (Macy and Schmeissner, 1998). The subsurface model was represented by a 1-cm by 1-cm grid of nodes that is 15 m long and 10 m deep. The slope of the wedge is ~3° reaching a maximum thickness of 55 cm at the edge. A single vertical-incident trace was produced every 1 m along the wedge beginning 20 cm from the start of the wedge. Figure 7.11 shows the resulting TSZ reflection from the model with wedge thickness increasing from 0–55 cm from left to right.

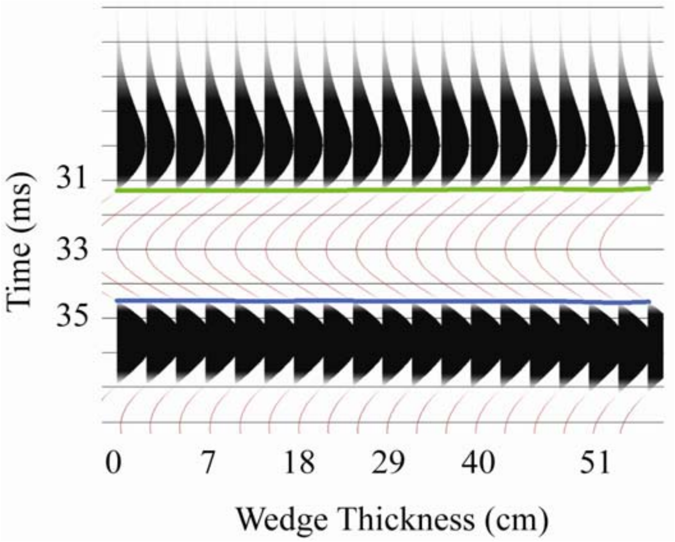

Figure 7.11. Synthetic traces representing the effect of the PSZ on SSR data. Although subtle, the trough broadens as the PSZ is increasing in thickness from left to right.

Frequency Results

Comparison of the three field seismic data sets shows that they are very similar in appearance. The trough bounded by the green and blue horizons in figure 7.6 appears to narrow from survey A to B to C, respectively. Figure 7.12 illustrates the time differences between the horizons and the frequency of sections A-C. Survey A, collected while at maximum drawdown, shows the largest time difference and lowest overall frequency. Survey B, acquired after the water table had recovered, exhibits a collective increase in frequency compared to A. Survey C, collected approximately nine months later during a period when the pump was not in use, shows the smallest horizon time difference and subsequently higher frequency content than A and B. As the main difference during the acquisition of the surveys was the pumping of the aquifer, we interpret the changes in frequency content to be related to changes in the unsaturated/saturated interface, particularly changes in the PSZ. The seismic data show an average change in frequency of ~8 Hz between surveys A and B, and ~5 Hz between surveys B and C.

The model data displayed in figure 7.11 show traces simulated along the partially-saturated wedge increasing in thickness from left to right. Figure 7.13 illustrates the decrease in frequency with increased PSZ thickness calculated from the synthetic traces. As the PSZ gets thicker from 0–55 cm, the dominant frequency drops ~5 Hz. A wider range of frequencies changes are seen in the data, which may be attributed to differences between the model and the actual subsurface. To generate the synthetic traces, values for V_{P1}, V_{P2}, V_{S1}, V_{S2}, ρ_1, and ρ_2 were required, of which only V_{P1} and V_{P2} were known. Assumed values were used for the others that are consistent with unsaturated and fully saturated sands. As the subsurface is not homogenous and isotropic, changes in stratigraphy and subsurface properties would lead to results that deviate from the model. Although the model does not perfectly replicate the actual subsurface at the site, it does show that changes in frequency can be expected with changes in the PSZ.

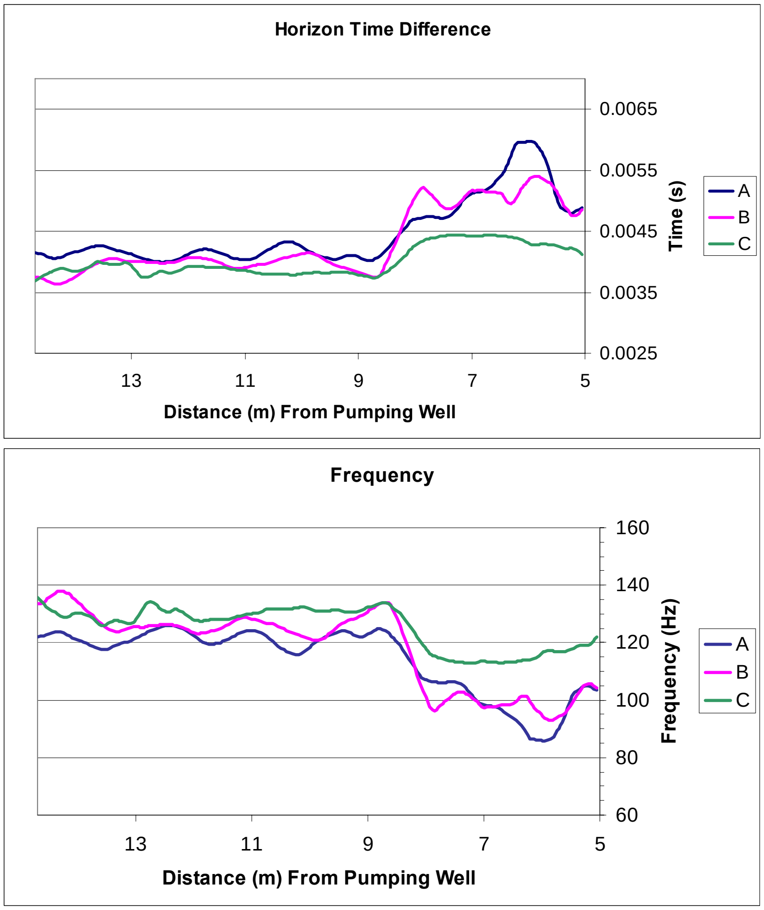

Figure 7.12. The top graph shows the difference in time in the horizons of sections A-C. The lower graph represents the corresponding frequencies of sections A-C.

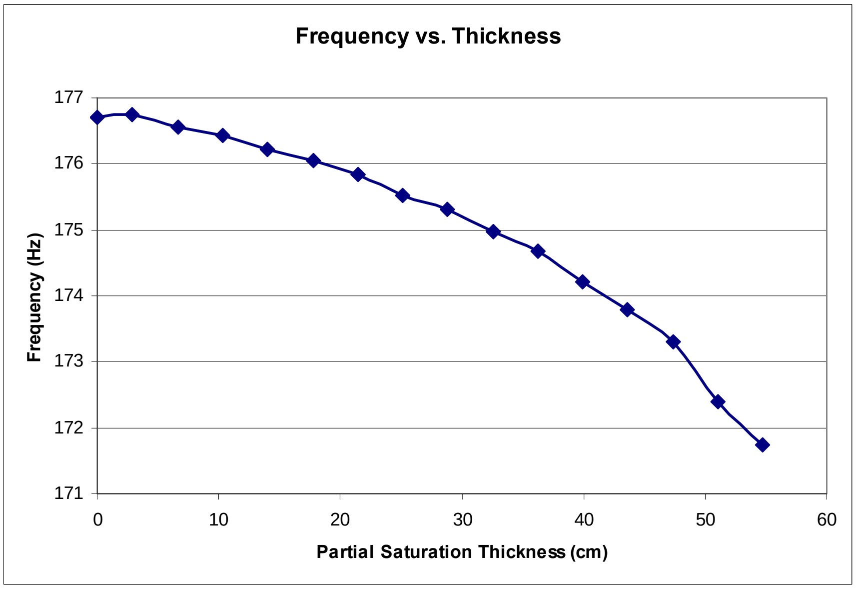

Figure 7.13. Dominant frequency versus PSZ thickness calculated from the modeled synthetic traces. As the thickness of the PSZ increases, the dominant frequency of the TSZ reflection decreases.

The frequency plot in figure 7.12 shows a distinct decrease at ~8.75 m. This may be controlled by stratigraphy, such as the presence of a discontinuous clay stringer that would be expected to affect the drainage characteristics along that portion of the line. The presence of fine-grained material would likely lead to an increase in the PSZ thickness as pore water would drain more rapidly in the surrounding sands. Surveys A and B are of lower frequency than C along this portion of the line, which may indicate that this zone was more sensitive to relative changes in the water table due to the finer-grained sediments, thus creating an overall thicker PSZ.

Conclusions

Imaging the cone of depression using shallow seismic reflection during a pumping test may be possible; however, it has not been documented in the literature to our knowledge, despite several attempts. Without prolonged drainage time, the length of which will vary with subsurface properties, some amount of pore-bound water will remain above the drawn-down water table. If there is a sufficient amount of water to produce a seismic reflection, temporal changes in the TSZ reflection will not be observed.

The data presented here show that detectable changes in the dominant frequency and AVO response of the TSZ reflection are observed in field data during a pumping test of an unconfined aquifer. The AVO responses correspond to different pumping conditions and varying distances from the pumping well, which can be explained by changes in partial water saturation above the water table. We show that lower seismic amplitudes observed during pumping (drainage) are consistent with the expected response of a thicker partially saturated zone. Recovery of the water table (imbibition) results in higher seismic amplitudes indicative of a thinner partially saturated zone. The techniques described here may be beneficial in observing changes in saturation and water table fluctuations and may help to constrain interpretations when combined with other geophysical and hydrogeologic data. Future work might focus on relating the changes in amplitude and frequency to PSZ properties, such as porosity and permeability and better characterizing the velocity profile of the PSZ to more accurately represent the subsurface.

Chapter 8

Acquisition and processing pitfall associated with clipped near-surface seismic reflection traces

Results of this study have been published under the following citation:

Sloan, S. D., Steeples, D. W., and P E. Malin, 2008, Acquisition and processing pitfall associated with clipping near-surface seismic reflection traces, Geophysics, **73**, W1–W5.

Introduction

Processing of clipped seismic traces may produce high-frequency wavelets leading to misinterpretation as reflections in both filtered shot gathers and CMP-stacked sections. To illustrate this effect we conducted a near-surface CMP seismic reflection survey using two different sources to compare the effects of various bandpass frequency filters on clipped traces. An event was observed in the clipped data set that replicated the frequency of the filter operators applied, similar to the effect of convolving a boxcar function with the filter operator. The anomaly exhibited hyperbolic moveout and was observed to imitate a reflection during the processing stages. The hyperbolic event was flattened by NMO corrections chosen for the target reflection and stacked in as a coherent event in the final section. Clipped data should be removed or corrected prior to processing to prevent the misinterpretation of high-frequency reflection-like artifacts in trace gathers and stacked sections.

Shallow seismic reflection data are commonly collected using dense receiver and source spacings that are required to image shallow reflectors and to prevent spatial aliasing of data. The close proximity of the source and the nearest receivers resulting from the short offsets may result in clipped traces where peaks and/or troughs have been squared off, depending on the energy of the source selected. Ultra-shallow surveys may require receiver spacing on the order of 20 cm or less, which can result in a relatively high percentage of clipped traces in the data set (Figure 8.1). This paper addresses a potential pitfall associated with data acquisition and processing in which clipped surface waves can lead to the misinterpretation as high-frequency reflections on filtered shot gathers and on stacked sections.

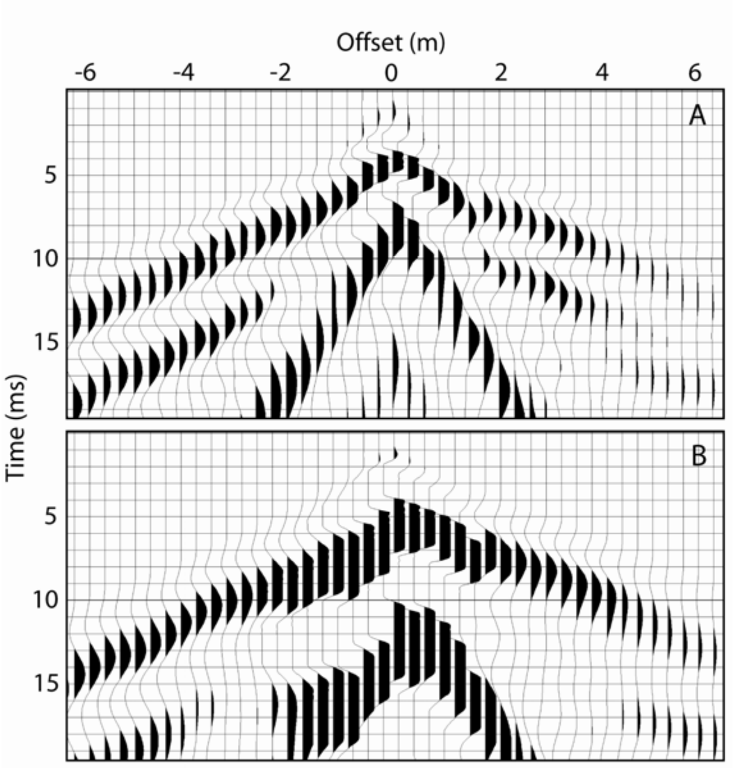

Figure 8.1. Field files acquired at the same source location using the (A) .22- and (B) .223-caliber rifles. (A) has clipped traces out to 0.6 m from the source while the clipping in (B) reaches as far as 2.0 m. The data are presented without any filtering, though a 9 dB attenuation was applied to prevent trace overlap.

The digital processing of clipped seismic traces can create high-frequency artifacts that appear to be “reflections” in both field records and stacked sections. Galbraith and MacMinn (1982) observed the effects of deconvolution on clipped traces, noting that each clipped peak or trough was split into two or more individual peaks and troughs after deconvolution. This led to the presence of anomalous peaks in processed stacked sections that could lead to its misinterpretation as a stratigraphic feature or other anomaly. This was not a problem if the clipped traces were either corrected or removed from the data set. Possible solutions used to eliminate gain errors such as clipping include: muting; filtering; polynomial interpolation (Galbraith and MacMinn, 1982); minimum error energy operators (MEEOs) (Nyman, 1977; Galbraith and MacMinn, 1982); and adaptive lattice filters (Khan, 1982).

Muting can be used to eliminate the clipped portion of traces, but may be tedious and time consuming, especially for large data sets. Filtering can be used to smooth gain-associated errors if they are not too severe; however, this method may produce additional problems for clipped traces, which will be addressed here. Nyman (1977) discusses the use of MEEOs for error correction. Galbraith and MacMinn (1982) compare this method to polynomial interpolation and determined that the MEEOs corrected gain-associated errors and clipping more effectively. Yet another method, described by Khan (1982), utilizes adaptive lattice filters to correct errors. Although our paper points out methods for correcting clipping errors, the primary focus is to show problems that can propagate through the data-processing stages and negatively impact data interpretation if clipped traces are not recognized and corrected or removed.

Data Acquisition & Processing

To illustrate how high-pass filtering of clipped data can produce artifacts on stacked CMP data, we conducted two CMP seismic reflection surveys using identical acquisition parameters with the exception of the source. The receiver line consisted of

144 Mark Products L40-A 100-HZ vertical geophones planted with a 10-cm interval. Data were recorded using a 0.125 ms sampling interval for 128 ms by two 72-channel Geometrics StrataView seismographs with 24-bit A/D conversion. The first survey was collected using a .22-caliber rifle firing long-rifle ammunition and a shot interval of 20 cm. The second survey was then conducted in the same manner using a .223-caliber rifle with a 55-grain bullet as the source. Data processing for the two data sets was identical and included geometry definition, CMP sorting, NMO corrections, CMP stacking, bandpass filtering, and AGC to produce a brute stack. Early muting was not applied, which allowed demonstration of the clipped-trace effects on the entire shot records.

Results

Figure 8.2 shows shot records from a single source location collected with the .22- and .223-caliber rifles with various bandpass filters applied. The target reflection from the water table is located at ~16 ms. Though the records are similar, the second arrival in the .223 data exhibits a separation at ~6 ms (indicated by the arrow, Figure 8.3) that is not seen in the .22 data. This separation becomes more pronounced as the frequency of the applied filter is increased. This event also appears to have a hyperbolic moveout and increases in frequency as the filter's frequency increases, without becoming distorted or decreasing in amplitude. The hyperbolic appearance could be mistaken for a very shallow reflection and, if left in the data set, may stack coherently. Hyperbola fitting of this pseudo-reflection yields a velocity of ~300 m/s, which is slower than the velocities of both the water table reflection (450-550 m/s) and the direct wave (400 m/s).

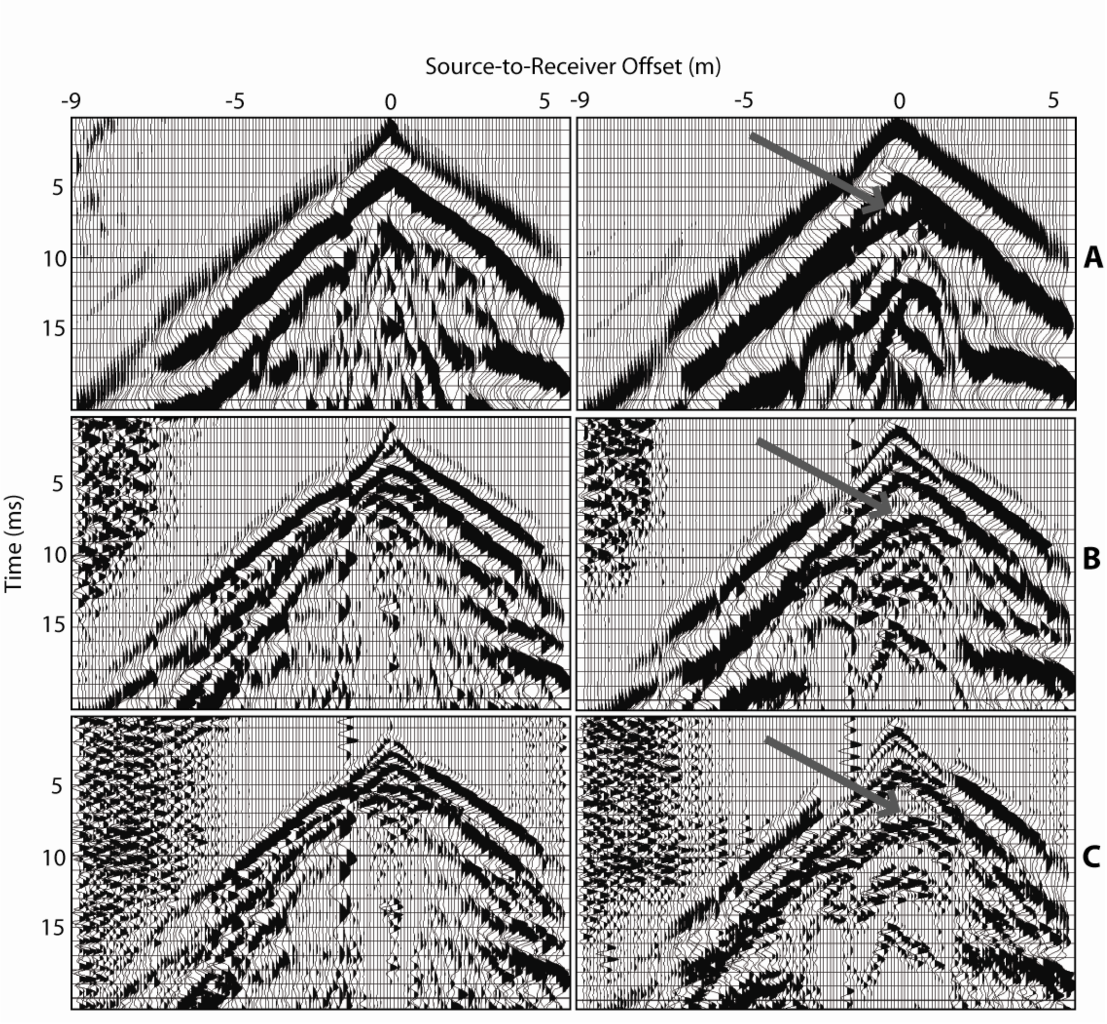

Figure 8.2. Field records collected with the .22-caliber rifle (left) and .223-caliber rifle (right) at the same location. Data are displayed with bandpass filters of 200–500 Hz (A), 600–900 Hz (B), and 1000–1300 Hz (C).

Velocity picks attained from the water table reflection at every fifth CMP location, ranging from 450–550 m/s, were used to apply NMO corrections to both data sets. Figure 8.3 shows the effects of the NMO corrections on the pseudo-reflection in CMP gathers from the .22 and .223 data sets at a coincident location. The pseudo-reflection event at ~7 ms has been flattened and is coherent in the .223 data, but is not apparent in the CMP gather of the .22 data. Figure 8.4 shows the brute stacks of both the .22 and .223 data with clipped traces included (A), clipped portions surgically muted (B), and with the clipped traces removed entirely (C). The data are displayed with a 600–900 Hz bandpass filter with 18 dB/octave rolloff slopes and no mutes have been applied. There is a coherent event at ~7 ms in the .223 stack, indicated by the arrow in (A) that is not present in the .22 stack, which corresponds to the event observed in the field records and NMO-corrected CMP gathers. Clipped traces present in the .22 data ranged from +/- 0.6 m source-to-receiver offset represented by 13 traces, or 12% of the 144. The .223 overpowered the geophones up to 2.0 m from the source, representing 41 of the 144 traces (28%) collected at each source location (Figure 8.1).

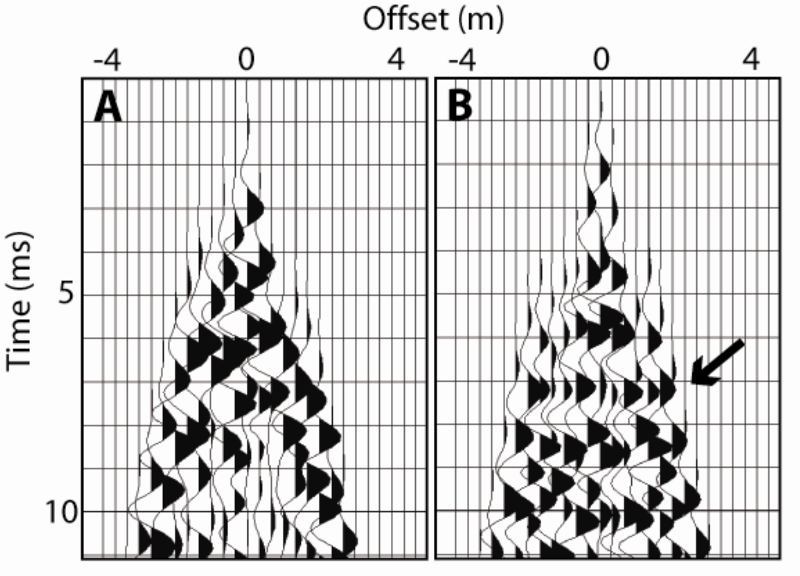

Figure 8.3. Coincident NMO-corrected CMP gathers from the .22 (A) and .223 (B) data sets. The event at ~7 ms, indicated by the arrow, has become flattened and coherent after NMO corrections were applied with a 15% stretch mute using velocity picks from the targeted water table reflection. Data are displayed with a 600–900 Hz bandpass filter without mutes or gains applied.

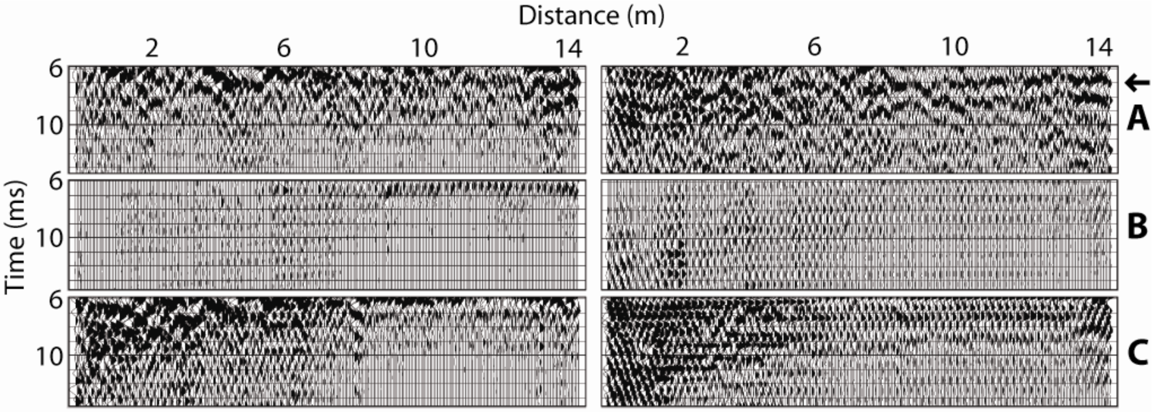

Figure 8.4. Brute stacks of the .22 (left) and .223 (right) data. Both data sets have been processed identically for comparison purposes. (A) shows a coherent event at ~7 ms in the .223 data, indicated by the arrow, that is not evident in the .22 data. (B) has had a surgical mute applied to remove the clipped portion of the traces. (C) shows the brute stacks after the clipped traces have been removed entirely.

Discussion

Figure 8.5 illustrates the effects of various bandpass filters with increasing frequency on an unclipped and clipped seismic trace and the corresponding amplitude spectra. As higher bandpass frequency filters are applied to the unclipped trace, high-frequency ring is introduced. The traces are recognizably noisier and the signal is diminished due to the decreasing bandwidth. However, as the same filters are applied to a clipped trace, the filter operator is replicated at the squared wavelet corners where the clipping occurs. The largest peaks and troughs in each of the filtered clipped traces occur at the same position as the squared corners where clipping occurs in the original trace, as indicated by the shaded area, which is essentially the equivalent to convolving the filter operator with a box-car function. Ringing does not occur in the filtered clipped traces as the frequency of the filter operator is increased because the bandwidth is artificially increased as additional cycles are introduced where clipping occurs. Corresponding amplitude spectra are shown for traces a, c, g, k, and o. As the frequency of the filter is increased, the spectra of the unclipped traces also become increasingly noisier while those of the clipped traces retain the same shape and smoothness across the frequency axis. Table 1 shows the passband of the filters applied to each trace.

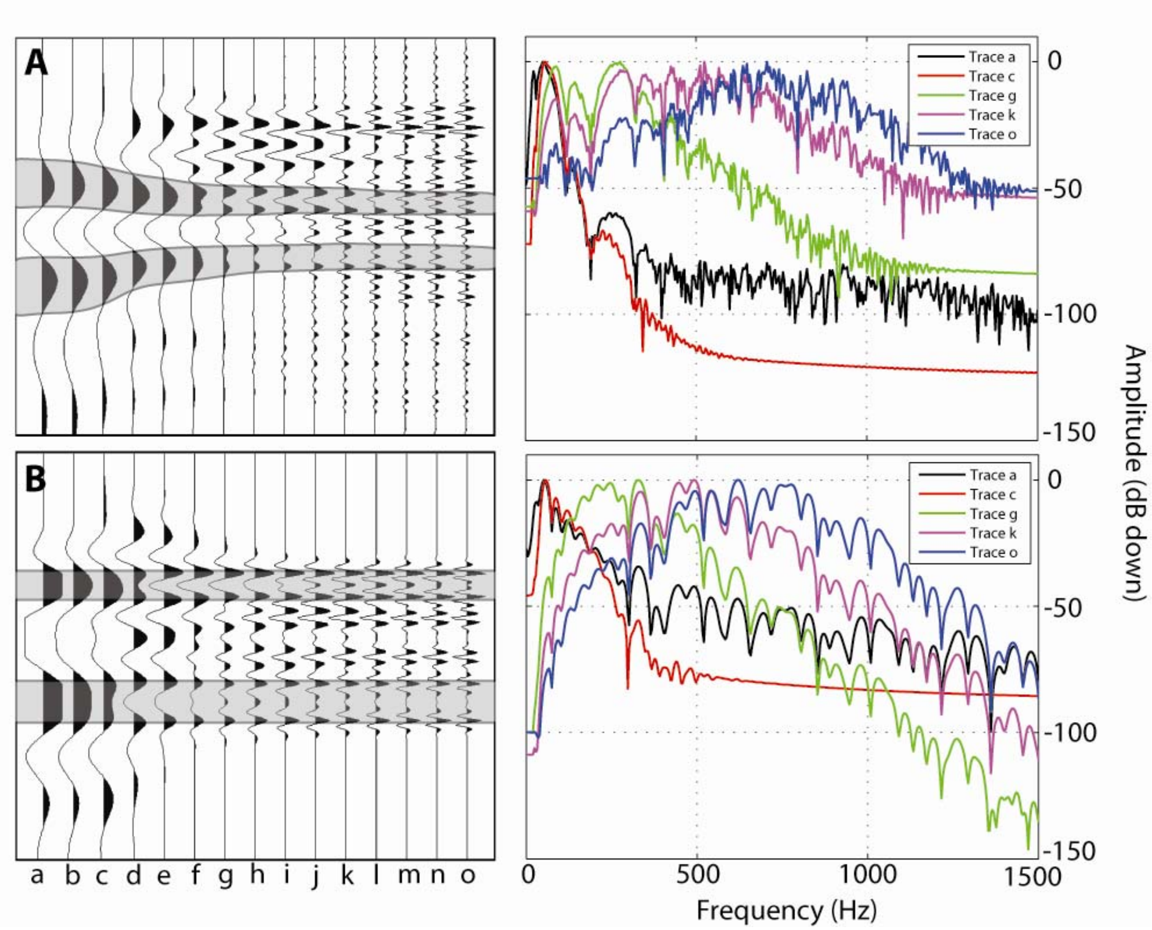

Figure 8.5. Illustration of an unclipped (A) and clipped (B) trace with various bandpass filters applied, increasing in frequency (traces a-o) from left to right. The corresponding amplitude spectra are shown on the right. (A) begins to ring at higher frequencies while the wavelet in (B) does not show the same ring, but appears to increase in frequency as higher frequency bandpass filters are applied to it. The high-frequency wavelet seen in B is the filter operator convolved with the corners at which clipping occurs in the data. Filter specifications for each trace are described in Table 1.

Table 8.1. Bandpass filters (Hz) applied to each trace in Figure 5. Filters were applied with 18 dB/octave rolloff slopes.

Trace	Filter Passband (Hz)
a	N/A
b	0-300
c	100-400
d	200-500
e	300-600
f	400-700
g	500-800
h	600-900
i	700-1000
j	800-1100
k	900-1200
l	1000-1300
m	1100-1400
n	1200-1500
o	1300-1600

Data presented in figure 8.4 demonstrate the effects of some of the processing steps that may prevent the described problem by comparing brute stacks including the clipped traces (A), with the clipped data surgically muted (B), and with the clipped traces removed (C). As seen in (A), processing the clipped traces can result in artifacts that appear as high-frequency reflections, which can lead to misinterpretations. Surgically muting the clipped portion of the traces, as in (B), effectively eliminates the artifact; however, this method may be time-consuming and tedious. The most reliable way would be to omit the clipped traces from the data set, as illustrated in (C). Although it may be fast and reliable, in the case with the .223 rifle this would reduce the total number of traces by ~30% and significantly lower the fold. In this case an early mute designed to delete the clipped data may be the most efficient method for removal as an early mute is necessary to remove the direct and refracted waves and would be applied to the data anyway. If removing the traces or muting are not viable options, the minimum error energy operator reported by Nyman (1977) and discussed by Galbraith and MacMinn (1982), can be used to attempt to correct clipping errors.

The hyperbolic appearance of the reflection-like event is due to a combination of clipping and frequency filtering. Figure 8.6 illustrates the same shot gather with: no filter applied (A); a 200–500 Hz bandpass filter (B); and a 600–900 Hz bandpass filter (C). The traces in the shot gather behave in the same manner as those described in figure 8.5. Although the event indicated by the arrows in the raw shot gather is linear, as frequency filters are applied the squared corners become individual peaks and troughs. This creates the separation observed in the same event in the shot gathers in B and C where the top of the event remains linear and the bottom appears hyperbolic. The separation appears to become larger with increasing frequency of the filters, but the separated events are actually at the same times in each gather, as indicated by the arrows. As the amplitudes decrease with offset and clipping diminishes, the clipped corners and filter-induced peaks come closer together, giving the event its hyperbolic appearance.

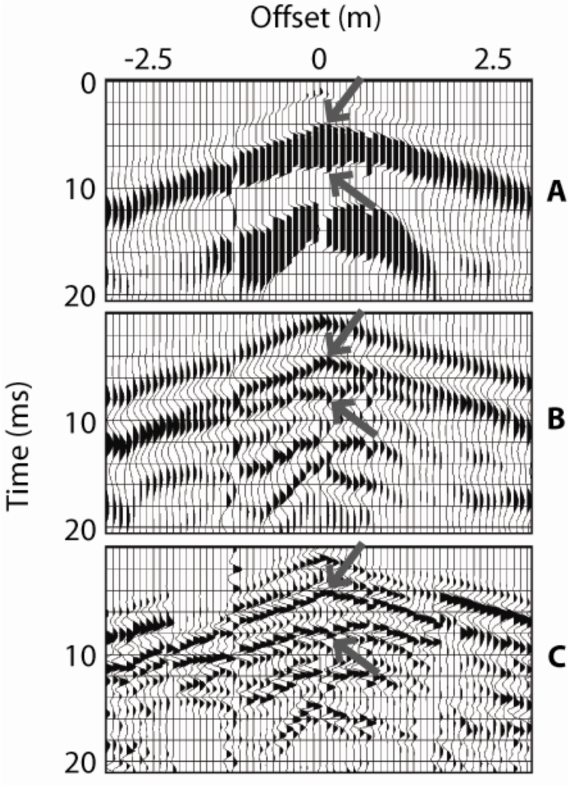

Figure 8.6. The same shot gather is shown with no filtering (A), a 200–500 Hz bandpass filter (B), and a 600–900 Hz bandpass filter (C). Arrows point to the same event as it changes with each filter. Filters were applied with 18 dB/octave rolloff slopes and the top shot gather has a 9 dB attenuation applied to prevent trace overlap.

Conclusions

The processing of clipped seismic traces is shown here to have the potential of creating artifacts that could be misinterpreted as high-frequency reflections in shot gathers and in stacked sections. As increasingly higher bandpass frequency filters are applied to an unclipped trace, the high-frequency noise level increases due to the decreased bandwidth. In contrast, the frequency of a clipped trace mirrors that of the filter that is applied to it by replicating the filter operator. It will continue to increase in frequency without distortion or the addition of high-frequency noise to the wavelet and exhibits no change in the bandwidth. Clipped data should be removed by muting or trace editing or corrected during the pre-processing stage to avoid the possible problems described. Field testing of potential seismic sources prior to conducting a survey is recommended and can prevent a problem before it occurs by selecting the source with the appropriate energy to meet the survey objectives. Clipping may occur as a result of physical limitations of geophones or by setting all of the bits that can be recorded by a digital sample to ones. It may be beneficial to check the data for digital samples that are the largest possible number that can come from the A/D converter, which may indicate the presence of clipped traces. As with all seismic projects, care should be taken during the processing stages to assure that quality control is maintained and that the processing steps or selected parameters are not introducing unwanted artifacts into the data set.

Chapter 9

Ultra-shallow imaging of the top of the saturated zone

Introduction

As the ability to image ever-shallower depths in the ultra-shallow subsurface using seismic-reflection techniques has improved, so has the array of applications for which these methods have been used, including determining depth to bedrock, cavity and tunnel detection, delineating near-surface stratigraphy, fault identification, and contaminant sinks or pathways, to name a few. Other geophysical methods, such as ground-penetrating radar (GPR), have routinely been used to image the upper 10 meters of the subsurface with high resolution, however every method has its limitations and will not work effectively in all geologic settings. The ability to accurately image ultra-shallow depths (less than 20 m) using seismic methods provides another tool for the geophysicist to complement other methods or to use when they are not successful. Surface seismic methods are non-invasive and may be desired when characterizing contaminated areas where the installation of observation wells or boreholes may exacerbate the problem by providing conduits for contaminants to flow from one stratum to another.

The study presented here demonstrates the ability of ultra-shallow seismic-reflection methods to image the top of the saturated zone (TSZ) at a depth of less than one meter. Previous studies have successfully imaged the TSZ (Birkelo et al., 1987; Bachrach and Nur, 1998a, b; Baker et al., 1999; Baker et al., 2000; Sloan et al., 2007) at depths greater than 2 m. The shallowest reflection published to date was reported by Baker et al. (1999) where the authors recorded two stratigraphic reflections at 0.63 and 1.46 m depth (8 and 15 ms two-way travel time, respectively). The reflection imaged by this study occurs at ~10 ms in time and 0.95 m in depth, making this the shallowest TSZ reflection reported in the literature to date. Figure 9.1 displays a common-source gather that illustrates the presence of a reflection hyperbola prior to processing. Observing reflections at very shallow depths requires dense sampling of the near-surface wavefield, often necessitating source and receiver spacing as small as 5–10 cm, to ensure events are sufficiently sampled to be identified and to prevent the misinterpretation of spatially aliased signal. High frequency content and relatively low seismic velocities are also helpful to resolve reflections from other events and prevent reflections from being masked by other wave trains, such as the airwave or ground roll.

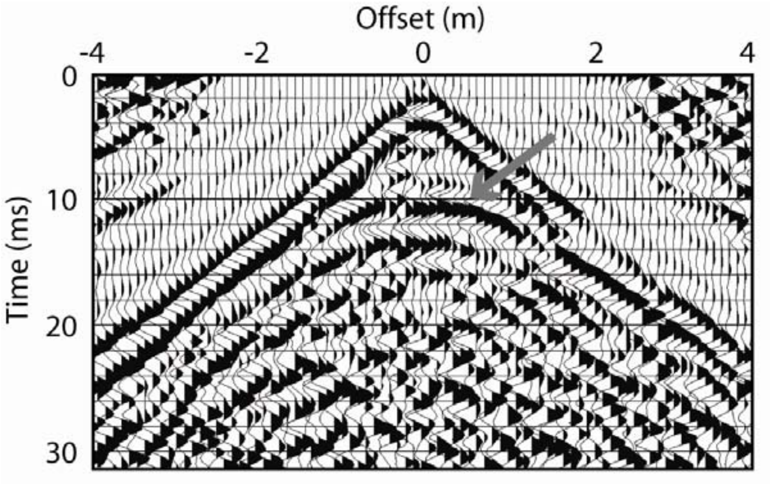

Figure 9.1. Common-source gather that shows the presence of the TSZ reflection at ~10 ms, indicated by the gray arrow. Data are displayed with a 350–700 Hz bandpass filter and a 30-ms AGC window.

Geologic Setting

The field site is a point bar on the Kansas River located near Lecompton, Kansas (Figure 9.2), adjacent to the Atchison Topeka & Santa Fe Railroad tracks. Surface geology includes alternating Pennsylvanian-aged shale and marine limestone layers of the Kanwaka Shale, Oread Limestone, and Lawrence Formation overlain by Quaternary alluvium deposits. The sandbar itself consists of a fining-upward sequence of medium- to coarse-grained sands typical of point bar deposits. A hand-dug hole at the site revealed ~0.95 m of medium- to coarse-grained sand overlying the water table.

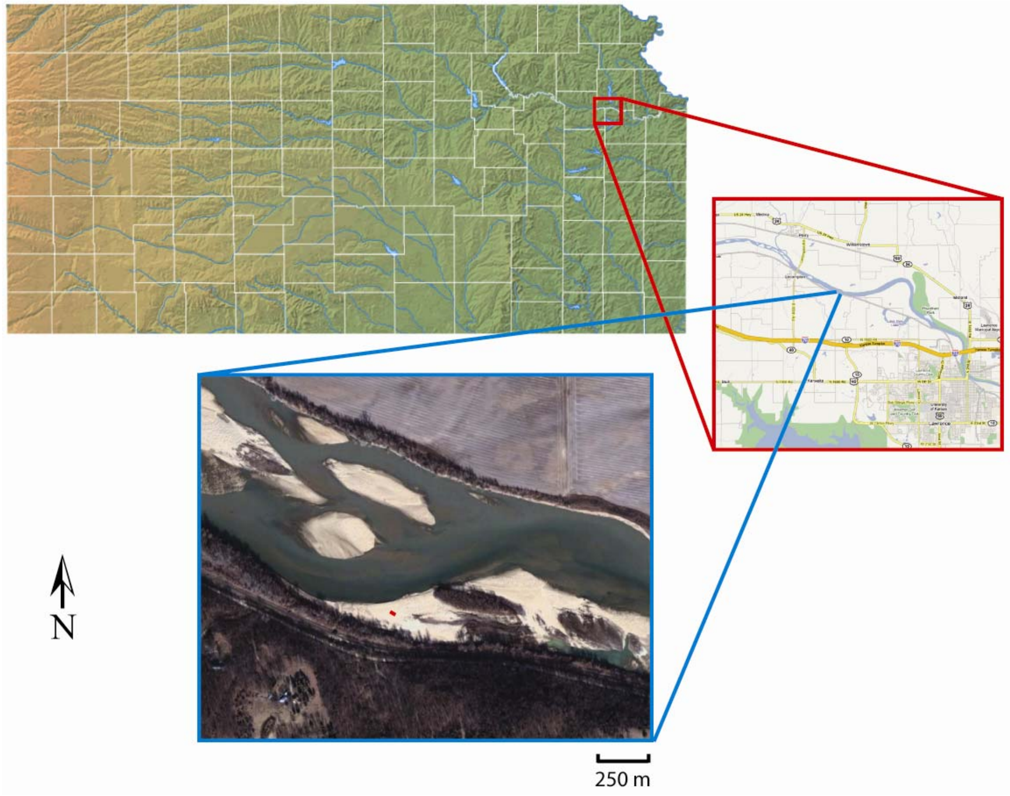

Figure 9.2. Site map indicating the location of the sandbar on the bank of the Kansas River near Lecompton, Kansas.

Data Acquisition & Processing

Two-dimensional, 72-fold common-midpoint (CMP) seismic-reflection data were acquired using 144 Mark Products 100-Hz L-40A2 vertical-component geophones planted on 10-cm intervals. The source was a rifle firing single .22-caliber short rounds into ~15-cm deep holes on 10-cm intervals centered between adjacent geophones. Holes were punched one at a time for each shot to prevent collapse and infill. Data were recorded by two 72-channel Geometrics StrataView seismographs with 24-bit A/D conversion using a 0.25-ms sampling interval and 256-ms trace lengths.

Data were processed using techniques commonly applied to near-surface seismic-reflection data. Data processing included geometry definition, CMP sorting, velocity analysis, normal-moveout (NMO) corrections, CMP stacking, bandpass filtering and automatic gain control (AGC). Early muting was not applied to confirm that the event is not an artifact due to clipping (Sloan et al., 2008) or incorrect mute tapers. Figure 9.3 illustrates a CMP gather prior to bandpass filtering (a), after filtering and AGC (b), and after NMO corrections and 7% stretch-mute limit (c). NMO-correction velocities ranged from 175–195 m/s with an average of ~180 m/s across the line. A very aggressive stretch mute was chosen due to the large stretch associated with low-velocity reflections and was selected to intercept the reflection prior to where the reflection and direct wave merge (±1.0 m offset) to ensure that direct-wave energy did not contribute to the stacked reflection. The dominant frequency of the TSZ reflection is ~450 Hz. Bandpass filter parameters included a pass band of 350–700 Hz with 16 and 12 dB rolloff slopes on the low and high sides, respectively. A 30-ms AGC window was also applied.

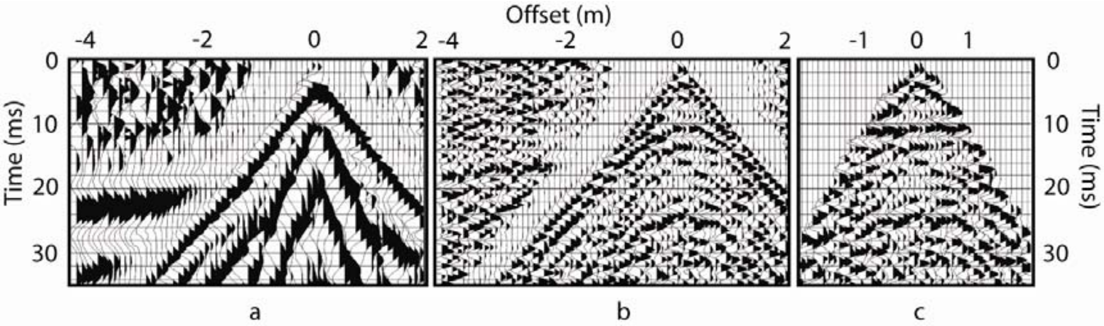

Figure 9.3. CMP gather displayed without processing (a), with a 350–700 Hz bandpass and 30-ms AGC window, and after NMO correction with a 7% stretch mute. The reflection is located at ~10.5 ms in (b) and (c).

Results

Figure 9.4 displays three CMP gathers from the survey. The reflection can clearly be identified as the hyperbolic event at ~10.5 ms. The direct wave and a refraction interpreted to be from the water table can also be identified as the linear events between 0 to -2 m and -2 to -4 m, respectively. The direct wave and TSZ reflection exhibit moveout velocities of 180 m/s. A velocity of 180 m/s and two-way travel time of 10.5 ms yields an approximate depth of 0.95 m to the reflector. Refraction analysis was used to crosscheck the validity of the reflection depth and velocity. First-break time analysis of the refraction yielded a velocity of ~1550 m/s and approximate depth of 0.98 m, which corresponds very well to the reflection information. Figure 9.5 shows the CMP-stacked section. The TSZ reflection is located at ~10.5 ms and ranges in depth from ~0.9–1.0 m in depth. A hand-dug hole at the site determined that the water table was located at ~0.95 m in depth.

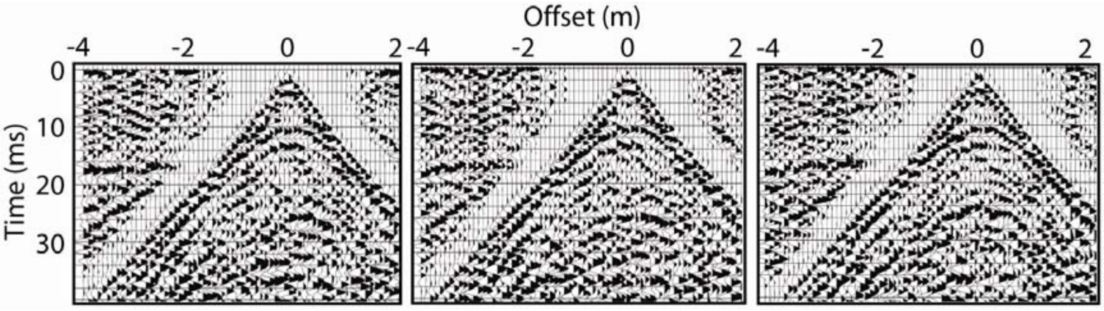

Figure 9.4. CMP gathers with the TSZ reflection occurring at ~10.5 ms and between offsets of ±1.0 m. The TSZ refraction is located at ~15 ms between offsets of –2 and –4 m. Data are displayed with a 350–700 Hz bandpass filter and a 30-ms AGC window.

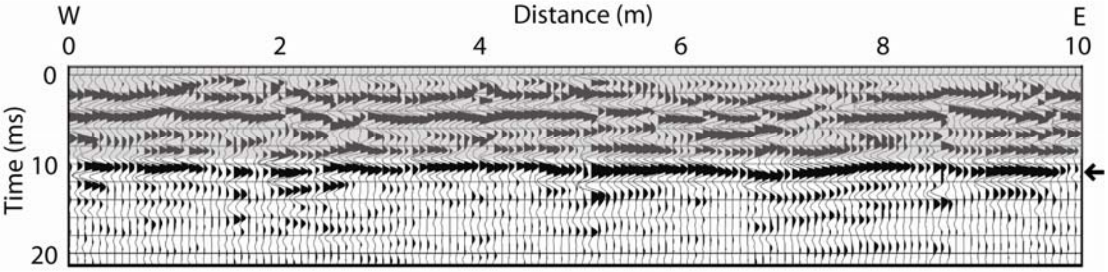

Figure 9.5. CMP-stacked section displaying the TSZ reflection between 10 and 11 ms, indicated by the arrow. The grayed box above the TSZ reflection encompasses coherently stacked direct-wave energy that would have been removed by an early mute. Early muting was not applied to ensure that the interpreted reflection is not an artifact associated with early-mute window or taper selection or an effect of filtering muted wavelets.

To image reflections in the upper two meters of the subsurface, both high frequencies (>400 Hz) and relatively low velocities (<300 m/s) must coincide (Baker et al., 1999). Figure 9.6 shows walkaway test records collected with .22-caliber short (a) and long-rifle ammunition (b). Short ammunition produces less energy and, therefore, less non-linear deformation, which preserves higher frequencies. Figure 9.7 displays the corresponding frequency-amplitude spectra for the .22-short (a) and .22-long-rifle walkaways. The short ammunition produces a relatively flat frequency response across a bandwidth of ~250–750 Hz. The long-rifle data yields frequencies that peak at ~500 Hz, but rapidly decay on either side.

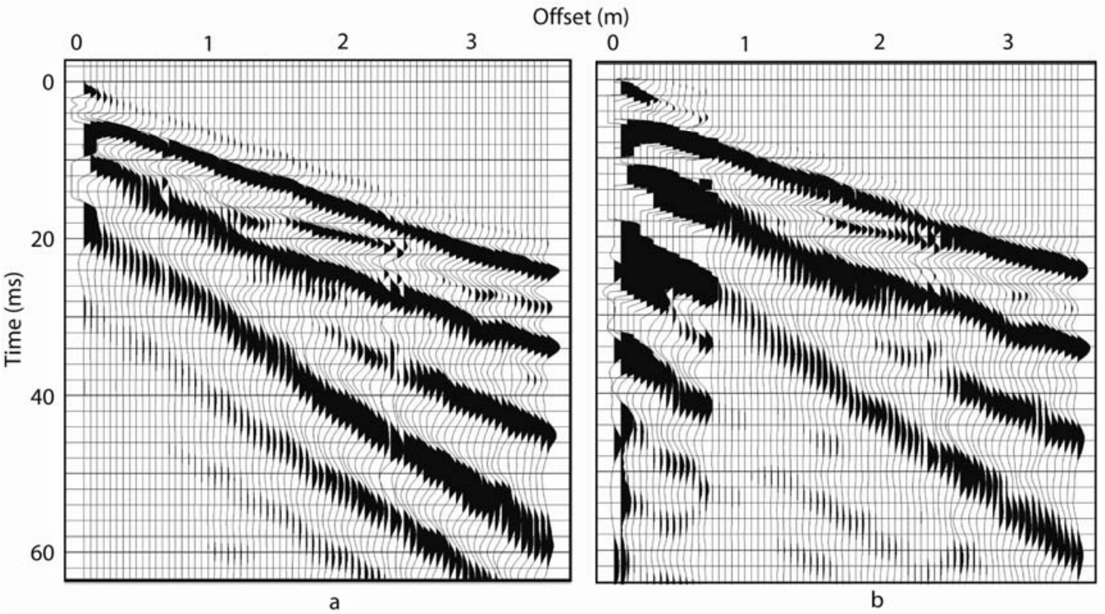

Figure 9.6. Walkaway-test data acquired with .22-caliber short (a) and long-rifle (b) ammunition. The first two traces are clipped in (a), compared to seven trace in (b), which would render 70% of the TSZ reflection unusable if CMP data were acquired with long-rifle ammunition.

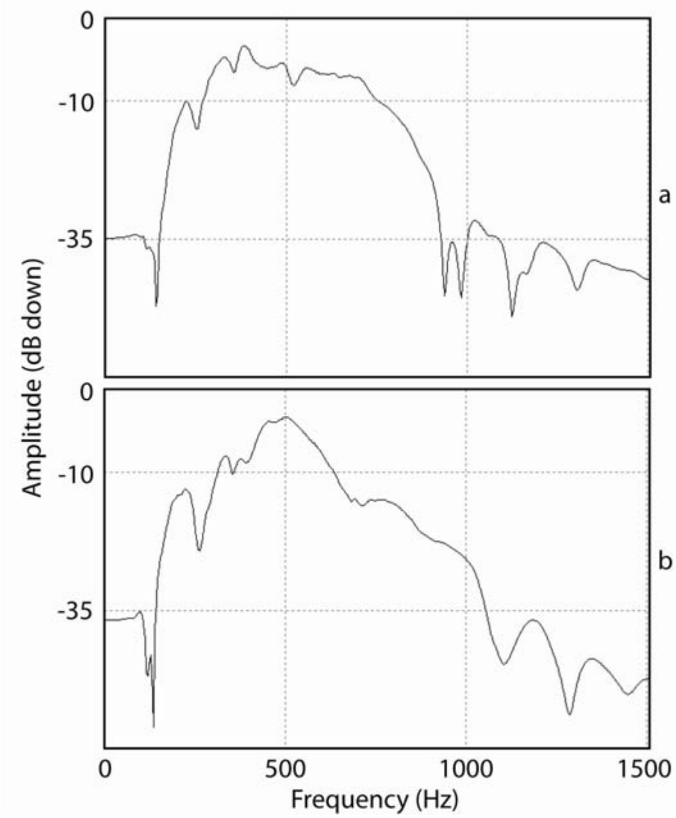

Figure 9.7. Frequency-amplitude spectra of the walkaway data collected with short (a) and long-rifle (b) ammunition. (a) exhibits a relatively flat frequency response from ~250–750 Hz while (b) peaks at ~500 Hz and rapidly decays on either side.

A source that produces less energy yields higher frequencies, but it also offers the advantage of overdriving fewer near-offset geophones and producing fewer clipped traces. The TSZ reflection is coherent from offsets of ±1.0 m. The short ammunition clipped the first and second traces (20 cm). The long-rifle ammunition clipped traces out to a source-to-receiver offset of 0.7 m, which would eliminate 70% of traces containing reflection information and make the identification of the TSZ reflection nearly impossible. To further reduce the chances of clipping, the source was positioned between adjacent geophones instead of inline with each geophone.

Although this puts the nearest geophones at 5 cm away from the source, the next geophones would be 15 cm away instead of 10 cm, potentially leading to fewer clipped traces.

Conclusions

The work presented here demonstrates the capability of ultra-shallow seismic-reflection methods to image the top of the saturated zone at depths less than one meter and provides another example of the ability of the technique to image the near surface at resolutions comparable to GPR. The top of the saturated zone was imaged at a depth of 0.95 m by using a source capable of generating frequencies up to 750 Hz while minimizing the clipping of critical near-offset traces. Due to the low seismic velocities and high frequencies at the site, the TSZ reflection is easily identified as a coherent event unobscured by other wave trains. The reflection exhibited a NMO velocity of 180 m/s and a dominant frequency of ~450 Hz, yielding a resolution potential of 10 cm. In the proper geologic setting, ultra-shallow seismic methods can be used in conjunction with other geophysical techniques for improved understanding of subsurface properties or where other methods are not suitable, providing geophysicists with another option when working in the shallow subsurface.

Chapter 10

Summary & Conclusions

Summary & Conclusions

The research presented in this dissertation has focused on imaging reflectors in the ultra-shallow subsurface less than 20 m deep. Topics discussed cover various aspects of survey design, acquisition, processing, and interpretation of two- and three-dimensional seismic reflection data. Although some of the techniques mentioned, such as the AVO analysis and pitfalls associated with clipped traces, were applied to 2D data, the concepts are also applicable to 3D data. Multiple conclusions, which are summarized in this section, can be drawn from the experiments presented here.

3D SSR surveys are relatively uncommon, although their popularity is increasing and more examples are appearing in the literature; however, 3D USR applications still remain rare. A 3D USR survey conducted near Lawrence, Kansas, demonstrated the ability of 3D USR methods to image multiple reflectors less than 20 m deep, including the top of the saturated zone (TSZ), a paleo-channel feature, and bedrock. Processing the data by dividing them into offset-dependent subsets based on the respective optimum window of each reflection was successful in negating the detrimental effects of NMO-correcting intersecting reflection hyperbolae that exhibited a vertical velocity change ranging from ~300–1600 m/s. Despite segregating the data set in time, data seams were not a problem in merging and stacking the subsets after an appropriate overlap taper was selected. It is possible, however, to generate processing artifacts using subsets and caution should be exercised throughout the processing stage to ensure that quality control is maintained.

The 3D survey was successful and the results are in agreement with previous studies conducted at the site.

Multiple 2D lines would be required to delineate the orientation of the channel and its topography; however, 3D data allowed the continuous tracking of the reflection in the subsurface, negating the need for interpolation of areas not imaged. This type of application could provide a non-invasive method of identifying preferential flow paths or sinks for contaminants, allowing for the identification of optimum placement of observation wells and more efficient remediation.

3D USR and SSR surveys have been shown by others to produce more accurate images of the subsurface than 2D data, but the high costs associated with acquiring and processing 3D data with the necessary high sampling densities of the shallow subsurface often preclude their use in limited-budget environmental and engineering applications. The 3D Autojuggie (3DAJ) may be a more cost-efficient alternative to conventional acquisition methods in certain settings. The ability to hydraulically plant and reposition up to 220 geophones simultaneously reduces the number of crew members necessary and of time required in the field. Cables, geophones, seismographs, etc. remain connected, further reducing time associated with rolling receiver lines and with open electronic circuits in cables.

The 3DAJ was shown to be able to acquire data comparable in quality to hand-planted geophones. Multiple reflections less than 20 m deep were imaged and results were consistent with those of other surveys at the site. Using the 3DAJ, a survey area of ~1225 m^2 was covered in ~19 hours with a crew of four people and a total fold of 210. In comparison, the conventional 3D survey previously acquired at the same test site covered an area of ~550 m^2 in ~10 hours with a crew of 10–12 people and a total fold of 48. This represents an 18% increase in square meters covered per hour, a 60–67% decrease in labor, and a 500% increase in fold. Developments, such as the 3DAJ, that increase the efficiency of acquiring 3D USR and SSR data may lead to better cost efficiency and increased use of 3D seismic methods in the future.

Amplitude-versus-offset (AVO) analysis techniques were applied to 2D USR data. Detectable changes in the dominant frequency and AVO response of the TSZ reflection were observed in field data during a pumping test of an unconfined aquifer. The AVO responses corresponded to different pumping conditions and varying distances from the pumping well, which can be explained by changes in partial water saturation above the water table. Lower seismic amplitudes observed during pumping (drainage) are consistent with the expected response of a thicker partially saturated zone. Recovery of the water table (imbibition) results in higher seismic amplitudes indicative of a thinner partially saturated zone. Despite water table elevation changes within resolution of the seismic data, temporal changes in the TSZ reflection were not observed. Without prolonged drainage time, the length of which will vary with subsurface permeability, some amount of pore-bound water will remain above the drawn-down water table. If there is a sufficient amount of water remaining to produce a seismic reflection, temporal changes in the TSZ reflection will not be observed.

The techniques described here may be beneficial in observing changes in saturation and water table fluctuations and may help to constrain interpretations when combined with other geophysical and hydrogeologic data. Future work might focus on relating the changes in amplitude and frequency to PSZ properties, such as porosity and permeability and better characterizing the velocity profile of the PSZ to more accurately represent the subsurface.

The processing of clipped seismic traces was shown to have the potential of creating artifacts that could be misinterpreted as high-frequency reflections in shot gathers and in stacked sections. As increasingly higher bandpass frequency filters are applied to an unclipped trace, the high-frequency noise level increases due to the decreased bandwidth. In contrast, the frequency of a clipped trace mirrors that of the filter that is applied to it by replicating the filter operator. It will continue to increase in frequency without distortion or the addition of high-frequency noise to the wavelet and exhibits no change in the bandwidth. Clipped data should be removed by muting or trace editing or corrected during the pre-processing stage to avoid the possible problems described. As with all seismic projects, care should be taken during the processing stages to assure that quality control is maintained and that the processing steps or selected parameters are not introducing unwanted artifacts into the data set.

The capability of ultra-shallow seismic-reflection methods to image the top of the saturated zone at depths less than one meter was demonstrated and provides another example of the ability of the technique to image the near surface at resolutions comparable to those attainable with GPR. The top of the saturated zone was imaged at a depth of 0.95 m by using a source capable of generating frequencies up to 750 Hz while minimizing the clipping of critical near-offset traces. Due to the low seismic velocities and high frequencies attained at the site, the TSZ reflection is easily identified as a coherent event unobscured by other wave trains. The reflection exhibited a NMO velocity of 180 m/s and a dominant frequency of ~450 Hz, yielding a resolution potential of 10 cm. In the proper geologic setting, ultra-shallow seismic methods can be used in conjunction with other geophysical techniques for improved understanding of subsurface properties or where other methods are not suitable, providing geophysicists with another option when working in the shallow subsurface.

Ever shallower depths and more complex geologic settings are continually being imaged and 2D and 3D shallow seismic reflection methods are being applied to a wider range of applications. Further research and development of the method will lead to improved techniques in data acquisition, processing, and interpretation and applications once thought impossible may become feasible. Water resources continue to become a bigger focus point in geophysics and the physical sciences in general and, as such, ultra-shallow seismic methods have been shown to be a reliable method for some hydrogeophysical applications and will continue to provide another tool to meet the needs of new challenges.

References

Allen, S. J., 1980, Seismic method: Geophysics, **45**, 1619–1633.

Anstey, N., 1986, Whatever happened to ground roll?: The Leading Edge, **5**, 40–45.

Bachrach, R., and A. Nur, 1998a, High-resolution shallow-seismic experiments in sand, Part 1: Water table, fluid flow, and saturation: Geophysics, **63**, 1225–1233.

Bachrach, R., and A. Nur, 1998b, Same wavelength GPR and ultra shallow seismic reflection on a river point bar: Sand stratigraphy and water table complexity: 68th Annual Meeting, SEG, Expanded Abstracts, 840–843.

Bachrach, R. and T. Mukerji, 2001a, Fast 3-D ultra shallow seismic reflection imaging using portable geophone mount: Geophysical Research Letters, **28**, 45–48.

Bachrach, R., and T. Mukerji, 2001b, AVO analysis of shallow seismic data: feasibility and analysis of 2D and 3D ultra shallow reflections: SAGEEP, Expanded Abstracts, Env. Eng. Geophys. Soc., Proceedings.

Bachrach, R. and T. Mukerji, 2004a, Portable dense geophone array for shallow and very shallow 3-D seismic reflection surveying—Part 1: Data acquisition, quality control, and processing: Geophysics, **69**, 1443–1455.

Bachrach, R., and T. Mukerji, 2004b, Portable dense geophone array for shallow and very shallow 3D seismic reflection surveying—Part 2: 3D imaging tests: Geophysics **69**, 1456–1469.

Baker, G. S., Schmeissner, C., Steeples, D. W., and R. G. Plumb, 1999, Seismic reflections from depths of less than two meters: Geophysical Research Letters, **26**, 279–282.

Baker, G. S., Steeples, D. W., Schmeissner, C., and K. T. Spikes, 2000, Ultrashallow seismic reflection monitoring of seasonal fluctuations in the water table: Environmental and Engineering Geoscience, **6**, 271–277.

Barnes, K. M., and R. F. Mereu, 1996, An application of the 3-D seismic technique or mapping near-surface stratigraphy near London, Ontario: J. Environ. Engin. Geophys., **1**, 171–177.

Bevan, M. J., A. L. Endres, D. L. Rudolph, and G. Parkin, 2005, A field scale study of pumping-induced drainage and recovery in an unconfined aquifer: Journal of Hydrology, **315**, 52–70.

Birkelo, B. A., Steeples, D. W., Miller, R. D., and M. A. Sophocleus, 1987, Seismic reflection of a shallow aquifer during a pumping test: Groundwater, **25**, 703–709.

Blair, J. D., Steeples, D. W., Vincent, P. D., Butel, N., and J. Powers, 2003, Analysis of the seismic response of rigidly interconnected geophones attached to steel media of various shapes: 73rd Annual International Meeting, SEG, Expanded Abstracts, 1263-1266.

Bradford, J. H., D. S. Sawyer, and C. A. Zelt, 1997, AVO analysis of low velocity, shallow sands (<50 m): 67th Annual Mtg., Soc. Expl. Geophys., Expanded Abstracts, 158–162.

Bradford, J. H., 2002, Depth characterization of shallow aquifers with seismic reflection, Part I—The failure of NMO velocity analysis and quantitative error prediction, Geophysics, **67**, 89–97.

Bradford, J. H., and D. S. Sawyer, 2002, Depth characterization of shallow aquifers with seismic reflection, Part II—Prestack depth migration and field examples, Geophysics, **67**, 98–109.

Brouwer, J. H., 2002, Improved NMO correction with a specific application to shallow-seismic data, Geophysical Prospecting, **50**, 225–237.

Buchholtz, H., 1972, A note on signal distortion due to dynamic (NMO) corrections: Geophysical Prospecting, **20**, 395–402.

Büker, F., Green, A. G., and H. Horstmeyer, 1998, Shallow 3-D seismic reflection surveying: Data acquisition and preliminary processing strategies: Geophysics, **63**, 1434-1450.

Büker, F., Green, A. G., and H. Horstmeyer, 2000, 3-D high-resolution reflection seismic imaging of unconsolidated glacial and glaciolacustrine sediments: processing and interpretation, Geophysics, **65**, 18–34.

Castagna, J. P., 1995, AVO Analysis-tutorial and review: in *Offset-dependent reflectivity – theory and practice of AVO analysis*, edited by J. P. Castagna and M. M. Backus, pp.3–36, Soc. Expl. Geophys.

Claerbout, J. F., 1971, Toward a unified theory of reflection mapping: Geophysics, **36**, 467–481.

Claerbout, J. F., 1972, Downward continuation of movement-corrected seismograms: Geophysics, **37**, 741–768.

Clark, J. M., Blair, J. D., and D. W. Steeples, 2004, Seismic response of geophones attached to tubing: 74th Annual International Meeting, SEG, Expanded Abstracts, 1452-1455.

Cordsen, A., Galbraith, M., and J. Peirce, 2000, Planning Land 3-D Seismic Surveys: Geophys. Developments, **9**, Soc. Expl. Geophys.

Corsmit, J., Versteeg, W. H., Brouwer, J. H., and K. Helbig, 1988, High-resolution 3-D reflection seismics on a tidal flat: acquisition, processing and interpretation: First Break, **6**, 9–23.

Czarnecki, G. P., 2006, Automated three-dimensional ultra-shallow seismic reflection data acquisition using a two-dimensional geophone array: MS Thesis, The University of Kansas, Lawrence.

Czarnecki, G. P., Tsoflias, G. P., Steeples, D. W., Sloan, S. D., and Eslick, R. C., 2006, An example of automated 3D ultra-shallow seismic acquisition: 76th Annual Mtg., Expanded Abstracts, Soc. Expl. Geophys., 1461-1465.

Dickey, H. P., Zimmerman, J. L., Plinsky, R. O., and R. D. Davis, 1977, Soil survey of Douglas County, Kansas, United States Department of Agriculture Experiment Station publication, **73**.

Domenico, S. N., 1976, Effect of brine-gas mixture on velocity in an unconsolidated sand reservoir, Geophysics, **41**, 882–894.

Dunkin, J. W., and F. K. Levin, 1973, Effect of normal moveout on a seismic pulse: Geophysics, **38**, 635–642.

Endres, A. L., and R. Knight, 1989, The effect of microscopic fluid distribution on elastic wave velocities: The Log Analyst, **30**, 437–445.

Endres, A. L., and R. Knight, 1997, Incorporating pore geometry and fluid pressure communication into modeling the elastic behavior of porous rocks: Geophysics, **62**, 106–117.

Endres, A. L., W. P. Clement, and D. L. Rudolph, 2000, Ground penetrating radar imaging of an aquifer during a pumping test: Ground Water, **38**, 566–576

Galbraith, M., and C. L. MacMinn, 1982, Error correction in field recorded seismic data: Journal of the Canadian Society of Exploration Geophysicists, **18**, 23–33.

Goforth, T., and C. Hayward, 1992, Seismic reflection investigations of a bedrock surface buried under alluvium: Geophysics, **57**, 1217–1227.

Green, A. G., Pugin, A., Beres, M., Lanz, E., Büker, F., Huggenberger, P., Horstmeyer, H., Grasmück, M., De Iaco, R., Holliger, K., and H. R. Maurer, 1995, 3-D high-resolution seismic and georadar reflection mapping of glacial, glaciolacustrine and glaciofluvial sediments in Switzerland: Ann. Symp. Environ. Engin. Geophys. Soc. (SAGEEP), Expanded Abstracts, 419–434.

Hill, S., Shultz, M., and J. Brewer, 1999, Acquisition footprint and fold-of-stack plots: The Leading Edge, **18**, 686–695.

House, J. R., Boyd, T. M., and F. P. Haeni, 1996, Haddam Meadows, Connecticut: A case study for the acquisition, processing, and relevance of 3-D seismic data as applied to the remediation of DNAPL contamination, *in* Weimer, P., and Davis, T. L., Eds., Applications of 3-D seismic data to exploration and production: Geophysical Developments Series **5**: Soc. Expl. Geophy., 257–265.

Hunter, J. A, Pullan, S. E., Burns, R. A., Gagne, R. M., and R. S. Good, 1984, Shallow seismic-reflection mapping of the overburden-bedrock interface with the engineering seismograph: Some simple techniques: Geophysics, **49**, 1381–1385.

Johnson, E. J., 2003, Imaging the cone of depression around a pumping well using shallow seismic reflection: M.S. thesis, 100 pp., The University of Kansas, Lawrence.

Khan, R. H., 1982, Seismic data error correction using adaptive lattice filters: 52nd Annual International Meeting, SEG, Expanded Abstracts, 124–126.

Knapp, R. W., and D. W. Steeples, 1986a, High-resolution common-depth-point seismic reflection profiling: Instrumentation: Geophysics, **51**, 276–282.

Knapp, R. W., and D. W. Steeples, 1986b, High-resolution common-depth-point seismic reflection profiling: Field acquisition parameter design: Geophysics, **51**, 283–294.

Knight, R., and R. Nolen-Hoeksema, 1990, A laboratory study of the dependence of elastic wave velocities on pore scale fluid distribution: Geophysical Research Letters, **17**, 1529–1532.

Krey, T. C., 1987, Attenuation of random noise by 2-D and 3-D CDP stacking and Kirchhoff migration: Geophysical Prospecting, **35**, 135–147.

La Bella, G., Loinger, E., and L. Savini, 1998, The cross-shooting methodology: Design, acquisition, and processing: The Leading Edge, **17**, 1549–1553.

Lanz, E., Pugin, A., Green, A., and Horstmeyer, H., 1996, Results of 2- and 3-D high-resolution seismic reflection surveying of surficial sediments: Geophysical Research Letters, **23**, 491–494.

Loper, G. B., and Pittman, R. R., 1954, Seismic recording on magnetic tape: Geophysics, **19**, 104–115.

Macy, B. K., and C. Schmeissner, 1998, Isomod v1.0: a finite-difference seismic modeling package: http://www.geo.ukans.edu/~brian/fdmod.html.

Mavko, G., 2003, The rock physics basis: SEG Continuing Education Course Notes.

Mavko, G., and T. Mukerji, 1998, Bounds on low-frequency seismic velocities in partially saturated rocks: Geophysics, **63**, 918–924.

Mayne, W. H., 1962, Common reflection point horizontal data stacking techniques: Geophysics, **27**, 927–938.

Miller, R. D., 1992, Normal moveout stretch mute on shallow-reflection data: Geophysics, **57**, 1502–1507.

Miller, R. D., Steeples, D. W., and M. Brannan, 1989, Mapping a bedrock surface under dry alluvium with shallow seismic reflections: Geophysics, **54**, 1528–1534.

Miller, R. D., and J. Xia, 1998, Large near-surface velocity gradients on shallow seismic reflection data, Geophysics, **63**, 1348–1356.

Miller, R. D., Raef, A. E. E., Byrnes, A. P., Lambrecht, J. L., and Harrison, W. E., 2004, 4-D high-resolution seismic reflection monitoring of miscible CO2 injected into a carbonate reservoir in the Hall-Gurney Field, Russell County, Kansas: 74th Annual Meeting, SEG, Expanded Abstracts, 2259–2262.

Nyman, D., 1977, The interpolation error operator: time series error detection and correction: Geophysics, **42**, 773–777.

Pullan, S. E., and J. A. Hunter, 1985, Seismic model studies of the overburden-bedrock reflection: Geophysics, **50**, 1684–1688.

Ralston, M. D., Steeples, D. W., Spikes, K., and J. Blair, 2001, Near-surface three-component seismic data acquisition using rigidly interconnected geophones: 71st Annual Meeting, SEG, Expanded Abstracts, 1411–1414.

Ralston, M. D., Steeples, D. W., Spikes, K., Blair, J., and T. Gang, 2002, Analysis of an automated three-component shallow seismic acquisition system: 72nd Annual Meeting, SEG, Expanded Abstracts, 1551–1554.

Resnick, J. R., 1995, Seismic data processing for AVO and AVA analysis: in Offset-dependent reflectivity – theory and practice of AVO analysis, edited by J. P. Castagna and M. M. Backus, pp.175–189, Soc. Expl. Geophys.

Schmeisnner, C. M., Spikes, K. T., and D. W. Steeples, 2001, Recording seismic reflections using rigidly interconnected geophones: Geophysics, **66**, 1838–1842.

Schmelzbach, C., and Juhlin, C., 2007, High-resolution 3-D seismic imaging of the upper crystalline crust at a nuclear-waste disposal study site on Avro Island, southeastern Sweden, 76th Annual Meeting, SEG, Expanded Abstracts, 1396–1400.

Sengbush, R. L., P. L. Lawrence, and F. J. McDonal, 1961, Interpretation of synthetic seismograms, Geophysics, **24**, 138–157.

Shatilo, A., and F. Aminzadeh, 2000, Constant normal-moveout (CNMO) correction: a technique and test results, Geophysical Prospecting, **48**, 473–488.

Siahkoohi, H. R., and West, G. F., 1998, 3-D seismic imaging of complex structures in glacial deposits: Geophysics, **63**, 1041–1052.

Sloan, S. D., 2005, The combined use of shallow seismic reflection and GPR techniques near Clay Center, KS: M.S. thesis, 46 pp., The University of Kansas, Lawrence.

Sloan, S. D., Tsoflias, G. P., Steeples, D. W., and P. D. Vincent, 2007, High-resolution ultra-shallow subsurface imaging by integrating near-surface seismic reflection and ground-penetrating radar data in the depth domain: Journal of Applied Geophysics, **62**, 281–286.

Sloan, S. D., Steeples, D. W., and P E. Malin, 2008, Acquisition and processing pitfall associated with clipping near-surface seismic reflection traces, Geophysics, **73**, W1–W5.

Sloan, S. D., Steeples, D. W., and Tsoflias, G. P., 2008, Imaging a shallow paleo-channel using 3D ultra-shallow seismic reflection methods: SAGEEP, **21**, 568–576.

Spikes, K. T., Vincent, P. D., and D. W. Steeples, 2005, Near-surface common-midpoint seismic data recorded automatically planted geophones: Geophysical Research Letters, **32**, L19302.

Spitzer, R., Green, A. G., and F. O. Nitsche, 2001, Minimizing field operations in shallow 3-D seismic reflection surveying: Geophysics, **66**, 1761–1773.

Spitzer, R., Nitsche, F. O., Green, A. G., and H. Horstmeyer, 2003, Efficient acquisition, processing, and interpretation strategy for shallow 3D seismic surveying: A Case Study: Geophysics, **68**, 1792–1806.

Steeples, D. W., Baker, G. S., and C. Schmeissner, 1999a, Toward the autojuggie: Planting 72 geophones in 2 sec: Geophysical Research Letters, **26**, 1085–1088.

Steeples, D. W., Baker, G. S., Schmeissner, C., and B. K. Macy, 1999b, Geophones on a board: Geophysics, **64**, 809–814.

Stone, D. G., 1994, Designing seismic surveys in two and three dimensions: Geophysical Reference Series, **5**, Society of Exploration Geophysicists.

Tsoflias, G. P., Steeples, D. W., Czarnecki, G., and Sloan, S. D., 2006, 3-D Autojuggie: automating deployment of two-dimensional geophone arrays for efficient ultra-shallow seismic-reflection surveys, Geophysical Research Letters, **33**, doi: 10.1029/2006GL025902.

van der Veen, M., Spitzer, R., Green, A. G., and P. Wild, 2001 Design and application of a towed land-streamer system for cost-effective 2-D and pseudo-3-D shallow seismic data acquisition: Geophysics, **66**, 482–500.

Vermeer, G. J. O., 2002, 3-D Seismic Survey Design: Geophysical Reference Series, **12**, Society of Exploration Geophysicists.

Vincent, P. D., 2005, Frequency-domain least-squares filtering of data from square-tubing mounted geophones: M.S. Thesis, The University of Kansas, Lawrence.

Vincent, P. D., Blair, J. D., Steeples, D. W., and G. P. Tsoflias, 2004, Effect of orientation of hollow-bar-mounted geophones on airwave coherency: 74th Annual International Meeting, SEG, Expanded Abstracts, 1345–1348.

Villella, A. C., Xia, J., and Miller, R. D., 1997, Delineation of salt dissolution sinkholes using minimal deployment shallow 3-D seismic reflection surveying: 67th Annual Meeting, SEG, Expanded Abstracts, 780–783.

Waddell, M. G., W. J. Domoracki, and T. J. Temples, 2001, Use of seismic reflection amplitude versus offset (AVO) techniques to image dense nonaqueous phase liquids (DNAPL), SAGEEP ’01: Symposium on the Application of Geophysics to Environmental and Engineering Problems, Env. Eng. Geophys. Soc., Proceedings.

Walton, G. G., 1972, Three-dimensional seismic method: Geophysics, **37**, 417–430.

Weatherby, B. B., 1948, The history and development of seismic prospecting: *in* Geophysical Case Histories, **1**, 7–20, Society of Exploration Geophysicists.

Westby, G. H., 1935, Discovery of a small producing structure in Okmulgee County, Oklahoma by reflection seismograph: Journal of the Society of Petroleum Geophysicists, **6**.

Wolf, A., 1937, The reflection of elastic waves from transition layers of variable velocity: Geophysics, **2**, 357–363.

Appendix A: Current Abstracts & Publications

Sloan, S. D., Tsoflias, G. P., and Steeples, D. W., 2006, Frequency effects of partially water-saturated zone thickness on shallow seismic reflection data: SEG Expanded Abstracts, 1362-1366.

Presented at the 76th Annual Meeting of the Society of Exploration Geophysicists in New Orleans, Louisiana.

Frequency effects of the partially water-saturated zone thickness on shallow seismic reflection data

Steven D. Sloan, Georgios P. Tsoflias, and Don W. Steeples, The University of Kansas*

Summary

High-resolution shallow seismic reflection (SSR) experiments were conducted during and after a pumping test of an agricultural irrigation well in an effort to image the cone of depression seismically. Despite water table fluctuations of ~0.5 m, we were unable to observe temporal elevation variations in the water table attributable to pumping. However, the seismic data sets showed variations in the frequency of the reflection from the top of the saturated zone (TSZ) and we propose that these changes are caused by changes in the thickness of the partially saturated zone above the water table resulting from applied pumping stresses. A model was developed to test our hypothesis simulating a wedge of increasing thickness that represents the zone of partial saturation. Synthetic seismic traces showed a decrease in reflection frequency with increasing thickness of the partially saturated zone. The results of the modeled data correlate with the differences observed in the field data and support our hypothesis that changes in the partially saturated zone introduce detectable frequency changes in SSR data.

Introduction

Several attempts have been made to image the cone of depression during a pumping test (Birkelo et al., 1987; Johnson, 2003; Sloan, 2005), but none have been singularly successful. Birkelo et al.'s (1987) experiment was unsuccessful in part due to a previously unknown clay layer that produced a perched water table. However, the authors observed a decrease in the dominant frequency of the reflection from a survey acquired before pumping in comparison to one collected while the water table was at maximum drawdown. Johnson (2003) also had problems imaging the cone of depression because of the subsurface geology and lack of drawdown. These two attempts suggested that an ideal site would have a water table within a thick sand unit that was free of fine-grained materials that would hinder the drawdown of the water table. The site chosen for the experiments presented here is an agricultural field located in north-central Kansas. The water table is located at ~5 m depth in an unconfined aquifer comprised of unconsolidated sands and gravels, coarsening downward below the water table. A hand-augured hole at the site revealed ~5 m of fine-to-coarse sand with a 0.3-m thick silty-sand layer at ~3.1 m depth.

An observation well installed ~6 m from the pumping well along the seismic lines showed a water table elevation change of ~0.5 m at maximum drawdown. After data acquisition and processing, we determined that our attempt at imaging the physical manifestation of the cone of depression was unsuccessful; however, a noticeable change in the frequency of the TSZ reflection was observed when comparing data collected during pumping with those collected after the water table had recovered. In light of this, we propose that instead of observing temporal shifts in the TSZ reflection caused by the raising and lowering of the water table, we are seeing changes in the character of the waveform caused by changes in the thickness of the zone of partial saturation above the TSZ.

We suggest that relatively rapid changes in elevation of the water table due to a continuous cycle of pumping and recovery have caused a thickening of the partially saturated zone. Such conditions would be expected to influence the velocity profile of the partially saturated zone. Sengbush et al. (1961) describe the effects of various velocity functions on a reflected wavelet as a process of linear filtering. A sharp interface represented by a step-velocity function produces a reflection having the same waveform as the source pulse. A gradational interface represented by a ramp-velocity function is the integral of the step function and thus produces a reflection that is the integrated source pulse. The effect of moving from a step-velocity function to a ramp-velocity function on a reflected wavelet is an overall lowering of the reflection frequency.

To help test our hypothesis we developed a numerical model that represents the partially saturated zone as a wedge of increasing thickness to observe its effects on synthetic seismic data. The synthetic seismic traces created using the model show a decrease in reflection frequency as the thickness of the partially saturated zone increases, which supports our observations of the field data. The velocity function chosen to represent the partially saturated zone is based on previous studies of the effects of partial saturation on seismic velocity as described by Knight and Nolen-Hoeksema (1990) and Mavko and Mukerji (1998).

Knight and Nolen-Hoeksema (1990) showed the effects of partial saturation on *P*-wave velocity (V_p) in a sandstone using two methods of partial saturation. One method increases water saturation (S_w) through imbibition, yielding velocities similar to those predicted by the Biot-Gassman-Domenico theory where velocities remain relatively constant with increasing saturation and increase rapidly at saturations greater than ~90%. The second method achieves partial saturation through drainage, where velocities follow more of a curved path, increasing exponentially with increased water saturation. Mavko and

Mukerji (1998) relate this difference in velocity response to patchy and uniform saturation. They define uniform saturation as fine-scale, uniform mixing and patchy saturation as heterogeneous saturation on a coarser scale. Saturation scales separating uniform from patchy behavior may be from 0.1-1 cm in the laboratory and tens of centimeters in the field. In this case velocity changes related to imbibition would correlate with uniform saturation and those related to drainage would correlate to patchy saturation. Mavko and Mukerji (1998) determined that patchy saturations always lead to higher velocities than uniform saturations and that patchy and uniform velocities approximate the upper and lower bounds of low-frequency velocity (Figure 1). It should be noted that the study by Knight and Nolen-Hoeksema (1990) was done using ultrasonic frequencies with a consolidated sandstone under laboratory conditions, so their results may not be representative of unconsolidated sands.

Methods: Data Acquisition and Processing

Common mid-point (CMP) seismic reflection surveys were conducted in the summers of 2003 and 2004 to image changes in the TSZ reflection during pumping of an agricultural irrigation well. The first survey (A) was conducted on August 13, 2003 after the pump had been allowed to run continuously for three days. Following aquifer recovery, ~18 hours after the pump was turned off, a second survey (B) was acquired. A third survey (C) was shot the following summer when, due to cooler temperatures, the pump had not been run for at least two weeks and water table fluctuations had been limited to natural processes. The pump was located ~5 m away from the east end of each of the surveys.

Each survey was conducted using 144 Mark Products L-40A 100-Hz geophones planted at a 10-cm interval. The source was a .22-caliber rifle firing single short ammunition into 15-cm deep pre-punched 2-cm diameter holes. The source interval was 10 cm beginning and ending 5 m off of each end of the spread. Data were recorded using two Geometrics 72-channel StrataView seismographs with 24-bit A/D conversion, 256 ms record lengths, and a 0.25 ms sampling interval. Acquisition parameters were identical for each survey.

Data were processed using techniques common to CMP seismic processing, including geometry definition, elevation corrections, trace editing, Butterworth filtering (100–250 Hz, 12 dB/octave rolloff slopes), early muting, *f-k* filtering to remove pump noise, CMP sorting, NMO corrections, iterative residual statics, CMP stacking, and AGC (60 ms window). Figure 2 shows the processed sections with selected horizons overlain. Horizon times and frequencies were picked using a commercial seismic interpretation software package.

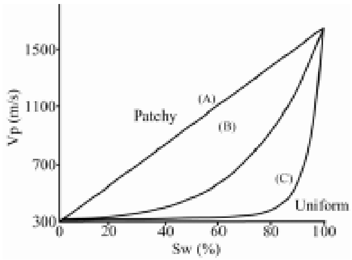

Figure 1. Illustration depicting the (A) patchy and (C) uniform saturation curves as upper and lower velocity bounds. (B) represents the velocity profile used in the numerical model (modified from Mavko, 2003).

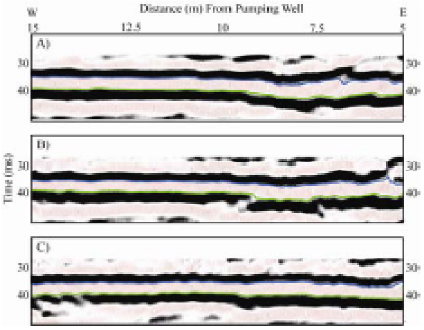

Figure 2. SSR stacks showing data collected at steady-state conditions during (A) drawdown, (B) recovery, and (C) undisturbed hydrologic conditions.

Model Description

To test our hypothesis of a decrease in reflection frequency with increasing thickness of the partially saturated zone, we created a density-normalized model of the subsurface (Figure 3) that represents the partially saturated zone as a wedge of increasing thickness. The wedge is subdivided into multiple layers with increasing velocities. The velocities used for the unsaturated (295 m/s) and saturated (1650 m/s) zones were derived from the field data. The velocity profile used for the wedge was determined using the previously mentioned work of Knight and Nolen-Hoeksema (1990) and Mavko and Mukerji (1998) by choosing an exponential curve that lies between the approximations of the upper and lower bounds (Figure 1). Heterogeneity within the subsurface sediments can cause changes in the height of the capillary fringe and roughness of the unsaturated/saturated interface, which led us to base our V_p/S_w function on patchy saturation where fluid and gas phases are mixed at a coarse scale. The velocity function exhibits a higher rate of change as water saturation approaches 100%.

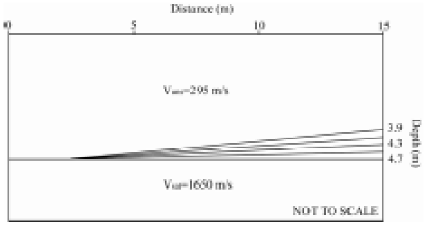

Figure 3. Illustration of the subsurface model used in modeling the effects of changes in thickness of the partially saturated zone (the wedge).

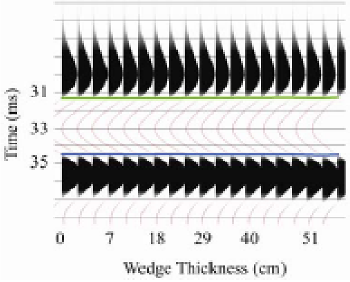

Figure 4. Synthetic traces representing the effect of the partially saturated zone on SSR data. The partially saturated zone is increasing in thickness from left to right as the trough broadens.

Synthetic seismic traces were generated using a finite-difference elastic wave-equation model that is fourth order in space and second order in time (Macy and Schmeissner, 1998). The subsurface model was represented by a 1-cm by 1-cm grid of nodes that is 15 m long and 10 m deep. The slope of the wedge is ~3° reaching a maximum thickness of 55 cm at the edge. A single vertical-incident trace was produced every 1 m along the wedge beginning 20 cm from the start of the wedge. Figure 4 shows the resulting TSZ reflection from the model with wedge thickness increasing from 0–55 cm from left to right.

Results

Comparison of the three field seismic data sets shows that they are very similar in appearance. The difference that is addressed here is that of reflection frequency. The trough bounded by the green and blue horizons (Figure 2) appears to narrow from survey A to B to C, respectively. Figure 5 illustrates the time differences between the horizons and the frequency of sections A-C. Survey A, collected while at maximum drawdown, shows the largest time difference and lowest overall frequency. Survey B, collected after the water table had recovered, exhibits a collective increase in frequency compared to A. Survey C, collected approximately nine months later during a period when the pump was not in use, shows the smallest horizon time difference and subsequently higher frequency content than A and B. The average frequencies of lines A-C are ~114, 118, and 125 Hz, respectively. As the main difference during the acquisition of the surveys was the pumping of the aquifer, we interpret the changes in frequency content to be related to changes in the unsaturated/saturated interface, particularly changes in the zone of partial saturation.

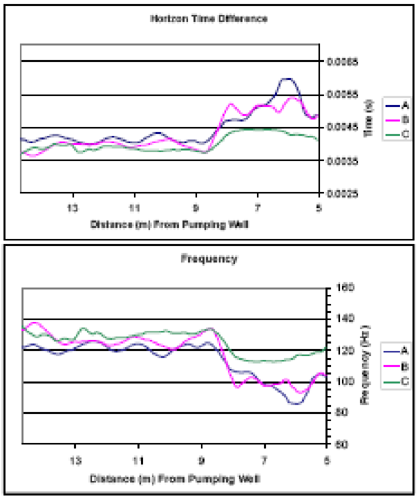

Figure 5. The top graph shows the difference in time in the horizons of sections A-C. The lower graph represents the corresponding frequencies of sections A-C.

The model data displayed in figure 4 show traces simulated along the partially-saturated wedge increasing in thickness from left to right. The trough bounded by the two horizons broadens from left to right indicating a decrease in frequency with increasing wedge thickness. This effect can be seen in figure 6, which illustrates the frequency of each trace along the wedge. There is an overall drop in frequency of ~5 Hz from a partially saturated zone thickness of 0 to 55 cm.

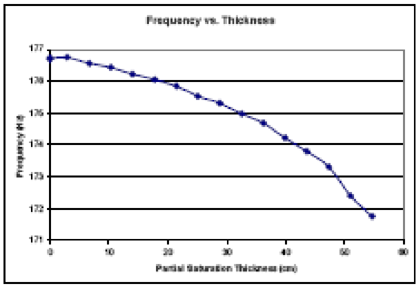

Figure 6. The graph illustrates the decrease in TSZ reflection frequency with increased thickness of the partially saturated zone in the modeled data.

Discussion & Conclusions

The frequency plot in figure 5 shows a distinct decrease at ~8.75 m. This may be caused by an increase in finer-grained sediments, which would create a thicker partially saturated zone due to an increase in bound pore water above the water table. The pump was run more or less continuously throughout the summer on ~5-day cycles where the pump would run for ~3 days and would then be shut off for ~2 days. These rapid changes in the elevation of the water table, combined with fine-scale soil heterogeneity, may have caused a thicker partially saturated zone. As the water table was lowered there may not have been sufficient time for all of the pore water to drain and as the water table quickly recovered, some air may have become trapped in the pore space. This could have created a zone of patchy partial saturation that was directly influenced by pumping-induced changes in the water table and would be in a constant state of flux due to the pumping/recovery cycles. This may be illustrated by survey C in figure 5, which is of higher frequency than A and B, most notably between 5 and 8.75 m. Surveys A and B are of lower frequency than C along this portion of the line and may indicate that this zone was more sensitive to relative changes in the water table due to the finer-grained sediments, thus creating an overall thicker partially saturated zone.

Although changes in the height of the water table were not imaged seismically, the data presented here show that changes in the dominant frequency of the TSZ reflection are observed in field data collected under different pumping stresses of an unconfined aquifer. These observations agree with results of the modeled data that show a decrease in reflection frequency with increased thickness of the partially saturated zone. Although there is an overall agreement between the model data and the field data, these are preliminary results of ongoing research. Further work is necessary to better characterize the velocity profile of the partially saturated zone and to refine the model to more accurately represent the subsurface.

Acknowledgments

The authors wish to thank Robert Eslick, Gerard Czarnecki, Paul Vincent, Jason Blair, and Jennifer Clark for assistance in the field and Ross Black for assistance with the numerical simulations. This research was supported under grants DE-FG02-03ER63656 and DE-FG07-97ER14826, Environmental Management Science Program, Office of Science and Technology, Office of Environmental Management, United States Department of Energy (DOE). However, any opinions, conclusions, or recommendations expressed herein are those of the authors and do not necessarily reflect the views of DOE.

References

Birkelo, B. A., Steeples, D. W., Miller, R. D., and M. Sophocleous, 1987, Seismic reflection study of a shallow aquifer during a pumping test: Groundwater, **25**, 703—709.

Johnson, E. J., 2003, Imaging the cone of depression around a pumping well using shallow seismic reflection: M.S. Thesis, The University of Kansas.

Knight, R., and R. Nolen-Hoeksema, 1990, A laboratory study of the dependence of elastic wave velocities on pore scale fluid distribution: Geophysical Research Letters, **17**, 1529—1532.

Macy, B. K., and C. Schmeissner, 1998, Isomod v1.0: a finite-difference seismic modeling package, http://www.geo.ukans.edu/~brian/fdmod.html.

Mavko, G., 2003, The rock physics basis: SEG Continuing Education Course Notes.

Mavko, G., and T. Mukerji, 1998, Bounds on low-frequency seismic velocities in partially saturated rocks: Geophysics, **63**, 918—924.

Sengbush, R. L., Lawrence, P. L., and F. J. McDonal, 1961, Interpretation of synthetic seismograms: Geophysics, **24**, 138—157.

Sloan, S. D., 2005, The combined use of shallow seismic reflection and GPR techniques at a field site near Clay Center, KS: M.S. Thesis, The University of Kansas.

Sloan, S. D., Tsoflias, G. P., and Steeples, D. W., 2007, Seismic AVO variations related to partial water saturation during a pumping test: SEG Expanded Abstracts, 1212-1216.

Presented at the 77th Annual Meeting of the Society of Exploration Geophysicists in San Antonio, Texas.

Seismic AVO variations related to partial water saturation during a pumping test

Steven D. Sloan, Georgios P. Tsoflias, Don W. Steeples, Department of Geology, The University of Kansas*

Introduction

High-resolution shallow seismic reflection (SSR) experiments were conducted during and after a pumping test of an agricultural irrigation well in an effort to image the cone of depression seismically. Despite water table fluctuations of ~0.5 m, we were unable to observe temporal elevation variations in the water table attributable to pumping. Amplitude-versus-offset (AVO) analysis was performed on three data sets, revealing differences in the amplitude response with changes in the applied pumping stress. We propose that these differences are caused by changes in the thickness of the partially-saturated zone (PSZ) above the water table resulting from changes in the height of the water table.

We suggest that relatively rapid changes in the elevation of the water table due to a continuous cycle of pumping and recovery have caused a thickening of the PSZ. Results of a pumping test by Bevan et al. (2005) showed an overall extension of ~20 cm of the capillary fringe throughout the test. Once hydraulic head levels were allowed to return to pre-pumping elevations, it was observed that soil-moisture content profiles stabilized ~20 cm below their pre-pumping elevations, suggesting a significant hysteretic effect caused by residual air trapped in the pore space during imbibition, i.e. after five days of recovery the subsurface zone affected by pumping had not returned to pre-pumping conditions. Figure 1 depicts the PSZ where A represents the water table without pumping and B is the water table during pumping once it has reached steady-state conditions, forming the cone of depression. The area between A and B represents the zone affected by pumping.

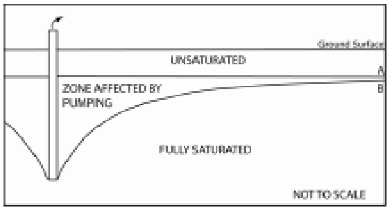

Figure 1. Illustration showing the water table with (B) and without (A) pumping and the zone affected by the raising and lowering of the water table.

To relate the observed changes in amplitude to the subsurface, we must first consider how the seismic properties of the subsurface might change under the different pumping conditions. The water table represents the fully saturated interface where water pressure is equal to atmospheric pressure. Immediately above the water table is the capillary fringe, which is also fully saturated but exhibits negative pore pressure, and the PSZ lies above the capillary fringe. The thicknesses of the capillary fringe and PSZ are controlled by the grain size of the surrounding sediments, but are also affected by other environmental factors. A previous study by Sloan et al. (2006) suggested that raising and lowering the height of the water table causes a thickening of the PSZ. During pumping, pore-bound water may remain above the drawn-down water table and as water levels return to pre-pumping conditions air can be trapped in the pore space beneath the water table. Such conditions would be expected to influence the seismic-velocity profile of the PSZ.

Knight and Nolen-Hoeksema (1990) showed the effects of partial saturation on *P*-wave velocity (V_p) in a sandstone using two different methods (Figure 2). One method increased water saturation (S_w) through imbibition, yielding velocities similar to those predicted by the Biot-Gassman-Domenico theorem where velocities remain relatively constant with increasing saturation and increase rapidly at saturations greater than ~90%. The second method achieved partial saturation through drainage, where velocities follow a curved path on the graph, increasing exponentially with increased water saturation. It should be noted that the study by Knight and Nolen-Hoeksema (1990) was done using ultra-sonic frequencies with a consolidated sandstone under laboratory conditions, so their results may not be representative of unconsolidated sands.

Mavko and Mukerji (1998) related this difference in velocity response to patchy and uniform saturation. They defined uniform saturation as fine-scale, uniform mixing and patchy saturation as heterogeneous saturation on a coarser scale. Saturation scales separating uniform from patchy behavior may be from 0.1-1 cm in the laboratory to tens of centimeters in the field. In this case velocity changes related to imbibition would correlate with uniform saturation, or a step velocity function, and those related to drainage would correlate to patchy saturation, or a ramp-velocity function. Mavko and Mukerji (1998) determined that patchy saturations always lead to higher velocities than uniform saturations and that patchy and uniform velocities approximate the upper and lower bounds of seismic velocity, respectively.

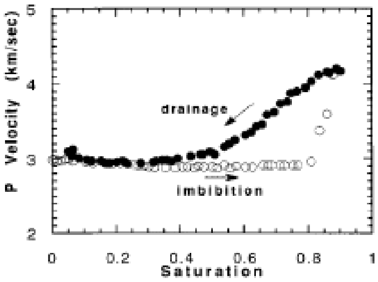

Figure 2. Plot displaying the changes in *P*-wave velocity with water saturation (from Knight and Nolen-Hoeksema, 1990).

Sengbush et al. (1961) describe the effects of various velocity functions on a reflected wavelet as a process of linear filtering. A sharp interface represented by a step-velocity function produces a reflection having the same waveform as the source pulse. A gradational interface represented by a ramp-velocity function (Figure 3) is the integral of the step function and thus produces a reflection that is the integrated source pulse. The effect of moving from a step-velocity function to a ramp-velocity function on a reflected wavelet is an overall lowering of the reflection frequency and decrease in amplitude. Wolf (1937) demonstrated that vertically-incident traces from a zone represented by a ramp-velocity function will exhibit a decrease in amplitude as the slope of the ramp increases.

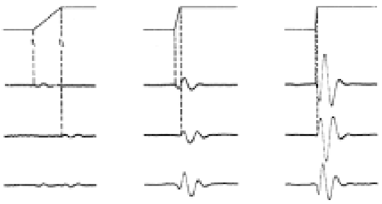

Figure 3. Illustration of the effects of a ramp velocity function on a reflection with changes in slope (from Sengbush et al., 1961). Reflection amplitudes decrease as the slope of the ramp increases.

Data acquisition and processing

Common mid-point (CMP) seismic reflection surveys were conducted in the summers of 2003 and 2004 to image changes in reflection from the top of the saturated zone (TSZ) during pumping of an agricultural irrigation well. The first survey (A) was conducted on August 13, 2003 after the pump had been allowed to run continuously for three days. Following aquifer recovery, ~18 hours after the pump was turned off, a second survey (B) was acquired. A third survey (C) was shot the following summer when, due to cooler temperatures, the pump had not been run for at least two weeks and water table fluctuations had been limited to natural processes. The pump was located ~5 m away from the east end of each of the surveys.

Each survey was conducted using 144 Mark Products L-40A 100-Hz geophones planted at a 10-cm interval. The source was a .22-caliber rifle firing single short ammunition into 15-cm deep pre-punched 2-cm diameter holes. The source interval was 10 cm beginning and ending 5 m off of each end of the spread. Data were recorded using two Geometrics 72-channel StrataView seismographs with 24-bit A/D conversion, 256-ms record lengths, and a 0.25-ms sampling interval. Acquisition parameters were identical for each survey, with the exception of the shot holes of (B) being punched on the opposite side of the spread from (A) to avoid using the same holes.

Data used for the AVO analysis were processed using commonly applied techniques for AVO data, as described by Castagna (1995) and Resnick (1995), to avoid unwanted changes in the amplitudes. Processes included geometry definition, elevation corrections, spherical spreading corrections, *f-k* filtering, CMP sorting, NMO corrections, and partial stacking.

AVO analysis

Although AVO techniques are widely used in hydrocarbon exploration, little work has been done in the shallow subsurface. The depth of targets in exploration usually constrain angles of incidence to ~30° or less (unless a wide-angle survey is conducted), but targets imaged by shallow (<200 m) and ultra-shallow (<20 m) surveys allow for a wide range of angles and large offsets relative to reflector depth. However, the near surface presents its own complexities that must be overcome to provide a data set of high enough quality to perform AVO analysis. The airwave, refraction, direct wave, and ground roll often prevent a wide range of offsets from being used due to interference with the reflections. Despite the associated problems, there are a few examples of using AVO for SSR surveys (Bradford et al., 1997; Bachrach and Mukerji, 2001; Waddell et al., 2001). Bachrach and Mukerji (2001) demonstrated that the unsaturated/saturated sand interface exhibits an increase in reflection amplitude with increasing offset.

AVO analysis was performed by partially stacking common offsets of five adjacent CMP gathers, each separated by 5 cm, into a supergather (Figure 4). Each of the three data sets was normalized to their respective RMS amplitudes. The RMS amplitudes were calculated for each trace from a window around the TSZ reflection from 32–48 ms for offsets ranging from 0-1 m (angles of incidence of 0–12°) in 10-cm increments. For V_1=295 m/s and V_2=1650 m/s, the critical angle of incidence is 10.3°, corresponding to a critical offset of 0.85 m, and angles greater than this will yield a reflection coefficient of 1.0. Figure 5 shows plots of the relative amplitude versus CMP offset within a supergather for a range of distances of the CMP supergather from the pumping well while the pump was running (drainage) and after it was shut off (imbibition). Exponential curves were fit to the data points using least-squares regression representing the AVO response during and after pumping. As the distance of the CMP supergather from the pumping well increases, the relative amplitude of each curve increases and the difference between the two curves in each plot decreases.

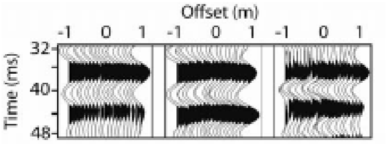

Figure 4. CMP supergathers from data collected during pumping (left), after pumping (center), and with no pumping (right).

Assuming that an increase in the PSZ thickness results from the drawdown of the water table, it is expected that the relative amplitude of the TSZ reflection would decrease with decreasing offset from the pumping well as the slope of the velocity ramp increases (Figure 3). As the water table returns to equilibrium, the slope of the velocity ramp decreases and the relative amplitude of the TSZ reflection is expected to increase relative to reflection amplitudes during drainage. At offsets farther from the pumping well there are smaller changes in the elevation of the water table and a lesser effect on the thickness of the PSZ, so differences between the during-pumping and after-pumping curves are less pronounced. Results of the AVO analysis support these expectations.

Figure 6 shows plots of relative amplitude versus CMP offset within a supergather for a range of distances from the pumping well for data collected while the pump was running and data from the following summer when the pump had not been used. The relative amplitudes decrease as the distance from the pumping well decreases during drainage. In comparison, the amplitudes of the data acquired without pumping remain relatively consistent despite changes in the distance from the pumping well. The consistency in amplitudes while there was no pumping indicates that changes in the elevation of the water table and subsequent effects on the PSZ thickness affect the amplitudes of the TSZ reflection during the pumping test.

Changes in the TSZ reflection amplitude may serve as a qualitative indicator of permeability near the water table. A more permeable material, such as a clean or well-sorted sand, would allow more drainage during drawdown. An increase in drainage would have a lesser effect on the thickness of the PSZ, resulting in a smaller change in amplitude. Conversely, lowering the water table in fine-grained material would increase the thickness of the PSZ and exhibit a larger variation in amplitude. Although the results of this study may not have a wide range of practical applications singularly, they could yield a more accurate representation of the subsurface properties when used in tandem with techniques that are sensitive to pore fluids such as ground-penetrating radar and electrical methods.

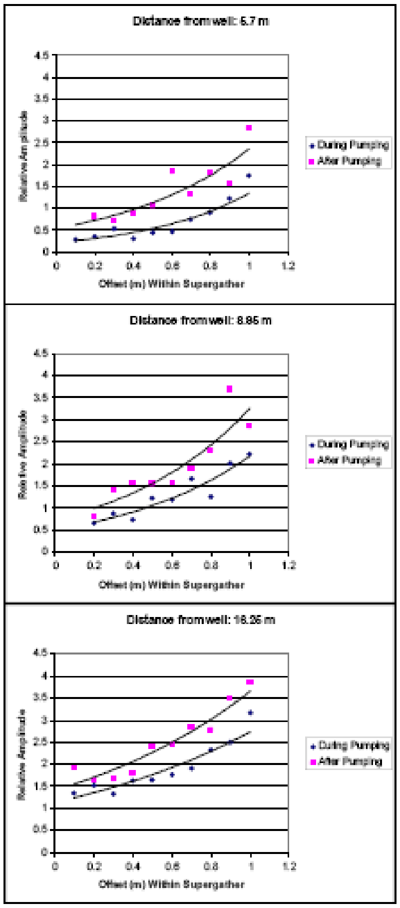

Figure 5. AVO curves from data collected during and after pumping for CMP supergathers at three different distances from the pumping well.

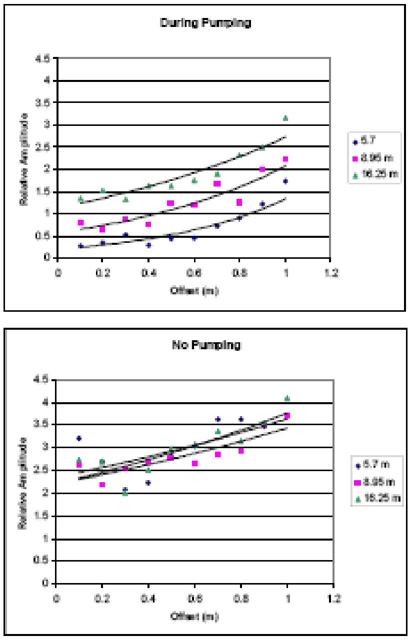

Figure 6. AVO curves from data collected during pumping (top) and without any pumping (bottom). As the distance from the pumping well increases from 5.7–16.25 m, the amplitude increases while the pump is running. When the pump had not been used, the curves are clustered together and display higher amplitudes, suggesting that changes in the PSZ resulting from elevation changes of the water table affect seismic reflection amplitudes.

Although these techniques require multiple surveys, which may limit the extent to which they are used, they may prove useful in understanding changes in water table and saturation fluctuations. This may be desirable in time-lapse studies at contaminated sites where non-invasive techniques are necessary. Further work is warranted to test the repeatability of the techniques and would ideally include the collection of soil moisture content measurements for direct comparison. Future work might focus on relating the changes in amplitude to the thickness of the PSZ and/or the soil permeability and better characterizing the velocity profile of the PSZ.

Conclusions

Although temporal changes in the height of the water table were not imaged seismically, the data presented here show that changes in the amplitude versus offset of the TSZ reflection are observed in field data collected under different pumping stresses of an unconfined aquifer. The techniques described here may be beneficial in observing changes in saturation and water table fluctuations and may help to constrain interpretations when combined with other geophysical and hydrogeologic data. Further work is necessary to better characterize the velocity profile of the partially saturated zone.

Acknowledgments

The authors wish to thank Robert Eslick, Gerard Czarnecki, Paul Vincent, Jason Blair, and Jennifer Clark for assistance in the field and Sally Hayden for editorial assistance. This research was supported under grants DE-FG02-03ER63656 and DE-FG07-97ER14826 by the Office of Science (BER), United States Department of Energy (DOE). However, any opinions, conclusions, or recommendations expressed herein are those of the authors and do not necessarily reflect the views of DOE.

Sloan, S. D., Tsoflias, G. P., and Steeples, D. W., 2007, Shallow seismic AVO variations related to partial water saturation during a pumping test: Geophysical Research Letters, 34, L22405, doi: 10.1029/2007GL031556.

GEOPHYSICAL RESEARCH LETTERS, VOL. 34, L22405, doi:10.1029/2007GL031556, 2007

Shallow seismic AVO variations related to partial water saturation during a pumping test

Steven D. Sloan,[1] Georgios P. Tsoflias,[1] and Don W. Steeples[1]

Received 3 August 2007; revised 6 October 2007; accepted 22 October 2007; published 27 November 2007.

[1] High-resolution shallow seismic reflection experiments were conducted during and after a pumping test of an agricultural irrigation well to image the cone of depression. Although variations in the reflection time from the top of the saturated zone were not observed, amplitude-versus-offset (AVO) analysis revealed changes in reflection amplitude responses that correlate temporally and spatially to expected changes to the partially saturated zone induced by the pumping and recovery of the aquifer. The AVO responses exhibit dependence on aquifer drawdown and recovery cycles and the distance from the pumping well. We propose that near-surface soil heterogeneity and relatively rapid changes in the water table elevation during irrigation cycles caused a thickening of the partially saturated zone above the water table, which resulted in detectable changes in seismic reflection amplitudes. This study offers insights about the response of shallow seismic reflections to changes in subsurface water saturation and the potential application of seismic techniques to hydrogeophysical problems.

Citation: Sloan, S. D., G. P. Tsoflias, and D. W. Steeples (2007), Shallow seismic AVO variations related to partial water saturation during a pumping test, *Geophys. Res. Lett.*, *34*, L22405, doi:10.1029/2007GL031556.

1. Introduction

[2] Multiple attempts have been made to image the cone of depression around an agricultural pumping well using shallow seismic reflection (SSR) techniques [*Birkelo et al.*, 1987; *Johnson*, 2003; *Sloan*, 2005], however none have been successful. The study described here was intended to image the cone of depression by conducting multiple SSR surveys during and after a pumping test. Despite water table fluctuations of ~0.5 m, which were within the resolution limits, we were unable to observe temporal changes in the reflection from the top of the saturated zone (TSZ) that were attributable to pumping. However, AVO analysis of the data revealed seismic amplitude variations that correspond to differences in the applied pumping stresses and distances from the pumping well. We suggest that the thickness of the partially saturated zone (PSZ) above the water table is affected by a continuous cycle of pumping and recovery of an unconfined aquifer. Relatively rapid changes in the height of the water table in concert with small scale soil heterogeneities have caused a thickening of the PSZ, which results in detectable changes in the AVO response of the TSZ reflection. Figure 1 illustrates the zone affected by pumping where (A) represents the water table surface prior to pumping and (B) is the water table during pumping once it has reached steady-state conditions, forming the cone of depression.

[3] In order to relate the observed changes in reflection amplitude to the subsurface, we consider how the seismic properties of the subsurface might change as a result of the pumping cycles. The water table represents the fully saturated interface where water pressure is equal to atmospheric pressure. Immediately above the water table is the fully saturated capillary fringe, which underlies the PSZ. At steady-state conditions the thicknesses of the capillary fringe and PSZ are controlled by the grain size of the surrounding sediments. The enlarged section in Figure 1 depicts the increase in water saturation (S_w) from some residual value in the unsaturated zone to 100% in the fully saturated zone. During pumping, pore-bound water may remain above the drawn-down water table and as water levels return to pre-pumping conditions air can be trapped in the pore space beneath the water table. Such conditions would be expected to influence the seismic-velocity profile of the PSZ.

[4] *Knight and Nolen-Hoeksema* [1990] showed the effects of partial saturation on *P*-wave velocity (V_p) in a sandstone using two different methods of varying water saturations (Figure 2). One method increased S_w through imbibition, yielding velocities similar to those predicted by the Biot-Gassman-Domenico equations [*Domenico*, 1976] where velocities remain relatively constant with increasing saturation and increase very rapidly at saturations greater than ~90%. The second method achieved partial saturation through drainage, where velocities follow more of a curved path on the graph and increase exponentially with increased water saturation. These observations were made at the pore scale using ultra-sonic frequencies and consolidated sandstone samples under laboratory conditions. We suggest that analogous seismic velocity behavior, although not at the pore scale, will result in the PSZ from drainage and imbibition during irrigation cycles.

[5] *Mavko and Mukerji* [1998] relate this difference in velocity response to patchy and uniform saturation. They define uniform saturation as fine-scale, uniform mixing and patchy saturation as heterogeneous saturation on a coarser scale. They determined that patchy saturations always lead to higher velocities than uniform saturations. Saturation scales separating uniform from patchy behavior may be from 0.1–1 cm in the laboratory to tens of centimeters in the field.

[6] In a homogenous medium, such as a clean, well-sorted sand, water will drain evenly as the water table is lowered, resulting in a vertical translation of the PSZ [*Bevan et al.*, 2005]. However, at our field site, thin, discontinuous

---

[1] Department of Geology, University of Kansas, Lawrence, Kansas, USA.

0094-8276/07/2007GL031556$05.00

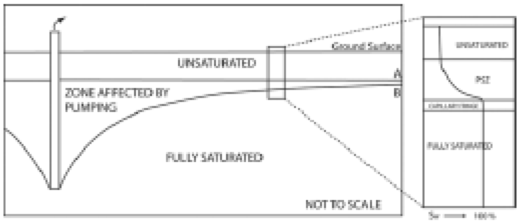

Figure 1. Illustration showing the water table before pumping (A), during pumping (B), and the zone affected by the raising and lowering of the water table. The enlarged section illustrates the soil-moisture profile.

clay layers interbedded with fine- and medium-grain sands form small scale heterogeneities. These varying near-surface soils have different field capacities, i.e. different abilities to retain moisture under gravity drainage. As the water table is drawn down, clays and silts will retain greater amounts of water than well-sorted sands causing patchy saturation. Localized areas of higher water saturation, which can be on the scale of 10 s of centimeters, will influence the seismic response. During imbibition, sediments will saturate more evenly, which is akin to uniform saturation. Although it is possible that the TSZ reflection coincides with a change in stratigraphy, we do not believe that a stratigraphic boundary is the controlling factor of the AVO response that we are observing in the data. Similar to our study, prior shallow seismic reflection experiments of fluctuating water table surfaces did not show changes in reflection times [*Birkelo et al.*, 1987; *Johnson*, 2003].

[7] We propose that we are observing a hysteretic effect analogous to that of *Knight and Nolen-Hoeksema* [1990], but on a larger scale due to patchy saturation caused by small scale subsurface heterogeneities. At the pore scale, hysteresis is possible because no interpore communication occurs with ultrasonic frequencies and seismic velocities are affected by fluid distribution [*Endres and Knight*, 1989]. At lower frequencies interpore communication does occur and the pore contents act as a single effective pore fluid [*Endres and Knight*, 1997]. Therefore a homogeneous medium will not exhibit a hysteretic velocity behavior. At our field site we suggest that lower frequencies respond to a velocity hysteretic effect caused by patchy saturations. *Endres et al.* [2000] also reported localized areas where, as the soil-moisture profile translated downward, sediments had higher water saturation and were detectable by GPR.

[8] *Sengbush et al.* [1961] describe the effects of various velocity functions on a reflected wavelet as a process of linear filtering. A sharp interface represented by a step-velocity function produces a reflection having the same waveform as the source pulse. A gradational interface represented by a ramp-velocity function produces a reflection that is the integrated source pulse. The effect of moving from a step-velocity function to a ramp-velocity function on a reflected wavelet is an overall lowering of the wavelet frequency and decrease in amplitude. Velocity changes related to imbibition would correlate with uniform saturation, approximated by a step-velocity function, and those related to drainage would correlate to patchy saturation, approximated by a ramp-velocity function.

2. Data Acquisition and Processing

[9] Common mid-point (CMP) seismic reflection surveys were conducted to image changes in the TSZ reflection during pumping of a shallow unconfined aquifer. Pre-pumping water table depth was ~4.7 m, measured at an observation well [*Sloan et al.*, 2007]. The first survey was conducted after the irrigation pump had been allowed to run continuously for three days at a rate of ~3785 L/min (1000 gal/min). Following aquifer recovery, ~18 hours after the pump was turned off, a second survey was acquired. A third survey was shot the following summer when, due to cooler temperatures, the pump had not been run for at least two weeks and water table fluctuations were limited to natural processes. The pumping well was located 5 m away from the east end of each of the surveys.

[10] Each survey was conducted using 144 Mark Products L-40A 100-Hz geophones planted at a 10-cm interval. The source was a .22-caliber rifle firing into 15-cm deep holes every 10 cm beginning and ending 5 m off of each end of the spread. Data were recorded using two Geometrics 72-channel StrataView seismographs with 24-bit A/D conversion, 256-ms record lengths, and 0.25-ms sampling interval. Acquisition parameters were identical for each survey. Data were processed using commonly applied techniques for AVO data, as described by *Castagna* [1995] and *Resnick* [1995]. Processing included geometry definition, elevation corrections, spherical spreading corrections, *f-k* filtering, CMP sorting, NMO corrections, and partial stacking.

3. AVO Analysis

[11] Although AVO methods and techniques are widely used in hydrocarbon exploration, little work has been done in shallow subsurface investigations. The near surface presents complexities that must be overcome to provide a data set of high enough quality to perform AVO analysis. The airwave, refractions, direct wave, and surface waves often prevent a wide range of offsets from being used due to

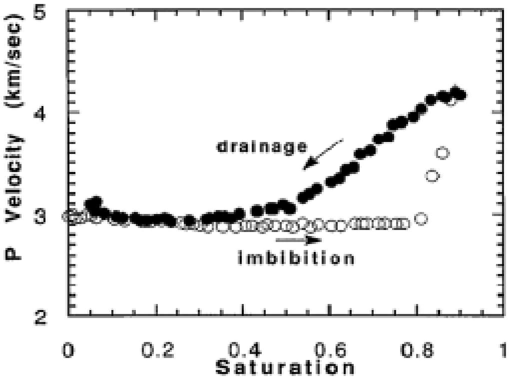

Figure 2. Plot displaying the changes in *P*-wave velocity with water saturation (from *Knight and Nolen-Hoeksema* [1990]).

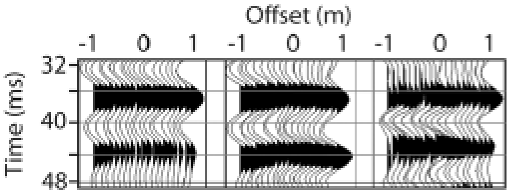

Figure 3. CMP supergathers from data collected (left) during pumping, (middle) during recovery, and (right) with no pumping.

interference with the reflections. Despite the associated problems, there are a few examples of SSR AVO studies [*Bradford et al.*, 1997; *Bachrach and Mukerji*, 2001; *Waddell et al.*, 2001]. *Bachrach and Mukerji* [2001] showed that the unsaturated/saturated sand interface exhibits an increase in reflection amplitude with increasing offset.

[12] Supergathers were created by partially stacking the common offsets of five adjacent CMP gathers (Figure 3). Each CMP gather was separated by 5 cm, covering a distance of 20 cm. Each of the three data sets was normalized to its respective RMS amplitude. The RMS amplitudes were calculated for each trace from a window around the TSZ reflection from 32–48 ms for offsets ranging from −1 to +1 m in 10-cm increments. The supergathers displayed in Figure 3 show data collected during pumping (drainage), after aquifer recovery (imbibition), and from the following summer when the pump was not used. The TSZ reflection consistently occurs at ~35 ms; however, the data collected during drainage (left) exhibit noticeably lower amplitudes and lower frequencies.

[13] Figures 4a, 4b, and 4c show plots of the relative amplitude versus CMP offset within a supergather for a range of distances from the pumping well during drainage and imbibition. The AVO response is represented by exponential curves fit to the data points using least-squares regression. For all distances from the pumping well, imbibition reflection amplitudes are greater than drainage reflection amplitudes, and reflection amplitudes increase overall with increasing offset. As the distance of the CMP supergather from the pumping well increases, the relative amplitude of each curve increases. Furthermore, the separation between the two amplitude curves in each plot is greatest near the pumping well. This effect is illustrated in Figure 4d using the difference of the two curves for each distance.

[14] Figures 4e and 4f show plots of relative amplitude versus CMP offset within a supergather for a range of distances from the pumping well for data collected during drainage and data from the following summer when the pump had not been used, respectively. During drainage, the relative amplitudes increase as the distance from the pumping well increases. In comparison, the amplitudes of the data acquired without pumping remain relatively consistent despite changes in the distance from the pumping well and display higher amplitudes than the drainage data.

4. Discussion

[15] The graphs in Figures 4a–4f show that seismic data collected during drainage exhibit lower amplitudes than those acquired both during imbibition and at no pumping conditions. This seismic amplitude relationship to pumping condition is observed at all distances from the pumping well and at all offsets within the supergathers. This observation is consistent with the seismic response expected from a patchy saturation velocity profile formed by drainage. Furthermore, the lowest amplitudes are observed at the supergather closest to the pumping well. As the distance of the supergather from the pumping well increases, so do the amplitudes, suggesting an increasingly sharper velocity transition away from the pumping well. As illustrated in Figure 1, drawdown will decrease as the distance from the pumping well increases. This response is illustrated by Figure 4d where as the distance from the pumping well increases, the separation between the curves decreases. Thus, as the distance from the pumping well increases, both hydrologic and geophysical responses decrease, suggesting a causal relationship. Figure 4e shows that as the distance from the pumping well increases, the amplitude increases while the pump is running. However, when the pump was not used and the water table was not drawn down, as in Figure 4f, the curves are clustered together and display higher amplitudes. These results further suggest that changes in the thickness of the PSZ due to elevation changes of the water table result in corresponding detectable seismic reflection amplitude changes.

[16] At undisturbed water table conditions (no pumping) it is expected that the PSZ will exhibit the most abrupt seismic velocity transition from unsaturated to fully-saturated conditions. As the water table is drawn down (drainage) and the thickness of the PSZ increases, the slope of the seismic velocity profile will also increase. The increase in the slope of the ramp-velocity function leads to lower seismic reflection amplitudes and frequencies [*Sengbush et al.*, 1961]. As the water table returns to equilibrium (imbibition) and the thickness of the PSZ decreases, the slope of the velocity ramp also decreases. This leads to an increase in reflection amplitudes and frequencies relative to those during drainage. The same PSZ disturbance behavior explains the seismic response as the distance from the pumping well increases and the drawdown of the water table decreases. At distances farther from the pumping well there are smaller changes in the elevation of the water table and a lesser effect on the thickness of the PSZ, which would lead to increasingly higher reflection amplitudes at farther distances. The observations of shallow seismic reflection amplitude response during pumping cycles are in agreement with the suggested PSZ thickness changes and analogous to the seismic velocity response to varying water saturation presented by *Knight and Nolen-Hoeksema* [1990] and *Mavko and Mukerji* [1998].

[17] Changes in the TSZ reflection amplitude may serve as an indicator of permeability near the water table. A more homogeneous and permeable material, such as a clean or well-sorted sand, would allow more uniform drainage during drawdown. Uniform drainage would have a lesser or no effect on the thickness of the PSZ, resulting in a smaller change in seismic amplitude. Conversely, lowering the water table in poorly-sorted heterogeneous soils would increase the thickness of the PSZ and exhibit a larger variation in amplitude. The results of this study could yield a more accurate representation of subsurface hydraulic

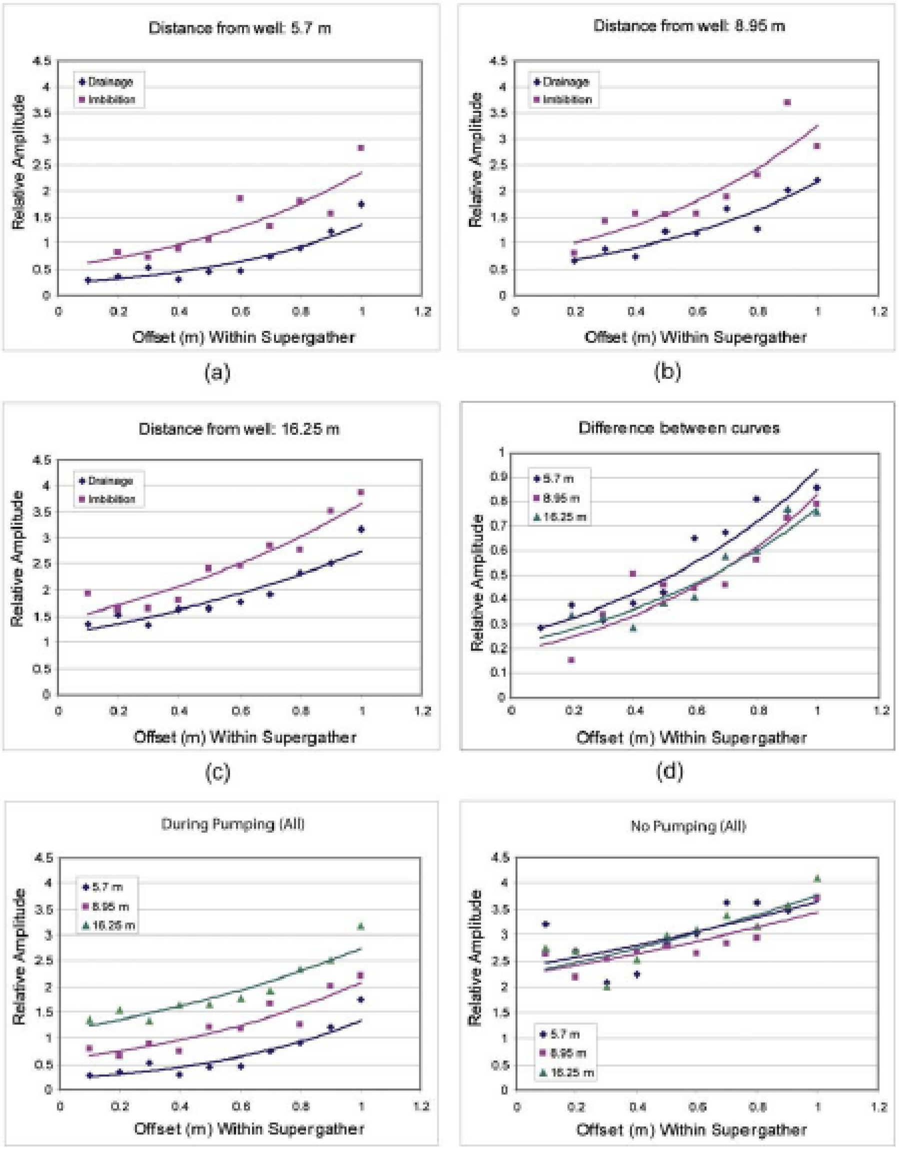

(a) (b)

(c) (d)

(e) (f)

Figure 4. (a, b, c) AVO curves from data collected during (drainage) and after (imbibition) pumping for CMP supergathers at three different distances from the pumping well. (d) The difference between the two curves for each distance. AVO curves for all data collected (e) during pumping and (f) without any pumping.

properties when used in tandem with techniques that are sensitive to pore fluids, such as ground-penetrating radar and electrical methods. These techniques may also prove useful in understanding changes in water table and saturation fluctuations, which may be desirable in time-lapse studies at contaminated sites where non-invasive techniques might be necessary. Future work will focus on quantitatively relating the changes in amplitude to the thickness of the PSZ by monitoring soil moisture content.

5. Conclusions

[18] Imaging the cone of depression using shallow seismic reflection during a pumping test may be possible; however, it has not been documented in the literature to our knowledge, despite several attempts. Without prolonged drainage time, the length of which will vary with subsurface properties, some amount of pore-bound water will remain above the drawn-down water table. If there is a sufficient amount of water to produce a seismic reflection, temporal changes in the TSZ reflection will not be observed.

[19] The data presented here show that detectable changes in the AVO response of the TSZ reflection are observed in field data during a pumping test of an unconfined aquifer. The AVO responses correspond to different pumping conditions and varying distances from the pumping well, which can be explained by changes in partial water saturation above the water table. We show that lower seismic amplitudes observed during pumping (drainage) are consistent with the expected response of a thicker partially saturated zone. Recovery of the water table (imbibition) results in higher seismic amplitudes indicative of a thinner partially saturated zone. The techniques described here may be beneficial in observing changes in saturation and water table fluctuations and may help to constrain interpretations when combined with other geophysical and hydrogeologic data.

[20] **Acknowledgments.** The authors wish to thank Robert Eslick, Gerard Czarnecki, Paul Vincent, Jason Blair, and Jennifer Clark for field support, and Sally Hayden for editorial assistance. This research was supported under grants DE-FG02-03ER63656 and DE-FG07-97ER14826, Environmental Management Science Program, Office of Science and Technology, Office of Environmental Management, United States Department of Energy (DOE). However, any opinions, conclusions, or recommendations expressed herein are those of the authors and do not necessarily reflect the views of DOE.

References

Bachrach, R., and T. Mukerji (2001), AVO analysis of shallow seismic data: Feasibility and analysis of 2D and 3D ultra shallow reflections, paper presented at Symposium on the Application of Geophysics to Engineering and Environmental Problems, Environ. and Eng. Geophys. Soc., Denver, Colo., 4–7 Mar.

Bevan, M. J., A. L. Endres, D. L. Rudolph, and G. Parkin (2005), A field scale study of pumping-induced drainage and recovery in an unconfined aquifer, *J. Hydrol.*, *315*, 52–70.

Birkelo, B. A., D. W. Steeples, R. D. Miller, and M. A. Sophocleous (1987), Seismic reflection study of a shallow aquifer during a pumping test, *Groundwater*, *25*, 703–709.

Bradford, J. H., D. S. Sawyer, and C. A. Zelt (1997), AVO analysis of low velocity, shallow sands (<50 m), 67th Annual Meeting, Soc. of Explor. Geophys., Dallas, Tex., 2–6 Nov.

Castagna, J. P. (1995), AVO Analysis-tutorial and review, in *Offset-Dependent Reflectivity–Theory and Practice of AVO Analysis*, edited by J. P. Castagna and M. M. Backus, pp. 3–36, Soc. Explor. of Geophys., Tulsa, Okla.

Domenico, S. N. (1976), Effect of brine-gas mixture on velocity in an unconsolidated sand reservoir, *Geophysics*, *41*, 882–894.

Endres, A. L., and R. Knight (1989), The effect of microscopic fluid distribution on elastic wave velocities, *Log Anal.*, *30*, 437–445.

Endres, A. L., and R. Knight (1997), Incorporating pore geometry and fluid pressure communication into modeling the elastic behavior of porous rocks, *Geophysics*, *62*, 106–117.

Endres, A. L., W. P. Clement, and D. L. Rudolph (2000), Ground penetrating radar imaging of an aquifer during a pumping test, *Ground Water*, *38*, 566–576.

Johnson, E. J. (2003), Imaging the cone of depression around a pumping well using shallow seismic reflection, M.S. thesis, 100 pp., Univ. of Kans., Lawrence.

Knight, R., and R. Nolen-Hoeksema (1990), A laboratory study of the dependence of elastic wave velocities on pore scale fluid distribution, *Geophys. Res. Lett.*, *17*, 1529–1532.

Mavko, G., and T. Mukerji (1998), Bounds on low-frequency seismic velocities in partially saturated rocks, *Geophysics*, *63*, 918–924.

Resnick, J. R. (1995), Seismic data processing for AVO and AVA analysis, in *Offset-Dependent Reflectivity–Theory and Practice of AVO Analysis*, edited by J. P. Castagna and M. M. Backus, pp. 175–189, Soc. of Explor. Geophys., Tulsa, Okla.

Sengbush, R. L., P. L. Lawrence, and F. J. McDonal (1961), Interpretation of synthetic seismograms, *Geophysics*, *24*, 138–157.

Sloan, S. D. (2005), The combined use of shallow seismic reflection and GPR techniques near Clay Center, KS, M.S. thesis, 46 pp., Univ. of Kans., Lawrence.

Sloan, S. D., G. P. Tsoflias, D. W. Steeples, and P. D. Vincent (2007), High-resolution ultra-shallow subsurface imaging by integrating near-surface seismic reflection and ground-penetrating radar data in the depth domain, *J. Appl. Geophys.*, *62*, 281–286.

Waddell, M. G., W. J. Domoracki, and T. J. Temples (2001), Use of seismic reflection amplitude versus offset (AVO) techniques to image dense nonaqueous phase liquids (DNAPL), Symposium on the Application of Geophysics to Environmental and Engineering Problems, Environ. and Eng. Geophys. Soc., Denver, Colo., 4–7 Mar.

S. D. Sloan, D. W. Steeples, and G. P. Tsoflias, Department of Geology, University of Kansas, Room 120 Lindley Hall, 1475 Jayhawk Boulevard, Lawrence, KS 66045, USA. (sloansd@ku.edu; don@ku.edu; tsoflias@ku.edu)

Sloan, S. D., Steeples, D. W., and Malin, P. E., 2008, Acquisition and processing pitfall associated with clipping near-surface seismic reflection traces: Geophysics, 73, W1-W5.

GEOPHYSICS, VOL. 73, NO. 1 (JANUARY-FEBRUARY 2008); P. W1–W5, 6 FIGS., 1 TABLE.
10.1190/1.2807051

Acquisition and processing pitfall associated with clipping near-surface seismic reflection traces

Steven D. Sloan[1], Don W. Steeples[1], and Peter E. Malin[2]

ABSTRACT

The processing of clipped seismic traces may produce high-frequency wavelets that can be misinterpreted as reflections in filtered shot gathers and common-midpoint (CMP) stacked sections. To illustrate this effect, a near-surface CMP seismic reflection survey was conducted using two sources to compare the effects of various band-pass frequency filters on clipped traces. An event observed in the clipped data set replicated the frequency of the filter operators applied, similar to the effect of convolving a boxcar function with the filter operator. The anomaly exhibited hyperbolic moveout and imitated a reflection during the processing stages. The hyperbolic event was flattened by NMO corrections chosen for the target reflection, and it stacked in as a coherent event in the final section. Clipped data should be removed or corrected before processing to prevent misinterpreting high-frequency reflection artifacts in trace gathers and stacked sections.

INTRODUCTION

Shallow seismic reflection data are commonly collected by using dense receiver and source spacings, which are required to image shallow reflectors and to prevent spatial aliasing of data. The close proximity of the source and the nearest receivers resulting from the short offsets can result in clipped traces in which peaks and/or troughs have been squared off, depending on the energy of the source selected. Ultrashallow surveys might require a receiver spacing of 20 cm or less, which can result in a relatively high percentage of clipped traces in the data set (Figure 1). This article addresses a potential pitfall associated with data acquisition and processing in which clipped surface waves can be misinterpreted as high-frequency reflections on filtered shot gathers and on stacked sections.

When clipped seismic traces are processed digitally, high-frequency artifacts can appear as reflections in field records and stacked sections. Galbraith and MacMinn (1982) observe the effects of deconvolution on clipped traces, noting that each clipped peak or trough is split into two or more individual peaks and troughs after deconvolution. This leads to the presence of anomalous peaks in processed stacked sections that could lead to their being misinterpreted as a stratigraphic feature or other anomaly. The presence of anomalous peaks is not a problem if clipped traces are corrected or removed from the data set. Possible solutions for eliminating gain errors such as clipping include muting, filtering, polynomial interpolation (Galbraith and MacMinn, 1982), minimum error energy operators (MEEOs) (Nyman, 1977; Galbraith and MacMinn, 1982), and adaptive lattice filters (Khan, 1982).

Muting can eliminate the clipped portion of traces but also can be tedious and time-consuming, especially for large data sets. Filtering can smooth gain-associated errors if they are not too severe; however, this method can produce additional problems for clipped traces. Nyman (1977) discusses the use of MEEOs for error correction. Galbraith and MacMinn (1982) determine that the MEEO method is more effective at correcting gain-associated errors and clipping than polynomial interpolation is. Yet another method, described by Khan (1982), uses adaptive lattice filters to correct errors.

Although our article points out methods for correcting clipping errors, the primary focus is to show problems that can propagate through the data-processing stages and negatively impact data interpretation if clipped traces are not recognized and corrected or removed.

DATA ACQUISITION AND PROCESSING

To illustrate how high-pass filtering of clipped data can produce artifacts on stacked common-midpoint (CMP) data, we conducted two CMP seismic reflection surveys using identical acquisition parameters, with the exception of the source. The receiver line consisted of 144 Mark Products L40-A 100-Hz vertical geophones planted with a 10-cm interval. Data were recorded using a 0.125-ms sampling interval for 128 ms by two 72-channel Geometrics StrataView seismographs with 24-bit analog-to-digital (A/D) conversion.

Manuscript received by the Editor 2 May 2007; revised manuscript received 25 July 2007; published online 29 November 2007.

[1] The University of Kansas, Department of Geology, Lawrence, Kansas, U.S.A. E-mail: sloansd@ku.edu; don@ku.edu.
[2] University of Auckland, Institute of Earth Science and Engineering, Auckland, New Zealand. E-mail: p.malin@auckland.ac.nz.

The first survey was collected using a .22-caliber rifle firing long-rifle ammunition and a shot interval of 20 cm. The second survey was conducted in the same manner using a .223-caliber rifle with a 55-grain bullet as the source. Data processing for the two data sets was identical and included geometry definition, CMP sorting, NMO corrections, CMP stacking, band-pass filtering, and automatic gain control (AGC) to produce a brute stack. Early muting was not applied, which allowed the clipped-trace effects to be seen on the entire shot records.

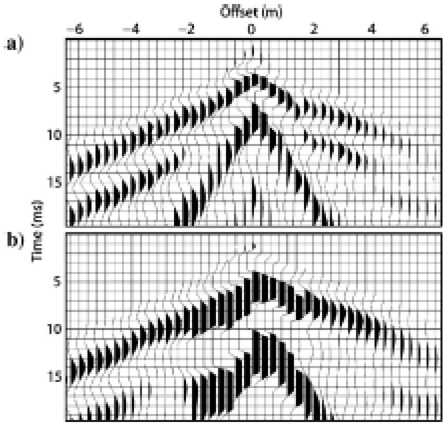

Figure 1. Field files acquired at the same source location using (a) a .22-caliber and (b) a .223-caliber rifle. (a) Clipped traces are out to 0.6 m from the source. (b) The clipping reaches as far as 2.0 m. The data are presented without any filtering, although a 9-dB attenuation was applied to prevent trace overlap.

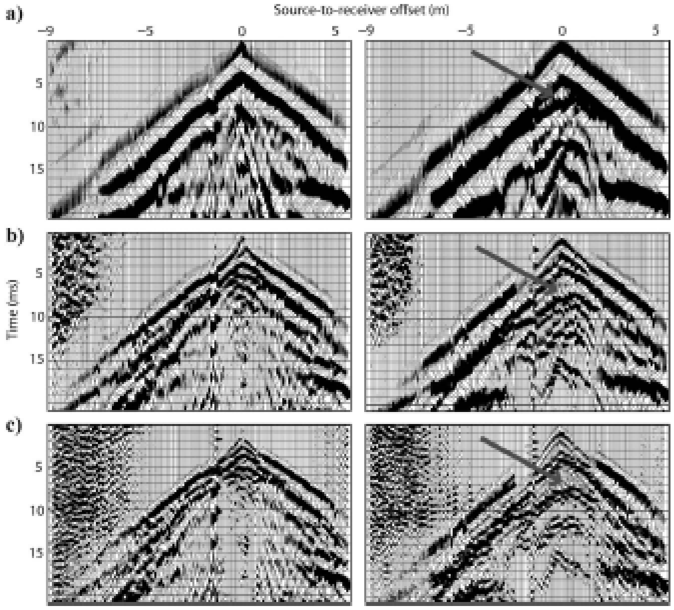

Figure 2. Field records collected with the .22-caliber rifle (left) and .223-caliber rifle (right) at the same location. Data are displayed with band-pass filters of (a) 200–500, (b) 600–900, and (c) 1000–1300 Hz.

RESULTS

Figure 2 shows shot records from a single source location collected with the .22- and .223-caliber rifles with various band-pass filters applied. The target reflection from the water table is located at approximately 16 ms. Although the records are similar, the second arrival in the data collected with the .223-caliber rifle exhibits a separation at approximately 6 ms (indicated by the arrow, Figure 2) that is not seen in the data collected by the .22-caliber rifle. This separation becomes more pronounced as the frequency of the applied filter increases.

This event, which also appears to have a hyperbolic moveout, increases in frequency as the filter's frequency increases, without becoming distorted or decreasing in amplitude. The hyperbolic appearance could be mistaken for a very shallow reflection and, if left in the data set, might stack coherently. Hyperbola fitting of this pseudoreflection yields a velocity of approximately 300 m/s, slower than the velocities of both the water-table reflection (450–550 m/s) and the direct wave (400 m/s).

Velocity picks obtained from the water-table reflection at every fifth CMP location, ranging from 450 to 550 m/s, were used to apply NMO corrections to both data sets. Figure 3 shows the effects of the NMO corrections on the pseudoreflection in CMP gathers from the .22-caliber and .223-caliber data sets at a coincident location. The pseudoreflection event at about 7 ms has been flattened and is coherent in the .223 data but not in the CMP gather of the .22 data.

Figure 4 shows the brute stacks of both the .22 and .223 data with clipped traces included (Figure 4a), clipped portions surgically muted (Figure 4b), and clipped traces removed entirely (Figure 4c). The data are displayed with a 600–900-Hz band-pass filter with 18-dB/octave roll-off slopes and no mutes. A coherent event at approximately 7 ms in the .223 stack, indicated by the arrow in Figure 4a, is not present in the .22 stack. This event corresponds to the event observed in the field records and NMO-corrected CMP gathers. Clipped traces in the .22 data ranged from ±0.6 m source-to-receiver offset represented by 13 traces, or 9% of the 144. The .223 data overpowered the geophones as far as 2.0 m from the source, representing 41 of the 144 traces (28%) collected at each source location (Figure 1).

DISCUSSION

Figure 5 illustrates the effects of various band-pass filters with increasing frequency on an unclipped and clipped seismic trace and the corresponding amplitude spectra. As filters with higher band-pass frequency are applied to the unclipped trace, high-frequency ring is introduced. The traces are recognizably noisier, and the signal is diminished because of the decreasing bandwidth. However, when the same filters are applied to a clipped trace, the filter operator is replicated at the squared wavelet corners where the clipping occurs.

The largest peaks and troughs in each of the filtered clipped traces occur at the same position as the squared corners where clipping occurs in the original trace, as indicated by the shaded area. This is essentially equivalent to convolving the filter operator with a boxcar function. Ringing does not occur in the filtered clipped traces when the frequency of the filter operator is increased, because the bandwidth increases artificially as additional cycles are introduced where clipping occurs.

Corresponding amplitude spectra are shown for traces a, c, g, k, and o. As the frequency of the filter is increased, the spectra of the unclipped traces also become increasingly noisier. Those of the clipped traces retain the same shape and smoothness across the frequency axis. Table 1 shows the passband of the filters applied to each trace.

Data demonstrate the effects of some of the processing steps that may prevent this problem by comparing brute stacks, including the clipped traces (Figure 4a), the clipped data surgically muted (Figure

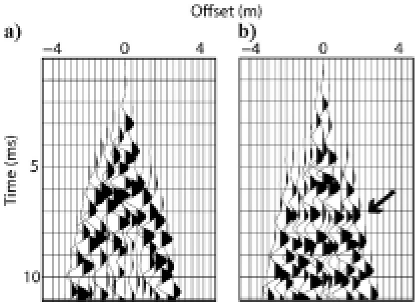

Figure 3. Coincident NMO-corrected CMP gathers from the (a) .22-caliber and (b) .223-caliber data sets. The event near 7 ms, indicated by the arrow, has become flattened and coherent after NMO corrections were applied with a 15% stretch mute, using velocity picks from the targeted water-table reflection. Data are displayed with a 600–900-Hz band-pass filter without mutes or gains applied.

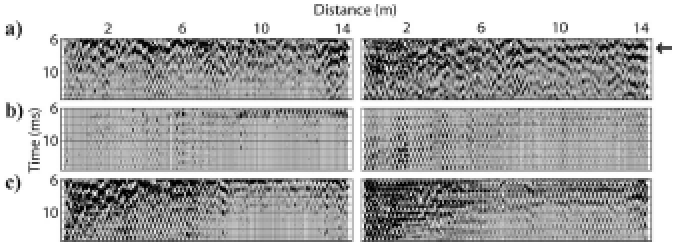

Figure 4. Brute stacks of the .22-caliber (left) and .223-caliber (right) data. Both data sets have been processed identically for comparison purposes. (a) A coherent event near 7 ms in the .223 data, indicated by the arrow, is not evident in the .22 data. (b) A surgical mute applied to remove the clipped portion of the traces. (c) The brute stacks after the clipped traces have been removed entirely.

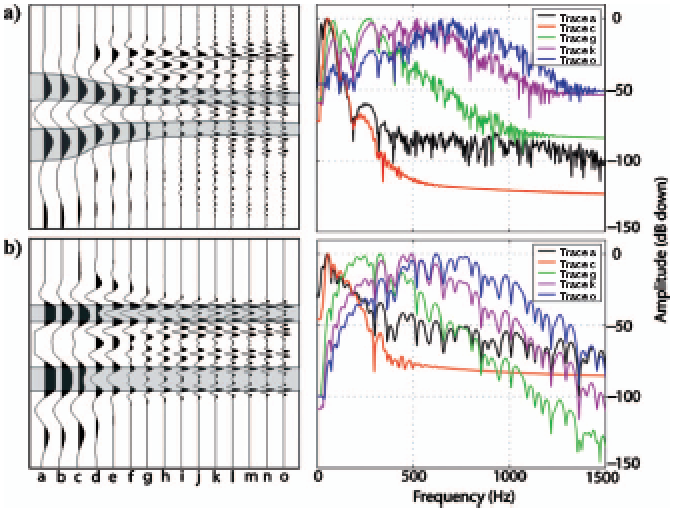

Figure 5. (a) An unclipped and (b) a clipped trace with various band-pass filters applied, increasing in frequency (traces a through o) from left to right. The corresponding amplitude spectra are shown on the right. View (a) begins to ring at higher frequencies. In (b), the wavelet does not show the same ring but appears to increase in frequency as higher-frequency band-pass filters are applied to it. The high-frequency wavelet seen in (b) is the filter operator convolved with the corners at which clipping occurs in the data. Filter specifications for each trace are described in Table 1.

4b), and the clipped traces removed (Figure 4c). As seen in Figure 4a, processing the clipped traces can result in artifacts that appear as high-frequency reflections, which can lead to misinterpretations. Surgically muting the clipped portion of the traces, as in Figure 4b, effectively eliminates the artifact; however, this method may be time-consuming and tedious. The most reliable way is to omit the clipped traces from the data set, as illustrated in Figure 4c.

Table 1. Band-pass filters (Hertz) applied to each trace in Figure 5. Filters were applied with 18-dB/octave roll-off slopes.

Trace	Filter passband (Hz)
a	N/A
b	0–300
c	100–400
d	200–500
e	300–600
f	400–700
g	500–800
h	600–900
i	700–1000
j	800–1100
k	900–1200
l	1000–1300
m	1100–1400
n	1200–1500
o	1300–1600

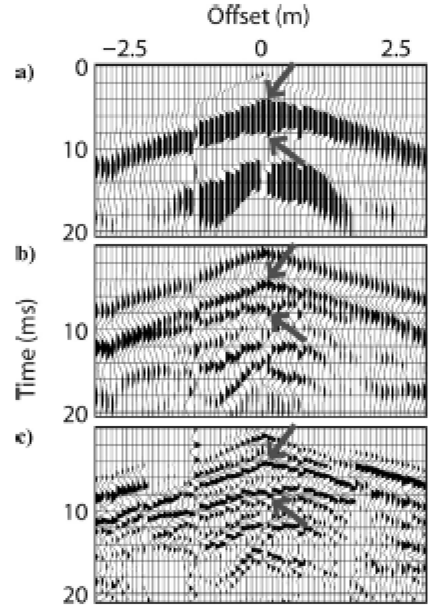

Figure 6. The same shot gather is shown with (a) no filtering, (b) a 200–500-Hz band-pass filter, and (c) a 600–900-Hz band-pass filter. Arrows point to the same event as it changes with each filter. Filters were applied with 18-dB/octave roll-off slopes. The top shot gather has a 9-dB attenuation applied to prevent trace overlap.

Omitting the clipped traces may be fast and reliable. However, in the case with the .223-caliber rifle, that would reduce the total number of traces by about 30% and would lower the fold significantly. In that case, an early mute designed to delete clipped data might be the most efficient method for removal because an early mute is necessary to remove the direct and refracted waves and would be applied to the data anyway. If removing the traces or muting is not a viable option, the minimum-error energy operator reported by Nyman (1977) and discussed by Galbraith and MacMinn (1982) could be used to attempt to correct clipping errors.

The hyperbolic appearance of the reflection event is from a combination of clipping and frequency filtering. Figure 6 illustrates the same shot gather with no filter applied (Figure 6a), a 200–500-Hz band-pass filter (Figure 6b), and a 600–900-Hz band-pass filter (Figure 6c). The traces in the shot gather behave in the same manner as those described in Figure 5.

The event indicated by the arrows in the raw shot gather is linear. However, as frequency filters are applied, the squared corners become individual peaks and troughs. That creates the separation observed in the same event in the shot gathers shown in Figure 6b and c, where the top of the event remains linear and the bottom appears hyperbolic. The separation appears to enlarge with increasing frequency of the filters, but the separated events are actually at the same times in each gather, as indicated by arrows. As amplitudes decrease with offset and clipping diminishes, the clipped corners and filter-induced peaks come closer together, giving the event its hyperbolic appearance.

CONCLUSION

The processing of clipped seismic traces has the potential of creating artifacts that could be misinterpreted as high-frequency reflections in shot gathers and stacked sections. As filters of increasingly higher band-pass frequency are applied to an unclipped trace, the high-frequency noise level increases because of the decreased bandwidth. In contrast, the frequency of a clipped trace mirrors that of the filter applied to it by replicating the filter operator. It will continue to increase in frequency without distortion or without adding high-frequency noise to the wavelet, and it exhibits no change in the bandwidth.

Clipped data should be removed by muting or trace editing or they should be corrected during the preprocessing stage to avoid the problems described. Field testing of potential seismic sources prior to conducting a survey is recommended and can prevent a problem by selecting the source with the appropriate energy to meet the survey objectives. Clipping can occur as a result of physical limitations of geophones or by setting all the bits that can be recorded by a digital sample to ones. It might be beneficial to check the data for digital samples which are the largest possible number that can come from the A/D converter, possibly indicating the presence of clipped traces.

As with all seismic projects, care should be taken during the processing stages to ensure that quality control is maintained and that the processing steps or selected parameters do not introduce unwanted artifacts into the data set.

ACKNOWLEDGMENTS

The authors would like to thank Paul Vincent, Robert Eslick, Gerard Czarnecki, and George Tsoflias for their time in the field; Sally Hayden for editorial assistance; and the editors and reviewers for their constructive comments. This research was supported by the Office of Science (BER), U. S. Department of Energy, grant DE-FG02-03ER63656. However, any opinions, conclusions, or recommendations expressed herein are those of the authors and do not necessarily reflect the views of the DOE.

REFERENCES

Galbraith, M., and C. L. MacMinn, 1982, Error correction in field recorded seismic data: Journal of the Canadian Society of Exploration Geophysicists, 18, 23–33.

Khan, R. H., 1982, Seismic data error correction using adaptive lattice filters: 52nd Annual International Meeting, SEG, Expanded Abstracts, 124–126.

Nyman, D., 1977, The interpolation error operator, Time series error detection and correction: Geophysics, 42, 773–777.

Sloan, S. D., Steeples, D. W., and Tsoflias, G. P., 2008, Imaging a shallow paleo-channel using 3D ultra-shallow seismic reflection methods: SAGEEP, 21, 568-576.

Presented at the 21st Annual Symposium on the Application of Geophysics to Engineering and Environmental Problems (SAGEEP) in Philadelphia, Pennsylvania.

IMAGING A SHALLOW PALEO-CHANNEL USING 3D ULTRA-SHALLOW SEISMIC REFLECTION METHODS

Steven D. Sloan, University of Kansas, Department of Geology, Lawrence, KS
Don W. Steeples, University of Kansas, Department of Geology, Lawrence, KS
Georgios P. Tsoflias, University of Kansas, Department of Geology, Lawrence, KS

Abstract

A 3D ultra-shallow seismic-reflection survey was conducted to image a shallow paleo-channel at a field site located near Lawrence, KS. An orthogonal survey design was used, with a patch consisting of 4 receiver lines with 48 receivers each and 12 source lines with 16 source locations each. The source and receiver intervals were 0.5 m, and the source line and receiver line intervals were 2 m. The survey design resulted in a total fold of 48, covering an area of 15.5 m x 35.5 m. Large variations in velocity were present, ranging from 300–600 m/s laterally and 300–1650 m/s vertically. As normal moveout corrections can not account for intersecting reflection hyperbolae due to large vertical velocity gradients, the data were processed by extracting offset-dependent subsets based on the optimum window for each reflection. The subsets were NMO corrected independently and stacked together using conventional 3D processing techniques. Despite the large lateral and vertical velocity variations, we were successful in imaging the water table, a paleo-channel, and bedrock located at depths of ~5, 7, and 16 m, respectively. Results of the 3D survey are in agreement with previous studies conducted at the site.

Introduction

There are multiple examples of three-dimensional (3D) shallow seismic reflection (SSR) surveys in the literature (Lanz et al., 1996; Buker et al., 1998; Buker et al., 2000; Spitzer et al., 2003), but they are still relatively uncommon and 3D ultra-shallow seismic reflection (USR) surveys are even harder to come by (Bachrach and Mukerji, 2004a,b). The dense source and receiver spacings necessary to properly sample the wavefield in the shallow subsurface quickly drive acquisition-related costs up as target depth decreases and increases exponentially faster when working in three dimensions. Although two-dimensional (2D) data are less cost- and labor-intensive to acquire, 3D SSR data can yield more accurate subsurface images and avoid artifacts and misinterpretations caused by out-of-plane reflections (Lanz et al., 1996).

The test site is an open field located several miles south of Lawrence, KS (Figure 1) near the Wakarusa River. Two-dimensional (2D) surveys previously acquired at the test site have imaged a channel feature at ~7 m depth, which coincides with a linear surface expression that is lower in elevation than the surrounding area. The objectives of the study presented here were to image multiple reflectors less than 20 m deep, including the top of the saturated zone (TSZ), the paleo-channel, and bedrock using 3D USR techniques. A small 3D USR survey was designed and acquired, covering an area of 15.5 m by 35.5 m. Data were processed using commonly applied SSR processing techniques.

One of the challenges encountered during processing is the presence of a large vertical velocity gradient. The negative effects of large vertical velocity gradients on normal-moveout (NMO) corrections have been demonstrated (Bradford, 2002; Bradford and Sawyer, 2002; Miller and Xia, 1998). Bradford (2002) and Bradford and Sawyer (2002) showed that depth estimates calculated using interval velocities determined by the Dix equation may exhibit an error of 10-100%. Prestack depth migration (PSDM) was found to produce a more accurate image at their test sites.

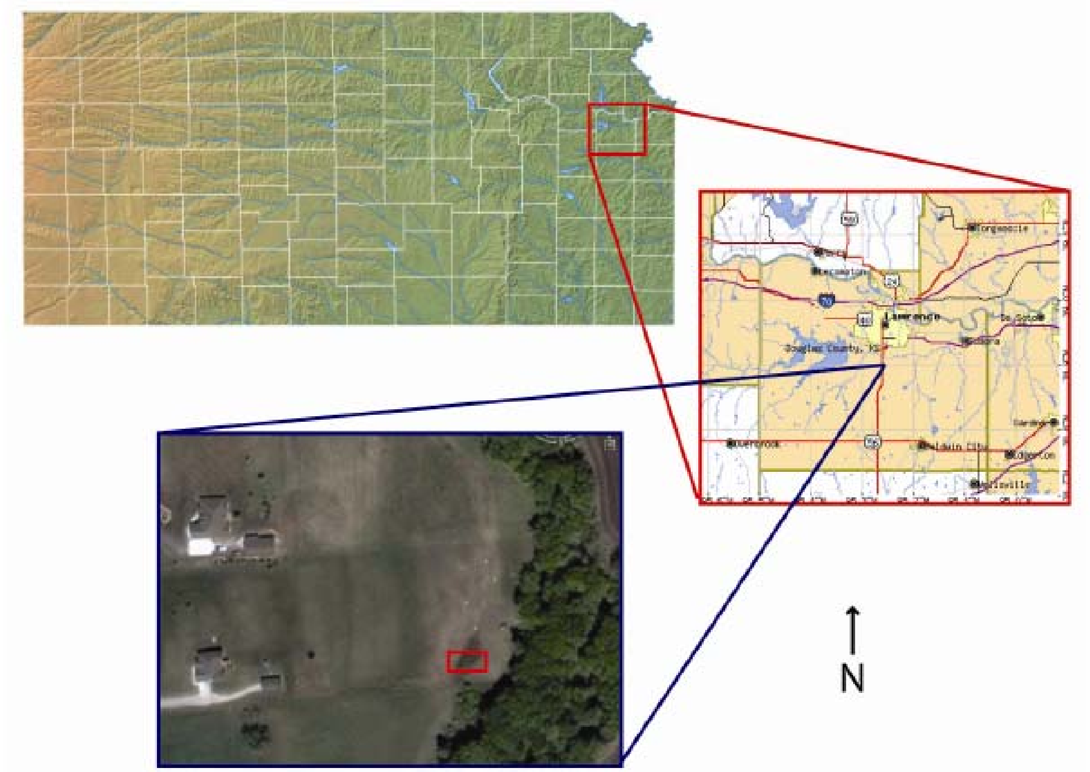

Figure 1: Site map indicating the location of the field site and the position of the survey, which is bounded by the red box. Note the N-S trending surface feature perpendicular to the survey. The back of the property is bounded by a creek, indicated by the wooded area on the aerial photograph.

Miller and Xia (1998) demonstrated the effects of NMO corrections on intersecting reflection hyperbolae due to large vertical velocity gradients. Effects such as stretch, sample reversion, sample compression, wavelet smear, and duplicate wavelet mapping require severe stretch mutes to prevent processing artifacts and a decrease in the signal-to-noise ratio (S/N) (Figure 2). Such severe muting may ultimately lead to degraded stacked sections. The authors successfully employed an optimum-window based processing scheme where reflections were segregated by offset and processed independently, resulting in a more accurate stack than that produced using a multiple-velocity NMO correction. NMO correction processes are not perfect and PSDM processing may be ideal, however many groups may not have the necessary software or computer code or resources to run it. We processed the data using a scheme similar to that described by Miller and Xia (1998).

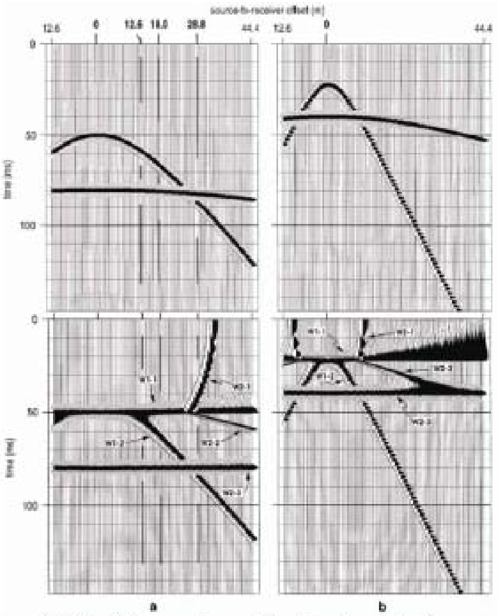

Figure 2: NMO corrections applied to intersecting reflection hyperbolae result in undesirable noise and artifacts that require severe stretch mutes to account for (modified from Miller and Xia, 1998).

Survey Design & Acquisition Parameters

An orthogonal survey design was employed with a patch consisting of four receiver lines (RLs), with 48 receivers each, and twelve source lines (SLs), with 16 source points each (Figure 3). The receiver and source line intervals (RLI, SLI) were both 2 m with receiver and source intervals (RI, SI) of 0.5 m. Each patch consisted of 192 shots, after which the patch was rolled. There were a total of six patch locations, including two lateral passes. Three patches were used in the first lateral pass, rolling two RLs each time in the crossline direction (S-N). The patch was then rolled in the inline direction (E) by half of the RL length and the second lateral pass was made in the opposite direction (N-S). This design led to a total fold of 48. Minimum and maximum recorded offsets were 0.35 and 23.11 m, respectively. The patch aspect ratio is ~1:6, leading to an offset distribution shifted towards the near offsets and an azimuthal bias along the long axis (Figure 3). The survey was acquired in ~10 hours with an eight-person crew and a total of 1152 recorded shots. The limiting factor ended up being the amount of time required to punch the holes for the source.

Common midpoint (CMP) data were collected using 192 (4x48) Mark Products L-40A 100-Hz vertical-component geophones. The source was a .22-caliber rifle firing short ammunition into ~15-cm deep pre-punched holes. Data were recorded using a 96-channel Bison and two 72-channel Geometrics StrataView seismographs with 24-bit A/D conversion. The sampling interval was 0.25 ms for 256 ms. Elevation data were also collected.

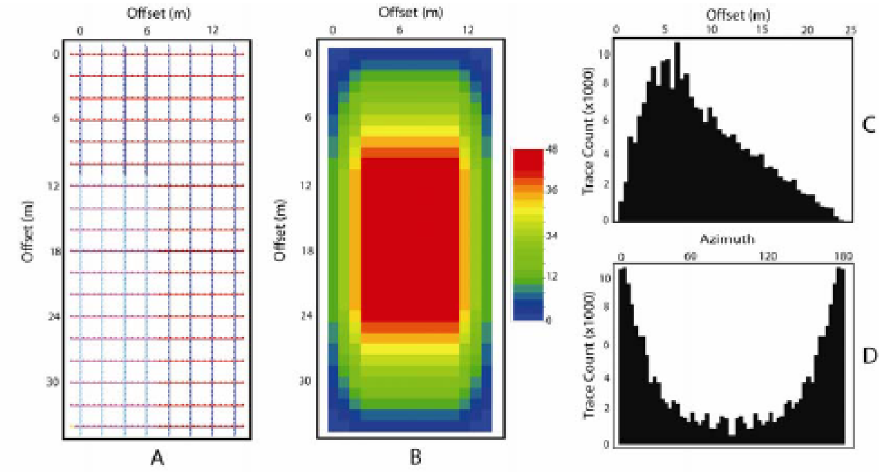

Figure 3: Survey design and attributes. (A) shows the receiver (blue) and source line (red) layout and the live patch (light blue and pink). (B) illustrates the resulting fold diagram, reaching a total fold of 48. (C) and (D) depict the trace counts for offset and azimuth, respectively, for the survey.

Data Processing

Data were processed using commonly applied techniques as described in Table 1. The data set was binned (0.25 x 0.25 m) and processed in its entirety through CMP sorting. At this point the data were divided into three subsets. Subset 1 (S1) includes the TSZ reflection ranging in offset from -14.99 to +14.99 m and 0-44 ms. Subset 2 (S2) includes the channel reflection with offsets ≥ ±15.0 m and 0-44 ms. The third subset (S3) includes the bedrock reflections, encompassing all offsets and limited in time from 44-100 ms.

Table 1: Processing applied to the 3D USR volume.

Data Processing			
Full Data Set	*	*Subset 1*	
Geometry Definition		NMO Corrections	~550 m/s
Binning	0.25x0.25 m	*Subset 2*	
Trace Editing		NMO Corrections	~1075 m/s
Elevation Statics		*Subset 3*	
Early Muting	5-sample taper	NMO Corrections	~1300 m/s
Surgical Muting	5-sample taper		
f-k Muting			
CMP Sort			
Residual Statics			
Subset Extraction	Offset segregation and muting, 3-sample tapers		
*Subset NMO Corrections			
Merge Subsets			
CMP Stack			
Butterworth Filtering	175-500 Hz, 18 dB/octave rolloff		
AGC	60-ms window		
3D Migration			

As seen in Figure 4, the bedrock reflection at ~52 ms is coherent at a wide range of offsets. Including it with the TSZ reflection would still lead to stretch-related artifacts, hence the necessity of a third subset. S1 and S2 were segregated based on the optimum window of the channel reflection, which is not identifiable until a source-to-receiver offset of 15 m. S3 was removed using a combination of early and tail mutes with a 3-sample overlap. Each subset was NMO corrected independently with its respective velocity function (Table 1), followed by merging all data and CMP stacking. A 175-500 Hz Butterworth filter with 18 dB/octave rolloff slopes and a 60-ms AGC window were also applied.

Several possible pitfalls exist with this processing scheme that should be noted. Cutting data in time without a taper can result in squared wavelet corners at the edges, which will mirror the filter operator applied and produce coherent high-frequency events that may stack constructively (Sloan et al., 2008). Even with a taper, dividing data in time and then recombining an lead to data seams. However, this was not a problem with this particular data set after selecting an appropriate taper overlap of 3 samples for the early and tail mutes. Static corrections should be calculated and applied prior to segregation as they would no longer be whole-trace shifts and may lead to erroneous results.

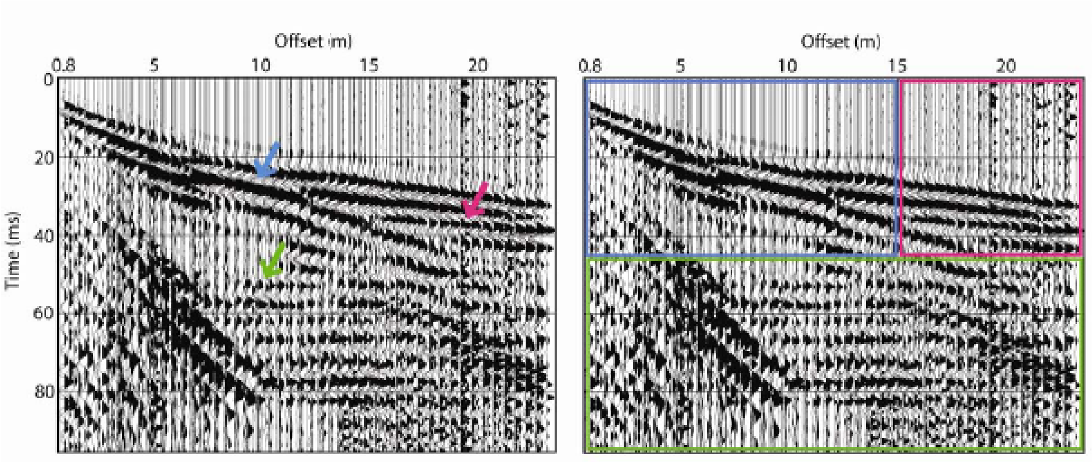

Figure 4: Raw shot gather indicating the presence of reflection hyperbolae before processing. Arrows mark the TSZ (blue), paleo-channel (pink), and bedrock (green). The same shot gather is displayed on the right showing the different subsets including S1 (blue), S2 (pink), and S3 (green). Data are displayed with a 175-500 Hz Butterworth filter with 18 dB/octave rolloff slopes and a 60-ms AGC window.

Results

Stacked sections were interpreted using a commercial seismic software package. Figure 5 shows a chair diagram with the interpreted TSZ reflection (blue), paleo-channel (pink), and bedrock (green). Figure 6 displays a 3D rendering of the surfaces. The TSZ, paleo-channel, and bedrock are located at ~5, 7, and 16 m, respectively. The interpreted channel features run approximately N-S and appears to dip slightly to the north. The channel features are coincident with a topographic low that can be identified in the aerial photograph in Figure 1 as the N-S trending linear surface expression. It is also worth noting that there is a creek that runs adjacent to the property and is within 30 m of the survey area. Figure 7 shows a time-amplitude slice from 30 ms. The two structural lows illustrated in Figure 6 are depicted by the black (left) and red (right) linear features. The channel surface in Figure 6 indicates that the two structural lows begin to merge into one towards the north. This is further supported by the 31-ms time slice in Figure 7 that shows the two features merging on the north side of the volume; however, this is also where the fold begins to decrease, which may have an effect on the interpretation.

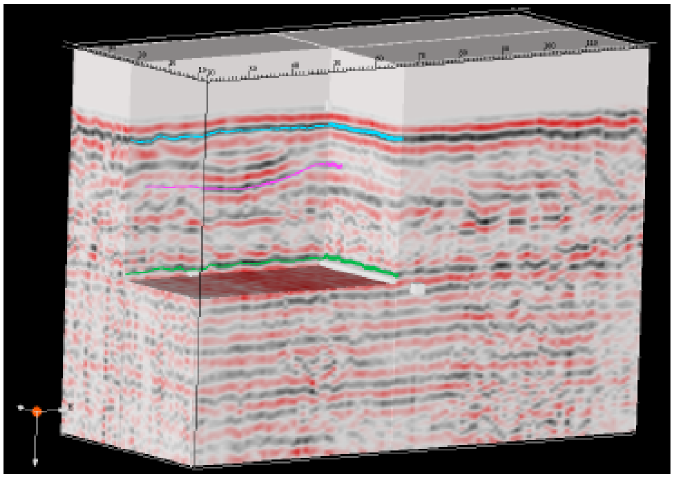

Figure 5: Chair diagram of the final stacked volume. The interpreted reflections are highlighted in blue (TSZ), pink (paleo-channel), and green (bedrock).

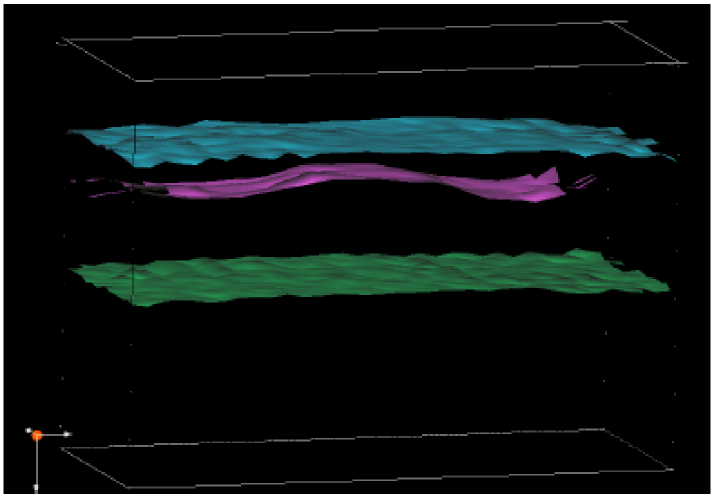

Figure 6: 3D graphic showing the TSZ (blue), channel (pink), and bedrock (green) surfaces.

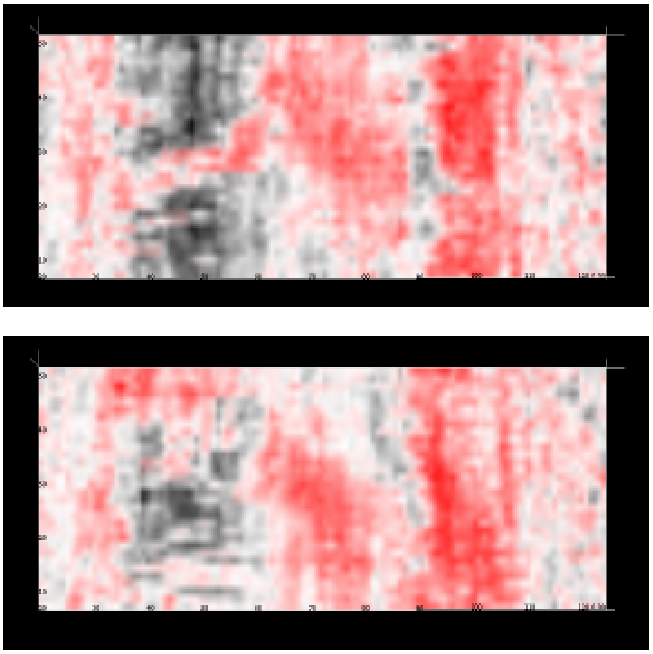

Figure 7: Time slice from 30 (top) and 31 ms (bottom). The paleo-channel is on the left side in black.

Conclusions

Processing the data by dividing them into offset-dependent subsets based on the respective optimum window of each reflection was successful in negating the detrimental effects of NMO-correcting intersecting reflection hyperbolae with a vertical velocity change of ~400-1650 m/s. Despite segregating the data set in time, data seams were not a problem in merging and stacking the subsets after an appropriate overlap taper was selected. However, it is possible to generate processing artifacts using subsets and caution should be exercised throughout the processing stage to ensure that quality control is maintained. The survey was successful in imaging multiple reflectors less than 20 m deep in three dimensions, including the top of the saturated zone, paleo-channel features, and bedrock. Future work includes a larger, more comprehensive 3D USR survey at the same site.

References

Bachrach, R., and Mukerji, T., 2004a, Portable dense geophone array for shallow and very shallow 3D seismic reflection surveying—Part 1: Data acquisition, quality control, and processing, Geophysics, 69, 1443-1455.

Bachrach, R., and Mukerji, T., 2004b, Portable dense geophone array for shallow and very shallow 3D seismic reflection surveying—Part 2: 3D imaging tests, Geophysics, 69, 1456-1469.

Bradford, J. H., 2002, Depth characterization of shallow aquifers with seismic reflection, Part I—The failure of NMO velocity analysis and quantitative error prediction, Geophysics, 67, 89-97.

Bradford, J. H., 2002, Depth characterization of shallow aquifers with seismic reflection, Part II—Prestack depth migration and field examples, Geophysics, 67, 98-109.

Büker, F., Green, A. G., and Horstmeyer, H., 1998, Shallow 3-D seismic reflection surveying: Data acquisition and preliminary processing strategies, Geophysics, 63, 1434-1450.
Büker, F., Green, A. G., and Horstmeyer, H., 2000, 3-D high-resolution reflection seismic imaging of unconsolidated glacial and glaciolacustrine sediments: processing and interpretation, Geophysics, 65, 18-34.
Lanz, E., Pugin, A., Green, A., and Horstmeyer, H., 1996, Results of 2- and 3-D high-resolution seismic reflection surveying of surficial sediments, Geophysical Research Letters, 23, 491-494.
Miller, R. D., and Xia, J., 1998, Large near-surface velocity gradients on shallow seismic reflection data, Geophysics, 63, 1348-1356.
Sloan, S. D., Steeples, D. W., and Malin, P. E., 2008, Acquisition and processing pitfall associated with clipping near-surface seismic reflection traces, Geophysics, 73, W1-W5.
Spitzer, R., Nitsche, F. O., Green, A. G., and Horstmeyer, H., 2003, Efficient acquisition, processing, and interpretation strategy for shallow 3D seismic surveying: A Case Study, Geophysics, 68, 1792-1806.

Acknowledgements

The authors would like to thank the Spring 2005 Near-Surface Seismology class for their time in the field and Sally Hayden for editorial assistance. This research was supported by the Office of Science (BER), U.S. Department of Energy, grant DE-FG02-03ER63656. However, any opinions, conclusions, or recommendations expressed herein are those of the authors and do not necessarily reflect the views of the DOE.